JOINT INSTITUTE FOR NUCLEAR RESEARCH

Bogoliubov Laboratory of Theoretical Physics

Proceedings

of the 2^{nd} South Africa - JINR Symposium

"Models and Methods in Few- and Many-Body Systems"

Edited by F Šimkovic

Dubna, Moscow region, Russia
September 8-10, 2010

Proceedings of the 2^{nd} South Africa - JINR SYMPOSIUM "Models and Methods in Few- and Many-Body Systems" (Dubna, September 5-10, 2010) / Eds. F. Šimkovic. -Dubna: JINR, 2010.-300p.;1 photo.

The 2^{nd} South Africa - JINR SYMPOSIUM "Models and Methods in Few- and Many-Body Systems" was organized by the Bogoliubov Laboratory of Theoretical Physics of the the Joint Institute for Nuclear Research in the period September 8-10, 2010. The main goal of the meeting was to extend the cooperation among physicists from the JINR and South Africa. This kind of brainstorming meeting discussed the scope, success and prospective of nuclear physics. However, related questions in particle, atomic, molecular, computational and mathematical physics and in other related areas were also considered. Speakers provided somewhat extended details of their research topic, questions addressed, and future trends in the field. The methods covered will serve as guidance not only for the pending collaboration but also as a substrate material for the students and young researchers at both sides that will enable them to participate in common research projects.

The financial support was provided by the Joint Institute for Nuclear Research and the National Research Foundation of South Africa.

Organizing Committee

chairman:

V. Voronov (JINR)

vice-chairman:

S. Sofianos (UNISA)
F. Šimkovic (JINR)

Members of the organizing committee:

Z. Vilakazi (iThemba LABS)
S. Rakityansky (Uni-Pretoria)
D. Heiss (Uni-Stellenbosch)
D. Kamanin (JINR)
A. Malykh (JINR)
S. Nedelko (JINR)
A. Belova, coordinator (JINR)


1959
БОРАТОРИЯ
ОРЕТИЧЕСКОЙ
ИЗИКИ
ИМЕНИ
БОГОЛЮБОВА

Contents

SESSION: *FEW-BODY*
Chairpersons: S.A. Sofianos and V.B. Belyaev

SESSION: *NUCLEAR STRUCTURE*
Chairpersons: R.G. Nazmitdinov and W.D. Heiss

SESSION: *NUCLEAR REACTIONS*
Chairpersons: R.V. Jolos and F. Šimkovic

SESSION: *HADRON SPECTROSCOPY*
Chairperson: S.B. Gerasimov

SESSION: FEW-BODY

Chairpersons: S.A. Sofianos and V.B. Belyaev

Power-series expansion of the multi-channel Jost matrix

S. A. Rakityansky* and N. Elander†

*Dept. of Physics, University of Pretoria, South Africa
†Div.of Molecular Physics, Dept. of Physics, Stockholm University, Stockholm, SE-106 91, Sweden

Abstract. For the Jost-matrix that describes the multi-channel scattering, the momentum dependencies at all the branching points on the Riemann surface are factorized analytically. The remaining single-valued matrix functions of the energy are expanded in the power-series near an arbitrary point in the complex energy plane. A systematic and accurate procedure has been developed for calculating the expansion coefficients. This makes it possible to obtain an analytic expression for the Jost-matrix (and therefore for the S-matrix) near an arbitrary point on the Riemann surface and thus to locate the spectral points (bound and resonant states) as the S-matrix poles.

Keywords: scattering, multi-channel, resonances, Jost matrix, effective-range expansion
PACS: 03.65.Nk, 03.65.Ge, 24.30.Gd

INTRODUCTION

Taylor-type power-series expansions are very common in physics. In quantum scattering theory, the most frequently used expansion of this kind is known as the effective-range expansion. In the case of a short-range potential, it represents the cotangent function of the scattering phase shift $\delta_\ell(k)$ in the form

$$k^{2\ell+1}\cot\delta_\ell(k)=\sum_{n=0}^{\infty}c_{\ell n}k^{2n} \tag{1}$$

where the right-hand side is a sum of terms proportional to even powers of the collision momentum k, and $c_{\ell n}$ are energy independent expansion coefficients. Originally (see, for example, Ref. [1] and Ref. [2] for a historical review), this expansion was suggested in nuclear physics for the S-wave nucleon-nucleon scattering in the form

$$k\cot\delta_0(k)=-\frac{1}{a}+\frac{1}{2}r_0k^2-Pr_0^3k^4+Qr_0^5k^6+\cdots\ , \tag{2}$$

where the first two parameters on the right-hand side, namely, a and r_0, were called the scattering length and the effective radius. The parameters in the higher terms of this expansion (P, Q, etc.) were known as the shape parameters. Such a name was given to them because they depended on the shape of a chosen NN-potential, while a and r_0 were determined mainy by the strength of the interaction and the range of the force.

Originally, some rather inconvenient integral formulae (see, for example, Ref. [2]) for calculating the parameters on the right hand side of Eq. (2) were suggested. The

expansion, however, was mainly used to parametrize the experimental data by choosing appropriate values for the first few coefficients. It is still frequently used for such purposes not only in nuclear physics but also for parametrizing the low-energy collisions between atoms and molecules (see, for example, Refs. [9, 10, 11, 12, 13, 14]). The expansion is also useful for simple analytical description of the scattering near the threshold energy. For example, in one of the latest works of this type the effective-range expansion is used to study the causality constraints on low-energy universality [15].

The traditional approach has one significant limitation, namely, the effective-range expansion is only applicable near the point $k = 0$, i.e. when the energy is close to the threshold. In Ref. [16], the expansion (1) was generalized in such a way that it was written as a series of powers of $(k - k_0)$ with an arbitrary complex k_0. In other words, instead of making the expansion around the threshold, one can do it around any point in the complex plane. By doing this, it is possible, for example, explore the complex k-plane in search for resonances. When $k_0 \neq 0$, the effective-range expansion is no longer a low-energy approximation.

Another limitation of the expansion (1) consists in the fact that it is written for a single-channel problem. For multi-channel problems, something similar was also suggested [17, 18, 19, 20, 21, 22]. In these papers, the authors tried to keep as much similarity with the single-channel case as possible. Their adherence to the functions of the type $\cot\delta$ limited the flexibility and clarity of the suggested equations.

In the present paper, we suggest a different approach to generalizing the effective-range expansion for multi-channel problems. Instead of considering the channel phase shifts and their cotangents, we look at the problem from a more general point of view. We obtain an expansion of the Jost matrix as a power series of $(E - E_0)$, where E is the energy and E_0 is an arbitrary point on the Riemann surface of energy. In other words, we are not limited to the threshold points, but can do the expansion of the Jost matrix practically anywhere on the Riemann surface. When the Jost matrix is obtained in an analytic form (first several terms of the expansion), the S matrix and all the observables can be easily calculated. Although it is possible, there is no need in introducing the generalized scattering length and other parameters. The Jost matrix expansion coefficients are more simple, clear, and convenient for this purpose.

MULTI-CHANNEL SCHRÖDINGER PROBLEM

Consider a quantum mechanical two-body problem which, after separation of the motion of its center of mass, is reduced to an effective problem of one body whose dynamics is governed by the Hamiltonian

$$H = H_0 + \mathscr{U} + h \tag{3}$$

consisting of the free-motion part H_0, the interaction operator $\mathscr{U}$, and the Hamiltonian h that describes the internal dynamics in the body (for example, the internal states of colliding atoms). Each internal state of the body corresponds to a different channel of

the scattering process. In general, there are infinite number of the internal states, i.e. the eigenstates of h,

$$h|n\rangle = E_n|n\rangle \ , \qquad n = 1,2,3,\ldots \infty \tag{4}$$

We assume that only N internal states are important. In other words, we approximate the internal Hamiltonian by the N terms

$$h \approx \sum_{n=1}^{N} |n\rangle E_n \langle n| \ . \tag{5}$$

The total Hamiltonian taken in the representation of the relative coordinate $\vec{r}$ and sandwiched between $\langle n|$ and $|n'\rangle$, becomes the $N \times N$ matrix

$$H_{nn'} = -\delta_{nn'} \frac{\hbar^2}{2\mu_n} \Delta_{\vec{r}} + \mathscr{U}_{nn'}(\vec{r}) + E_n \delta_{nn'} \ , \tag{6}$$

where μ_n is the reduced mass in the channel n. An eigenstate of this Hamiltonian, corresponding to the eigenvalue E, is a column-matrix

$$\Psi(E,\vec{r}) = \begin{pmatrix} \psi_1(E,\vec{r}) \\ \psi_2(E,\vec{r}) \\ \vdots \\ \psi_N(E,\vec{r}) \end{pmatrix} \tag{7}$$

where each row describes the relative motion in the corresponding channel. Therefore the eigenvalue equation $H\Psi = E\Psi$ is reduced to a set of coupled differential equations for the channel wave functions

$$\left[\frac{\hbar^2}{2\mu_n} \Delta_{\vec{r}} + (E - E_n) \right] \psi_n(E,\vec{r}) = \sum_{n'=1}^{N} \mathscr{U}_{nn'}(\vec{r}) \psi_{n'}(E,\vec{r}) \ . \tag{8}$$

The eigenenergies E_n of the internal Hamiltonian are the thresholds for the corresponding channels.

To avoid unnecessary complicated notation, we assume that the relative motion in each channel has a single value ℓ_n of the angular momentum. This does not compromise the generality of our consideration. Indeed, we can always treat the states with different values of angular momentum (or of any other quantum number) as different channels, but perhaps with the same threshold energies.

Therefore the angular dependence of the channel wave function can be factorized in the simple way

$$\psi_n(E,\vec{r}) = \frac{u_n(E,r)}{r} Y_{\ell_n m_n}(\theta,\varphi) \tag{9}$$

Substituting Eq. (9) into (8), then multiplying by $Y^*_{\ell_n m_n}(\theta,\varphi)$ and integrating over the angles, we obtain the system of coupled equations for the radial parts of the channel

wave functions,

$$\left[\partial_r^2 + k_n^2 - \frac{\ell_n(\ell_n+1)}{r^2}\right] u_n(E,\vec{r}) = \sum_{n'=1}^{N} V_{nn'}(r) u_{n'}(E,\vec{r}) \ , \tag{10}$$

where

$$V_{nn'}(r) = \frac{2\mu_n}{\hbar^2} \int Y^*_{\ell_n m_n}(\theta,\varphi) \mathscr{U}_{nn'}(\vec{r}) Y_{\ell_{n'} m_{n'}}(\theta,\varphi)\, d\Omega_{\vec{r}} \tag{11}$$

and the channel momentum is defined as

$$k_n = \sqrt{\frac{2\mu_n}{\hbar^2}(E - E_n)} \ . \tag{12}$$

In what follows, we assume that the interaction potential is non-singular and of the short range, i.e.

$$\int_0^\infty |V_{nn'}(r)|\, r\, dr < \infty \qquad \text{for all } n, n' \ . \tag{13}$$

This condition means that all matrix elements of the potential are less singular than $1/r^2$ at the origin and vanish faster than $1/r^2$ at infinity.

The boundary conditions for Eqs. (10) are derived from the requirement that any physical solution must be regular at the point $r = 0$ and have special behaviour when $r \to \infty$, which is different for bound, resonant, and scattering states. In Sect. , we consider these conditions in more detail.

MULTI-CHANNEL JOST MATRIX

A system of N linear second-order differential equations of the type (10) has $2N$ linearly independent column-solutions and only half of them are regular at the origin (see, for example, Ref. [23]). Combining these regular columns in a square matrix, we obtain the so called fundamental matrix of the regular solutions,

$$\Phi(E,r) = \begin{pmatrix} \phi_{11}(E,r) & \phi_{12}(E,r) & \cdots & \phi_{1N}(E,r) \\ \phi_{21}(E,r) & \phi_{22}(E,r) & \cdots & \phi_{2N}(E,r) \\ \vdots & \vdots & \vdots & \vdots \\ \phi_{N1}(E,r) & \phi_{N2}(E,r) & \cdots & \phi_{NN}(E,r) \end{pmatrix} \ . \tag{14}$$

Any other regular solution can only be a linear combination of the columns of this fundamental matrix. In particular, any physical solution of Eqs. (10) is a linear combination of the columns of the corresponding fundamental matrix,

$$\begin{pmatrix} u_1 \\ u_2 \\ \vdots \\ u_N \end{pmatrix} = C_1 \begin{pmatrix} \phi_{11} \\ \phi_{21} \\ \vdots \\ \phi_{N1} \end{pmatrix} + C_2 \begin{pmatrix} \phi_{12} \\ \phi_{22} \\ \vdots \\ \phi_{N2} \end{pmatrix} + \cdots + C_N \begin{pmatrix} \phi_{1N} \\ \phi_{2N} \\ \vdots \\ \phi_{NN} \end{pmatrix} \tag{15}$$

This guaranties its correct behaviour when $r \to 0$. As far as the asymptotic behaviour ($r \to \infty$) is concerned, its correct form can be achieved by proper choice of the combination coefficients C_n.

Under the condition (13), far away from the origin the right hand sides of Eqs.(10) vanish and these equations decouple,

$$\left[\partial_r^2 + k_n^2 - \frac{\ell_n(\ell_n+1)}{r^2}\right] u_n(E,\vec{r}) \approx 0 \ , \quad \text{when } r \to \infty \ . \tag{16}$$

In addition to the fact that for different n Eqs. (16) are independent from each other, their solutions are known. Indeed, these are the Riccati-Bessel equations. As a pair of linearly independent solutions of each of them, we can take the Riccati-Hankel functions $h_{\ell_n}^{(\pm)}(k_n r)$.

The system (16) consists of N linear second-order differential equations and thus has $2N$ linearly independent column-solutions which can be chosen in many different ways. The most convenient choice is the following set of $2N$ columns grouped in two square matrices

$$W^{(\mathrm{in})} = \begin{pmatrix} h_{\ell_1}^{(-)}(k_1 r) & 0 & \cdots & 0 \\ 0 & h_{\ell_2}^{(-)}(k_2 r) & \cdots & 0 \\ \vdots & \vdots & \vdots & \vdots \\ 0 & 0 & \vdots & h_{\ell_N}^{(-)}(k_N r) \end{pmatrix} \tag{17}$$

$$W^{(\mathrm{out})} = \begin{pmatrix} h_{\ell_1}^{(+)}(k_1 r) & 0 & \cdots & 0 \\ 0 & h_{\ell_2}^{(+)}(k_2 r) & \cdots & 0 \\ \vdots & \vdots & \vdots & \vdots \\ 0 & 0 & \vdots & h_{\ell_N}^{(+)}(k_N r) \end{pmatrix} \tag{18}$$

that represent the in-coming and out-going spherical waves in all the channels. These $2N$ columns form a basis in the space of solutions. In other words, any column-solution of Eq. (16) is a linear combination of these $2N$ columns. In particular, each column of matrix (14) at large distances becomes such a combination. The combination coefficients have two subscripts: one to indicate which column of (14) is expanded and the other is the summation subscript. Similarly to Eqs. (17, 18), we can group these coefficients in square matrices which do not depend on r. Thus we have

$$\Phi(E,r) \underset{r\to\infty}{\longrightarrow} W^{(\mathrm{in})}(E,r)F^{(\mathrm{in})}(E) + W^{(\mathrm{out})}(E,r)F^{(\mathrm{out})}(E) \ , \tag{19}$$

where, by analogy with the single-channel case (see, for example, Ref. [24]), the energy-dependent matrices $F^{(\mathrm{in/out})}(E)$ can be called Jost matrices. It is not difficult to show that they determine the S-matrix

$$S(E) = F^{(\mathrm{out})}(E)\left[F^{(\mathrm{in})}(E)\right]^{-1} \tag{20}$$

and thus give complete description of the underlying physical system. The spectral points $E = \mathscr{E}_n$ (bound states and resonances) are those where the inverse matrix $\left[F^{(\mathrm{in})}(E)\right]^{-1}$ does not exist, i.e. the points where

$$\det F^{(\mathrm{in})}(\mathscr{E}_n) = 0 \,. \tag{21}$$

TRANSFORMATION OF THE SCHRÖDINGER EQUATION

At large distances, the fundamental regular matrix $\Phi(E,r)$ is the linear combination (19) with the r-independent coefficient matrices $F^{(\mathrm{in/out})}(E)$. We can, however, look for $\Phi(E,r)$ in the same form at any point r, but with the coefficient matrices depending on r,

$$\Phi(E,r) \equiv W^{(\mathrm{in})}(E,r)\mathscr{F}^{(\mathrm{in})}(E,r) + W^{(\mathrm{out})}(E,r)\mathscr{F}^{(\mathrm{out})}(E,r) \,. \tag{22}$$

Now, instead of one unknown function $\Phi(E,r)$, we have two unknown functions, $\mathscr{F}^{(\mathrm{in})}(E,r)$ and $\mathscr{F}^{(\mathrm{out})}(E,r)$, which therefore cannot be independent of each other. In principle, we can arbitrarily impose any (reasonable) additional condition relating them. The most convenient is to demand that

$$W^{(\mathrm{in})}(E,r)\frac{\partial}{\partial r}\mathscr{F}^{(\mathrm{in})}(E,r) + W^{(\mathrm{out})}(E,r)\frac{\partial}{\partial r}\mathscr{F}^{(\mathrm{out})}(E,r) = 0 \,, \tag{23}$$

which is standard in the theory of differential equations, and is known as the Lagrange condition within the variation parameters method [25]. Looking at Eq. (19), we see that the Lagrange condition is certainly satisfied at large distances. Therefore, by imposing it, we do not change the asymptotic behaviour of the solution.

Starting from the coupled-channel radial Schrödinger equation (10), it is not difficult to obtain the corresponding equations for the new unknown matrices $\mathscr{F}^{(\mathrm{in/out})}(E,r)$. To this end, the ansatz (22) is simply substituted into Eq. (10). After the substitution, the equation is transformed and simplified, using the following: firstly, the fact that matrices $W^{(\mathrm{in/out})}(E,r)$ solve Eq. (16) (i.e. Eq. (10) without the right-hand side); secondly, the Lagrange condition (23); thirdly, introducing the diagonal matrix of the channel momenta

$$K = \begin{pmatrix} k_1 & 0 & \cdots & 0 \\ 0 & k_2 & \cdots & 0 \\ \vdots & \vdots & \vdots & \vdots \\ 0 & 0 & \cdots & k_N \end{pmatrix} \,; \tag{24}$$

and finally using known Wronskian of the Riccati-Hankel functions,

$$W^{(\mathrm{in})}\left[\partial_r W^{(\mathrm{out})}\right] - \left[\partial_r W^{(\mathrm{in})}\right] W^{(\mathrm{out})} = 2iK \,. \tag{25}$$

The derivation can be found in Ref. [26].

As a result, we obtain the following system of first-order differential matrix-equations

$$\partial_r \mathscr{F}^{(\mathrm{in})} = -\frac{1}{2i} K^{-1} W^{(\mathrm{out})} V \left[W^{(\mathrm{in})} \mathscr{F}^{(\mathrm{in})} + W^{(\mathrm{out})} \mathscr{F}^{(\mathrm{out})} \right] , \tag{26}$$

$$\partial_r \mathscr{F}^{(\mathrm{out})} = \frac{1}{2i} K^{-1} W^{(\mathrm{in})} V \left[W^{(\mathrm{in})} \mathscr{F}^{(\mathrm{in})} + W^{(\mathrm{out})} \mathscr{F}^{(\mathrm{out})} \right] , \tag{27}$$

which are equivalent to the initial second-order Schrödinger equation (10). Since these equations are of the first order, the boundary conditions for them can only be imposed at a single point. The natural way of doing this is to demand that matrix (22) is regular at the origin, then

$$\mathscr{F}^{(\mathrm{in})}(E,0) = \mathscr{F}^{(\mathrm{out})}(E,0) \tag{28}$$

because both $h_\ell^{(+)}(z)$ and $h_\ell^{(-)}(z)$ are singular at $z=0$, but their singularities exactly cancel each other in the combination

$$h_\ell^{(+)}(z) + h_\ell^{(-)}(z) \equiv 2 j_\ell(z) . \tag{29}$$

The choice of the common value for the functions in Eq. (28) determines the overall normalization of the fundamental matrix (22), because Eqs. (26,27) are linear and homogeneous. In the single-channel case, the regular solution is usually normalized in such a way that it coincides with the Riccati-Bessel function when $r \to 0$ [24]. From Eq. (29), it is clear that if we want that our approach gives the traditional single-channel solution when $N=1$, we should use the following boundary conditions for Eqs. (26,27)

$$\mathscr{F}^{(\mathrm{in})}(E,0) = \mathscr{F}^{(\mathrm{out})}(E,0) = \frac{1}{2} I , \tag{30}$$

where I is the diagonal unit matrix.

Thanks to the fact that the in-coming and out-going waves in the fundamental matrix (22) are factorized, it is easy to construct the physical solutions with proper asymptotics. For example, the bound states at large distances can have only the out-going waves. This is achieved by finding such combination coefficients in Eq. (15), i.e. in

$$u_n = \sum_{n'} \Phi_{nn'} C_{n'} = \sum_{n'n''} \left[W^{(\mathrm{in})}_{nn''} \mathscr{F}^{(\mathrm{in})}_{n''n'} + W^{(\mathrm{out})}_{nn''} \mathscr{F}^{(\mathrm{out})}_{n''n'} \right] C_{n'} \tag{31}$$

that all the columns involving the in-coming waves, disappear when $r \to \infty$. In other words, for the physical wave function of a bound state, we have

$$\sum_{n'} \mathscr{F}^{(\mathrm{in})}_{nn'}(E,r) C_{n'} \underset{r\to\infty}{\longrightarrow} \sum_{n'} F^{(\mathrm{in})}_{nn'}(E) C_{n'} = 0 . \tag{32}$$

The last equation is a system of linear homogeneous equations for the unknown combination coefficients C_n. It has a non-trivial solution if and only if the corresponding determinant is zero. This results in Eq. (21) which can have solutions at discrete values

of the energy. Actually, the resonant states are found in the same way, i.e. by solving the same Eq. (21), but at complex values of $\mathscr{E}_n$. This approach therefore offers a unified way of finding both the bound and resonant states as well as the S-matrix (20) for the scattering states. The corresponding physical wave functions are obtained with correct asymptotic behaviour (analytically factorized Riccati-Hankel functions).

RIEMANN SURFACE

For a fixed (generally speaking, complex) value of the energy E, each of the N channel momenta (12) can have two different values

$$k_n = \pm\sqrt{\frac{2\mu_n}{\hbar^2}(E-E_n)}\,, \qquad n = 1,2,\ldots,N\,, \tag{33}$$

depending on the choice of the sign in front of the square root. On the other hand, all these momenta are involved as papameters in Eqs. (26, 27). This means that the Jost matrices $F^{(\mathrm{in/out})}(E)$ are not single-valued functions of E. At each point E, the Jost matrices have 2^N different values.

In complex analysis, the multi-valued functions are treated as single-valued, but defined on a multi-layered complex surface which is called Riemann surface. In our case, each layer (sheet) of this surface corresponds to a different combination of the signs of N channel momenta, and thus the Riemann surface of the energy consists of 2^N sheets.

When we move around a threshold point, we go from one layer to another. Indeed, a point on a circle centered at the threshold E_n, can be parametrized as $E = E_n + \rho\exp(i\varphi)$, where ρ is the distance from E_n and φ is the polar angle. The corresponding channel momentum

$$k_n = \sqrt{\frac{2\mu_n\rho}{\hbar^2}}e^{i\varphi/2} \tag{34}$$

changes its sign after one full circle ($\varphi = 2\pi$) and comes back to its initial value after two full circles ($\varphi = 4\pi$). This means that the sheets of the Riemann surface are connected to each other and thus form a united multi-layer manifold. The threshold points E_n ($n = 1,2,\ldots,N$) are the branching points on this manifold. By moving around these points, we can continuously reach any of the 2^N sheets.

In principle, we can construct the Riemann surface rather arbitrarily by making cuts and appropriate connections of the layers. In quantum theory, it is standard that each layer is cut along the real energy axis. The cut starts at the branching point and goes to infinity in the positive direction. The edges of the cuts of different layers are interconnected in such a way that the corresponding channel momenta appropriately change their signs.

The simplest two-layer Riemann surface for the single-channel case is easy to visualize (see, Fig. 1). The two-channel problem with two branching points and four

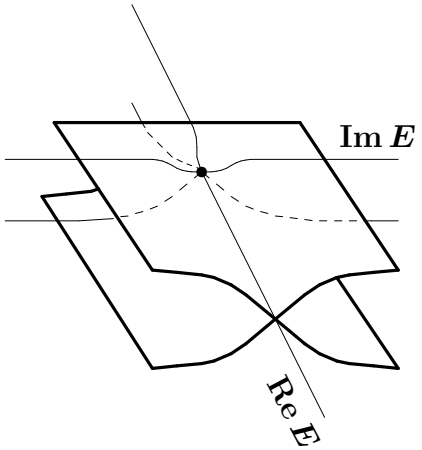

FIGURE 1. Riemann surface of the energy for a single-channel problem.

interconnected layers is much more involved. These connections for the three intervals, $E < E_1$, $E_1 < E < E_2$, and $E > E_2$ are schematically shown in Fig. 2) [27]. When $N > 2$,

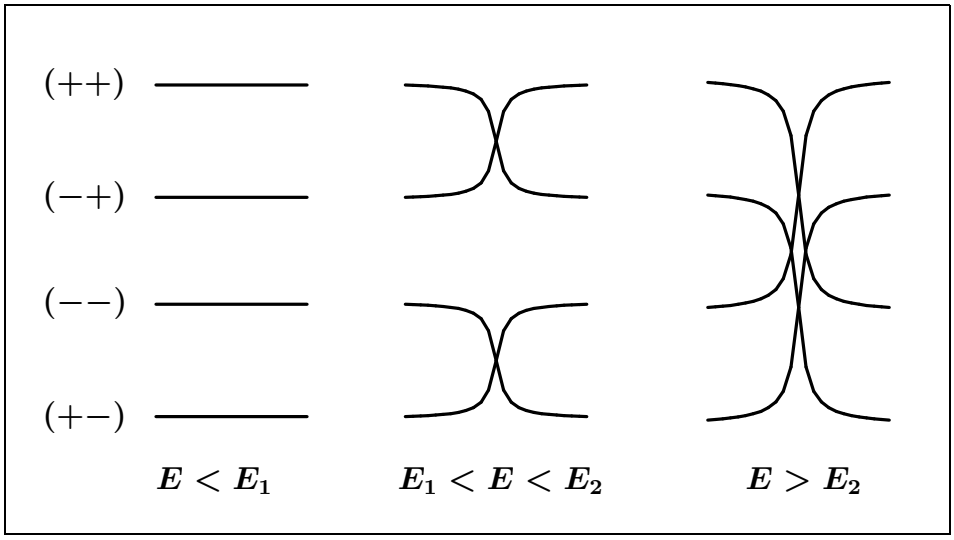

FIGURE 2. Schematically shown interconnections of the layers of the Riemann surface for a two-channel problem at three different energy intervals. The layers correspond to different combinations of the signs (indicated in brackets) of $\mathrm{Im}\, k_1$ and $\mathrm{Im}\, k_2$.

the surface is so complicated that it is not worthwhile even trying to visualize it.

In the present paper, we construct the Jost matrices in such a way that in their matrix elements the dependences on odd powers of all channel momenta are factorized analytically (see Sec.). The remaining matrices depend only on even powers of all the momenta k_n and thus are single-valued functions of variable E. This saves us the trouble of dealing with the complicated multi-layered manifold. Moreover, using the analytically factorized dependence on k_n, we can establish some of the symmetry properties of Jost matrices, i.e. we can relate their values at some points belonging to different layers of

the Riemann surface (see Sec.).

COMPLEX ROTATION

When the potential is cut off at certain radius R, the right-hand sides of Eqs. (26,27) vanish for $r > R$ and the derivatives $\partial_r \mathscr{F}^{(\mathrm{in/out})}$ become zero, i.e. these functions do not change beyond this point. Therefore, in the spirit of the variable phase approach, the functions $\mathscr{F}^{(\mathrm{in/out})}(E,r)$ are the Jost matrices for the potential which is cut off at the point r. In general, when the potential asymptotically vanishes at large distances, we have

$$\mathscr{F}^{(\mathrm{in/out})}(E,r) \underset{r\to\infty}{\longrightarrow} F^{(\mathrm{in/out})}(E) \ . \tag{35}$$

Therefore, the Jost matrices can be calculated by numerical integration of the differential equations (26,27) from $r = 0$ up to a sufficiently large radius R where the limit (35) is reached within a required accuracy.

This works perfectly for real values of the energy E. However, when we consider complex energies (for example, in search for resonances), a technical difficulty arises. This difficulty is caused by the asymptotic behaviour of the Riccati-Hankel functions [28],

$$h_\ell^{(\pm)}(kr) \underset{|kr|\to\infty}{\longrightarrow} \mp i \exp\left(\pm ikr \mp i\frac{\ell\pi}{2}\right) \ . \tag{36}$$

As is seen, when k is complex, either $h_\ell^{(+)}(kr)$ or $h_\ell^{(-)}(kr)$ exponentially diverges, depending on the sign of $\mathrm{Im}\, k$. As a result, either the first or the second of the equations (26,27) does not give a numerically convergent solution. This difficulty is circumvented by using the deformed integration path shown in Fig. 3. Instead of integrating the differential equations along the real axis from $r = 0$ to $r = R$, we can reach the final point via the intermediate point $r = R'$ in the complex plane. Moreover, we can safely ignore the arc $R'R$ since the potential is practically zero at that distance.

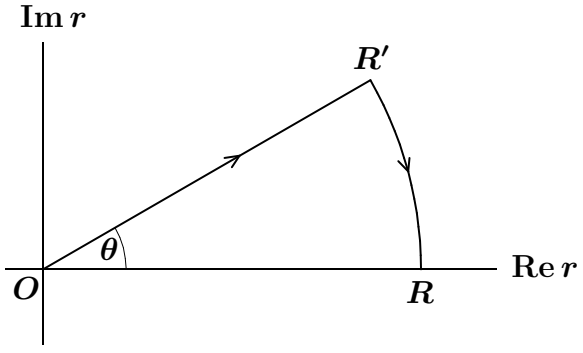

FIGURE 3. A deformed path for integrating the differential equations.

Why does this complex rotation help? The answer can be found by looking at Eq. (36). Indeed, the asymptotic behaviour (divergent or convergent) of the functions $h_\ell^{(\pm)}(kr)$ is

determined by the sign of $\mathrm{Im}\,(kr)$. If $k = |k|e^{i\varphi}$, we can always find such a rotation angle θ in $r = |r|e^{i\theta}$ that the product

$$kr = |kr|e^{i(\varphi+\theta)}$$

has either positive or negative (or even zero) imaginary part. Various technical details of using complex rotation in calculating the Jost functions and Jost matrices can be found in Refs. [29, 30, 31, 32, 33, 34, 35, 36, 37, 38].

FACTORIZATION

Eqs. (26,27) are very convenient for numerical calculation of the Jost matrices. However, for the purpose of power-series expansion of these matrices, we need to further transform them. The idea of such a transformation is based on the relation between the two pairs of linearly independent solutions of the Riccati-Bessel equation, namely, between the Riccati-Hankel functions $h_\ell^{(\pm)}$ and the pair of Riccati-Bessel j_ℓ and Riccati-Neumann y_ℓ functions,

$$h_\ell^{(\pm)}(z) = j_\ell(z) \pm i y_\ell(z) \; . \tag{37}$$

Introducing the diagonal matrices

$$J = \frac{1}{2}\left[W^{(\mathrm{in})} + W^{(\mathrm{out})}\right] = \begin{pmatrix} j_{\ell_1}(k_1 r) & 0 & \cdots & 0 \\ 0 & j_{\ell_2}(k_2 r) & \cdots & 0 \\ \vdots & \vdots & \vdots & \vdots \\ 0 & 0 & \vdots & j_{\ell_N}(k_N r) \end{pmatrix} , \tag{38}$$

$$Y = \frac{i}{2}\left[W^{(\mathrm{in})} - W^{(\mathrm{out})}\right] = \begin{pmatrix} y_{\ell_1}(k_1 r) & 0 & \cdots & 0 \\ 0 & y_{\ell_2}(k_2 r) & \cdots & 0 \\ \vdots & \vdots & \vdots & \vdots \\ 0 & 0 & \vdots & y_{\ell_N}(k_N r) \end{pmatrix} , \tag{39}$$

as well as the new unknown matrices

$$\mathscr{A}(E,r) = \mathscr{F}^{(\mathrm{in})}(E,r) + \mathscr{F}^{(\mathrm{out})}(E,r) \; , \tag{40}$$

$$\mathscr{B}(E,r) = i\left[\mathscr{F}^{(\mathrm{in})}(E,r) - \mathscr{F}^{(\mathrm{out})}(E,r)\right] \; , \tag{41}$$

we obtain another (equivalent) representation of the fundamental matrix of regular solutions,

$$\Phi(E,r) = J(E,r)\mathscr{A}(E,r) - Y(E,r)\mathscr{B}(E,r) \; . \tag{42}$$

Combining Eqs. (26,27), it is easy to obtain an equivalent system of differential equations for the new unknown matrices,

$$\partial_r \mathscr{A} = -K^{-1} Y V \left(J\mathscr{A} - Y\mathscr{B}\right) \; , \tag{43}$$

$$\partial_r \mathscr{B} = -K^{-1} J V \left(J\mathscr{A} - Y\mathscr{B}\right) \; , \tag{44}$$

with the boundary conditions

$$\mathscr{A}(E,0) = I\,, \qquad \mathscr{B}(E,0) = 0\,, \tag{45}$$

which immediately follow from (30). Similarly to the limit (35), these matrices also should converge to their asymptotic values

$$\mathscr{A}(E,r) \underset{r\to\infty}{\longrightarrow} A(E)\,, \qquad \mathscr{B}(E,r) \underset{r\to\infty}{\longrightarrow} B(E)\,, \tag{46}$$

from which the Jost matrices can be obtained,

$$F^{(\mathrm{in})}(E) = \frac{1}{2}\left[A(E) - iB(E)\right]\,, \qquad F^{(\mathrm{out})}(E) = \frac{1}{2}\left[A(E) + iB(E)\right]\,. \tag{47}$$

Now, we use the fact that the Riccati-Bessel and Riccati-Neumann functions can be represented by absolutely convergent series,

$$j_\ell(kr) = \left(\frac{kr}{2}\right)^{\ell+1} \sum_{n=0}^{\infty} \frac{(-1)^n\sqrt{\pi}}{\Gamma(\ell+3/2+n)n!}\left(\frac{kr}{2}\right)^{2n} = k^{\ell+1}\tilde{j}_\ell(E,r)\,, \tag{48}$$

$$y_\ell(kr) = \left(\frac{2}{kr}\right)^{\ell} \sum_{n=0}^{\infty} \frac{(-1)^{n+\ell+1}}{\Gamma(-\ell+1/2+n)n!}\left(\frac{kr}{2}\right)^{2n} = k^{-\ell}\tilde{y}_\ell(E,r)\,, \tag{49}$$

where we factorize the the functions $\tilde{j}_\ell$ and $\tilde{y}_\ell$, which do not depend on odd powers of k and thus are single-valued functions of the energy E.

Let us look for the matrices $\mathscr{A}$ and $\mathscr{B}$ in the form

$$\mathscr{A}_{ij} = \frac{k_j^{\ell_j+1}}{k_i^{\ell_i+1}}\tilde{\mathscr{A}}_{ij}\,, \qquad \mathscr{B}_{ij} = k_i^{\ell_i}k_j^{\ell_j+1}\tilde{\mathscr{B}}_{ij}\,, \tag{50}$$

where certain powers of the channel momenta are factorized in each individual matrix element. When the representations (48, 49, 50) are substituted into Eqs. (43,44), all the channel-momenta factors cancel out, and we remain with the equations for the tilded functions,

$$\partial_r\tilde{\mathscr{A}} = -\tilde{Y}V\left(\tilde{J}\tilde{\mathscr{A}} - \tilde{Y}\tilde{\mathscr{B}}\right)\,, \tag{51}$$

$$\partial_r\tilde{\mathscr{B}} = -\tilde{J}V\left(\tilde{J}\tilde{\mathscr{A}} - \tilde{Y}\tilde{\mathscr{B}}\right)\,, \tag{52}$$

where the matrices $\tilde{J}$ and $\tilde{Y}$ differ from (38) and (39) by the diagonal factors,

$$J = \begin{pmatrix} k_1^{\ell_1+1} & 0 & \cdots & 0 \\ 0 & k_2^{\ell_2+1} & \cdots & 0 \\ \vdots & \vdots & \vdots & \vdots \\ 0 & 0 & \vdots & k_N^{\ell_N+1} \end{pmatrix}\tilde{J}\,, \qquad Y = \begin{pmatrix} k_1^{-\ell_1} & 0 & \cdots & 0 \\ 0 & k_2^{-\ell_2} & \cdots & 0 \\ \vdots & \vdots & \vdots & \vdots \\ 0 & 0 & \vdots & k_N^{-\ell_N} \end{pmatrix}\tilde{Y}\,. \tag{53}$$

The main advantage of Eqs. (51,52) is that they do not involve any coefficients or functions depending on odd powers of the channel momenta. This means that their solutions, i.e. the matrices $\tilde{\mathscr{A}}(E,r)$ and $\tilde{\mathscr{B}}(E,r)$, are single-valued functions of the energy. The multi-valuedness of the initial matrices $\mathscr{A}(E,r)$ and $\mathscr{B}(E,r)$ as well as the fact that they are defined on a complicated Riemann surface, are determined by the momentum-factors separated in Eqs. (50).

SYMMETRY OF THE JOST MATRICES

As an example of usefulness of the analytic structure of the Jost matrices, established in the previous section, let us consider the relation between $F^{(\mathrm{in})}$ and $F^{(\mathrm{out})}$. If $\tilde{A}(E)$ and $\tilde{B}(E)$ are the asymptotic values of $\tilde{\mathscr{A}}(E,r)$ and $\tilde{\mathscr{B}}(E,r)$, respectively, then according to Eqs. (47, 50), we have the following semi-analytic expressions for the Jost matrices

$$F^{(\mathrm{in})}_{mn} = \frac{k_n^{\ell_n+1}}{2k_m^{\ell_m+1}}\tilde{A}_{mn} - \frac{ik_m^{\ell_m}k_n^{\ell_n+1}}{2}\tilde{B}_{mn} , \tag{54}$$

$$F^{(\mathrm{out})}_{mn} = \frac{k_n^{\ell_n+1}}{2k_m^{\ell_m+1}}\tilde{A}_{mn} + \frac{ik_m^{\ell_m}k_n^{\ell_n+1}}{2}\tilde{B}_{mn} . \tag{55}$$

If we change the signs of all the channel momenta to the opposite, the matrices $\tilde{A}(E)$ and $\tilde{B}(E)$ remain unchanged while the factorized momenta generate a common factor $(-1)^{\ell_m+\ell_n} = (-1)^{\ell_m-\ell_n}$ and the sign between the two terms in Eqs. (54, 55) is also changed to the opposite. In other words,

$$F^{(\mathrm{in})}_{mn}(-k_1,-k_2,\ldots,-k_N) = (-1)^{\ell_m+\ell_n}F^{(\mathrm{out})}_{mn}(k_1,k_2,\ldots,k_N) , \tag{56}$$

where for the sake of clarity, we replaced the single independent variable E with the set of channel momenta. This means that the two Jost matrices $F^{(\mathrm{in})}$ and $F^{(\mathrm{out})}$ are not completely independent. Their values at different points on the Riemann surface are the same. The S matrix can be re-written as

$$S_{mn} = (-1)^{\ell_m+\ell_n}F^{(\mathrm{in})}_{mn}(-k_1,-k_2,\ldots,-k_N)\left[F^{(\mathrm{in})}_{mn}(k_1,k_2,\ldots,k_N)\right]^{-1} , \tag{57}$$

which is well known in the case of a single-channel problem. The symmetry property (56) is the simplest one (but perhaps the most important) and can be established in a different way (see, for example, Ref. [24]). Its simple proof is given here to merely demonstrate how the factorized semi-analytic expressions (54, 55) can be used. Establishing the other symmetry properties is beyond the scope of the present paper.

POWER-SERIES EXPANSION

Eqs. (51,52) define the matrices $\tilde{\mathscr{A}}(E,r)$ and $\tilde{\mathscr{B}}(E,r)$ that are single-valued functions of the parameter E, i.e. they are defined on a single sheet of the complex E-plane.

Moreover, since the matrices $\tilde{J}(E,r)$ and $\tilde{Y}(E,r)$ are holomorphic, the solutions of these equations are holomorphic as well (Poincare theorem [39]). This means that $\tilde{\mathscr{A}}(E,r)$ and $\tilde{\mathscr{B}}(E,r)$ can be expanded in the power series around an arbitrary point E_0 on the complex plane of the energy,

$$\tilde{\mathscr{A}}(E,r) = \sum_{n=0}^{\infty}(E-E_0)^n\alpha_n(E_0,r)\ , \tag{58}$$

$$\tilde{\mathscr{B}}(E,r) = \sum_{n=0}^{\infty}(E-E_0)^n\beta_n(E_0,r)\ , \tag{59}$$

where the unknown expansion coefficients α_n and β_n are $(N\times N)$-matrices depending not only on variable r but also on the choice of the point E_0.

Eqs. (51,52) involve matrices $\tilde{J}$ and $\tilde{Y}$ for which we can obtain the expansions of the same kind but with known coefficients,

$$\tilde{J}(E,r) = \sum_{n=0}^{\infty}(E-E_0)^n\gamma_n(E_0,r)\ , \tag{60}$$

$$\tilde{Y}(E,r) = \sum_{n=0}^{\infty}(E-E_0)^n\eta_n(E_0,r)\ . \tag{61}$$

Simple recurrency relations for calculating the expansion coefficients (matrices) $\gamma_n(E_0,r)$ and $\eta_n(E_0,r)$ are derived in the Appendix .

Substituting the expansions (58, 59, 60, 61) into Eqs. (51,52), and equating the coefficients of the same powers of $(E-E_0)$, we obtain the following system of differential equations for the unknown matrices α_n and β_n

$$\partial_r\alpha_n = -\sum_{i+j+k=n}\eta_i V(\gamma_j\alpha_k-\eta_j\beta_k)\ , \tag{62}$$

$$\partial_r\beta_n = -\sum_{i+j+k=n}\gamma_i V(\gamma_j\alpha_k-\eta_j\beta_k)\ , \qquad n=0,1,2,\ldots \tag{63}$$

The boundary conditions (45) are independent of E. As is easy to see, this implies that

$$\alpha_n(E_0,0)=\delta_{n0}I\ , \qquad \beta_n(E_0,0)=0\ . \tag{64}$$

In other words, all these matrices vanish at the origin, except for the matrix α_0 which becomes a diagonal unit matrix at $r=0$.

If we denote the asymptotic values of the matrices α_n and β_n as

$$\alpha_n(E_0,r)\underset{r\to\infty}{\longrightarrow}a_n(E_0)\ , \qquad \text{and} \qquad \beta_n(E_0,r)\underset{r\to\infty}{\longrightarrow}b_n(E_0)\ , \tag{65}$$

then in vicinity of any chosen point E_0 on the Riemann surface, we can obtain semi-analytic expressions for the Jost matrices in the form

$$F_{mn}^{(\mathrm{in})} = \sum_{j=0}^{M} (E-E_0)^j \left[\frac{k_n^{\ell_n+1}}{2k_m^{\ell_m+1}} (a_j)_{mn} - \frac{ik_m^{\ell_m} k_n^{\ell_n+1}}{2} (b_j)_{mn} \right] , \tag{66}$$

$$F_{mn}^{(\mathrm{out})} = \sum_{j=0}^{M} (E-E_0)^j \left[\frac{k_n^{\ell_n+1}}{2k_m^{\ell_m+1}} (a_j)_{mn} + \frac{ik_m^{\ell_m} k_n^{\ell_n+1}}{2} (b_j)_{mn} \right] , \tag{67}$$

where M is the maximal power of our expansion. The non-analytic quantities in Eqs. (66, 67), i.e. the matrices a_j and b_j, are obtained by numerical integration of differential equations (62, 63) with the boundary conditions (64) from $r = 0$ to certain large value $r = R$ (in some cases, this should be done along the deformed contour shown in Fig. 3). For a given energy E, the choice of the sheet of the Riemann surface, where the Jost matrices are considered, is done by appropriately choosing the signs in front of the square roots (33) for calculating the channel momenta used in Eqs. (66, 67). The central point E_0 of the expansion as well as the numerically obtained matrices a_j and b_j are the same for all the layers of the Riemann surface.

In principle, the power-series expansions (66, 67) includes infinite number of terms. In practice, however, we may take into account just a few terms ($M < \infty$) and therefore have to solve certain number of equations in the infinite system (62, 63). It should be emphasized that not all equations of this system are coupled to each other. Indeed, due to the condition $i + j + k = n$ on their right-hand sides, the equations for α_M and β_M (for any $M \geqslant 0$) are only linked to the corresponding equations with $n < M$. For example, the first pair of equations,

$$\partial_r \alpha_0 = -\eta_0 V (\gamma_0 \alpha_0 - \eta_0 \beta_0) , \tag{68}$$

$$\partial_r \beta_0 = -\gamma_0 V (\gamma_0 \alpha_0 - \eta_0 \beta_0) , \tag{69}$$

is self-contained and is not linked to any other equation of the system. The second pair is linked only to the first one, and so on. This means that by considering a finite number of equations of this system, we do not introduce an additional truncation error.

CONSTRUCTING POTENTIALS WITH GIVEN SPECTRUM

There are many possible applications of the expansions (66, 67). An example where they undoubtedly are very convenient, is the problem of adjusting the parameters of a multi-channel potential in such a way that it generates a bound or a resonant state at a given energy E_0. Indeed, for this purpose it is needed to find such parameters that

$$\det F^{(\mathrm{in})}(E_0) = 0 . \tag{70}$$

If we perform the expansion around the given point E_0 then the sum on the right-hand side of Eq. (66) includes only one non-zero term ($j = 0$). Therefore to put a spectral

point at the energy E_0, we need to minimize the function

$$f(x_1,x_2,\ldots,x_L) = \left|\det\left[\frac{k_n^{\ell_n+1}}{2k_m^{\ell_m+1}}(a_0)_{mn} - \frac{ik_m^{\ell_m}k_n^{\ell_n+1}}{2}(b_0)_{mn}\right]\right| , \tag{71}$$

where $x_1,x_2,\ldots,x_L$ are the parameters of the adjusted potential. For each choice of the parameters, we need to solve the system of two differential equations (68, 69) only once, which is not difficult to do.

NUMERICAL EXAMPLE

In order to demonstrate the efficiency and accuracy of the proposed method, we do numerical calculations for a well-studied model. For this purpose, we use the two-channel potential suggested by Noro and Taylor [40]

$$V(r) = \begin{pmatrix} -1.0 & -7.5 \\ -7.5 & 7.5 \end{pmatrix} r^2 e^{-r} , \tag{72}$$

which is given in arbitrary units such that $\mu_1 = \mu_2 = \hbar c = 1$. The threshold energies for the two channels of the Noro and Taylor model are $E_1 = 0$ and $E_2 = 0.1$, and the angular momentum is zero in both channels, $\ell_1 = \ell_2 = 0$. This potential has an attractive well in the first channel, a repulsive barrier in the second, and rather strong coupling between the channels. As a result, it generates a rich spectrum of bound and resonant states (see Fig. 4) as well as a non-trivial energy dependence of the channel and transition cross sections (see Figs. 5, 6, and 7) [26]. This model is therefore a difficult testing ground for any new method designed for describing multi-channel processes.

As a first test, we do the power series expansions of the Jost matrices (66, 67) around the point $E_0 = 5 + i0$ on the real axis and with six terms, i.e. with $M = 5$. The central point of the expansion was chosen to be not far from the first resonance, where the channel cross sections have some non-trivial energy dependence. As is seen in Figs. 5, 6, and 7, the thin curves representing the approximate cross sections, reproduce the corresponding exact cross sections rather well within a wide energy interval.

Since the approximate Jost matrices (66, 67) coincide with the exact matrices on a segment of the real axis, they must be valid also at the nearby points of the complex energy surface. Comparing the exact and approximate values of $\det F^{(\mathrm{in})}(E)$ at complex E around the point E_0 on the third sheet $(--)$ of the Riemann surface (see Fig. 2), we found the domains within which the relative accuracy is better than 1%, 5%, and 10%. These domains are shown in Fig. 8.

It is seen that the first resonance is within the domain of 1% accuracy and therefore must be reproduced by the approximate Jost matrix. And indeed, its determinant has zero at $E = 4.768178 - i0.000686$ which is very close to the exact value $E = 4.768197 - i0.000710$. With more terms in the expansion, the difference becomes

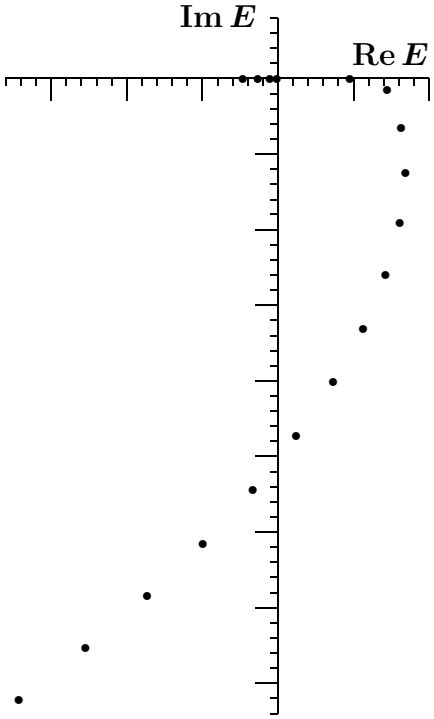

FIGURE 4. Spectral points generated by the potential (72) and given in Table 1.

smaller, and with $M = 10$ all the digits are the same.

The other place where we tested the expansion, was the point $E_0 = 7.5 - i2.0$ on the third sheet $(--)$ of the Riemann surface. This point is almost in the middle between the second and the third resonances. Fig. 9 shows how the domain of 1% accuracy increases with increasing number of terms ($M = 5, 7, 10$) in the expansions (66, 67). As is seen in Fig. 9, even with $M = 5$ both resonances are reproduced relatively well (the filled and open circles represent the exact and approximate positions of the resonances). The zeros of the exact Jost matrix determinat are at $E = 7.241200 - i0.755956$ and $E = 8.171217 - i3.254166$ while the expansion with $M = 5$ gives $E = 7.131204 - i0.768670$ and $E = 8.241795 - i2.982867$. We deliberately chose the point E_0 far away from both resonances. If it is close to any of them, the resonance can be found very accurately.

CONCLUSION

In the present paper, we show that each matrix element of multi-channel Jost matrix can be written as a sum of two terms, and each term can be factorized in such a way that it assumes the form of a product of certain combination of the channel momenta k_n times an analytic single-valued function of the energy E. This means that all the branching points of the Riemann energy-surface are given in the Jost matrix explicitly via the channel-momentum factors. The remaining energy-dependent factors in all its matrix elements are defined on single energy plane which does not have any branching points

TABLE 1. Spectral points $E = E_r - i\Gamma/2$ generated by the potential (72) and shown in Fig. 4.

E_r	Γ	Γ_1	Γ_2
-2.314391	0	0	0
-1.310208	0	0	0
-0.537428	0	0	0
-0.065258	0	0	0
4.768197	0.001420	0.000051	0.001369
7.241200	1.511912	0.363508	1.148404
8.171217	6.508332	1.596520	4.911812
8.440526	12.562984	3.186169	9.376816
8.072643	19.145630	4.977663	14.167967
7.123813	26.025337	6.874350	19.150988
5.641023	33.070140	8.816746	24.253394
3.662702	40.194674	10.768894	29.425779
1.220763	47.339350	12.709379	34.629971
-1.657821	54.460303	14.624797	39.835506
-4.949904	61.523937	16.507476	45.016461
-8.635366	68.503722	18.352084	50.151638
-12.696283	75.378773	20.155213	55.223560
-17.117760	82.129712	21.915313	60.214399

anymore.

For these energy-dependent functions, we derive a system of first-order differential equations. Then, using the fact that the functions are analytic, we expand them in the power series and obtain a system of differential equations that determine the expansion coefficients. A systematic procedure developed in the present paper, allows us to accurately calculate the power-series expansion of the Jost matrices practically at any point on the Riemann surface of the energy. Actually, the expansion is done for the single-valued functions of the energy, while the choice of the sheet of the Riemann surface is done by appropriately choosing the signs of the channel momenta in the momentum-dependent factors.

The expansion suggested in the present paper, makes it possible to obtain a semi-analytic expression for the Jost-matrix (and therefore for the S-matrix) near an arbitrary point on the Riemann surface and thus to locate the spectral points (bound and resonant states) as the S-matrix poles. Alternatively, the expansion can be used to parametrise experimental data, where the unknown expansion coefficients are the fitting parameters. Such a parametrisation will have the correct analytic properties. The efficiency and accuracy of the suggested expansion is demonstrated by an example of a two-channel

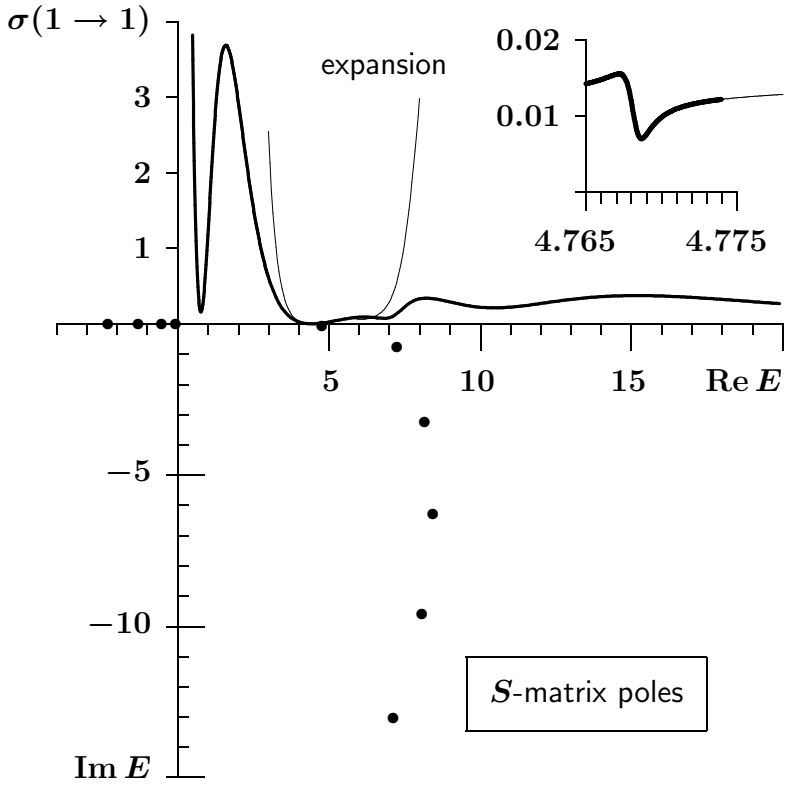

FIGURE 5. Energy dependence of the elastic scattering cross section in channel 1 for the potential (72). Few of the S-matrix poles (see Table 1 and Fig. 4) are shown in the lower part of the Figure. The thick curve represents the exact cross section, while the thin curve shows the cross section obtained with the expansions (66, 67) where $E_0 = 5 + i0$ and $M = 5$.

model.

APPENDIX: EXPANSION OF THE RICCATI FUNCTIONS

As is given by Eqs. (48, 49), the Riccati-Bessel and Riccati-Neumann functions can be factorized as

$$j_\ell(kr) = k^{\ell+1}\,\tilde{j}_\ell(E,r)\;, \qquad y_\ell(kr) = k^{-\ell}\tilde{y}_\ell(E,r)\;, \tag{73}$$

where the tilded functions depend on k^2, i.e. on the energy. These functions are holomorphic and thus can be expanded in Taylor series at an arbitrary point $E = E_0$,

$$\tilde{j}_\ell(E,r) = \sum_{n=0}^{\infty}(E-E_0)^n g_{\ell n}(E_0,r)\;, \qquad \tilde{y}_\ell(E,r) = \sum_{n=0}^{\infty}(E-E_0)^n t_{\ell n}(E_0,r)\;, \tag{74}$$

where the coefficients are given by the derivatives

$$g_{\ell n}(E_0,r) = \frac{1}{n!}\left[\frac{d^n}{dE^n}\tilde{j}_\ell(E,r)\right]_{E=E_0} = \frac{1}{n!}\left[\frac{d^n}{dE^n}\frac{j_\ell(kr)}{k^{\ell+1}}\right]_{E=E_0}\;, \tag{75}$$

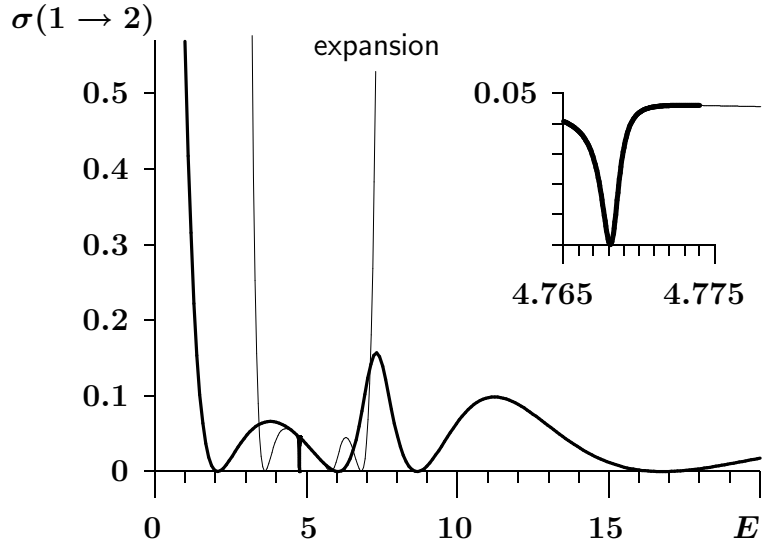

FIGURE 6. Cross section energy dependence of the inelastic transition $(1 \to 2)$ for the potential (72). The thick curve represents the exact cross section, while the thin curve shows the cross section obtained with the expansions (66, 67) where $E_0 = 5 + i0$ and $M = 5$.

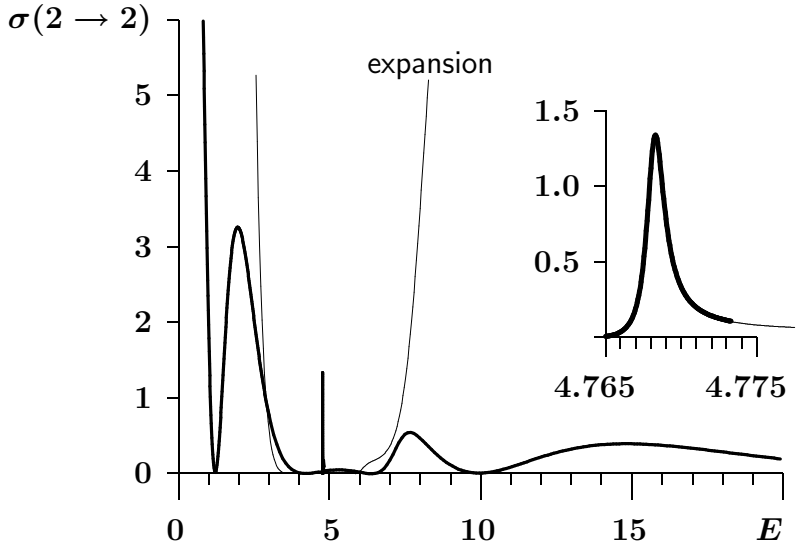

FIGURE 7. Energy dependence of the elastic scattering cross section in channel 2 for the potential (72). The thick curve represents the exact cross section, while the thin curve shows the cross section obtained with the expansions (66, 67) where $E_0 = 5 + i0$ and $M = 5$.

$$t_{\ell n}(E_0, r) = \frac{1}{n!}\left[\frac{d^n}{dE^n}\tilde{y}_\ell(E, r)\right]_{E=E_0} = \frac{1}{n!}\left[\frac{d^n}{dE^n}k^\ell y_\ell(kr)\right]_{E=E_0} . \tag{76}$$

In order to find these derivatives, we use the following relations [28]

$$\frac{d}{dz}\left[\frac{j_\ell(z)}{z^{\ell+1}}\right] = -\frac{j_{\ell+1}(z)}{z^{\ell+1}} \qquad \text{and} \qquad \frac{d}{dz}\left[z^\ell y_\ell(z)\right] = z^\ell y_{\ell-1}(z) . \tag{77}$$

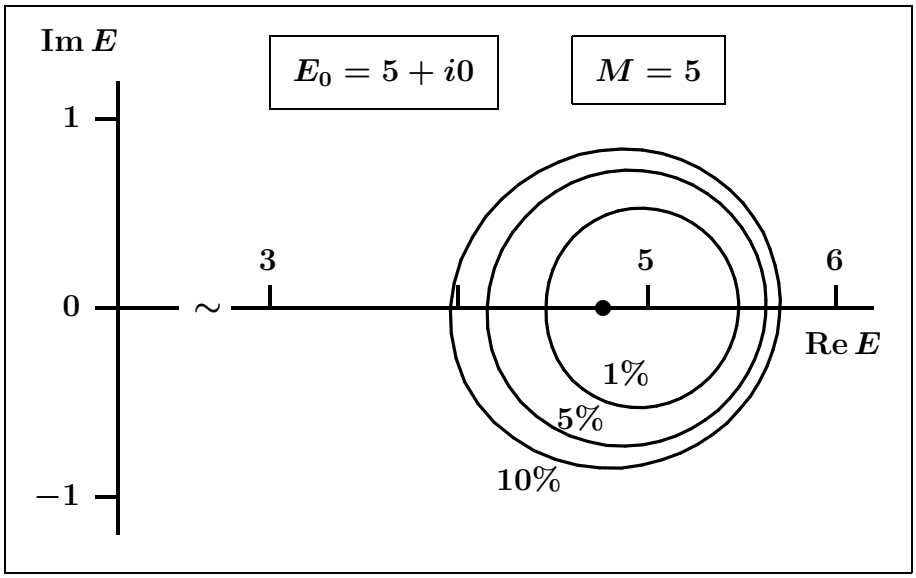

FIGURE 8. The domains within which the Jost matrix determinant for the potential (72) is reproduced, using the first five terms ($M = 5$) of the expansion (66), with the accuracy better than 1%, 5% and 10%. The expansion was done around the point $E_0 = 5$ on the real axis.

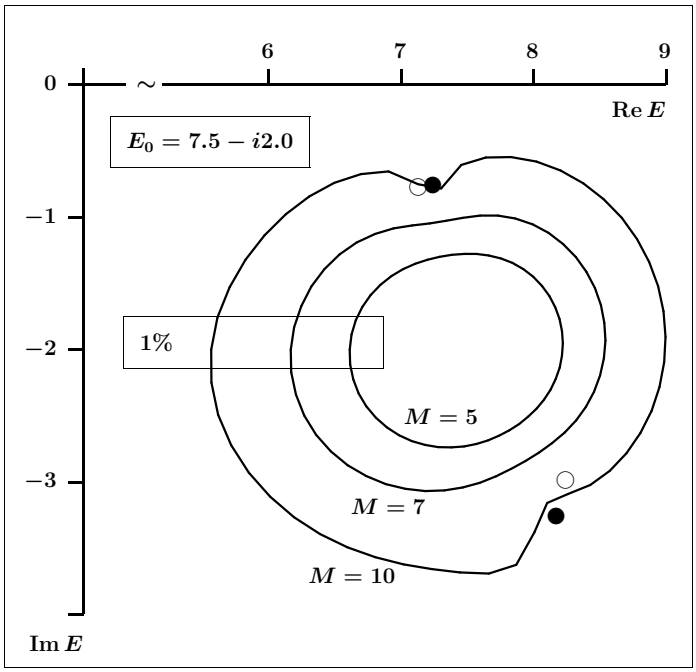

FIGURE 9. Growth of the 1% accuracy domain with the increase of the number M of terms in expansions (66), which were done around $E_0 = 7.5 - i2.0$ for the potential (72). Filled circles indicate the exact position of two resonances, while the open circles are their approximate positions obtained with $M = 5$.

After a simple but lengthy algebra, we finally obtain

$$g_{\ell n}(E_0,r) = \frac{1}{n!}\left[\left(-\frac{\mu r}{\hbar^2}\right)^n \frac{j_{\ell+n}(kr)}{k^{\ell+n+1}}\right]_{E=E_0} , \tag{78}$$

$$t_{\ell n}(E_0,r) = \frac{1}{n!}\left(\frac{\mu r}{\hbar^2}\right)^n \left[k^{\ell-n} y_{\ell-n}(kr)\right]_{E=E_0} . \tag{79}$$

The matrices γ_n and η_n of Eqs. (60, 61) are diagonal with each row having the functions (78, 79) with μ and k for the corresponding channel. These functions should be the same for all sheets of the Riemann surface, i.e. for any choice of the signs of channel momenta. This is so indeed since $j_\ell(-z) = (-1)^{\ell+1} j_\ell(z)$ and $y_\ell(-z) = (-1)^\ell y_\ell(z)$.

REFERENCES

1. H. A. Bethe, "*Theory of the Effective Range in Nuclear Scattering*", Phys. Rev. **76**, 38-50 (1949)
2. M. L. Goldberger, K. M. Watson, "*Collision Theory*", John Wiley & Sons, New York, 1964.
3. G. J. Kynch, Proc. Phys. Soc. **A 65**, 83, 94 (1952)
4. B. R. Levy, J. B. Keller, J. Math. Phys. **4**, 54 (1963)
5. R. F. Dashen, J. Math. Phys. **4**, 338 (1963)
6. V. V. Babikov, Sov. J. Nucl. Phys. **1**, 793-802 (1965)
7. V. V. Babikov, Physics-Uspekhi **92**, 3-26 (1967)
8. V. V. Pupyshev, S. A. Rakityansky, Zeit. Phys. **A 348**, 227 (1994)
9. Yea-Hwang Uang, W. C. Stwalley, "*The possibility of a* $^4He_2$ *bound state, effective range theory, and very low energy* He-He *scattering*", J. Chem. Phys. **76**, 5069-5072, (1982).
10. S. J. Buckman, J. Mitroy, "*Analysis of low-energy electron scattering cross sections via effective-range theory*", J. Phys. B: At. Mol. Opt. Phys. **22**, 1365-1384, (1989).
11. M. Marinescu, "*Computation of the scattering length and effective range in molecular physics*", Phys. Rev. **A 50**, 3177-3180, (1994).
12. F. Arnecke, H. Friedrich, J. Madronero, "*Effective-range theory for quantum reflection amplitudes*", PHys. Rev. **A 74**, 062702, (2006).
13. Z. Idziaszek, G. Karwasz, "*Applicability of Modified Effective-Range Theory to positron-atom and positron-molecule scattering*", Phys. Rev. **A 73**, 064701, (2006).
14. Z. Idziaszek, G. Karwasz, "*Shape resonances in modified effective range theory for electron-molecule collisions*", ArXiv, physics.atom-ph, 0708.2991, (2007).
15. H.-W. Hammera, Dean Lee, "*Causality and the effective range expansion"*, ArXiv, nucl-th, 1002.4603, (2010)
16. S. A. Rakityansky, N. Elander, "*Generalized effective-range expansion*", J. Phys. A: Math. Theor. **42**, 225302 (2009)
17. M. H. Ross, G. L. Shaw, "*Scattering length and effective range theory for multi-channel processes*", Annals of Physics **9**, 391-415, (1960).
18. M. H. Ross, G. L. Shaw, "*Multichannel effective range theory*", Annals of Physics **13**, 147-186, (1961).
19. P. Nath, G. L. Shaw, "*Multichannel effective-range theory from the* N/D *formalism*", Phys. Rev. **138 B**, (3), 702, (1965).
20. M. W. Kermode, "*Effective range theory for multi-channel scattering*", Nucl. Phys. **A 99**, 605-624, (1967).
21. D. W. L. Sprung, M. W. Kermode, S. Klarsfeld, "*On the application of effective-range theory to the* $^3S_1 - {}^3D_1$ *state of the neutron-proton system*", J.Phys.G: Nucl.Phys. **8**, 923-935, (1982).
22. L. Rosenberg, "*Multichannel effective-range theory with long-range interactions*", Phys. Rev. **A 57**, 1862-1869, (1998).
23. L. Brand, "*Differential and Difference Equations*", John Wiley & Sons, Inc., New York, 1966.
24. J. R. Taylor, "*Scattering Theory*", John Wiley & Sons, New York, 1972.

25. J. Mathews and L. R. Walker, "*Mathematical Methods of Physics*", W. A. Benjamin, New York, 1964.
26. S. A. Rakityansky, N. Elander, "*Analyzing the contribution of individual resonance poles of the S-matrix to two-channel scattering*", Int.J.Quant.Chem. **106**, 1105-1129, (2006).
27. W. R. Frazer, A. W. Hendry, Phys. Rev. **134 B**, 1307 (1964).
28. Abramowitz M and Stegun A (ed) 1964 *Handbook of Mathematical Functions* (Washington DC: NBS)
29. S. A. Rakityansky, S. A. Sofianos, K. Amos. "A method of calculating the Jost function for analytic potentials", Nuovo Cim. **B 111**, pp. 363-378 (1996).
30. S. A. Sofianos and S. A. Rakityansky, "Exact method for locating potential resonances and Regge trajectories", J. Phys. A: Math. Gen. **30** 3725 (1997).
31. S. A. Sofianos, S. A. Rakityansky, and G. P. Vermaak, "Sub-threshold resonances in few-neutron systems", Journal of Phys. **G 23**, pp. 1619-1629 (1997).
32. S. A. Rakityansky, S. A. Sofianos, "Jost function for coupled partial waves", J. of Phys. **A 31**, pp. 5149-5175 (1998).
33. S. A. Sofianos, S. A. Rakityansky, S. E. Massen, "Jost Function for Singular Potentials", Phys. Rev. **A 60**, pp. 337-343 (1999).
34. S. A. Rakityansky, S. A. Sofianos, "Jost function for coupled channels", Few-Body Syst. Suppl. **10**, pp. 93-96 (1999).
35. S. E. Massen, S. A. Sofianos, S. A. Rakityansky, S. Oryu, "Resonances and off-shell characteristics of effective interactions", Nucl. Phys. **A 654**, pp. 597-611 (1999).
36. S. A. Rakityansky, "Unified treatment of bound, scattering, and resonant states in semiconductor nano-structures", Phys. Rev. **B 68**, 195320 (2003).
37. S. A. Rakityansky, "Modified Transfer-matrix for nano-structures with arbitrary potential profile", Phys. Rev. **B 70** (20), 205323 (2004).
38. S. A. Rakityansky, S. A. Sofianos and N. Elander, "Pade approximation of the S-matrix as a way of locating quantum resonances and bound states", J. Phys. A: Math. Theor. **40**, 14857-14869 (2007).
39. S. Lefschetz, "Differential Equations: Geometric Theory", Interscience Publishers, New York, 1957.
40. T. Noro, H. S. Taylor, J. Phys. B: Atom. Mol. Phys. **13**, L377 (1980).

Solution of three-dimensional Faddeev equations: ultracold Helium trimer calculations with a public quantum three-body code

E. A. Kolganova*, V. Roudnev† and M. Cavagnero†

*BLTP JINR, 141980 Dubna, Moscow region, Russia
†Department of Physics and Astronomy, University of Kentucky, Lexington, Kentucky, 40506-0055, USA

Abstract. We present an illustration of using a quantum three-body code being prepared for public release. The code is based on iterative solving of the three-dimensional Faddeev equations. The code is easy to use and allows users to perform highly-accurate calculations of quantum three-body systems. The previously known results for He_3 ground state are well reproduced by the code.

Keywords: three-body atomic systems, Faddeev equations, Helium trimer, ultracold collisions
PACS: 21.45.-v, 31.15.ac, 34.10.+x, 36.90.+f, 02.70.Jn

INTRODUCTION

The quantum few-body problem is important for investigating physical processes at practically all possible length and energy scales. For instance, three-body models can be employed for describing nuclear reactions [1, 2, 3, 4], electron- and positron-atom collisions [5, 6], and chemical reactions [7]. The developments of the last decade demonstrated the importance of three-body processes for understanding the dynamics of ultracold gases [8]. An ability to solve a few-body problem directly would also be beneficial to theorists for testing, for instance, effective-field theories [9, 10].

The three-body problem, however, has sufficient intrinsic complexity that it often inhibits or prevents non-experts in few-body calculations from considering realistic three-body models and from employing physically correct representations [11]. Accordingly, a standard, easily operable and rigorously constructed tool for three-body calculations will be beneficial for a broad physical community. Such a tool should be tested independently to ensure its usability and applicability. This work is a result of a collaboration between the authors of this tool, developed at the University of Kentucky, and a research group in JINR performing independent tests.

In the following sections we describe the equations being solved and report the results of the tests we have performed.

FORMALISM

The three-body code being tested is based on solving Faddeev equations in configuration space. The complete and mathematically rigorous theory of Faddeev equations can be

found in books on the topic [12, 13, 14]. Here we only sketch out the gross features important for understanding and using the code.

We start by describing the physical model from the three-body Hamiltonian

$$H = H_0 + V_{3\mathrm{b}}(\mathbf{x}_i, \mathbf{y}_i) + \sum_i V_i(\mathbf{x}_i)\,, \tag{1}$$

where H_0 stands for the kinetic energy of the three particles, $V_i(\mathbf{x}_i)$ is the interaction potential acting in the pair i, and $V_{3\mathrm{b}}(\mathbf{x}_i, \mathbf{y}_i)$ is a short-range three-body interaction. (In the following description the latter will be omitted only for simplicity. Taking into account the three-body interactions, however, does not produce any practical or principal difficulties.) The configuration space of the three particles is described in terms of 3 sets of Jacobi coordinates

$$\begin{aligned} \mathbf{x}_i &= \left(\frac{2m_j m_k}{m_j + m_k}\right)^{1/2} (\mathbf{r}_j - \mathbf{r}_k) \\ \mathbf{y}_i &= \left(\frac{2m_i(m_j + m_k)}{m_i + m_j + m_k}\right)^{1/2} \left(\mathbf{r}_i - \frac{m_j \mathbf{r}_j + m_k \mathbf{r}_k}{m_j + m_k}\right) \end{aligned} \tag{2}$$

The set of coordinates i describes a partitioning of the three particles into a pair (jk) and a separate particle i. Faddeev decomposition represents the wave function Ψ in terms of a sum over all possible partitioning of the three-body system

$$\Psi = \sum_i \Phi_i(\mathbf{x}_i, \mathbf{y}_i)\,. \tag{3}$$

Faddeev components, Φ_i, satisfy the following set of equations [12]

$$(-\Delta_{\mathbf{x}} - \Delta_{\mathbf{y}} + V_i(\mathbf{x}_i) - E)\Phi_i(\mathbf{x}_i, \mathbf{y}_i) = V_i(\mathbf{x}_i) \sum_{k \neq i} \Phi_k(\mathbf{x}_k, \mathbf{y}_k)\ , \tag{4}$$

where $\mathbf{x}_i$ and $\mathbf{y}_i$ are mass-weighted Jacobi coordinates, V_i is the interaction potential in the i-th pair and E is the total energy of the system. It is not difficult to prove that the exact wave function of the three body system can be uniquely constructed from the Faddeev components by means of Eq. (3).

The equations in six-dimensional space can hardly be solved directly, and some partial analysis is necessary. We consider the states with zero total angular momentum. The angular degrees of freedom corresponding to collective rotation of the three-body system can be separated [15] and the kinetic energy operator reduces to

$$H_0 = -\frac{\partial^2}{\partial x^2} - \frac{\partial^2}{\partial y^2} - (\frac{1}{x^2} + \frac{1}{y^2})\frac{\partial}{\partial z}(1 - z^2)^{\frac{1}{2}}\frac{\partial}{\partial z}\,, \tag{5}$$

where x, y and z are so called intrinsic coordinates

$$x = |\mathbf{x}|, \quad y = |\mathbf{y}|, \quad z = \frac{(\mathbf{x}, \mathbf{y})}{xy}, \qquad x, y \in [0, \infty),\ \ z \in [-1, 1]\ \ . \tag{6}$$

In the case of identical bosons Faddeev components take identical functional form, which makes it possible to reduce the system of three equations (4) to one equation

$$(H_0+V(x)-E)\phi(x,y,z) = -V(x)P\phi(x,y,z)\,, \tag{7}$$

where

$$P\phi(x,y,z) \equiv xy(\frac{\phi(x^+,y^+,z^+)}{x^+y^+}+\frac{\phi(x^-,y^-,z^-))}{x^-y^-})$$

and $x^{\pm}(x,y,z)$, $y^{\pm}(x,y,z)$, and $z^{\pm}(x,y,z)$ are

$$\begin{aligned} x^{\pm}(x,y,z) &= (\frac{1}{4}x^2+\frac{3}{4}y^2\mp\frac{\sqrt{3}}{2}xyz)^{1/2}\,, \\ y^{\pm}(x,y,z) &= (\frac{3}{4}x^2+\frac{1}{4}y^2\pm\frac{\sqrt{3}}{2}xyz)^{1/2}\,, \\ z^{\pm}(x,y,z) &= \frac{\pm\frac{\sqrt{3}}{4}x^2\mp\frac{\sqrt{3}}{4}y^2-\frac{1}{2}xyz}{x^{\pm}(x,y,z)\,y^{\pm}(x,y,z)}\,. \end{aligned} \tag{8}$$

Assuming that in each two-body subsystem only one bound state exists, we can write the asymptotic boundary conditions for the Faddeev component ϕ as follows

$$\phi(x,y,z) \sim \varphi_2(x)\,\mathrm{e}^{-k_y y} + A(x/y,z)\,\frac{\mathrm{e}^{-k_3(x^2+y^2)^{1/2}}}{(x^2+y^2)^{1/4}}\,, \tag{9}$$

where $\varphi_2(x)$ stands for the wave function of the two-body subsystem bound state, $k_y=\sqrt{E_2-E_3}$, $k_3=\sqrt{-E_3}$, E_2 is the two-body bound state energy, and E_3 the energy of the three-body system. For three-body bound states the first term corresponds to virtual decay into a particle and a two-body bound system, while the second term corresponds to a virtual decay with an amplitude $A(x/y,z)$ into three single particles. The term corresponding to the latter configuration can generally be neglected for the states below the three-body threshold. Therefore, at sufficiently large distances R_x and R_y, the asymptotic boundary conditions for the Faddeev component are

$$\frac{\partial}{\partial x}\ln\phi(x,y,z)\bigg|_{x=R_x} = -k_x \equiv i\sqrt{E_2}\,, \qquad \frac{\partial}{\partial y}\ln\phi(x,y,z)\bigg|_{y=R_y} = -k_y\,. \tag{10}$$

For bound state calculations Dirichlet or Neumann boundary conditions can also be employed.

The important property of the Faddeev components which makes them suitable for numerical solution is their simple asymptotic form. For instance, each of the Faddeev components holds only bound states of the corresponding two-body subsystem. In this respect the $\mathbf{x}_i$ coordinate is the internal coordinate of the corresponding two-body cluster and the $\mathbf{y}_i$ coordinate plays the role of a reaction coordinate for all the states below the 3-body (break-up) threshold. This simple physical meaning of the coordinates suggest a natural requirement for discretizing the corresponding degrees of freedom: the discrete analogs of the $\mathbf{x}_i$ coordinate should reproduce the spectrum of the i-th cluster

correctly, and discrete analogs of the $\mathbf{y}_i$ coordinate must describe the scattering states reasonably well. These necessary requirements are easy to check prior to performing actual calculations, and they also provide a solid ground for a reasonable degree of automation for choosing the parameters of the numerical scheme. Another advantage of the Faddeev equations is the asymptotic decoupling of the components. The right-hand side of the equation (4) is, roughly speaking, exponentially small if the third particle is at larger distance than the typical size of the two-body bound state. This means that at longer distances $|\mathbf{y}_i| > y_{\max}$ the Faddeev components rapidly decouple, and calculations can be performed in the regions as small as the size of the largest two-body subsystem bound state.

The advantages of the Faddeev approach can be exploited even further when dealing with short-range interactions; i.e. assuming that the potentials V_i are zero (or negligible) outside the region $|\mathbf{x}_i| < x_{\max}$. To clarify this, consider the component Φ_i in the asymptotic region $|\mathbf{y}_i| \to \infty$, $\mathbf{x}_i \in \sup V_i$, where it satisfies a Schrödinger equation with the corresponding channel Hamiltonian

$$(H_0 + V_i(\mathbf{x}_i) - E)\Phi_i(\mathbf{x}_i, \mathbf{y}_i) \approx 0 \,,$$

where H_0 is the free three-body Hamiltonian. This property of Φ_i suggests that, rather than calculate Φ_i directly, we instead calculate τ_i (Eq. 11), which is better localized in configuration space

$$\tau_i \equiv (H_0 + V_i(\mathbf{x}_i) - E)\Phi_i(\mathbf{x}_i, \mathbf{y}_i) \,. \tag{11}$$

These τ_i are non-zero only for small $x_i \equiv |\mathbf{x}_i| < x_{\max}$ and small $y_i \equiv |\mathbf{y}_i| < y_{\max}$. Accordingly, they are localized to a region that can be *much smaller than the typical size of a two-body bound state*. This feature leads to substantial computational savings [16]. The τ_i satisfy the following integral equations

$$\tau_i = -V_i \sum_{j \neq i} R_{2j}(E)\tau_j \,, \tag{12}$$

where $R_{2j}(E)$ are the resolvents of the corresponding channel Hamiltonians. Since $\sup \tau_i \subset \sup V_i$, the τ_i are more suitable for numerical approximation than the original Faddeev components. Furthermore, if the equation is being solved using an iterative technique, then no explicit representation for the integral operators $R_{2j}(E)$ is required. In this case we only need to calculate the action of the integral operator on the τ_i, which can be done with high computational efficiency by numerically solving the corresponding differential equation with appropriate boundary conditions. We call this computational scheme a Localized Component Method (LCM).

COMPUTER CODE

In order to construct a discrete analogue of the system of equations (12) we employ quintic Hermite splines together with the orthogonal collocations method [17]. A detailed description of the procedure is given in [18]. This high-order method guarantees fast convergence with respect to the number of grid points, sparse matrix structure for the

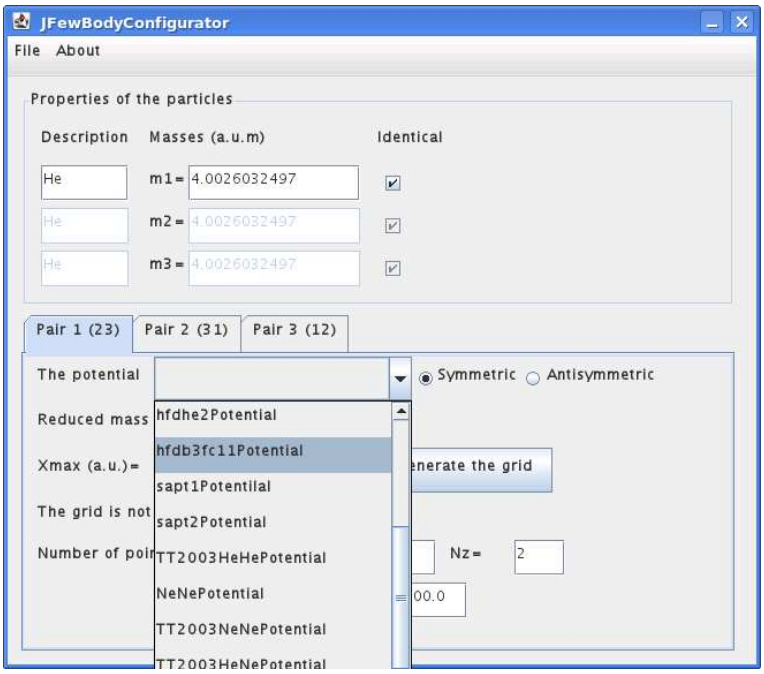

FIGURE 1. A screenshot of the configurator.

discrete analog of the equation (4), and fast calculation of matrix elements that makes it possible to avoid storing big matrices in computer memory.

The code is written in Java and consists of two parts. The first part is a configurator that simplifies composing the necessary configuration files. The configurator allows the user to set masses of the interacting atoms, to specify identical particles in the system, to choose a potential model, to set the cutoff distances R_x and R_y and to set the number of grid points to be employed in the calculation. It also generates a mesh with L_2-optimal point distribution which ensures the best possible approximation of the three-body wave function in the asymptotic region. In Fig. 1 we show an example of the configurator screenshot.

The second part is the three-body computational kernel based on the LCM approach. The kernel is currently capable of three-body calculations below the three-body threshold with a limitation of no more than one two-body bound state contributing to each asymptotic channel. This includes bound states, elastic scattering and chemical reactions below the first vibrational excitation threshold. Typical computational time can take from minutes to hours, depending on the physical system and the size of the grid.

RESULTS

We apply the code to the calculation of binding energies of the Helium trimer $^4He_3$ three-atomic system, to verify that we can reproduce the known calculated properties of helium trimer ground and excited states. This system is very particular about the approach being used, as the trimer binding energy is extremely small and a large volume

of the configuration space should be treated, but the interaction features very strong repulsion at short distances, which requires very precise numerical methods to be used.

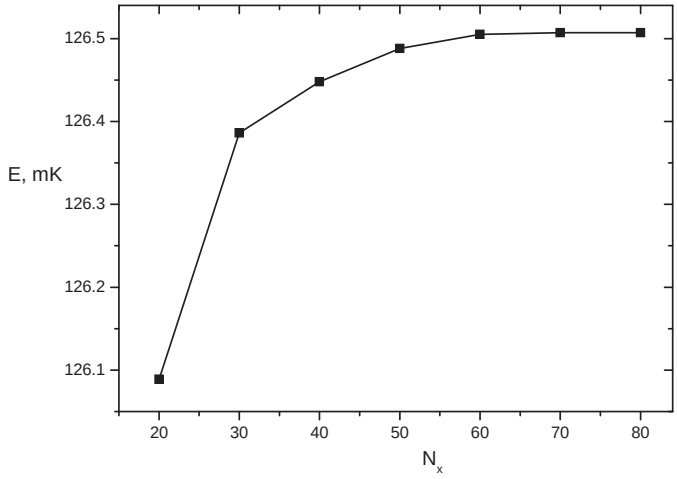

FIGURE 2. Convergence of the Helium trimer ground state energy on the grids of $N_x = N_y$ points; $N_z = 5$.

Experimentally, helium dimers have been observed for the first time in 1993 by the Minnesota group [19], and in 1994 by Schöllkopf and Toennies [20]. Later on, Grisenti *et al.* [21] measured a bond length of 52 ± 4 Å for $^4He_2$, which indicates that this dimer is the largest known diatomic molecular ground state. Based on this measurement they estimated a scattering length of 104^{+8}_{-18} Å and a dimer energy of $1.1^{+0.3}_{-0.2}$ mK [21]. In the latter investigation [22] the trimer pair distance is found to be $1.1^{+0.4}_{-0.5}$ nm in agreement with theoretical predictions for the ground state.

TABLE 1. Dimer energy ε_d, ^{4}He$-^4$He scattering length $\ell_{sc}^{(1+1)}$, bond length $< R >$ and root mean square radius $\sqrt{< R^2 >}$ for the potentials used, as compared to the experimental values of Ref. [21].

Potential model	ε_d (mK)	$\ell_{sc}^{(1+1)}$ (Å)	$< R >$ (Å)	$\sqrt{< R^2 >}$ (Å)
LM2M2 [23]	-1.30348	100.23	52.001	70.926
Exp. [21]	$-1.1^{+0.3}_{-0.2}$	104^{+8}_{-18}	52^{+4}_{-4}	-

Many theoretical calculations of these systems were performed for various interatomic potentials [23, 24]. Variational [26, 25], hyperspherical [8, 27, 28] and Faddeev techniques [16, 18, 29, 30, 31, 32] have been employed in this context. It was found that the Helium trimer has two bound states of total angular momentum zero: a ground state of about 126 mK and an excited state of Efimov-type of about 2.28 mK. Experimentally this Efimov-type[33] excited state has not yet been observed (see, e.g., [34] and refs. therein). It should be mentioned, however, that the year 2006 is noticeable due the first convincing experimental evidence for the Efimov effect in an ultracold gas of Caesium atoms [35, 36].

In present calculations we employed the code based on the Faddeev differential equations (5) with boundary conditions (10). As He-He interaction we used the semi-empirical LM2M2 potential [23]. We use $m_{^4\mathrm{He}} = 4.0026032197\ a.u.m$ for the mass of

TABLE 2. Results for binding energies of the $^4He_3$ trimer for LM2M2 potential.

	present	[29]	[18]	[30]	[31]	[32]	[27]	[28]	[26]
$\left\|E_{^4He_3}\right\|$ (mK)	126.507	126.45	126.41	126.2	126.39	125.9	125.52*	126.15	125.6*
$\left\|E^*_{^4He_3}\right\|$ (mK)	2.276		2.271		2.268	2.282		2.274	2.245*

* In original paper the energy value is given in cm^{-1} ($1cm^{-1}$ = 1.4387752 K).

the ^{4}He atom and $\frac{\hbar^2}{m_{^4\mathrm{He}} k_B} = 12.11928\,\mathrm{K\,\AA^2}$, unlike many three-body calculations, see, e.g., [34], where a rounded value of the coefficient has been used.

Investigation of the bound state energy convergence with respect to the number of grid points demonstrates that even a moderate number of points in variables x and y is sufficient to get up to six accurate figures for the energy of the ground state (Fig. 2).

The ^{4}He dimer binding energies, ^{4}He–^{4}He scattering lengths and mean values of the radius $< R >$ and $\sqrt{< R^2 >}$ obtained with the LM2M2 potential [23] are shown in Table 1 in comparison with experimental data [21]. All the values agree with an experimental estimation of Ref.[21] within quoted errors. The scattering length $\ell_{\mathrm{sc}}^{(1+1)}$ of the system is bigger than the range of the potential by an order of magnitude. All these features

characterize the Helium dimer as the weakest, as well as the biggest, diatomic molecule found so far. Due to the fact that the energy of the dimer is so small, one should expect that the $E_{^4\mathrm{He}_3}$ trimer indeed possesses the theoretically predicted state of the Efimov type (see, [33, 34]).

In Table 2 the results of trimer binding energies calculations obtained with LM2M2 potential are summarized. The binding energies of the ^{4}He trimer ground ($E_{^4\mathrm{He}_3}$) and exited ($E^*_{^4\mathrm{He}_3}$) states are presented. These results demonstrate good agreement between different methods and show that the code competes well even against variational methods. It should be mentioned that the energy estimates obtained with the code are non-variational, and further variational improvements of the results are possible.

We are planning to continue testing the code within current applicability limits, including scattering calculations, systems of distinguishable particles and modeling clusters of other rare gas atoms.

ACKNOWLEDGMENTS

This work is supported by Heisenberg-Landau Program (EK) and the NSF grant PHY-0903956 (VR and MC).

REFERENCES

1. J. L. Friar, B. F. Gibson, G. Berthold, W. Glöckle, Th. Cornelius, H. Witala, J. Haidenbauer, Y. Koike, G. L. Payne, J. A. Tjon, and W. M. Kloet, *Phys. Rev.* **C 42**, 1838–1840 (1990).
2. S. L. Yakovlev, I. N. Filikhin, *Phys. Atom. Nucl.* **60**, 1794–1802 (1997).
3. E. Garrido, D. V. Fedorov and A. S. Jensen, *Phys. Rev.* **C 59**, 1272–1289 (1999).
4. I. Filikhin, A. Gal, V. M. Suslov, *Nucl. Phys.* **A 743**, 194–207 (2004).
5. C.-Y. Hu, S. L. Yakovlev and Z. Papp, *Nucl. Instr. and Methods in Physics Research* **B 247**, 25–30 (2006).
6. C. W. McCurdy, M. Baertschy, T. N. Rescigno, *J. Phys.* **B 37**, R137–R187 (2004).
7. G. A. Parker, R. B. Walker, B. K. Kendrick, and R. T. Pack, *J. Chem. Phys.* **117**, 6083–6085 (2002).
8. B. D. Esry, C. H. Greene, Y. Zhou and C. D. Lin, *J. Phys.* **B 29**, L51–L57 (1996).
9. E. Braaten and H.-W. Hammer, *Phys. Rev. Lett.* **87**, 160407 (2001); P. F. Bedaque, E. Braaten, and H.-W. Hammer, *Phys. Rev. Lett.* **85**, 908–911 (2000).
10. I. R. Afnan and D. R. Phillips, *Phys. Rev.* **C 69**, 034010 (2004).
11. T. Gonzalez-Lezana, J. Rubayo-Soneira, S. Miret-Artes, F. A. Gianturco, G. Delgado-Barrio, and P. Villarreal, *Phys. Rev. Lett.* **82**, 1648–1651 (1999).
12. L. D. Faddeev and S. P. Merkuriev, *Quantum Scattering Theory for several particle systems*. Doderecht: Kluwer Academic Publishers, 1993.
13. V. B. Belyaev, *Lectures on the Theory of Few-Body Systems*, Springer Verlag, 1990.
14. E. Schmidt and H. Ziegelmann, *The Quantum Mechanical Three Body Problem*, Pergamon, 1974.
15. V. V. Kostrykin, A. A. Kvitsinsky, and S. P. Merkuriev, *Few-Body Systems*, **6**, 97–113 (1989).
16. V. A. Roudnev, *Chem. Phys. Lett.* **367**, 95–101 (2003).
17. C. de Boor and B. Swartz, *SIAM J. Numer. Anal.* **10**, 582–606 (1973).
18. V. A. Roudnev, S. L. Yakovlev, S. A. Sofianos, *Few-Body Systems*, **37**, 179–196 (2005).
19. F. Luo, G. C. McBane, G. Kim, C. F. Giese, W. R. Gentry, *J. Chem. Phys.* **98**, 3564–3567 (1993).
20. W. Schöllkopf and J. P. Toennies, *Science*, **266**, 1345–1348 (1994).
21. R. Grisenti, W. Schöllkopf, J. P. Toennies, G. C. Hegerfeld, T. Köhler, M. Stoll, *Phys. Rev. Lett.* **85**, 2284–2287 (2000).
22. R. Brühl, A. Kalinin, O. Kornilov, J. P. Toennies, G. C. Hegerfeld, M. Stoll, *Phys. Rev. Lett.* **95**, 06002 (2005).

23. R. A. Aziz and M. J. Slaman, *J. Chem. Phys.* **94**, 8047–8053 (1991).
24. K. T. Tang, J. P. Toennies, and C. L. Yiu, *Phys. Rev. Lett.* **74**, 1546–1549 (1995).
25. D. Bressanini, M. Zavaglia, M. Mella, G. Morosi, *J. Chem. Phys.* **112**, 717–722 (2000).
26. S. Orlandini, I. Baccarelli, F. A.Gianturco, *Comp. Phys. Comm.* **180**, 384–391 (2009).
27. D. Blume, C. H. Greene, *J. Chem. Phys.* **112**, 8053–8067 (2000).
28. P. Barletta and A. Kievsky, *Few-Body Systems*, **45**, 123–125 (2009).
29. E. A. Kolganova, *Physics of Particles and Nuclei*, **41**, 1108–1110 (2010).
30. M. Salci, E. Yarevsky, S. B. Levin, N. Elander, *Int. J. Quant. Chem.* **107**, 464–468 (2007).
31. R. Lazauskas, J. Carbonell, *Phys. Rev.* **A 73**, 062717(11) (2006).
32. A. K. Motovilov, W. Sandhas, S. A. Sofianos, E. A. Kolganova, *Eur. Phys. J.* **D13**, 33–41 (2001).
33. V. Efimov, *Nucl. Phys.* **A 210**, 157–188 (1973); *Phys. Lett.* **B 33** 563–564 (1970).
34. E. A. Kolganova, A. K. Motovilov, W. Sandhas, *Physics of Particles and Nuclei* **40**, 206–235 (2009).
35. T. Kraemer, M. Mark, P. Waldburger, J. G. Danzl, C. Chin, B. Engeser, A. D. Lange, K. Pilch, A. Jaakkola, H.-C. Nagerl and R. Grimm, *Nature* **440**, 315–318 (2006).
36. B. D. Esry and C. H. Greene, *Nature* **440**, 289–290 (2006).

A few-body method for many-body systems

S.A. Sofianos*, R.M. Adam† and V.B. Belyaev**

*Physics Department, University of South Africa, P.O. Box 392, Pretoria 0001, South Africa
†South African Nuclear Energy Corporation, P.O. Box 582, Pretoria 0001, South Africa
**Joint Institute for Nuclear Research, Dubna 141980, Russia

Abstract. We used the Faddeev expansion of the potential in pairwise acting forces and the expansion of the resulting amplitudes in Potential Harmonics to obtain an integrodifferential equation valid for A boson systems. By introducing suitable transformation and taking limits $A \to \infty$ this equation is reduced into an Integro–Differential Equation suitable for handling bound states of large number of bosons. The new equation depends only on the input two-body interaction, it is quite simple, and the kernel has a simple analytic form. We employ the new equation to obtain results for $A \in (10-100)$ ^{87}Rb atoms interacting via a semi-realistic inter-atomic interactions and confined by an externally applied trapping potential $V_{\rm trap}(r)$. Our results are in excellent agreement with those previously obtained using the Potential Harmonic Expansion Method (PHEM) and the Diffusion Monte Carlo (DMC) method.

Keywords: static properties of condensates, hyperspherical methods, many-body theory
PACS: 03.75.Hh, 31.15.Ja, 24.10.Cn

INTRODUCTION

The study the A-boson bound state problem for systems up to $A = 4$ can be achieved using several methods. Among these methods those based on Faddeev-type equations and on Hyperspherical Harmonics Expansion (HHE) methods were extensively used during the last few decades to study in a rigorous way not only bosonic but fermionic systems as well. Going beyond the A=4 system, however, is not at present practical within the Faddeev scheme as the resulting equations (either in momentum or configuration space) are too complicated while in the HHE schemes, apart from the complexity of the equations, one faces also the question of convergence in the expansion especially when the interparticle forces have a short range repulsive core. Therefore alternative methods have to be used instead.

One such method is the Integro–Differential Equation Approach (IDEA) valid for A–body systems suggested by Fabre de la Ripelle and collaborators [1, 2]. It is based on the expansion of the Faddeev amplitudes in terms of Potential Harmonics (PH) [3, 4, 5] and it has been successfully applied in few–body calculations [6, 7], in realistic fermion systems [8], in unequal mass particle systems [9, 10, 11, 12] as well as in model calculations for the $A = 16$ system [13]. In all applications, the binding energies obtained are in good agreement with other results in the literature obtained by other methods.

When however the number of particles increases, the number of degrees of freedom also increases and the numerical complexity becomes intractable and one has no alternative but to use methods suitable for handling many-body systems. The typical number of atoms involved in the Bose-Einstein condensation (BEC), for example, is $10^3 - 10^6$

[14] and consequently studies of the BEC phenomenon are naturally based on quantum Monte Carlo type methods, such as, the Diffusion Monte Carlo (DMC) [15, 16], the Variational Monte Carlo (VMC) [17] and the practically exact Green Function Monte Carlo (GFMC) [18] methods.

A different approach to Monte Carlo methods is the one based directly on the PH expansion and it has been employed by Das and collaborators [19, 20, 21] to study the BEC phenomenon for ^{87}Rb atoms using repulsive inter-boson interactions. This Potential Harmonics Expansion Method (PHEM) requires the solution of a large number of differential equations which in turn requires the evaluation of Jacobi polynomials $P_K^{\alpha,\beta}(z)$ with $\alpha = (D-5)/2$, $\beta = 1/2+\ell$, D being the dimensionality of the A-boson system, $D = 3(A-1)$, ℓ is the partial wave for the system, and z is an angular variable. Furthermore, it requires the use of the so-called weight function $W(z) \equiv (1-z)^{\alpha}(1+z)^{\beta}$. It is clear that the accuracy in calculating the relevant quantities suffers with increasing A and the $W(z)$ has a spike similar to a δ-function for $z \sim -1$ which is difficult to treat numerically.

In the present work we also start by expanding the wave function for the A-body system system in to Faddeev components which in turn are expanded in terms of PH. The resulting system is then projected on the space of the pair (ij) resulting in the aforementioned IDEA equation which depend on two variables only, namely, the hyperradius r and the angular variable z while the corresponding kernel is expressed in terms of Jacobi polynomials $P_K^{\alpha,\beta}(z)$ and the weight function $W(z)$ and therefore one faces similar difficulties as in the PHEM. However, these difficulties can be removed by obtaining appropriate limits for $A \to \infty$. The new equation thus obtained, are quite simple, and the kernel depends on the much simpler Associated Laguerre polynomials $L_K^{1/2}$ which are independent of α [22]. The kernel can be even further simplified to have an analytic form, which does not depend on any polynomial, is independent from α, and only depends linearly on the number of particles A.

In what follows, we describe, in Sect. , how one can obtain from the IDEA, the new integro-differential equation suitable for large number of particles A. We then apply it, in Sect. , to obtain results, first, for the hybrid nuclear model for ^{16}O system where the particles are assumed to interact via short range strong forces of Wigner type; second, we apply it to ^{87}Rb atoms for various A and the results obtained are compared to those of the PHEM and the DMC methods. Our conclusions are summarized in Sect. .

THE FADDEEV-HHE FORMALISM

In the IDEA formalism the A-body wave function can be written as

$$\Psi(\mathbf{x}) = H_{[L_m]}(\mathbf{x}) \sum_{i<j\leq A} F(\mathbf{r}_{ij}, r) \tag{1}$$

where $H_{[L_m]}(\mathbf{x})$ is a harmonic polynomial of minimal degree L_m for the ground state, $\mathbf{x}$ is the coordinate vector $\mathbf{x} = (\mathbf{x}_1, \mathbf{x}_2, \cdots, \mathbf{x}_A)$, $\mathbf{r}_{ij} = \mathbf{x}_i - \mathbf{x}_j$, in terms of the particle coordinates $\mathbf{x}_i$ while r is the hyperradius, $r = \left[2/A \sum_{i<j\leq A} r_{ij}^2\right]^{1/2}$. The functions $F(\mathbf{r}_{ij}, r)$

are two–body amplitudes obeying the Faddeev-type equation

$$\begin{aligned}\left[T+\frac{A(A-1)}{2}V_{[L_m]}(r) \quad - \quad E\right] H_{[L_m]}(\mathbf{x})\,F(\mathbf{r}_{ij},r) \\ = \quad -\left[V(r_{ij})-V_0^{[L_m]}(r)\right] H_{[L_m]}(\mathbf{x}) \sum_{k<l\leq A} F(\mathbf{r}_{kl},r)\,. \qquad (2)\end{aligned}$$

The hypercentral potential $V_0^{[L_m]}(r)$ is the average potential $V(r_{ij})$ taken over the $[L_m]$ state on the unit hypersphere $r=1$ of surface element $\mathrm{d}\Omega$

$$V_0^{[L_m]}(r)=\frac{\int H^*_{[L_m]}(\mathbf{x})V(r_{ij})H_{[L_m]}(\mathbf{x})\,\mathrm{d}\Omega}{\int |H_{[L_m]}(\mathbf{x})|^2\;\mathrm{d}\Omega}\,. \qquad (3)$$

We note that for ground states, the pairs are in an S–state and the amplitude F is a function of the hyperradius and $r_{ij}=|\mathbf{x}_i-\mathbf{x}_j|$ only.

The amplitudes can be expanded in terms of any set of harmonic polynomials such as the Hyperspherical Harmonics (HH). Expansion in terms of HH, however, results in a system of coupled differential equations which is impractical for numerical calculations especially when hard core potentials are employed or the number of particles considered is large. In addition it gives rise to degeneracy for a given grand orbital L and thus converged solutions are difficult to obtain.

A more efficient expansion can be made in terms of Potential Harmonics (PH) $\mathscr{P}^{\ell,m}_{2K+\ell}(\Omega_{ij})$ [3, 4, 5] which form a complete basis for expanding continuous functions depending only on the relative coordinate r_{ij}. For systems in which the pair (ij) is in an ℓ-state while the other pairs are in an S-state, these polynomials are given by

$$\mathscr{P}^{\ell,m}_{2K+\ell}(\Omega_{ij})=N_{K,\ell}Y_{\ell m}(\omega_{ij})\left(\frac{r_{ij}}{r}\right)^{\ell}P_K^{\alpha,\beta+\ell}(2\frac{r_{ij}^2}{r^2}-1) \qquad (4)$$

Here $Y_{\ell m}(\omega_{ij})$ is the spherical harmonic, $P_K^{\alpha,\beta}(z)$ is a Jacobi polynomial, and $N_{K,\ell}$ is a normalization constant which can be obtained from

$$\int_{(r=1)}\mathscr{P}^{\ell,m*}_{2K+\ell'}(\Omega_{ij})\mathscr{P}^{\ell',m'}_{2K'+\ell'}(\Omega_{ij})\,\mathrm{d}\Omega=\delta_{KK'}\delta_{\ell\ell'}\delta_{mm'}. \qquad (5)$$

The $\mathscr{P}^{\ell,m}_{2K+\ell}(\Omega_{ij})$ are eigenfunctions of the operator $\hat{L}^2(\Omega)$

$$\left[\hat{L}^2(\Omega)+L(L+D-2)\right]\mathscr{P}^{\ell,m}_{2K+\ell}(\Omega_{ij})=0\,,\qquad L=2K+\ell\,, \qquad (6)$$

where $L^2(\Omega)$ is given by [3]

$$\hat{L}^2(\Omega)=\frac{4}{W(z)}\frac{\partial}{\partial z}(1-z^2)W(z)\frac{\partial}{\partial z}+2\frac{\hat{\ell}^2(\omega_{ij})}{1+z}+2\frac{\hat{L}^2(\Omega_{N-1})}{1-z}\,. \qquad (7)$$

The angular variable z is defined by

$$z=\cos 2\varphi=2\frac{r_{ij}^2}{r^2}-1\,,\qquad \cos\varphi=\frac{r_{ij}}{r}\,. \qquad (8)$$

Letting

$$F(r_{ij},r) = P(z,r)/r^{\mathscr{L}_m+1}\,, \tag{9}$$

where $\mathscr{L}_m = L_m + (D-3)/2$, and projecting on the r_{ij}–space one gets the IDEA equation for an A–particle system (see, for example, [2])

$$\begin{aligned} -\frac{\hbar^2}{m}\left[\frac{\partial^2}{\partial r^2} \right. &- \left. \frac{\mathscr{L}_m(\mathscr{L}_m+1)}{r^2} + \frac{4}{r^2}T(z) + \frac{A(A-1)}{2}V_0^{[L_m]}(r) - E\right]P(z,r) \\ &= -\left[V(r_{ij}) - V_0^{[L_m]}(r)\right]\left[P(z,r) + \int_{-1}^{+1} \mathscr{F}(z,z')\; P(z',r)\; dz'\right]. \end{aligned} \tag{10}$$

where $T(z)$ is the kinetic energy operator

$$T(z) = \frac{1}{W_{[L_m]}(z)}\;\frac{\partial}{\partial z}\;(1-z^2)W_{[L_m]}(z)\;\frac{\partial}{\partial z} \tag{11}$$

and $W_{[L_m]}(z)$ is the weight function which, for bosonic systems, is given by

$$W_{[L_m]}(z) = (1-z)^{\alpha}(1+z)^{\beta} \tag{12}$$

where $\alpha = (D-5)/2 + L_m - 2\ell_m$ and $\beta = 1/2 + \ell_m$. The kernel $\mathscr{F}(z,z')$ is the projection function which is expressed in terms of the Jacobi polynomials $P_K^{\alpha,\beta}(z)$,

$$\mathscr{F}(z,z') = W_{[L_m]}(z')\sum_K\;\frac{(f_K^2-1)}{h_K}P_K^{\alpha,\beta}(z)P_K^{\alpha,\beta}(z')\,. \tag{13}$$

The normalization h_K is given by

$$h_K = \int_{-1}^{+1}\left(P_K^{\alpha,\beta}(z)\right)^2 W_{[L_m]}(z)dz\,, \tag{14}$$

and the constant $f_K^2 - 1$ by

$$f_K^2 - 1 = \frac{2(A-2)P_K^{\alpha,\beta}(-1/2) + [(A-2)(A-3)/2]P_K^{\alpha,\beta}(-1)}{P_K^{\alpha,\beta}(+1)}\,. \tag{15}$$

When the number of particles A is large, the calculations with the above formalism becomes time consuming and cumbersome. There are two main reasons for this, the first one being the evaluation of the Jacobi polynomials $P_K^{\alpha,\beta}$ since the value of α becomes huge and the polynomials are highly oscillatory; the second reason stems from the behavior of the weight function which for $z \to -1$ is peaked at 2^{α}.

In our approach we consider first the factorization

$$r_{\rm ij} = r\zeta/\sqrt{\alpha}\,. \tag{16}$$

with $z = 2\zeta^2/\alpha - 1$. Then for $\alpha \to \infty$ we have the following limits,

$$P_K^{\alpha,\beta}(2r_{ij}^2/r^2 - 1) \underset{\alpha\to\infty}{\longrightarrow} (-1)^K L_K^{1/2}(\alpha r_{ij}^2/r^2) \equiv (-1)^K L_K^{1/2}(\zeta^2) \tag{17}$$

and

$$W(z) = C_W \frac{2^{\alpha+1/2+\ell}}{\alpha^{1/2+\ell}} \zeta^{\ell+1} \mathrm{e}^{-\zeta^2} \tag{18}$$

where C_W is the normalization constant for the weight function. For $\ell = 0$

$$\begin{aligned} h_K & \underset{\alpha\to\infty}{\longrightarrow} \int_0^{\sqrt{\alpha}} \left[L_K^{1/2}(\zeta^2)\right]^2 \mathrm{e}^{-\zeta^2} \zeta^2 \,\mathrm{d}\zeta \\ & \simeq \frac{1}{2} \int_0^{\infty} \left[L_K^{1/2}(x)\right]^2 \mathrm{e}^{-x} \sqrt{x} \,\mathrm{d}x \\ & = \frac{1}{2} \frac{\Gamma(K+3/2)}{K!} . \end{aligned} \tag{19}$$

In order to evaluate the kinetic energy $\hat{T}P(z,r)$, we consider first the factorization

$$P(\zeta, r) = \frac{\mathrm{e}^{\zeta^2/2}}{\zeta} Q(\zeta, r) . \tag{20}$$

Then

$$\hat{T}\,P = \frac{1}{W}\frac{\partial}{\partial z}(1-z^2) W \frac{\partial}{\partial z} P \tag{21}$$

$$\equiv \frac{\alpha}{4} \frac{\mathrm{e}^{\zeta^2/2}}{\zeta} \left[\frac{\mathrm{d}^2}{\mathrm{d}\zeta^2} + 3 + 2\ell_m - \zeta^2 - \frac{2\ell_m}{\zeta^2} \right] Q(\zeta, r) \tag{22}$$

Therefore, Eq. (10) (we consider here the case where $L_m = 0$, $\mathscr{L}_m = \mathscr{L} \equiv (D-3)/2$, and $\ell_m = 0$) becomes

$$\begin{aligned} & \frac{\hbar^2}{m} \left[H_r + \frac{\alpha}{r^2} H_\zeta + \frac{A(A-1)}{2} V_0(r) - E \right] Q(\zeta, r) \\ = & -\left[V(r_{ij}) - V_0(r)\right] \left[Q(\zeta, r) + \int_0^{\sqrt{\alpha}} \mathscr{F}_E(z, z')\, Q(\zeta', r)\, \mathrm{d}\zeta' \right] . \end{aligned} \tag{23}$$

where

$$H_r = -\frac{\partial^2}{\partial r^2} + \frac{\mathscr{L}(\mathscr{L}+1)}{r^2} , \tag{24}$$

and

$$H_\zeta = \frac{\alpha}{4} \left[-\frac{\partial^2}{\partial \zeta^2} + \zeta^2 - 3 \right] . \tag{25}$$

The kernel $\mathscr{F}_E$ is given by

$$\mathscr{F}_E(\zeta, \zeta') = \zeta \mathrm{e}^{-\zeta^2/2} \sum_K \frac{2K!}{\Gamma(K+3/2)} (f_K^2 - 1) L_K^{1/2}(\zeta^2) L_K^{1/2}(\zeta'^2) \zeta' \mathrm{e}^{-\zeta'^2/2} , \tag{26}$$

We see that equation (23) is free from the δ-function type peak and, apart from the easily evaluable constant f_K^2-1, the kernel $\mathscr{F}_E$ does not depend on α.

Equation (23) can be even further simplified by noting that

$$\begin{aligned}\sum_K (f_K^2-1)\frac{K!}{\Gamma(K+3/2)}L_K^{1/2}(\zeta^2)L_K^{1/2}(\zeta'^2) \\ \underset{\alpha\to\infty}{\longrightarrow} 2(A-2)\sum_K\left(\frac{1}{4}\right)^K L_K^{1/2}(\zeta^2)L_K^{1/2}(\zeta'^2)/h_K \\ -2(A-2)\frac{1}{4}L_1^{1/2}(\zeta^2)L_1^{1/2}(\zeta'^2)/h_1 - L_1^{1/2}(\zeta^2)L_1^{1/2}(\zeta'^2)/h_1 \\ -2(A(A-2)/h_0 + [A(A-1)/2-1]/h_0 \end{aligned} \tag{27}$$

and thus by making use of the relation [23]

$$\sum_{K=0}^{\infty}\left(\frac{1}{4}\right)^K \frac{K!}{\Gamma(K+3/2)}L_K^{1/2}(\zeta^2)L_K^{1/2}(\zeta'^2) = \frac{4}{\sqrt{3\pi}}\,\mathrm{e}^{(\zeta^2+\zeta'^2)/3}\,\frac{\sinh(\frac{3}{4}\zeta\zeta')}{\zeta\zeta'}\,. \tag{28}$$

we obtain

$$\begin{aligned}\frac{\hbar^2}{m}\left\{H_r \;+\; \frac{4}{r^2}H_\zeta + \frac{A(A-1)}{2}V_0(r) - E\right\}Q(\zeta,r) \\ = \;-\left[V(r_{ij})-V_0(r)\right]\left[Q(\zeta,r)+\int_0^{\sqrt{\alpha}}\mathscr{F}_I(\zeta,\zeta')Q(\zeta',r)\,\mathrm{d}\zeta'\right]\end{aligned} \tag{29}$$

The new form of the kernel $\mathscr{F}_I$ is

$$\begin{aligned}\mathscr{F}_I(\zeta,\zeta') \;=\; \frac{2(A-2)}{\sqrt{3}}\left\{\left[A-3-\frac{2}{3}(\zeta^2-\frac{3}{2})(\zeta'^2-\frac{3}{2})\right]\zeta\zeta'\mathrm{e}^{-(\zeta^2+\zeta'^2)/2}\right. \\ \left. +\;\frac{4}{\sqrt{3}}\left[\mathrm{e}^{-[(5(\zeta-\zeta')^2+2\zeta\zeta')/6]} - \mathrm{e}^{-[(5(\zeta+\zeta')^2-2\zeta\zeta')/6]}\right]\right\}\end{aligned} \tag{30}$$

The kernel (30) has a simple form and its computation is straightforward.

In the presence of a trapping potential $V_{\mathrm{trap}}(r)$ which depends on the hyperradius only, the modifications needed are trivial and consists of replacing H_r by

$$H_r = -\frac{\partial^2}{\partial r^2} + \frac{\mathscr{L}(\mathscr{L}+1)}{r^2} + V_{\mathrm{trap}}(r) \tag{31}$$

The solution of the two-dimensional equations (23) and (29) can be readily obtained. However, the Adiabatic Approximation can also be employed. In this case we may write, as usual, $Q(\zeta,r) = Q_\lambda(\zeta,r)u_\lambda(r)$ to obtain

$$\begin{aligned}\frac{\hbar^2}{m}\left[\frac{4}{r^2}H_\zeta \;+\; U_\lambda(r)\right]Q_\lambda(\zeta,r) = -\left[V(\frac{r}{\sqrt{\alpha}}\zeta)-V_0(r)\right] \\ \times\;\left[Q_\lambda(\zeta,r)+\int_0^{\sqrt{\alpha}}\mathscr{F}_n(\zeta,\zeta')Q_\lambda(\zeta',r)\,\mathrm{d}\zeta'\right], \qquad n=E,\,I\end{aligned} \tag{32}$$

and

$$u''_\lambda(r) + \left[k_\lambda^2 + V_{\rm eff}(r)\right] u_\lambda(r) = 0 \tag{33}$$

where the effective potential $V_{\rm eff}$ is given by

$$V_{\rm eff}(r) = \frac{\mathscr{L}(\mathscr{L}+1)}{r^2} + \frac{A(A-1)}{2} V_0(r) - U_\lambda(r) + V_{\rm trap}(r) \tag{34}$$

It is noted that the hypercentral potential V_0 contains effects from the higher partial waves, albeit in an approximate way, and can be omitted in which case the results are S-projected. It is further noted that the $\mathscr{L}(\mathscr{L}+1)/r^2$ or the $V_{\rm trap}(r)$ can be included in the first equation (32) without affecting the final results.

RESULTS

We first analyze the behavior of the term $f_K^2 - 1$ as $\alpha \to \infty$. In table 1 we present the results for $A = 20$ and $A = 1000$ for the two terms, $T_1 = (A-2)2P_K^{\alpha,1/2}(-1/2)/P_K^{\alpha,1/2}(1)$ and $T_2 = (A-2)(A-3)/2\ P_K^{\alpha,1/2}(-1)/P_K^{\alpha,1/2}(1)$ for $K = 0, 1, \cdots, 7$. We see that both

TABLE 1. Comparison of the two terms T_1 and T_2 of $f_K^2 - 1$ (see text) for $K = 0, \cdots, 7$. for $A = 20$ and $A = 1000$.

	$A = 20$			$A = 1000$		
K	T_1	T_2	$f_K^2 - 1$	T_1	T_2	$f_K^2 - 1$
0	36.	153	189	1996.0000000	497503.	499499.
1	7.5	-8.5	-1	497.5000000	-498.5000000	-1.0000000
2	1.1004464	0.7589286	1.8593750	123.5018775	0.8319426	124.3338201
3	0.0729391	-0.0915948	-0.0186557	30.5345323	-0.0019425	30.5325898
4	-0.0086754	0.0137392	0.0050638	7.5185722	0.0000058	7.5185780
5	-0.0016333	-0.0024376	-0.0040709	1.8437195	-0.0000000	1.8437195
6	0.0002636	0.0004951	0.0007588	0.4502550	0.0000000	0.4502550
7	0.0000479	-0.0001125	-0.0000646	0.1095002	-0.0000000	0.1095002

terms as well as the total term $f_K^2 - 1$ become very small as K increases. Consequently only few terms in the expansion (26) are required to achieved convergence. Furthermore, the behavior of the second term (only the $K = 0, 1$ are significant for large α) justifies our approximation (27).

We next present, in Fig. 1, the kernel $\mathscr{F}_I(\zeta, \zeta')$ for $A = 20$ and $A = 1000$ particles. We see that, apart from the strength, its shape and spread is not drastically changed and in both cases the kernel becomes insignificant beyond $\zeta \sim 4$.

We employed the new equation, Eq. (29), to solve first, as a model problem, the ^{16}O system where results exist in the literature. To obtain the solution, we use the Galerkin method and B-splines to reduce the problem, as usual, to an eigenvalue one. In this model nuclear problem, the particles are assumed to interact via Wigner-type forces. The results obtained using the analytic expression (30) and designated as IDEA-I, are given in Table I. Despite the fact that the $A = 16$ case corresponds to a rather small number of particles, the accuracy achieved by the new equation for strong nuclear forces is less than 1% of the exact values obtained by solving the IDEA [13] or using the Hyperspherical Harmonics

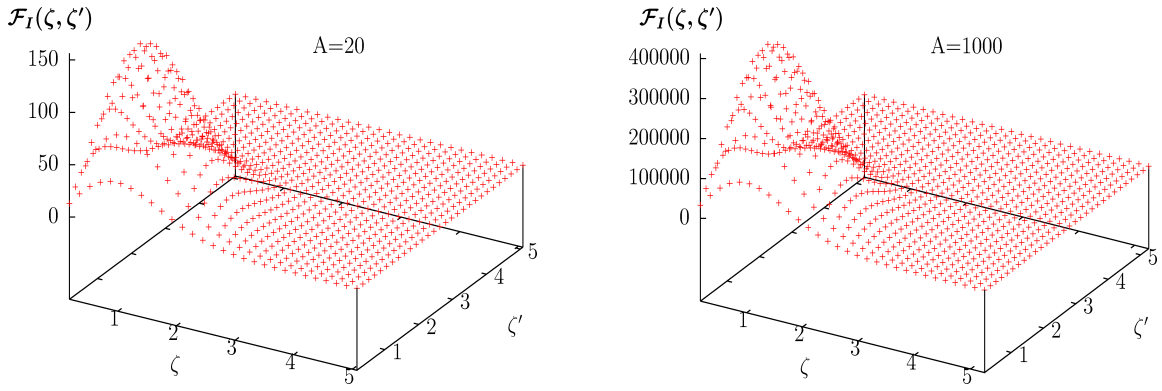

FIGURE 1. The kernel $\mathscr{F}_I(\zeta,\zeta)$ for $A=20$ and $A=1000$.

TABLE 2. Binding energies (in MeV) obtained for $A=16$ with nuclear forces and by using the kernel (30).

Potential	IDEA-I	IDEA(exact)	HHEM [27]
Volkov [24]	1643	1640	–
S3[25]	1247	1246	1235
MT-V [26]	1377	1376	1363

Expansion Method (HHEM) [27]. The slightly higher deviation from the results of the HHEM can be attributed to the slow convergence rate of the HHE expansion for the S3 [25] potential having a practically repulsive hard core and for the semi-realistic Yukawa type MT-V [26] potentials.

We turn now our attention to the case where A bosons are confined in a magnetic trap which is approximated by a spherically symmetric harmonic oscillator potential

$$V_{\rm trap}(r)=\sum_{i=1}^{A}\frac{1}{2}m\omega^2x_i^2=\frac{1}{4}m\omega r^2 \tag{35}$$

In our calculations we use oscillator units (o.u) in which the energy and length are $\hbar\omega$ and $\sqrt{\hbar/m\omega}$ respectively, where ω is the harmonic oscillator circular frequency. In these units $\hbar^2/m=1$.

As a first example we employ a Gaussian potential

$$V(r_{ij})=V_0\exp[-r_{ij}^2/r_0^2] \tag{36}$$

with $V_0=3.1985\times10^6$ o.u and $r_0=0.005$ o.u which corresponds to the Joint Institute for Laboratory Astrophysics (JILA) ^{87}Rb experiment [28] with $a_{\rm sc}=100$ bohr and trap frequency $\nu=200$ Hz. The results obtained by employing the kernel (26), designated as IDEA-E, and the kernel (30), are shown in Table 3. The ground state energy for $A=3$ differs, as expected, from the corresponding value obtained within the PHEM [19] by 25%, for $A=5$ by 3.26%. For $A=10$, however, the agreement is already within 0.2%. Going beyond $A>10$, the differences from the results of PHEM are very small and can be mainly attributed to the overall numerical inaccuracies. It should be noted here

TABLE 3. Results (in o.u) obtained with IDEA-E (Eq. (23)) and IDEA-I (Eq. (29)) using the Gaussian potential (36).

A	IDEA-E	IDEA-I	PHEM
3	6.009	6.009	4.500
5	7.758	7.758	7.505
10	15.003	15.003	15.034
15	22.501	22.501	22.567
20	30.000	30.001	30.107
25	37.501	37.501	37.654
30	45.009	45.001	45.207
35	52.509	52.501	52.768

TABLE 4. Same as 3 using the sech potential (37).

A	IDEA-I	PHEM[21]	DMC[29]
10	15.143	15.1490	15.1539
20	30.625	30.6209	30.639
50	78.701	78.8704	
100	165.038	164.907	

that the binding energy per particle is of the order of $E_b/A \sim 1.50$. It should be further noted that the IDEA-E and the IDEA-I results are, to all practical purposes, identical and therefore we shall employ from now on only the kernel (30).

As a second example we use the semi-realistic potential

$$V(r_{ij}) = V_0 \,\mathrm{sech}^2(r_{ij}/r_0) \tag{37}$$

Following Das *et al.* [21] we use $V_0 = 1.81847 \times 10^9$ o.u and $r_0 = 0.001$ o.u.. We present our results in Table 4 and compare them with those of the PHEM and of the DMC results of Blume and Greene [29].

We endeavored to carry out calculations for up to $A = 100$ where a very good agreement is achieved in all cases for $A \geq 10$ with both the PHEM [21] DMC [29] methods. Going beyond $A = 100$ requires more refine calculations and rather an exact solution of Eq. (29), the reason being that the extreme adiabatic approximation give rise to a multitude of eigenpotentials $U_\lambda(r)$ very close to each other and the results, albeit not differing much, depend nevertheless on which eigenpotential $U_\lambda(r)$ is used. This is shown in Fig. 2 where two effective potentials, Eq. (34), corresponding to $\lambda = 1$ and $\lambda = 20$ are plotted for the case $A = 500$. This multitude of eigenpotentials close to each other does not appear in the case where forces having an attractive well are used.

CONCLUSIONS

Our conclusions can be summarized as follows:
i) Using the transformation $r_{\rm ij} = r\zeta/\sqrt{\alpha}$ and using the asymptotic form of the Jacobi

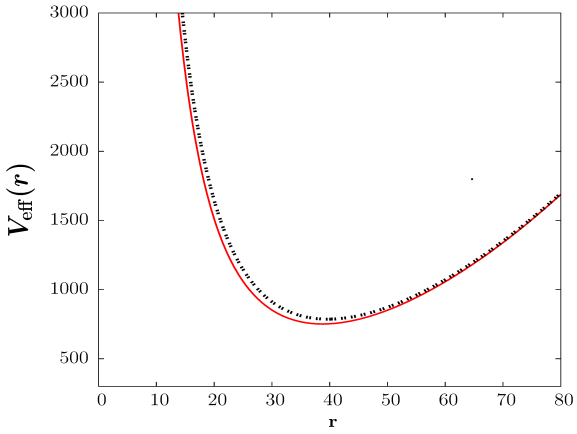

FIGURE 2. Two eigenpotentials $V_{\rm eff}(r)$ corresponding to $\lambda = 1$ and $\lambda = 20$ for $A = 500$.

polynomials $P_K^{\alpha,\beta}(z)$ which for large A are approximated by the Laguerre polynomials $L_K^{1/2}(\zeta)$ that do not depend on A, we obtained an integro-differential equation describing bound states of large number of bosons. This transformation simplifies the kinetic energy term, the weight function, and the corresponding projection function. As a result the new integro-differential equation with a fully analytic and simple kernel can be easily applied to A-body bosonic systems.

ii) The IDEA formalism is similar to the PHEM of Ref. [3] employed by Das and collaborators [19, 20, 21]. In the PHEM one has to solve a large number of differential equations which in the IDEA are transformed, with the help of Potential Harmonics, into a single integro-differential equation. (Technical details on this transformation can be found in Refs. [2, 5, 12].) Therefore, our equation for large A can also be considered as a simplified version not only of the IDEA method but also of the traditionally used PHEM.

iii) We tested the new equation by calculating the ground state binding energy of the model nuclear problem for the ^{16}O system where the short range nuclear force was of Wigner type. The good agreement achieved, with the three different type forces having a soft core, a hard core, and of Yukawa type, as compared to the results obtained using the IDEA and the HHEM methods implies that the new equation can be safely used to calculate binding energies of large number ($A \geq 10$) particles interacting via strong forces.

iv) Application of our scheme to Bose-Einstein condensates consisting of A-atoms trapped by an external field, we obtained results which are in excellent agreement with those of PHEM and the Diffusion Monte Carlo (DMC) method, at least up to $A = 100$. Going beyond this number requires improved numerical methods or a direct solution of the equation as a two-variable integro-differential equation without resorting to the EAA approximation which give rise to a plethora of eigenpotentials that are very close to each other.

v) When A increases, the centrifugal part $\mathscr{L}(\mathscr{L}+1)/r^2$ becomes extremely large and extends outwards while the inter-atomic potential is constant and restricted to smaller distances. Therefore the main contribution in the effective potential stems from the

centrifugal and the trapping potentials which generate a harmonic oscillator–type well which moves outwards as the number of particles A increases.

vi) The overall good results obtained, indicate that the derived equation can be used in studies of bound A-boson systems as an alternative to competing methods such as the variational and hyperspherical harmonics methods. Our approximations should become better with increasing A *i.e* for $\alpha \rightarrow \infty$.

REFERENCES

1. M. Fabre de la Ripelle, Few–Body Systems **1**, 181 (1986).
2. M. Fabre de la Ripelle, H. Fiedeldey, and S. A. Sofianos, Phys. Rev. C **38**, 449 (1988).
3. M. Fabre de la Ripelle, Annals of Physics NY **147**, 281 (1983).
4. M. Fabre de la Ripelle, Few-Body Systems **1**, 181 (1986).
5. M. Fabre de la Ripelle, *Models and Methods in Few-Body Physics (Springer Lecture Notes in Physics* **273** ed L.S. Ferreira, A.C. Fonseca, and L. Streit (Springer-Verlag, New-York, 1987) p302.
6. M. Fabre de la Ripelle, H. Fiedeldey, and S. A. Sofianos, , Few-Body Systems 6, 157 (1989).
7. W. Oehm, S. A. Sofianos, H. Fiedeldey, and M. Fabre de la Ripelle, Phys. Rev. C **42**, 2322 (1990); Phys. Rev. C **43**, 25 (1991); Phys. Rev. C**44**, 81 (1991).
8. M. Fabre de la Ripelle, S. A. Sofianos, and R. M. Adam, Annals of Physics **316**, 107 (2004).
9. R.M. Adam and H. Fiedeldey, J. Phys. G: Nucl. Part. Phys. **19**, 703 (1993).
10. R.M. Adam in *Models and Methods in Few- and Many-Body Systems*, Proc. of the DST-UNISA-JINR Symposium, Skukuza, South Africa, February 5-9, 2009, edited by S.A. Sofianos (Unisa Press, 2007).
11. S. A. Sofianos, G. J. Rampho, R.M. Adam, Modern Physics Letters **A 24**, 1027 (2009).
12. S. A. Sofianos, G. J. Rampho, R.M. Adam, Physics of Particles and Nuclei, **40**, 757 (2009).
13. M. Fabre de la Ripelle, H. Fiedeldey, and S. A. Sofianos, Phys. Let. B **205**, 163 (1988).
14. F. Dalfovo, S. Giorgini, L.P. Pitaevskii, and S. Stingari, Rev. Mod. Phys. **71**, 463 (1999).
15. D. M. Ceperley and B. J. Adler, Phys. Rev. Lett. **45**, 566 (1980).
16. P. J. Reynolds, D. M. Ceperley, B. J. Adler, and W. A. Lester, J. Chem. Phys. **77**, 5593 (1982).
17. J. L. DuBois and H. R. Glyde, Phys. Rev. A **63**, 023602 (2001).
18. V. R. Pandharipande, J. G. Zabolitzky, S. C. Pieper, R. B. Wiringa, and U. Helmbrecht, Phys. Rev. Lett. **50**, 1678 (1983).
19. T. K. Das and B. Chakrabarti, Phys. Rev. A **70**, 063601 (2004).
20. B. Chakrabarti, A. Kundu, and T. K. Das, J. Phys. B: At. Mol. Opt. Phys. **38**, 2457 (2005).
21. T. K. Das, S. Canuto, A. Kundu, and B. Chakrabarti, Phys. Rev. A **75**, 042705 (2007).
22. M. Fabre de la Ripelle, private communication.
23. *Higher Transcendental Functions*, edited by A.Erdélyi, (McGraw-Hill, New York, 1955) (Vol. III, formula (15) p. 272).
24. A. B. Volkov, Nucl. Phys. **74**, 33 (1965).
25. I. R. Afnan and Y. C. Tang, Phys. Rev. A **175**, 1337 (1968).
26. J. G. Zabolitzky, K. E. Schmidt, and M. H. Kalos, Phys. Rev. C **25**, 1111 (1982).
27. M. Fabre de la Ripelle, Young-Ju Jee, and S. Y. Larsen Ann. Phys. (N.Y) **212**, 195 (1991).
28. M. H. Anderson, J, R. Ensher, M. R. Mathews, C. E. Wieman, and E. A. Cornell, Science **269**, 198 (1995).
29. D. Blume and C. H. Greene, Phys. Rev A **63**, 063601 (2001).

S-matrix parametrization as a way of locating quantum resonances and bound states: multichannel case

P. O. G. Ogunbade and S. A. Rakityansky

Department of Physics, University of Pretoria, Lynnwood Road, Pretoria 0002, South Africa

Abstract. A method is proposed for analytic continuation of the multi-channel S-matrix given at a finite number of discrete points on the real axis of the energy. Using its values at these points, it is possible to calculate the S-matrix at complex energies on any sheet of the Riemann surface within a wide band along the real axis. The method is based on the established analytic properties of the multi-channel Jost matrices and a rational (Padé-type) approximation of the S-matrix obtained at real collision energies. Numerical examples demonstrate the stability and accuracy of the proposed method.

Keywords: Jost matrices, quantum resonances, Padé approximation

INTRODUCTION

It is often necessary to identify the spectral points (i.e. bound and resonance states) and extract their energies and widths from experimental scattering data available over some energy range. For a single-channel problem, a method for solving such a problem was proposed in Ref. [1].

The main idea is based on the coincidence principle [2]: two analytic functions coinciding on a curve segment are identical everywhere in the complex plane. Therefore, if we find a good analytic approximation of the S-matrix on the real axis, we may expect that it is also valid at the nearby points of the complex plane (or Riemann surface). In particular, such an approximate S-matrix should have the same singularities, i.e. the spectral points, which thus can be located.

In Ref. [1], the given S-matrix values are fitted using a meromorphic function of the Padé type, which is a ratio of two polynomials. In this work, we extend the method to a multi-channel problem, where before using the Padé approximation, the threshold branching points are explicitly factorized in each element of the Jost matrix.

RATIONAL APPROXIMATION OF THE S-MATRIX

We assume that the complex-valued matrices[1] $\mathbf{S}_\ell(E)$ are known at discrete points within a finite energy segment $[E_{\min}, E_{\max}]$ along the real axis. These can be either the experimental points or the values obtained theoretically using some numerical procedure.

[1] In this paper, all the matrices are labeled using bold symbols.

Let us look for an approximate matrix $\widetilde{\mathbf{S}}_\ell(E)$ such that its difference from the given ("exact") values $\mathbf{S}_\ell(E)$ is minimal on the segment $[E_{\min}, E_{\max}]$. Keeping in mind the coincidence principle, we hope that the more accurately we approximate the S-matrix on the real axis, the less different will be the poles of $\widetilde{\mathbf{S}}_\ell(E)$ at complex energies from the corresponding poles of the "exact" $\mathbf{S}_\ell(E)$.

In this work, the functional form we chose for the approximate S-matrix is known in numerical analysis as the matrix Padé approximant of the order $[M,M]$ given by

$$\widetilde{\mathbf{S}}_\ell(E) = \mathbf{P}(E)[\mathbf{Q}(E)]^{-1} = \left[\sum_{m=0}^{M} \mathbf{p}_m E^m\right] \cdot \left[\sum_{m=0}^{M} \mathbf{q}_m E^m\right]^{-1} \tag{1}$$

where the $\mathbf{p}_m$ and $\mathbf{q}_m$ are some unknown matrices of fitting parameters.

The form of the Padé approximation that we use is different from the standard approach in the following. The standard matrix Padé approximant [3, 4] requires the function to have a Taylor series representation. Our method, however, uses only the values of the function at discrete points on the real axis. Similarly to the single-channel case, the order $[M,M]$ (equal orders of the "numerator" and "denominator") of the Padé approximant ensures that at high energies $\mathbf{S}_\ell(E) \to \mathbf{I}$ [5] where $\mathbf{I}$ is the identity matrix. The other difference is that we incorporate the correct low energy behaviour of the S-matrix into our fitting procedure which is discussed next.

Multi-Channel Jost matrices

Consider an N-channel problem with the threshold energies E_n^{th}, channel momenta

$$k_n = \sqrt{\frac{2\mu_n}{\hbar^2}(E - E_n^{\text{th}})}, \tag{2}$$

and channel angular momenta ℓ_n ($n = 1,2,\ldots,N$). The multi-channel S-matrix can be written as the "ratio"

$$\mathbf{S}_\ell(E) = \mathbf{F}_\ell^{(\text{out})}(E) \cdot \left[\mathbf{F}_\ell^{(\text{in})}(E)\right]^{-1} \tag{3}$$

of the Jost matrices $\mathbf{F}_\ell^{(\text{in/out})}(E)$ which are the amplitudes of the incoming and outgoing spherical waves in the asymptotic behaviour

$$\mathbf{\Phi}_\ell(E,r) \underset{r\to\infty}{\longrightarrow} \mathbf{H}^{(-)}{}_\ell(E,r)\mathbf{F}_\ell^{(\text{in})}(E) + \mathbf{H}^{(+)}{}_\ell(E,r)\mathbf{F}_\ell^{(\text{out})}(E) \tag{4}$$

of the fundamental matrix $\mathbf{\Phi}_\ell$ of regular solutions of the system of radial Schrödinger equations. Here the diagonal matrices

$$\mathbf{H}^{(\pm)} = \mathtt{diag}\{h_{\ell_1}^{(\pm)}(k_1 r), h_{\ell_2}^{(\pm)}(k_2 r), \ldots, h_{\ell_N}^{(\pm)}(k_N r)\} \tag{5}$$

are composed of the Riccati-Hankel functions. Looking for the fundamental matrix $\mathbf{\Phi}_\ell(E,r)$ in the form

$$\mathbf{\Phi}_\ell(E,r) = \mathbf{J}_\ell(E,r)\mathbf{A}(E,r) - \mathbf{N}_\ell(E,r)\mathbf{B}(E,r) \tag{6}$$

where **J** and **N** are diagonal matrices composed of the Riccati-Bessel and Riccati-Neumann functions,

$$\mathbf{J} = \mathtt{diag}\{j_{\ell_1}(k_1 r), j_{\ell_2}(k_2 r), \ldots, j_{\ell_N}(k_N r)\} \ , \tag{7}$$

$$\mathbf{N} = \mathtt{diag}\{n_{\ell_1}(k_1 r), n_{\ell_2}(k_2 r), \ldots, n_{\ell_N}(k_N r)\} \ , \tag{8}$$

we obtain [6] (from the Schrödinger equation) the following system of differential equations for the new unknown matrices $\mathbf{A}(E,r)$ and $\mathbf{B}(E,r)$

$$\begin{cases} \partial_r \mathbf{A} = -\mathbf{K}^{-1}\mathbf{N}\mathbf{V}(\mathbf{J}\mathbf{A} - \mathbf{N}\mathbf{B}) \\ \partial_r \mathbf{B} = -\mathbf{K}^{-1}\mathbf{J}\mathbf{V}(\mathbf{J}\mathbf{A} - \mathbf{N}\mathbf{B}) \end{cases} \tag{9}$$

with the boundary conditions

$$\mathbf{A} \underset{r\to 0}{\longrightarrow} \mathbf{I}, \qquad \mathbf{B} \underset{r\to 0}{\longrightarrow} \mathbf{0} \tag{10}$$

where the diagonal momentum matrix **K** is given by

$$\mathbf{K} = \mathtt{diag}\{k_1, k_2, \ldots, k_N\} \ . \tag{11}$$

The matrices **A** and **B** are related to the Jost matrices via their asymptotic values

$$\mathbf{F}^{(\mathrm{in})}(E) = \lim_{r\to\infty} \frac{1}{2}\left[\mathbf{A}(E,r) - i\mathbf{B}(E,r)\right] \ , \tag{12}$$

$$\mathbf{F}^{(\mathrm{out})}(E) = \lim_{r\to\infty} \frac{1}{2}\left[\mathbf{A}(E,r) + i\mathbf{B}(E,r)\right] \ . \tag{13}$$

At any finite r, the expressions on the right hand sides of Eqs. (12, 13) give the corresponding Jost matrices for the potential truncated at the point r (similarly to the variable-phase approach).

Since Eqs. (9) involve the channel momenta, their solutions and therefore the Jost matrices (being functions of E) depend on the energy via all k_n. This makes them multivalued functions of the energy. Indeed, for any chosen E, we have two possibilities for choosing the sign in front of the square root

$$k_n = \pm\sqrt{\frac{2\mu_n}{\hbar^2}(E - E_n^{\mathrm{th}})}, \tag{14}$$

for each channel momentum. Therefore the Jost matrices have 2^N different values at each point E. In other words, they are defined on the Riemann surface consisting of 2^N interconnecting sheets. The branching points are at the threshold energies $E_n^{(\mathrm{th})}$.

The complications caused by the multivaluedness of the matrices **A** and **B** can be avoided in the following way. Let us consider the well known power series expansions

of the Riccati-Bessel and Riccati-Neumann functions [7],

$$
\begin{aligned}
j_\ell(kr) &= k^{\ell+1}\sum_{n=0}^{\infty} k^{2n}\left[\frac{(-1)^n\sqrt{\pi}}{\Gamma(\ell+\frac{3}{2}+n)n!}\left(\frac{r}{2}\right)^{2n+\ell+1}\right] \\
&= k^{\ell+1}\sum_{n=0}^{\infty} k^{2n}\gamma_{\ell n}(r) = k^{\ell+1}\widetilde{j}_\ell(E,r) \qquad (15)\\
n_\ell(kr) &= k^{-\ell}\sum_{n=0}^{\infty} k^{2n}\left[\frac{(-1)^{n+\ell+1}\sqrt{\pi}}{\Gamma(-\ell+\frac{1}{2}+n)n!}\left(\frac{r}{2}\right)^{2n-\ell}\right] \\
&= k^{-\ell}\sum_{n=0}^{\infty} k^{2n}\eta_{\ell n}(r) = k^{-\ell}\widetilde{n}_\ell(E,r). \qquad (16)
\end{aligned}
$$

where the odd powers of the momenta are factorized, namely, the factors $k^{\ell+1}$ and $k^{-\ell}$. Such a factorization for the matrices $\mathbf{J}$ and $\mathbf{N}$ gives

$$
\begin{aligned}
\mathbf{J} &= \mathtt{diag}\left\{k_1^{\ell_1+1}, k_2^{\ell_2+1}, \ldots, k_N^{\ell_N+1}\right\}\widetilde{\mathbf{J}} \\
\mathbf{N} &= \mathtt{diag}\left\{k_1^{-\ell_1}, k_2^{-\ell_2}, \ldots, k_N^{-\ell_N}\right\}\widetilde{\mathbf{N}}
\end{aligned} \qquad (17)
$$

After the factorization, the remaining series involve only the even powers of k and thus the functions $\widetilde{\mathbf{J}}$ and $\widetilde{\mathbf{N}}$ are single-valued functions of the energy.

Substituting the factorized expressions for $\mathbf{J}$ and $\mathbf{N}$ into Eqs. (9) and looking for matrices $\mathbf{A}$ and $\mathbf{B}$ in the factorized form

$$
A_{mn} = \frac{k_n^{\ell_n+1}}{k_m^{\ell_m+1}}\widetilde{A}_{mn}\,, \qquad B_{mn} = k_m^{\ell_m}\,k_n^{\ell_n+1}\,\widetilde{B}_{mn} \qquad (18)
$$

we see that all the factors composed of the odd powers of the momenta cancel out and the matrices $\widetilde{\mathbf{A}}$ and $\widetilde{\mathbf{B}}$ satisfy the following modified coupled differential equations

$$
\begin{cases}
\partial_r\widetilde{\mathbf{A}} = -\widetilde{\mathbf{N}}\mathbf{V}\,(\widetilde{\mathbf{J}}\widetilde{\mathbf{A}} - \widetilde{\mathbf{N}}\widetilde{\mathbf{B}}) \\
\partial_r\widetilde{\mathbf{B}} = -\widetilde{\mathbf{J}}\mathbf{V}\,(\widetilde{\mathbf{J}}\widetilde{\mathbf{A}} - \widetilde{\mathbf{N}}\widetilde{\mathbf{B}})\,,
\end{cases} \qquad (19)
$$

with the boundary conditions

$$
\widetilde{\mathbf{A}} \underset{r\to 0}{\longrightarrow} \mathbf{I}, \qquad \widetilde{\mathbf{B}} \underset{r\to 0}{\longrightarrow} \mathbf{0}\,. \qquad (20)
$$

It is seen that the differential equations (19) do not involve any channel momenta k_n. This means that $\widetilde{\mathbf{A}}(E,r)$ and $\widetilde{\mathbf{B}}(E,r)$ are single-valued matrix functions of the energy E.

Therefore, the Jost matrices have the following structure

$$
F_{mn}^{(\mathrm{in})}(E) = \frac{1}{2}\left[\frac{k_n^{\ell_n+1}}{k_m^{\ell_m+1}}\widetilde{A}_{mn}(E) - i\,k_m^{\ell_m}\,k_n^{\ell_n+1}\,\widetilde{B}_{mn}(E)\right], \qquad (21)
$$

$$
F_{mn}^{(\mathrm{out})}(E) = \frac{1}{2}\left[\frac{k_n^{\ell_n+1}}{k_m^{\ell_m+1}}\widetilde{A}_{mn}(E) + i\,k_m^{\ell_m}\,k_n^{\ell_n+1}\,\widetilde{B}_{mn}(E)\right], \qquad (22)
$$

They are multi-valued functions and the branching points are determined by the factors

$$\frac{k_n^{\ell_n+1}}{k_m^{\ell_m+1}} \qquad \text{and} \qquad k_m^{\ell_m} k_n^{\ell_n+1}. \tag{23}$$

Apparently, the "in" and "out" Jost matrices are related to each other on different sheets of the Riemann surface, namely,

$$F_{mn}^{(\text{out})}(E,k_1,k_2,\dots) = (-1)^{\ell_m+\ell_n} F_{mn}^{(\text{in})}(E,-k_1,-k_2,\dots), \tag{24}$$

and thus

$$\begin{aligned}\mathbf{S}(E) &= \mathbf{F}^{(\text{out})}(E)\left[\mathbf{F}^{(\text{in})}(E)\right]^{-1} \\ &= (-1)^{\ell_n+\ell_m}\mathbf{F}^{(\text{in})}(E,-k_1,-k_2,\dots,k_N)\left[\mathbf{F}^{(\text{in})}(E,k_1,k_2,\dots,k_N)\right]^{-1}.\end{aligned} \tag{25}$$

It is important to point out that according to equation (24) not all the parameters in equation (1) are independent. This symmetry property (24) enables us to reduce the number of fitting parameters in half and also improves the quality of the approximation since the correct structure of the S-matrix, given by equation (25), is taken into account.

FITTING PARAMETERS

To begin with, we expand the matrices $\widetilde{\mathbf{A}}$ and $\widetilde{\mathbf{B}}$ in power series of E, since they are single-valued matrix functions (see the statement following equation (19)), we have

$$\widetilde{\mathbf{A}}(E) \approx \sum_{\mu=0}^{M} \boldsymbol{\alpha}^{(\mu)} E^{\mu}, \qquad \widetilde{\mathbf{B}}(E) \approx \sum_{\mu=0}^{M} \boldsymbol{\beta}^{(\mu)} E^{\mu}. \tag{26}$$

It is clear from equation (26) that we have to determine $2(M+1)$ unknown matrices $\boldsymbol{\alpha}^{(\mu)}$ and $\boldsymbol{\beta}^{(\mu)}$ $(\mu = 0,1,2,\dots,M)$.

Let us assume that there are $2(M+1)$ S-matrix data given on the interval $[E_{\min}, E_{\max})]$ of the real energy axis. The method of calculating the parameters $\boldsymbol{\alpha}^{(\mu)}$ and $\boldsymbol{\beta}^{(\mu)}$ is as follows. We multiply equation (25) by $\mathbf{F}^{(\text{in})}$ from the right and re-write it as

$$\mathbf{F}^{(\text{out})}(E_i,k_1,k_2,\dots) = \mathbf{S}(E_i)\mathbf{F}^{(\text{in})}(E_i,k_1,k_2,\dots), \qquad i = 1,2,\dots,2(M+1). \tag{27}$$

Substituting equations (21) and (22), into equation (27), after some matrix algebra and rearrangements, we find that this is a linear system of equations for $\alpha_{mn}^{(\mu)}$ and $\beta_{mn}^{(\mu)}$, given by

$$\begin{aligned}\sum_{\mu=0}^{M}\Bigg[&\frac{k_n^{\ell_n+1}}{k_m^{\ell_m+1}}\Big(S_{mm}(E_i)-1\Big)\alpha_{mn}^{(\mu)} - \imath\, k_m^{\ell_m} k_n^{\ell_n+1}\Big(S_{mm}(E_i)+1\Big)\beta_{mn}^{(\mu)} \\ &+ \sum_{\substack{j=1\\ j\neq m}}^{N} S_{mj}(E_i)\left(\frac{k_n^{\ell_n+1}}{k_j^{\ell_j+1}}\alpha_{jn}^{(\mu)} - \imath\, k_j^{\ell_j} k_n^{\ell_n+1}\beta_{jn}^{(\mu)}\right)\Bigg] E_i^{\mu} = 0\end{aligned} \tag{28}$$

where $m,n = 1,2,\ldots,N$; $i = 1,2,\ldots,2(M+1)$. Similarly to the single channel case, we can simplify the last equation by including into it the correct behaviour of the S-matrix at zero collision energy [5]:

$$S_{mm}(E) \xrightarrow[k_m\to 0]{} 1 + \mathrm{O}(k_m^q), \quad q \geq \ell + 1$$
$$S_{mn}(E) \xrightarrow[k_m\to 0]{} \mathrm{O}(k_m^q), \quad m \neq n,\ q \geq \ell + 1/2,$$

we thus obtain

$$\sum_{\mu=1}^{M} \left[\frac{k_n^{\ell_n+1}}{k_m^{\ell_m+1}} \Big(S_{mm}(E_i) - 1 \Big) \alpha_{mn}^{(\mu)} - \imath k_m^{\ell_m} k_n^{\ell_n+1} \Big(S_{mm}(E_i) + 1 \Big) \beta_{mn}^{(\mu)} \right.$$
$$\left. + \sum_{\substack{j=1 \\ j\neq m}}^{N} S_{mj}(E_i) \left(\frac{k_n^{\ell_n+1}}{k_j^{\ell_j+1}} \alpha_{jn}^{(\mu)} - \imath k_j^{\ell_j} k_n^{\ell_n+1} \beta_{jn}^{(\mu)} \right) \right] E_i^{\mu} = \delta_{mn} - S_{mn}(E_i) \tag{29}$$

where $i = 1,2,\ldots,2M$, $\alpha_{mn}^{(0)} = \delta_{mn}$, $\beta_{mn}^{(0)} = 0$ and δ_{mn} is the Kronecker delta ($m,n = 1,2,\ldots,N$).

Having obtained the parameters $\boldsymbol{\alpha}^{(\mu)}$ and $\boldsymbol{\beta}^{(\mu)}$, we can search the spectral points at complex energies as the roots of the determinant of the matrix function $\mathbf{F}^{\mathrm{in}}$ (i.e. the poles of the S-matrix (25))

$$\mathtt{det}\left[\mathbf{F}^{\mathrm{in}}(E) \right] = 0, \tag{30}$$

where the matrix elements of $\mathbf{F}^{\mathrm{in}}$ are given by

$$F_{mn}^{\mathrm{in}}(E) = \frac{1}{2} \sum_{\mu=0}^{M} \left[\frac{k_n^{\ell_n+1}}{k_m^{\ell_m+1}} \alpha_{mn}^{(\mu)} - \imath k_m^{\ell_m} k_n^{\ell_n+1} \beta_{mn}^{(\mu)} \right] E^{\mu}. \tag{31}$$

NUMERICAL EXAMPLES

As an illustration of how the suggested method works, we performed numerical calculations for two two-channel problems, namely: exactly solvable model of coupled square-wells [8, 5] and Noro-Taylor model potential [9]. The test conducted here is mainly for $\ell_1 = \ell_2 = 0$, although any channel angular momenta can be handled by our method. In both cases N fitting points (input energies) were chosen and uniformly distributed on the interval $E_{\min} \leqslant E \leqslant E_{\max}$ on the real axis i.e.

$$E_n = E_{\min} + \frac{E_{\max} - E_{\min}}{N-1}(n-1), \qquad n = 1,2,\ldots,N \tag{32}$$

The exact values of the **S**-matrix at the fitting points were calculated using a very accurate method, which is based on a combination of the complex rotation and a direct calculation of the Jost matrix function as described in [6]. The locations of the exact spectral points were obtained by the same method.

The first of the testing potentials is an exactly solvable model problem coupled by square-well potentials [5], shown in Figure 1. The units in this model are chosen in such a way that $\mu_1 = \mu_2 = \hbar c = 1$. The channel threshold energies are $E_1^{\text{th}} = 0.0$ and $E_2^{\text{th}} = 2.0$, while the interaction potential have the forms

$$\begin{aligned} \mathbf{V}(r) &= \begin{cases} \mathbf{U} & \text{for } 0 \le r \le 1 \\ \mathbf{0} & \text{otherwise} \end{cases} \\ \mathbf{U} &= -\begin{pmatrix} 2.0 & 0.5\lambda \\ 0.5\lambda & 2.0 \end{pmatrix}, \qquad \lambda = 0 \text{ or } 1. \end{aligned} \tag{33}$$

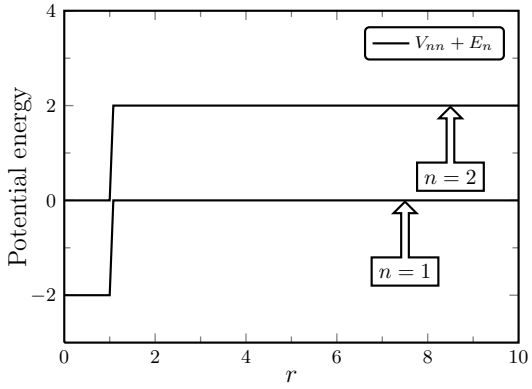

FIGURE 1. Square-well diagonal channel potentials (33). The potentials are shifted by the threshold energies E_n.

Although, this model problem is known to have exact analytical solution [5], numerical calculations as discussed above were employed to generate the **S**-matrix and the spectral points. In the absence of coupling between the channels (i.e. $\lambda = 0$), the diagonal potentials each generates a single bound state. These bound states are located at $E_1 = -0.2035507418$ and $E_2 = 1.7964592582$. When the coupling is switched on ($\lambda = 1$) only the lower bound state survived with shifted energy: $E_1 = -0.2430965098$. The bound state of the upper potential $V_{22}(r) + E_2^{\text{th}}$ can now decay into the continuum of the lower potential $V_{11}(r) + E_1^{\text{th}}$, thus turning into a resonance. The corresponding pole of the **S**-matrix is located on an unphysical sheet of the complex energy Riemann surface at $E_2 = 1.8315168862 - i0.0290733625$.

To give some indication of the accuracy of the rational approximation Table 1 shows the positions of the bound states and resonance for a series of approximants ranging from $N = 2$ to $N = 10$, with $E_{\text{min}} = 1$ and $E_{\text{max}} = 8$.

The second test case is shown in Figure 2. It supports bound states, resonances and sub–threshold resonances [1]. In the units such that $\mu_1 = \mu_2 = \hbar = 1$, the potential has the form

$$\mathbf{V}(r) = \begin{pmatrix} -1.0 & -7.5 \\ -7.5 & 7.5 \end{pmatrix} r^2 e^{-r} \tag{34}$$

The thresholds energies are $E_1^{\text{th}} = 0$ and $E_2^{\text{th}} = 0.1$. The exact **S**-matrix corresponding

TABLE 1. Convergence of the poles of the approximate $\tilde{\mathbf{S}}(E)$ found for the potential (33) using N fitting points evenly distributed over the interval $1 \leqslant E \leqslant 8$. All values are given in the arbitrary units such that $\mu_1 = \mu_2 = \hbar = 1$. λ is the switching parameter.

		$\lambda = 0$		$\lambda = 1$	
ID	N	$\mathrm{Re}\,E$	$\mathrm{Im}\,E$	$\mathrm{Re}\,E$	$\mathrm{Im}\,E$
E_1	2	0.9346579288	-0.2046585820	0.9696684253	-0.1914384518
	5	-0.2020229243	-1.24×10^{-12}	-0.2422637171	-1.1×10^{-14}
	7	-0.2035497226	-1.46×10^{-11}	-0.2430955910	-2.2×10^{-11}
	10	-0.2035506639	1.54×10^{-10}	-0.2430964602	-8.4×10^{-10}
	Exact	-0.2035507418		-0.2430965098	
E_2	2	1.2144390251	6.71×10^{-16}	1.2539964140	-0.0861903892
	5	1.7964492680	3.03×10^{-15}	1.8315169134	-0.0290733682
	7	1.7964492581	-2.12×10^{-14}	1.8315168861	-0.0290733625
	10	1.7964492581	4.54×10^{-13}	1.8315168861	-0.0290733625
	Exact	1.7964492582		1.8315168862	-0.0290733625

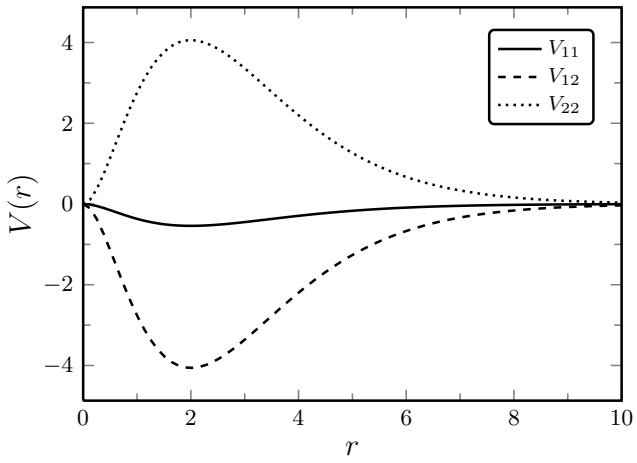

FIGURE 2. The Noro–Taylor potential [9] model given in Equation (34).

to this potential has an infinite number of poles forming a string that goes down the E-plane to infinity. The exact locations of the first six of the S-wave resonance states are given in Table 2. We compared the S-wave resonance poles obtained using $N = 30$ of the approximated $\tilde{\mathbf{S}}$-matrix where $E_{\min} = 1$ and $E_{\max} = 10$ with the exact locations. Figure 3 shows the accuracy of the proposed method. Just as it was expected, the most significant poles i.e. those that are close to the real axis and the fitting segment were reproduced correctly. The fitting points on the real E-axis are indicated by vertical bars. In Table 3, the exact and approximate $\tilde{\mathbf{S}}$-matrix poles are compared for the first five resonances generated by the potential (34).

TABLE 2. The S-wave resonance poles, $\hbar^2 k_n^2 = 2\mu_n(E - E_n^{\text{th}})$, of the exact **S**-matrix obtained for the Noro–Taylor potential (34). They were obtained using the rigorous Jost-function method described in [6]. All the values are given in the arbitrary units such that $\mu_1 = \mu_2 = \hbar = 1$.

no.	$\mathrm{Re}\,E$	$\mathrm{Im}\,E$	$\mathrm{Re}\,k_1$	$\mathrm{Im}\,k_1$	$\mathrm{Re}\,k_2$	$\mathrm{Im}\,k_2$
1	4.768197	−0.000710	3.088105	−0.000230	3.055551	−0.000232
2	7.241200	−0.755956	3.810742	−0.198375	3.784482	−0.199752
3	8.171217	−3.254166	4.119051	−0.790028	4.095577	−0.794556
4	8.440526	−6.281492	4.354528	−1.442520	4.333805	−1.449417
5	8.072643	−9.572815	4.538158	−2.109405	4.520027	−2.117867
6	7.123813	−13.012669	4.686027	−2.776909	4.670234	−2.786299

TABLE 3. Comparison of the first five resonance points for the potential (34) for $\ell = 0$. They (Exact) were obtained using the rigorous Jost-matrix function method [6] and the Padé approximation (Approx.) with the number of fitting points $N = 30$ evenly distributed over the interval $1 \leqslant E \leqslant 10$ (the units are such that $\mu_1 = \mu_2 = \hbar = 1$.

ℓ	**no.**		$\mathrm{Re}\,E$	$\mathrm{Im}\,E$
0	1	Exact	4.768197	−0.000710
		Approx.	4.768197	−0.000710
	2	Exact	7.241200	−0.755956
		Approx.	7.241200	−0.755956
	3	Exact	8.171217	−3.254166
		Approx.	8.171199	−3.254177
	4	Exact	8.440526	−6.281492
		Approx.	8.431643	−6.261440
	5	Exact	8.072643	−9.572815
		Approx.	8.846481	−9.353923

CONCLUSION

In this paper, we propose a method by which one can obtain an approximate analytic expression for the S-matrix valid at complex energies when the S-matrix is given at a set of points on the real axis of the energy. Such an expression can be used, for example, to locate the poles of the multichannel S-matrix which may correspond to bound and resonant states of a system. Compared to the previous description [1] we have here extended it from single-channel case to multichannel problems. The only requirements for this method is a table of the S-matrix data along the real E-axis for which rational-fraction analytical continuation to complex energy plane has been proven to converge rapidly.

The numerical examples show that the proposed method is stable and accurate. With just a few fitting points, it reproduces the bound states and the most significant reso-

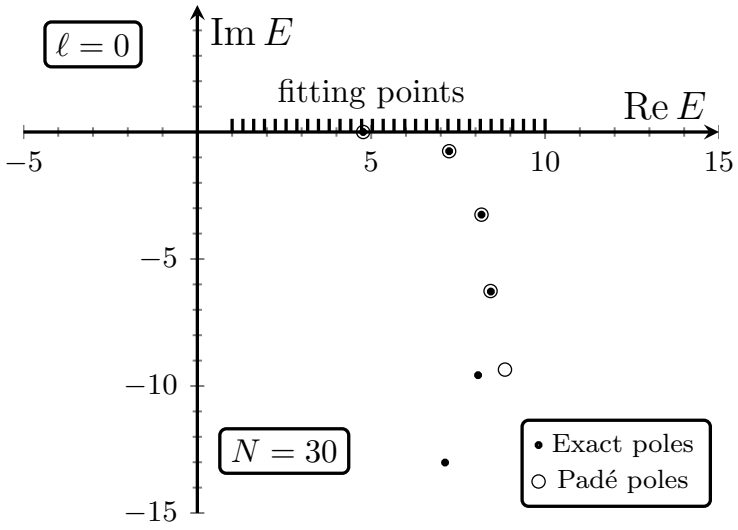

FIGURE 3. The exact positions of the *S*-wave resonance poles (dots) on the complex energy plane for the potential (34), and the corresponding poles of the Padé approximation (open circles). The corresponding fitting points on the Re E-axis are indicated by vertical bars.

nances to the accuracy that is sufficient for any practical purposes.

ACKNOWLEDGMENTS

P.O.G.O acknowledges financial support by the South Africa Nuclear Human Asset and Research Programme as well as National Research Foundation of South Africa.

REFERENCES

1. S. A. Rakityanski, S. A. Sofianos, and N. Elander, *J. Phys. A: Math. Theor.* **40**, 14857–14869 (2007).
2. R. P. Boas, *Invitation to Complex Analysis*, Random House, New York, 1987.
3. W. H. Press, S. A. Teukolsky, W. T. Vetterling, and B. P. Flannery, *Numerical Recipes in FORTRAN*, Cambridge University Press, Cambridge, 1992.
4. G. A. Baker, and J. L. Gammel, editors, *The Padé Approximant in Theoretical Physics*, Academic, New York, 1970.
5. R. G. Newton, *Scattering Theory of Waves and Particles*, Springer-Verlag, New York, 1982, 2nd edn.
6. S. A. Rakityanski, and N. Elander, *Int. J. Quantum Chem.* **106**, 1105 (2006).
7. M. Abramowitz, and I. A. Stegun, *Handbook of Mathematical Functions*, National Bureau of Standards, Washington, D.C., 1964.
8. S. Han, and W. P. Reinhardt, *J. Phys. B: At. Mol. Opt. Phys.* **28**, 3347–3367 (1995).
9. T. Noro, and H. S. Taylor, *J. Phys. B: Atom. Molec. Phys.* **13**, L377 (1980).

A new method of description of three-particle Coulombic systems

V. B. Belyaev* and A. A. Naumkin*,†

*BLTP JINR, 141980 Dubna, Moscow region, Russia
†Department of Physics, Moscow State University, 119992 Moscow, Russia

Abstract. We present a method for treatment of three charged particles. The proposed method has universal character and is applicable both for bound and continuum states. A finite rank approximation is used for Coulomb potential in three-body system Hamiltonian, that results in a system of one-dimensional coupled integral equations. Preliminary numerical results for three-body atomic and molecular systems like H^-, He, $pp\mu$ and other are presented.

Keywords: three-body atomic systems, hyperspherical functions, finite rank operator, bound states
PACS: 03.65.Ge, 31.15.-p, 31.15.xj, 36.10.Ee

INTRODUCTION

The quantum three-body problem emerges in various fields of physics, and different methods of treating it are developed. However, there are no universal methods able to solve it in case of charged particles in the continuum. These problem is important in atomic and molecular physics and in nuclear astrophysics.

The main purpose of the work is to develop a procedure applicable to treatment of three charged particles in continuum. One of the ways to construct it is to make an approximation on operator level, i.e. in the Hamiltonian of three-body system under consideration. After that any boundary conditions can be used. The idea of our work was inspired by earlier paper of N. Aronszajn et al, who introduced the so-called method of intermediate Hamiltonians. This method was applied to calculate lower bounds for eigenvalues of some differential operators. N. W. Bazley and D. W. Fox applied it to He atom and other physical systems [1, 2]. They constructed sequence of intermediate Hamiltonians using finite rank operators. These operators are defined in the whole space of full Hamiltonian. In opposite to that we will apply finite rank approximation in a subspace of the three-body system Hamiltonian, namely in the angular space of hyperspherical variables. This results in a system of coupled one-dimensional integral equations.

In the following sections we review a method of intermediate Hamiltonians, hypersperical coordinates, derive system of integral equations and report the results of calculations.

HYPERSPHERICAL COORDINATES

There are different ways to formulate the three-body problem. We use hyperspherical coordinates, and in this section we give a brief review of them. Complete theory, derivations etc can be found, e.g., in [5].

We start with the three-body system Hamiltonian:

$$H = -\sum_{i=1}^{3} \frac{1}{2m_i}\nabla_i^2 + \sum_{i<j} V_{ij}(\mathbf{r}_i - \mathbf{r}_j), \tag{1}$$

where i enumerates different particles and corresponding sets od Jackobi coordinates.is a numb$\mathbf{r}_i$ is a position vector of the i-th particle. The scaled Jackobi coordinates are introduced as follows:

$$\begin{aligned} \mathbf{x}_i &= \left[\frac{m_j m_k}{m_j + m_k}\right]^{1/2} (\mathbf{r}_j - \mathbf{r}_k) \\ \mathbf{y}_i &= \left[\frac{m_i(m_j+m_k)}{m_1+m_2+m_3}\right]^{1/2} \left(-\mathbf{r}_i + \frac{m_j\mathbf{r}_j + m_k\mathbf{r}_k}{m_j+m_k}\right) \end{aligned} \tag{2}$$

and the Hamiltonian (1) takes the form

$$H = -\frac{1}{2}\nabla_{\mathbf{x}}^2 - \frac{1}{2}\nabla_{\mathbf{y}}^2 + V, \tag{3}$$

where $V = V_{13} + V_{23} + V_{31}$ — a sum of pair potentials. Taking $\mathbf{x}$ and $\mathbf{y}$ in spherical coordinates $(\mathbf{x},\mathbf{y}) \to (x,\theta_1,\varphi_1,y,\theta_2,\varphi_2)$, one obtains:

$$\hat{H} = -\frac{1}{2x^2}\frac{\partial}{\partial x}\left(x^2\frac{\partial}{\partial x}\right) - \frac{1}{2x^2}\Delta_{\Omega_1} - \frac{1}{2x^2}\frac{\partial}{\partial x}\left(x^2\frac{\partial}{\partial x}\right) - \frac{1}{2y^2}\Delta_{\Omega_2} + V, \tag{4}$$

Now let us introduce hyperspherical variables:

$$x = \rho\cos\alpha, \quad y = \rho\sin\alpha \tag{5}$$

Here ρ is hyperradius, α — hyperangle. Hamiltonian expressed in terms of this variables has the form:

$$\hat{H} = -\frac{1}{2}\left(\frac{\partial^2}{\partial\rho^2} + \frac{5}{\rho}\frac{\partial}{\partial\rho}\right) - \frac{1}{2\rho^2}\left[\frac{\partial^2}{\partial\alpha^2} + 4\cot 2\alpha\frac{\partial}{\partial\alpha} + \frac{1}{\cos^2\alpha}\Delta_{\Omega_1} + \frac{1}{\sin^2\alpha}\Delta_{\Omega_2}\right] + V \tag{6}$$

Angular part of a kinetic energy operator is the hypermomentum operator:

$$\hat{K} = \frac{\partial^2}{\partial\alpha^2} + 4\cot 2\alpha\frac{\partial}{\partial\alpha} + \frac{1}{\cos^2\alpha}\Delta_{\Omega_1} + \frac{1}{\sin^2\alpha}\Delta_{\Omega_2}, \tag{7}$$

and its eigenfunctions are hyperspherical harmonics:

$$\mathscr{Y}_K^{l_1 m_1 l_2 m_2}(\alpha,\Omega_1,\Omega_2) = c_K^{l_1 l_2}(\sin\alpha)^{l_1}(\cos\alpha)^{l_2} P_n^{(l_1+\frac{1}{2},l_2+\frac{1}{2})}(\cos 2\alpha) Y_{l_1 m_1}(\Omega_1) Y_{l_2 m_2}(\Omega_2), \tag{8}$$

where

$$c_K^{l_1 l_2} = \left[\frac{2n!(K+2)(n+l_1+l_2+1)!}{\Gamma(n+l_1+3/2)\Gamma(n+l_2+3/2)} \right]^{1/2}. \quad (9)$$

Let us consider system of three particles with masses m_1, m_2, m_3 and charges q_1, q_2, q_3. The Coulomb potential has the form:

$$V(\mathbf{x}, \mathbf{y}) = \frac{b_1}{x_1} + \frac{b_2}{x_2} + \frac{b_3}{x_3}, \quad (10)$$

where $b_i = \sqrt{\frac{m_j m_k}{m_j + m_k}} q_j q_k$. In hyperspherical coordinates:

$$V(\rho, \Omega) = \frac{1}{\rho} \left(\frac{b_1}{\cos\alpha_1} + \frac{b_2}{\cos\alpha_2} + \frac{b_3}{\cos\alpha_3} \right) \quad (11)$$

Here α_i — hyperangles corresponding to different sets of Jacobi coordinates.

FINITE RANK OPERATORS

Finite rank operators are widely used in different problems of mathematical physics. They allow one to reduce complexity of a problem and proceed to its solution. E.g., in [4] finite-rank operator was used to describe nuclear part of full Hamiltonian in a problem of low energy $\pi - {}^3He$ scattering.

N. W. Bazley and D. W. Fox used finite rank operators to calculate lower bounds of eigenvalues of Schrödinger eqution [1, 2]. Let us shortly review the method of intermediate Hamiltonians they used.

We suppose that full Hamiltonian H can be presented as a sum of H^0, that has known eigenvalues and eigenfunctions, and a positively definite H'. The exactly solvable Hamiltonian H^0 is assumed to have ordered discrete energy levels $E_1^0 \leq E_1^0 \leq ...$ below its continuum spectrum. The corresponding eigenfunctions are ψ_1^0, and we have

$$H^0 \psi_i^0 = E_i^0 \psi_i^0. \quad (12)$$

Since $H = H^0 + H'$, where H' is positively definite, $H^0 \leq H$ and $E_1^0 \leq E_1$. Thus, the full Hamiltonian H and H^0 are linked by a sequence of intermediate Hamiltonians:

$$H^0 \leq H^k \leq H^{k+1} \leq H. \quad (13)$$

To construct the Hamiltonians H^k, we introduce a system of k linearly independent functions $p_1, p_2, ..., p_k$. The set of functions $p_1, p_2, ...$ is defined in the whole space of definition of the Hamiltonian H. Projection of some wavefunction φ on these functions is given by

$$P^k \varphi = \sum_{i=1}^{k} \alpha_k p_k \quad (14)$$

The projection P^k increases with k:

$$0 \leq \langle \varphi | P^k \varphi \rangle \leq \langle \varphi | P^{k+1} \varphi \rangle \leq \langle \varphi | \varphi \rangle \tag{15}$$

$$0 \leq \langle \varphi | H' P^k \varphi \rangle \leq \langle \varphi | H' P^{k+1} \varphi \rangle \leq \langle \varphi | H' \varphi \rangle \tag{16}$$

From Eq. (16) we can see that $H'P^k \leq H'P^{k+1} \leq H'$, and we now define intermediate Hamiltonian as

$$H^k = H^0 + H'P^k \tag{17}$$

It is important to to emphasize that the finite rank operator H^k acts on the functions $p_1, p_2, ...$ in the same way as full Hamiltonian H:

$$H^k|i\rangle = H|i\rangle, \quad i = 1, \ldots, k \tag{18}$$

This is the main property of a some finite rank operators which we use in our work.

Following this idea, we construct such an operator in the angular space of definition of operator (7). The Coulomb potential in hyperspherical variables has the form $V(\rho, \Omega) = \frac{1}{\rho} f(\Omega)$, where $f(\Omega)$ is the angular part of potential. We use a finite rank approximation in it. Namely, the function $f(\Omega)$ is replaced by a finite rank operator:

$$f(\Omega) \to \hat{f}^N = \sum_{i,j}^{N} f|\varphi_i\rangle d_{ij} \langle \varphi_j | f \tag{19}$$

Here φ_j are some auxiliary functions defined in angular space, $d_{ij} = \langle \varphi_i | f | \varphi_j \rangle^{-1}$ — inverse matrix element.

FORMALISM

Here we derive a system of coupled one-dimensional integral equations using the finite rank approximation. Wavefunction of an arbitrary system in bound state satisfies the Schrödinger equation:

$$(H_0 + V)|\Psi\rangle = E|\Psi\rangle \tag{20}$$

Here H_0 is kinetic energy, V — interaction potential. This equation can be written in integral form using free Green function:

$$|\Psi\rangle = (E - H_0)^{-1} V|\Psi\rangle = -G_E V|\Psi\rangle \tag{21}$$

Let us rewrite it in coordinate representation:

$$\Psi(\mathbf{R}) = -\int d\mathbf{R}' G_E(\mathbf{R}, \mathbf{R}') V(\mathbf{R}') \Psi(\mathbf{R}'), \tag{22}$$

where $\mathbf{R} = (\mathbf{x}, \mathbf{y}) = (\rho, \Omega)$, and use the Coulombic potential: $V(\mathbf{R}) = \frac{1}{\rho} f(\Omega)$. We obtain integral equation for the wavefunction Ψ in hyperspherical coordinates:

$$\Psi(\rho, \Omega) = -\int \rho'^5 d\rho' d\Omega' G_E(\rho, \rho'; \Omega, \Omega') \frac{1}{\rho'} f(\Omega') \Psi(\rho', \Omega') \tag{23}$$

Using finite rank operator (19) instead angular part of potential $f(\Omega)$, we obtain representation for the wavefunction Ψ:

$$\Psi(\rho,\Omega) = -\sum_{i,j}^{N} \int \rho'^4 d\rho' d\Omega' G_E(\rho,\rho';\Omega,\Omega') f(\Omega') \varphi_i(\Omega')\, d_{ij} C_j(\rho'), \qquad (24)$$

where $C_j(\rho') = \int d\Omega'' \varphi_j(\Omega'') \Psi(\rho,\Omega'')$.

In order to obtain a system of integral equations for coefficients $C_i(\rho)$, we use integral operator: $\int d\Omega\, \varphi_k(\Omega) f(\Omega) \ldots$

$$C_k(\rho) = -\sum_{i,j}^{N} \int d\rho'\, \rho'^4 \int d\Omega\, d\Omega'\, \varphi_k(\Omega) f(\Omega) G_E(\rho,\rho';\Omega,\Omega') f(\Omega') \varphi_i(\Omega')\, d_{ij} C_j(\rho') \qquad (25)$$

or

$$C_k(\rho) = -\sum_{i,j} \int d\rho'\, M_{ki}(\rho,\rho') d_{ij} C_j(\rho'), \qquad (26)$$

$$M_{ki}(\rho,\rho') = \rho'^4 \int d\Omega\, d\Omega'\, \varphi_k(\Omega) f(\Omega) G_E(\rho,\rho';\Omega,\Omega') f(\Omega') \varphi_i(\Omega') \qquad (27)$$

The Green function $G_E(\mathbf{R},\mathbf{R}')$ has quite a simple form in Jacobi coordinates; an analytical expression for it is derived in [6]. However, it has the simplest form in the momentum representation. To exploit this we insert full sets of hyperspherical functions $\sum |\mathscr{Y}^{l_1 l_2}_{KLM}\rangle\langle\mathscr{Y}^{l_1 l_2}_{KLM}|$ into the matrix element 27 and use a hyperspherical representation for a wavefunction of free particles:

$$G_E(\mathbf{x},\mathbf{y}) = \iint \frac{d\mathbf{p}d\mathbf{q}}{(2\pi)^6} \exp(i\mathbf{p}\mathbf{x} + i\mathbf{q}\mathbf{y}) \frac{2m/\hbar^2}{p^2+q^2+\kappa^2},$$

We obtain

$$\frac{1}{(2\pi)^3} e^{i\mathbf{q}\mathbf{x}+i\mathbf{p}\mathbf{y}} = \frac{1}{(\kappa\rho)^2} \sum_{KLMl_1l_2} i^K J_{K+2}(\kappa\rho)\, \mathscr{Y}^{l_1 l_2}_{KLM}(\Omega_\rho)\, \mathscr{Y}^{l_1 l_2}_{KLM}(\Omega_\kappa),$$

where $\kappa^2 = p^2 + q^2$. This allows us to derive the three-body free Green function in hyperspherical representation:

$$\begin{aligned} G^K_E(\rho,\rho') &= \iint \mathscr{Y}^{l_1 l_2}_{KLM}(\Omega)\, G_E(\mathbf{R},\mathbf{R}')\, \mathscr{Y}^{l_1 l_2}_{KLM}(\Omega_\kappa) d\Omega\, d\Omega' = \\ &= \int_0^\infty \frac{\kappa\, d\kappa}{(2\pi)^3} \left(\frac{\rho'}{\rho}\right)^2 J_{K+2}(\kappa\rho) J_{K+2}(\kappa\rho') \frac{1}{\kappa^2 + 2mE} = \\ &= \frac{1}{(2\pi)^3} \left(\frac{\rho'}{\rho}\right)^2 \begin{cases} I_{K+2}(\kappa_0\rho) K_{K+2}(\kappa_0\rho'), & 0 \le \rho \le \rho' \\ K_{K+2}(\kappa_0\rho) I_{K+2}(\kappa_0\rho'), & 0 \le \rho' \le \rho \end{cases} \end{aligned}$$

Here $J_n(x)$, $I_n(x)$ and $K_n(x)$ are Bessel function and modified Bessel functions of first and second kind, respectively. Now we can calculate the kernels of integral equations ((25)):

$$M_{ki}(\rho,\rho') = \sum_{KLMl_1l_2} G^K_E(\rho,\rho') \langle\varphi_k|f|\mathscr{Y}^{l_1 l_2}_{KLM}\rangle\langle\mathscr{Y}^{l_1 l_2}_{KLM}|f|\varphi_i\rangle \qquad (28)$$

We derived a system of coupled one-dimensional integral equations (26). Now one need to calculate the kernel and solve this system numerically. At this stage of treating the Coulomb three-body problem the finite rank approximation makes it sufficiently easier.

CALCULATION AND RESULTS

We constructed the finite rank operator (19) using hyperspherical functions. They have been chosen for convenience, but one can use some other complete set of orthonormalized functions defined in angular space.

It is important to mention that the representation (25) for solution of Schrödinger equation is not a well known hyperspherical expansion. One can see it from the definition of $C_i(\rho)$.

We performed calculations using finite rank operators constructed on 1, 3 and 6 auxiliary functions. In calculation the kernel (28) we should summate an infinite number of terms, but we stopped at values of the hypermomentum K equal to 6, 10 and 14. In order to solve integral equations, the variables ρ and ρ' were discretized with 100 mesh points.

We calculated binding energies of the ground state of such systems: $He, H^-, H_2^+, pp\mu$ and $dd\mu$. Results of these calculations are presented in Table 1 and 1. Table 1 shows a convergence of calculated binding energies with K_{max} for finite rank operator(19) constructed on 6 auxiliary functions, Table 2 shows a convergence of calculated binding energies with the rank of operator N, when the summation stops at $K_{max} = 14$.

TABLE 1. Calculated and exact binding energies, eV

	E_{ex}, eV	$K_{max} = 6$	$K_{max} = 10$	$K_{max} = 14$
H^-	14.34	18	16.2	15.6
He	79.0	95	87	85
H_2^+	16.25	10,1	13.5	15.1
$pp\mu$	2782	1690	2290	2332
$dd\mu$	2988	1845	2195	2654

TABLE 2. Calculated and exact binding energies, eV

	E_{ex}, eV	$N = 1$	$N = 3$	$N = 6$
H^-	14.34	18.2	17.1	15.6
He	79.0	95	89	85
H_2^+	16.25	11	13.7	15.1
$pp\mu$	2782	1850	2101	2332
$dd\mu$	2988	1990	2480	2654

The exact energies are taken from [7].

CONCLUSION

Binding energies of different three-body Coulombic systems were calculated within a finite rank approximation method. The finite rank approximation is made in an angular part of potential in three-body Hamiltonian. This method was tested on some of these systems earlier in [3]. The results obtained shows it can be useful for solving the Coulombic three-body problem.

Calculations were performed at various conditions, i.e. different dimension of the finite rank operator, limit of inner summation, number of mesh points. Results demonstrate reasonable agreement with known values of binding energies. Accuracy of calculation can be improved by takin into account more terms.

We suppose the proposed method will be also applicable to three charged particles in continuum.

REFERENCES

1. N. W. Bazley, D. W. Fox, Phys. Rev. **124**, 483-492 (1961).
2. N. W. Bazley, Phys. Rev. **120**, 144–149 (1960).
3. V. B. Belyaev, I. I. Schlyk, Nucl. Phys. A **790**, 792–795 (2006).
4. V. B. Belyaev, J. Wrzecionko, M. I. Sakvarelidze, Phys. Lett. B **83**, 19–21 (1979).
5. C. D. Lin, Phys. Rep. **257**, 1–83 (1995).
6. A. M. Badalyan, Yu. A. Simonov, Yad. Fiz. **3**, 1032–1047 (1966).
7. A. Martin, J.-M. Richard, T. T. Wu, Phys. Rev. A **46**, 3697–3703 (1992).

SESSION: NUCLEAR STRUCTURE

Chairpersons: R.G. Nazmitdinov and W.D. Heiss

Fragmentation and scales in nuclear giant resonances

W. D. Heiss*, R. G. Nazmitdinov† and F. D. Smit**

*National Institute for Theoretical Physics, Stellenbosch Institute for Advanced Study, and Institute of Theoretical Physics, University of Stellenbosch, 7602 Matieland, South Africa
†Department de Física, Universitat de les Illes Balears, E-07122 Palma de Mallorca, Spain and Bogoliubov Laboratory of Theoretical Physics, Joint Institute for Nuclear Research, 141980 Dubna, Russia
**iThemba LABS, PO Box 722, Somerset West 7129, South Africa

Abstract. We propose a general approach to characterise fluctuations of measured cross sections of nuclear giant resonances. Simulated cross sections are obtained from a particular, yet representative self-energy which contains all information about fragmentations. Using a wavelet analysis, we demonstrate the extraction of time scales of cascading decays into configurations of different complexity of the resonance. We argue that the spreading widths of collective excitations in nuclei are determined by the number of fragmentations as seen in the power spectrum. An analytic treatment of the wavelet analysis using a Fourier expansion of the cross section confirms this principle. A simple rule for the relative life times of states associated with hierarchies of different complexity is given.

Keywords: nuclear reactions, giant resonances
PACS: 24.30.Cz, 24.60.Ky, 24.10.Cn

INTRODUCTION

Nuclear Giant Resonances (GR) have been the subject of numerous investigations over several decades [1]. Some of the basic features such as centroids and collectivity (in terms of the sum rules) are reasonably well understood within microscopic models [2, 3]. However, the question of how a collective mode like the GR dissipates its energy is one of the central issues in nuclear structure physics.

According to accepted wisdom, GRs are essentially excited by an external field through a one-body interaction. It is natural to describe these states as collective 1p-1h states. Once excited, the GR progresses to a fully equilibrated system via direct particle emission and by coupling to more complicated configurations (2p-2h, 3p-3h, etc). The former mechanism gives rise to an escape width, while the latter yields spreading widths ($\Gamma^{\downarrow}$). An understanding of lifetime characteristics associated with the cascade of couplings and scales of fragmentations arising from this coupling (cf [4, 5, 6, 7]) remains a challenge. Recent high energy-resolution experiments of the Isoscalar Giant Quadrupole Resonance (QR) [8, 9, 10] provide new insights into this problem.

It has been shown by Shevchenko *et al.* [8] that the fine structure of the QR observed in (p, p') experiments is largely probe independent. Furthermore, a study of the fine structure using wavelet analysis [11, 12, 13] reveals energy scales [9, 10] in the widths of the fine structure displaying a seemingly systematic pattern, as can be seen in Figs.8

and 9 of Ref.[10]. The power spectrum patterns vary with the structure of the nucleus being studied. They are obtained by summing the wavelet coefficients (an integrated overlap of the mother wavelet and the excitation energy spectrum) onto the wavelet energy-scale axis. While the physical meaning of the results of such an analysis is still being debated, we try here to offer a general explanation. However, we do not embark on a specific microscopic analysis, but rather make use of general and well-established techniques of many-body theory. Gross effects due to nuclear deformation and coupling to the continuum [5] are not discussed; we rather focus on the decay of the QR into configurations of various complexity.

SELF-ENERGY AND CROSS SECTION

To proceed we use the Green's function approach. A central role is played by the self-energy whose finer structure is imparted upon the Green's function via the solution of Dyson's equation which reads [14]

$$G_{\alpha,\beta}(\omega) = G^0_{\alpha,\beta}(\omega)) + G^0_{\alpha,\gamma}(\omega)\Sigma_{\gamma,\gamma'}(\omega)G_{\gamma',\beta}(\omega) \tag{1}$$

which is solved by

$$G_{\alpha,\beta}(\omega) = ((G^0_{\alpha,\beta}(\omega))^{-1} - \Sigma_{\alpha,\beta}(\omega))^{-1}, \tag{2}$$

where we assume $G^0(\omega) = \delta_{\alpha,\beta}/(\omega - \varepsilon)$ to be diagonal in the basis $\alpha, \beta, \ldots$ while the complicated pole structure of $G(\omega)$ is generated by that of the self-energy $\Sigma_{\alpha,\beta}(\omega)$. The pole structure of G carries over to the scattering matrix given by

$$\begin{aligned} T_{\alpha,\beta}(\omega) &= \Sigma_{\alpha,\beta}(\omega) + \Sigma_{\alpha,\beta'}(\omega)G^0_{\beta',\alpha'}(\omega)T_{\alpha',\beta}(\omega) &(3)\\ &= \Sigma_{\alpha,\beta}(\omega) + \Sigma_{\alpha,\beta'}(\omega)G_{\beta',\alpha'}(\omega)\Sigma_{\alpha',\beta}(\omega) &(4)\end{aligned}$$

from which a cross section $\sim |T_{\alpha,\alpha}(\omega)|^2$ is obtained.

Within the excitation energy range of the QR the nucleus has a high density of complicated states of several tens of thousands per MeV and even more for heavy nuclei. These many states appear in the self-energy as poles in the complex energy plane close to the real axis. The small widths imply they are long-lived states and traditionally classed as compound states. The simpler intermediate structure of the excitation is expressed by the substantial fluctuations of the corresponding residues associated with the poles of the self-energy $\Sigma(\omega)$ [15]. In other words, while the individual pole positions of $\Sigma(\omega)$ are virtually unstructured [16], it is the variation of the corresponding residues that bears all the information about intermediate structure. Note that our approach differs from a traditional microscopic calculation in that from the outset we start from a random distribution of pole terms representing compound states. Traditional microscopic approaches cannot address such finer structures [17].

We assume that the QR, being a collective 1p-1h state, decays via a cascade progressing through (2p-2h)-, (3p-3h)-configurations and so forth to the eventual compound states. In turn, each of the intermediate states (including the initial QR) can either decay directly to the ground state or via some more complicated intermediate state. Below

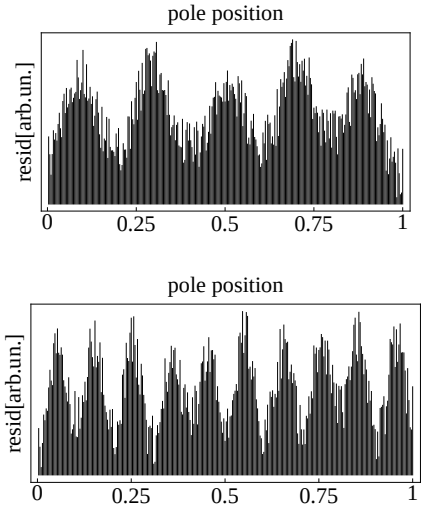

FIGURE 1. Schematic illustration of the residues of the self-energy: for 5 (top) and 10 (bottom) intermediate states. The heights of each of the 300 bars which are situated at the real parts of the poles of the self-energy illustrate the relative variation of the residues. The randomisation is clearly discernible.

we will show that it is this mixture that is seen in the cross section and extracted by wavelet analysis, and it is the variety and cascading complexity of states that invokes the structure of the residues of the poles of the self-energy. Of importance to note is that the number of states available within the energy domain of the QR increases with its complexity: for example, five (2p-2h)-states, ten (3p-3h)-states, down to several thousand compound states (the numbers six or eleven should be taken as examples without claim for quantitative correctness). Moreover, the corresponding life times are expected to increase in line with their increasing complexity, which is in accordance with their decreasing spreading widths (below we come back to this particular aspect of scaling).

As a typical case study we investigate here a wavelet analysis of a simulated cross section that results from a particular input for the self-energy. Since arbitrary units are used, we concentrate on the energy interval [0,1] and use for the pole position $\varepsilon = 0.5 - i0.5$ of the single pole of G_0 (see Eq.(2)). The number of compound states is assumed to be 300; this is of course much less than the experimental level density in the region of a QR for a medium or heavy nucleus, but it suffices for our demonstration. The real parts of the pole positions are assumed to be randomly distributed with a uniform distribution of the mean distance 1/300; the imaginary parts are randomly distributed in the interval [0.004,0.007].

For illustration we consider as a specific example four different sets of residues of the self-energy. The self-energy reads

$$\Sigma(\omega) = \sum_{k=1}^{300} \frac{r_k}{\omega - \omega_k} \tag{5}$$

where each residue r_k is the sum of four subsets; each subset is distributed by a Lorentzian with specific widths γ_i, $i = 1,\ldots,4$ around the four sets of positions $p_i \approx 1/f_i$.

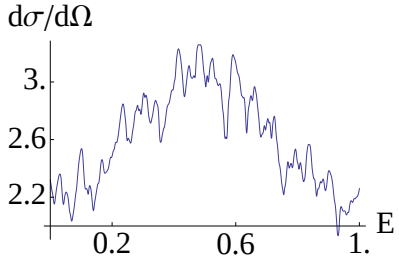

FIGURE 2. Simulated cross section in arbitrary units and power spectrum (right). The abscissa of the cross section is the unit energy interval.

Formally it reads

$$r_k = \sum_{i=1}^{4} h_{i,k}, \quad h_{i,k} = s \sum_{j=1}^{f_i} \frac{\gamma_i^2}{(\frac{k}{300} - j \cdot p_i)^2 + \gamma_i^2} \tag{6}$$

with an overall strength $s = 10^{-5}$. This order of magnitude is based on the mean value of the widths of the compound states being about 10^{-4} to 10^{-5} times smaller than the $\Gamma^{\downarrow}(\gamma_i)$.

The poles at the complex positions ω_k occur in the lower ω-plane with ω being the energy variable. If only $i = 1$ was to occur with $f_1 = 5$, a typical pattern of the residues $h_{1,k}$ is illustrated by the top of Fig.1; similarly for $f_2 = 10$ with $h_{2,k}$ being illustrated by the bottom of Fig.1. The inclusion of further terms would simply add additional peaks to the pattern. In the case presented below we have chosen $f_3 = 16$ and $f_4 = 28$ totalling to 5+10+16+28 additional peaks (not easily visualised, but beautifully discernible in the final analysis). We stress again that the four values f_i were chosen for demonstration purposes and that more than four - or other values - are equally suitable.

These arbitrary numbers used in the example chosen describe particular fragmentations of the QR into altogether 5, 10, 16 and 28 states of increasing complexity. The widths γ_i giving rise to the Lorentzian shape of the residues are in reality determined by the product of the density of the compound states and the coupling of the i-th group to the compound states. The widths are the spreading widths of the respective states considered [15]. As the complexity increases with label i we shall assume $\gamma_1 > \gamma_2 > \gamma_3 > \gamma_4$. In the simulation we endow each γ_i with a random fluctuation with mean value $\gamma_i/4$. As stated above we refrain from specifying a microscopic structure causing the residue pattern assumed for the self-energy; below it becomes clear that guidance comes from experiment.

We also assume that each set f_i is uniformly distributed over the whole energy interval. This is similar in spirit to the assumption used in the local scaling dimension approach [6]. The positions p_i in Eq.(6) are set to be $\sim 1/f_i$ which spreads the actual $j \cdot p_i$ positions equidistantly over the whole interval with j running from 1 to f_i; however, we endow them with a small random fluctuation with mean value $p_i/8$. Note that the random fluctuation of widths and positions generate a mild degree of asymmetry in the energy interval [0,1], resulting in slightly different patterns in the intervals [0,0.5] and [0.5,1]. The near equality of the positions, that is - apart from slight random fluctuations

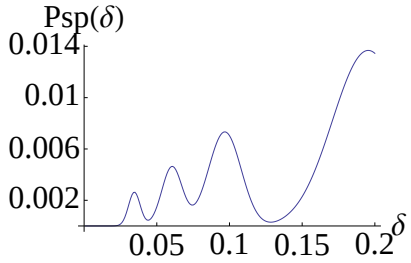

FIGURE 3. Power spectrum from the cross section in Fig 2. The energy values δ refer to the wavelet parameters.

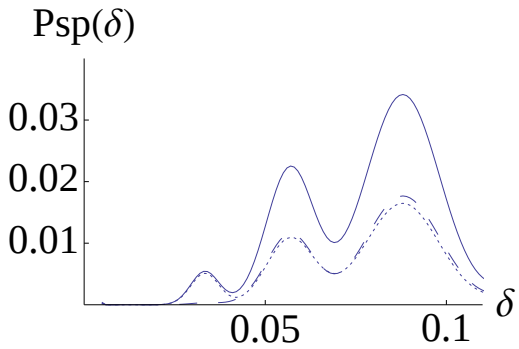

FIGURE 4. Power spectrum for a particular asymmetric situation discussed in text. The dotted curve originates from a scan of the interval [0,0.5], the dashed curve from [0.5,1] and the solid curve from the total interval. Note that the peak on the far left is virtually absent in the dashed curve while fully present in the dotted curve. Units as in Fig.2 and 3.

- the regular pattern of the various fragments as illustrated in Fig.1, is basically dictated by experimental findings: *if there is no near regular pattern there will be no discernible structure in the power spectrum of the wavelet analysis*. However, we shall return below to the case where regular patterns may occur only in a smaller portion of the interval.

The first obvious choice for the widths assumes simply $\gamma_i = 1/(2f_i)$ yielding the simulated cross section shown in Fig.2 (below a precise analytic expression confirming the $1/(2f_i)$-law is given). A variation of such a choice is rather significant, we shall return to this aspect in detail.

THE WAVELET ANALYSIS

The analysis using a Morlet-type mother wavelet

$$\Psi(\omega,\delta) = \frac{1}{\sqrt{\delta}} \cos\frac{k(\omega-\omega_0)}{\delta} \exp -\frac{(\omega-\omega_0)^2}{2\delta^2} \tag{7}$$

is used to calculate the coefficients

$$C(\delta,\omega_0) = \int \frac{\mathrm{d}\sigma(\omega)}{\mathrm{d}\Omega}\Psi(\omega,\delta)\,\mathrm{d}\omega \tag{8}$$

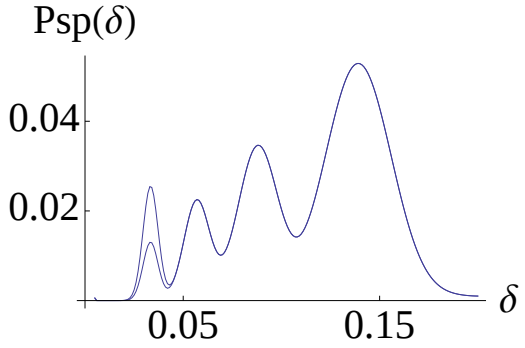

FIGURE 5. Power spectrum: dependence of height at the maximum on spreading width. The curve with the lower value of the most left maximum is identical to the one in Fig.3., while the higher peak is due to a decrease of its spreading width or an increase of its life time. Units as in Fig.2 and 3.

from which the power spectrum

$$Psp(\delta) = \int |C(\delta, \omega_0)|^2 \, \mathrm{d}\omega_0$$

is obtained as a function of the scaling parameter δ. It is shown in Fig.3; if not indicated otherwise we use the value $k = 6$ for the wave number of the mother wavelet. There is in fact a k-dependence of the positions of the maxima of the power spectrum which is given in analytic terms below. A contour plot of $C(\delta, \omega_0)$ is illustrated in Fig.6.

In Fig.3 we clearly discern the four maxima that are produced by the four different values f_i of the number of fragmentations. In fact, the fragmentation into $f_1 = 5$ produces (for $k = 6$) the maximum at $\delta_1^{\max} = 1/f_1 = 0.2$; similarly, the other three maxima occur at $\delta_i^{\max} = 1/f_i$, $i = 2,3,4$. This is one of our major findings:
the maxima of the power spectrum occur at

$$\delta_i^{\max} \approx k/(2\pi) \cdot I/f_i$$

with I being the interval of the whole range of the QR considered and f_i the number of fragmentations. The factor $k/(2\pi)$ originates from the analytic expression given in (7) below. Here we note that this result does not depend on whether we use a real wavelet as in Eq.(7) or its complex version where the cosine-function is replaced by its complex counterpart $\cos(.) + i\sin(.)$.

The asymmetry found in some experimental data can obviously be accounted for by our analysis. We refer to cases where the analysis yields a pattern in the first half of the whole resonance being different from that in the second half, or in principle for any subdivision of the whole resonance. For illustration, we take $f_4 = 14$ while leaving all other parameters unchanged. In this way the total of 28 maxima of the residues r_{f_4} are confined to only 14 within the left half of the interval. The effects are clearly seen in Fig.4. Note that the positions of the maxima still remain unchanged. This type of asymmetry is clearly discernible in Fig.9 of Ref.[10]: from the two-dimensional wavelet transform the wavelet power would give a similarly different pattern when taken at different portions of the whole interval.

The folding (integration) of the cross section with the Morlet wavelet has to be done numerically. In order to obtain an analytic expression relating the number of fragmentations f_i to the positions of the maxima of the power spectrum, we consider an expansion of a cross section into a Fourier series

$$\frac{\mathrm{d}\sigma(\omega)}{\mathrm{d}\Omega} = \sum_m c_m \sin(m\pi\omega/I) + \sum_m c'_m \cos(m\pi\omega/I). \tag{9}$$

An intermediate structure manifests itself, if a few terms in Eq.(9) are appreciably stronger than the others. For Fig.2 the terms with $c_{10} \approx c_{20} \approx c_{32} \approx c_{56}$ (and similarly for the primed coefficients) are dominant; of course, terms for different m-values also occur but are smaller by roughly an order of magnitude or more (here our analysis does not focus on $m \leq 4$: while giving larger contributions such values would correspond to $\delta \geq 0.5$ and represent gross and bulk structure). Performing analytically the wavelet-transform of each term in Eq.(9) (see Appendix), one obtains an analytic evaluation of the positions and heights of the maxima of the power spectrum. For each $\sin(m\pi x)-$ or $\cos(m\pi x)-$term the positions of the local maxima in the power spectrum turn out to be

$$\mathrm{Max}_m = \frac{k+\sqrt{2+k^2}}{2m\pi} I. \tag{10}$$

For $k = 6$ (and the unity interval I) this yields 0.2, 0.1, 0.0625 and 0.036 for $m = 10, 20, 32$ and 56, respectively, as verified in Fig.3. Note that a different choice of k moves the positions of the local maxima, yet the $\sim 1/m$ law prevails. The expression (10) provides an obvious tool to be used to ascertain the number of fragmentations when the maxima are determined from an analysis of experimental data. Clearly, the number f_m of fragmentations introduced above is related to the value m in Eq.(9) by $m = 2f_m$.

Furthermore, an increased value of k can resolve a peak in the power spectrum that is caused by two near values of f_i. In fact, the distance between adjacent maxima (say $m = 17$ and $m = 18$) roughly doubles when k is doubled.

While - for fixed k - the $1/f_i$ dependence of the maxima of the power spectrum is an important finding, even more significant is the result that the values at the maxima (the heights) also obey the same $1/f_i$-law *if the corresponding Fourier coefficients are about equal*. Indeed, a straight line can be drawn through the maxima in Fig.3 since the four values $c_m, m = 10, 20, 32, 56$ are about equal. We recall that, for example, $\sin(10\pi x)$ generates $f_k = 5$ peaks of a width $\gamma_k = 1/(2f_k)$ in the energy (unit) interval for the cross section. This can be exploited in a realistic analysis: a deviation from this straight-line-rule signals effectively a deviation from the spreading width being assumed to be $1/(2f_i)$. This is illustrated in Fig.4 where the spreading width $1/(2f_4)$ has been decreased to $1/(2.8f_4)$. As a result, the value of the first peak becomes enhanced. Since the spreading width is related to the life time of the states, we conclude: *the life times are proportional to f_i if the heights of the maxima lie on a straight line; an increased (decreased) height signals an even longer (shorter) life time.*

In this context we note that the *number* of peaks and troughs in Fig.5 on the horizontal lines matches exactly the values of the f_i: five on the top, further down ten, then sixteen and twenty eight on the bottom. The actual values of these peaks and troughs determine the heights of the bumps in the power spectrum, that is the information about the life

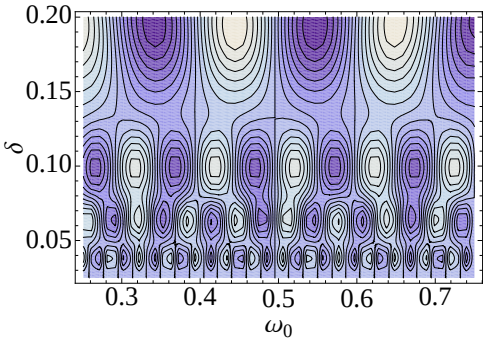

FIGURE 6. Wavelet contour plot of cross section shown in Fig.3. The symbols δ and ω_0 refer to the Morlet wavelet parameters used in Eq.(7). The (positive) maxima are in light shading and the (negative) minima in dark. For the top pattern the contours range from 0.4 to -0.4.

times of the respective fragmented states. A similar wavelet transform obtained from experimental data is presented in Figs.8 and 9 in Ref.[10]; note that our schematic 'in vitro' illustration is of course much more symmetric.

CONCLUSION

While in experiments the chaotic nature of the nucleus usually shows at higher excitation energies [16], the pertinent structure revealed in the analysis may come as a surprise. We are of course familiar with order in the nuclear many body system as shown in shell effects and simple collective states. The fragmentations of the QR may be due to a different quality: it could be a manifestation of *self-organising structures* [18, 19, 20]. Indeed, the life time of increasingly complex configurations of the QR is increasing toward the compound states and the ground state. There is no generally accepted definition of conditions under which the self-organising structures are expected to arise. We may speculate that in the case considered here, once the nuclear QR state is created, it is driven to an unstable hierarchy of configurations (metastable states) by quantum selection rules which connect these different complex configurations due to internal mixing. This problem needs of course a dedicated study on its own and is beyond the scope of the present paper.

We summarise the major points of our findings: (i) the position of the peaks in the power spectrum indicate the number of fragmentations of a particular intermediate state; the more complex states lie to the left of the simpler states (see Eq.(10)); (ii) the resolution of poorly resolved peaks can be improved by a higher value of k; (iii) the values (heights) at the peaks are related to the spreading widths, implying knowledge about the life times: if they lie on a straight line, the life times are proportional to the number of fragmentations, if they lie above (below) the straight line the corresponding life times are longer (shorter). Finally, we mention that a pronounced gross structure of the experimental cross section as found in lighter nuclei, would have no effect upon our findings. In fact, such gross structure had to occur at the far right end (values of δ appreciably larger than those used in the literature) of the power spectrum.

APPENDIX

The wavelet transform of each term in Eq.(9) is for the $\sin m\pi\omega$-term (with $m\pi = a$)

$$\frac{1}{\sqrt{\delta}}\int_0^1 \mathrm{d}x \sin ax \cos\frac{k(x-\varepsilon)}{\delta}\exp-\frac{(x-\varepsilon)^2}{2\delta^2} = -\sqrt{\frac{\pi}{2}}\frac{\sqrt{\delta}}{2}\exp(-\frac{(a\delta+k)^2}{2})\cdot$$
$$\Im(\exp(-ia\varepsilon)\mathrm{Erf}\frac{1+ia\delta^2-\varepsilon+i\delta k}{\sqrt{2}\delta}) + \Im(\exp(-ia\varepsilon+2a\delta k)\mathrm{Erf}\frac{1+ia\delta^2-\varepsilon-i\delta k}{\sqrt{2}\delta})$$
$$+\Im(\exp(ia\varepsilon)\mathrm{Erf}\frac{-ia\delta^2-\varepsilon-i\delta k}{\sqrt{2}\delta}) + \Im(\exp(ia\varepsilon+2a\delta k)\mathrm{Erf}\frac{-ia\delta^2-\varepsilon+i\delta k}{\sqrt{2}\delta})$$

and similar for the $\cos m\pi\omega$-term where the $\Im$ is replaced by $\Re$. Here Erf denotes the error function. The positions of the maxima in Fig 3 are the zeros of the derivative with respect to δ of the square of the expression above (we assume that the maxima are isolated). This amounts to finding the zeros of the derivative. The derivative reads

$$\begin{aligned}
&\frac{-1+\exp(2ia\varepsilon)}{16\delta^{3/2}}\Big\{ i\sqrt{2\pi}\delta\exp(-\frac{k^2+a^2\delta^2+2ia\varepsilon}{2}) \\
&\Big(\exp(ak\delta)(-1+2a\delta(-k+a\delta))\Im\mathrm{Erf}(\frac{\varepsilon+i\delta(k-a\delta)}{\sqrt{2}\delta}) \\
+\;& \exp(-ak\delta)(-1+2a\delta(k+a\delta))\Im\mathrm{Erf}(\frac{\varepsilon-i\delta(k+a\delta)}{\sqrt{2}\delta})\Big) \\
-\;& 4\exp(-\frac{\varepsilon(\varepsilon+2i\delta(k+2a\delta))}{2\delta^2})(1+\exp(\frac{2i\varepsilon k}{\delta})(-i(1+\exp(2ia\varepsilon))\varepsilon \\
+\;& a(-1+\exp(2ia\varepsilon))\delta^2\Big\}.
\end{aligned}$$

This expression has three terms: two within the big round brackets and a third before the closing curly bracket. For the parameter range of interest, owing to the exponential factors only the first term within the round brackets contributes substantially while the other two terms are smaller by many orders of magnitude. This first term, in turn, is governed by the factor $(-1+2a\delta(-k+a\delta))$. It vanishes, and thus the whole expression, for $\delta = (k+\sqrt{2+k^2})/(2a) = (k+\sqrt{2+k^2})/(2m\pi)$ being the expression given in Eq.(10).

ACKNOWLEDGMENTS

WDH is thankful for the hospitality which he received from the Nuclear Theory Section of the Bogoliubov Laboratory, JINR during his visit to Dubna. The authors gratefully acknowledge enlightening discussions with J. Carter, R. Fearick and P. von Neumann-Cosel. This work is partly supported by JINR-SA Agreement on scientific collaboration, by Grant No. FIS2008-00781/FIS (Spain) and RFBR Grants No. 08-02-00118 (Russia).

REFERENCES

1. M. N. Harakeh and A. van der Woude, *Giant Resonances: Fundamental High-Frequency Modes of Nuclear Excitation* Clarendon Press, Oxford, 2001.
2. A. Bohr and B. R. Mottelson, *Nuclear Structure*, v.II World Scientific, Singapore, 1998.
3. P. Ring and P. Schuck, *The Nuclear Many-Body Problem* Springer-Verlag, New York, 1980.
4. R. Lauritzen, F. P. Bortignon, R. A. Broglia, and V. G. Zelevinsky, *Phys. Rev. Letters* **74**, 5190 (1995).
5. V. V. Sokolov and V. G. Zelevinsky, *Phys. Rev. C***56**, 311 (1997).
6. H. Aiba and M. Matsuo, *Phys. Rev. C***60**, 034307 (1999).
7. D. Lacroix and P. Chomaz, *Phys. Rev. C***60**, 064307 (1999).
8. A. Shevchenko, J. Carter, R. W. Fearick, S. V. Förtsch, H. Fujita, Y. Fujita, Y. Kalmykov, D. Lacroix, J. J. Lawrie, P. von Neumann-Cosel, R. Neveling, V. Yu. Ponomarev, A. Richter, E. Sideras-Haddad, F. D. Smit, and J. Wambach, *Phys. Rev. Letters* **93**, 122501 (2004).
9. A. Shevchenko, G. R. J. Cooper, J. Carter, R. W. Fearick, Y. Kalmykov, P. von Neumann-Cosel, V. Yu. Ponomarev, A. Richter, I. Usman and J. Wambach, *Phys. Rev. C* **77**, 024302 (2008).
10. A. Shevchenko, O. Burda, J. Carter, G. R. J. Cooper, R. W. Fearick, S. V. Förtsch, Y. Fujita, Y. Kalmykov, D. Lacroix, J. J. Lawrie, P. von Neumann-Cosel, R. Neveling, V. Yu. Ponomarev, A. Richter, E. Sideras-Haddad, F. D. Smit, and J. Wambach, *Phys. Rev. C* **79**, 044305 (2009).
11. I. Daubechies, *Ten Lectures on Wavelets*, SIAM, Vol.**61** (1992).
12. S. Mallat, *A Wavelet Tour of Signal Processing* Academic Press, San Diego, 1998.
13. H. L. Resnikoff and R. O. Wells Jr., *Wavelet Analysis: The Scalable Structure of Information* Springer-Verlag, New York, 2002.
14. J.-P. Blaizot and G. Ripka, *Quantum Theory of Finite Systems* The MIT Press, London, 1986.
15. F. J. W. Hahne and W. D. Heiss, *Ann. Physics* **89**, 68 (1975).
16. T. Guhr, A. Müller-Groeling, and H. Weidenmüller, Phys. Rep. **299**, 189 (1998); H. A. Weidenmüller and G. E. Mitchell, *Rev. Mod. Physics* **81**, 539 (2009).
17. C. L. Bai, H. O. Zhang, X. Z. Zhang, F. R. Xu, H. Sagawa, and G. Coló, *Phys. Rev. C* **79**, 041301(R) (2009).
18. P. Bak, C. Tang, and K.Wiesenfeld, *Phys. Rev. Letters* **59**, 381 (1987).
19. H. J. Jensen, *Self-Organized Criticality: Emergent Complex Behaviour in Physical and Biological Systems* Cambridge University Press, Cambridge, 1998.
20. D. Sornette, *Critical Phenomena in Natural Sciences. Chaos, Fractals, Selforganization and Disorder: Concepts and Tools* Springer, Berlin, 2000.

Novel method for solution of coupled radial Schrödinger equations

S. N. Ershov[*], **J. S. Vaagen**[†] and **M. V. Zhukov**[**]

[*]*Joint Institute for Nuclear Research, Dubna, Russia.*
[†]*Institute of Physics and Technology, University of Bergen, Norway.*
[**]*Fundamental Physics, Chalmers University of Technology, S-41296 Göteborg, Sweden.*

Abstract. One of the major problems in numerical solution of coupled differential equations is the maintenance of linear independence for different sets of solution vectors. A novel method for solution of radial Schrödinger equations is suggested. It consists of rearrangement of coupled equations in a way that is appropriate to avoid usual numerical instabilities associated with components of the wave function in their classically forbidden regions. Applications of the new method for nuclear structure calculations within the hyperspherical harmonics approach, are given.

Keywords: Schröfinger equation, solution of coupled differential equations, hyperspherical harmonics
PACS: 02.30.Hq, 21.60.Gx, 24.10.Eq

INTRODUCTION

Systems of coupled Schrödinger equations often appear in problems of quantum mechanics and applications to nuclear physics, quantum chemistry etc. A variety of methods has been developed to solve systems of coupled radial Schrödinger equations. A widespread approach consists of two steps. First, sets of linear independent solutions are calculated and then, exploiting the linearity of the coupled equations, a suitable combination of different sets with the required boundary conditions is found. A major problem in numerical solution of the coupled equations is the difficulty of maintaining the linear independence of the solution vectors. There always exists a region of radii where some components of the wave function are classically forbidden and others not. The components with negative radial kinetic energy will in general consist of an exponentially growing and an exponentially decreasing part. If the integration is continued through a classically forbidden region, the exponentially growing components of the wave function in the most strongly closed channels increase faster and soon start to dominate the entire wave function matrix. The small components become insignificant on the scale of the relative accuracy of the calculation. Eventually different solutions become linearly dependent and, thus, useless for finding linear combinations with required boundary conditions. In the classically allowed region, the uneven growth of the components does not occur, since the components are mainly oscillating. But all problems involve integration through at least one classically forbidden region, and instability from developing nearly dependent solutions causes serious numerical inaccuracy. This difficulty arises from the natural properties of solutions rather then from any particular method for their construction.

To maintain linear independence, different stabilizing transformations during propagation were suggested [1, 2, 3, 4, 5]. After several propagation steps these regularization procedures can be applied to re-establish the linear independence of the columns in the wave function matrix. Usually these transformations are rather awkward and tedious. Another approach to overcome the difficulty is to use a so-called invariant imbedding method, in which the propagated quantity is not the wave function matrix $\mathbf{\Psi} = \{\psi_{in}(r)\}$ but rather its logarithmic derivative $\mathbf{\Psi}'\mathbf{\Psi}^{-1}$ [6, 7] or its inverse matrix $\boldsymbol{R} = \mathbf{\Psi}\mathbf{\Psi}'^{-1}$ [8]. These methods found broad applications, especially for large coupled-channels calculations. In other approaches radial wave functions are expanded in terms of orthonormal basis functions, chosen to account for some dynamical features in the most effective way. Then a solution of the differential equations is reduced to a set of linear equations for expansion coefficients. Such an approach, for example, is realized in program [9].

In the past three decades, a lot of research (see, for example, [10, 11] and references therein) has been performed in the area of numerical integration of the Schrödinger equation. The main goal is to construct numerical methods that are both accurate and computational efficient. The development of these methods is still an active subject. Here, we suggest a novel method for solution of radial Schrödinger equations. It consists in rearrangement of coupled equations in a way that is appropriate to avoid the usual numerical instabilities associated with components of the wave function in their classically forbidden regions. Applications of the new method to nuclear structure calculations within the hyperspherical harmonics approach, are given.

THEORY

Consider the system of the N coupled radial Schrödinger equations

$$\left(\frac{d^2}{dr^2} + \frac{2mE}{\hbar^2} - \frac{\mathscr{L}_i(\mathscr{L}_i+1)}{r^2}\right)\psi_{in}(r) = \sum_{j=1}^{N} V_{ij}(r)\,\psi_{jn}(r) \tag{1}$$

where E is a total energy, $\mathscr{L}_i$ is an angular orbital momentum in the channel i. The first index of $\psi_{in}(r)$ denotes the i-th component of wave functions ($i = 1, \ldots, N$) while the second index n marks different linear independent solutions. The $N \times N$ matrix of coupling potentials $V_{ij}(r)$ is assumed symmetric, i. e. $V_{ij}(r) = V_{ji}(r)$. Note that potentials include the factor $2m/\hbar^2$ and have dimension fm^{-2}. In general, the system (1) of the N linear differential equations of second order has $2N$ linearly independent solutions called the fundamental ones; N solutions have a regular behaviour at the origin while the N others have irregular behaviour. Any solution of the system (1) can be written as a linear combination of these fundamental solutions. Only solutions that satisfy definite boundary conditions imposed at the origin and infinity, have physical meaning. At the origin the boundary condition demands that wave functions have a regular behaviour

$$\psi_{in}(r \to 0) \to 0 \tag{2}$$

while at infinity the boundary condition depends on the sign of energy E. For bound states ($E < 0$) the problem is of the eigenvalue type and for any given eigenvalue (E_n)

the solution of (1) decays exponentially for large values of r

$$\psi_{in}(r \to \infty) \to \exp(-k_n r) \tag{3}$$

where $k_n = \sqrt{2m \mid E_n \mid /\hbar^2}$. For continuum states ($E > 0$) the solutions oscillate at infinity

$$\psi_{in}(r \to \infty) \to H^{(-)}_{\mathscr{L}_i}(k r)\, \delta_{in} - H^{(+)}_{\mathscr{L}_i}(k r)\, S_{in} \tag{4}$$

where $k = \sqrt{2m \mid E \mid /\hbar^2}$. Here $H^{(\pm)}_{\mathscr{L}_i}(x) = G_{\mathscr{L}_i}(x) \pm \imath F_{\mathscr{L}_i}(x)$ are the Coulomb functions of index $\mathscr{L}_i$ [12] describing the in- and out-going spherical waves. $F_{\mathscr{L}_i}(x)$ and $G_{\mathscr{L}_i}(x)$ are regular and irregular Coulomb functions, respectively, $\imath = \sqrt{-1}$. The S_{in} is the S-matrix element for the outgoing amplitude in channel i from an incoming plane wave in channel n.

Our aim is to find solutions of system (1) satisfying boundary conditions (2,3,4) for radius changing from zero to some maximal value $r = r_{max}$. The general method to solve the boundary value problem for coupled equations (1) is to construct a set of linear independent solutions and after that find a linear combination of these solutions which satisfies the required asymptotic behaviour. Numerical integration within a long radial interval tends to accumulate errors and induces a loss of linear independence of solutions. Thus it is convenient to divide the radial space into nonoverlapping domains by points b_I, $0 = b_0 < b_1 < \ldots < b_{max} = r_{max}$ and solve differential equations separately in each of the intervals. Then the partial solutions are assembled into a global solution that is continuous and smooth across the whole region and satisfies the given boundary conditions. The transparent and straightforward way to perform this task is to reformulate the coupled differential equations (1) as a system of coupled integral equations. It has also the advantage that integral equations contain the explicit structure of required solutions.

Integral formulation

Boundary value problems for a system of ordinary differential equations (1) can be reformulated as a system of Fredholm integral equations. For technical reasons it is simpler to solve Volterra integral equations with variable upper or lower limits. System of Volterra equations corresponds to the solution of the initial value problem. If only open channels exist then solutions of Fredholm and Volterra systems are different by a constant matrix. Since the total normalization is not important all solutions are acceptable. If closed and opened channels coexist, then solutions of Volterra equations can not substitute the solutions of Fredholm systems within the entire range of a radial variable. Numerical solutions of Volterra equations with variable upper limit are regular at the origin but at large radii they will have exponentially increasing components in closed channels. Numerical solutions of Volterra equations with variable lower limit can contain exponentially decreasing components in closed channels but can not guarantee the regular behaviour of wave functions at the origin. A solution of this dilemma is well known and commonly used. It consists of a combination of solutions for both type

of Volterra equations: wave functions and their first derivatives are matched at some intermediate radius. Thus the obtained wave functions are solutions of the original system of Schrödinger equations (1) for all radii and satisfy the required boundary conditions. If at least one open channel exists then a matching procedure is always possible. Let $N = N_{op} + N_{cl}$, where N_{op} (N_{cl}) is the number of open (closed) channels. Then, there are N regular solutions for outward integrations of Volterra equations with variable upper limit, while the number of linear independent solutions for Volterra equations with variable lower limit is larger and equal to $N + N_{op} = N_{cl} + 2N_{op}$. This number is composed of the N_{cl} sets with exponentially decreasing components in closed channels, N_{op} sets with components oscillating asymptotically like regular functions F_i or N_{op} sets with components oscillating like irregular G_i. The extra freedom in number of linear independent solutions always allows to match them and define simultaneously necessary S-matrix elements. When only closed channels exist, i. e. for bound state problems, the number of linear independent solutions for inward and outward integration is the same and equal to N. Then matching procedure is only possible at discrete values of the energy which are energies of bound states, respectively.

Consider the following systems of Volterra integral equations with variable upper or lower limit r

$$\psi_{in}(r) - \frac{1}{k}\int_0^r dr' \left(f_i(kr)\,g_i(kr') - g_i(kr)\,f_i(kr')\right) \sum_{j=1}^{N} V_{ij}(r')\,\psi_{jn}(r') = \delta_{in}\,f_i(kr) \qquad (5)$$

$$\psi_{in}(r) + \frac{1}{k}\int_r^\infty dr' \left(f_i(kr)\,g_i(kr') - g_i(kr)\,f_i(kr')\right) \sum_{j=1}^{N} V_{ij}(r')\,\psi_{jn}(r') = \delta_{in}\,g_i(kr) \qquad (6)$$

where δ_{in} is the Kronecker symbol, and where the Green's function $(f_i(kr)\,g_i(kr') - g_i(kr)\,f_i(kr'))/k$ is composed of two linear independent solutions $f_i(kr)$ and $g_i(kr)$ of the free Schrödinger equation

$$\left(\frac{d^2}{dr^2} + \frac{2mE}{\hbar^2} - \frac{\mathscr{L}_i(\mathscr{L}_i+1)}{r^2}\right) f_i(kr) = 0 \qquad (7)$$

Free solutions are normalized by demanding that the Wronskian relation $W(f_i, g_i) = f_i(x)\,g_i'(x) - f_i'(x)\,g_i(x) = -1$. They have explicit representation via Bessel functions [12] of the first J_ν and second Y_ν kinds for $E > 0$

$$f_i(x) = \sqrt{\frac{\pi x}{2}}\,J_{\mathscr{L}_i+1/2}(x) \quad ; \quad g_i(x) = -\sqrt{\frac{\pi x}{2}}\,Y_{\mathscr{L}_i+1/2}(x) \qquad (8)$$

and modified Bessel functions I_ν and K_ν for $E < 0$

$$f_i(x) = \sqrt{x}\,I_{\mathscr{L}_i+1/2}(x) \quad ; \quad g_i(x) = \sqrt{x}\,K_{\mathscr{L}_i+1/2}(x) \qquad (9)$$

The functions $f_i(kr)$ and $g_i(kr)$ have regular and irregular behaviour at the origin, respectively. Hence solutions of Volterra systems (5) and (6) also define sets of N linear independent solutions of the Schrödinger equations (1) with regular or irregular

behaviour at the origin, respectively. Below we consider only system (5), for system (6) a derivation can be made in a similar way.

Labelling the wave function $\psi_{in}(r)$ in the interval I as $\psi^I_{in}(r)$ and using the equations (5) we can write

$$\begin{aligned}\psi^I_{in}(r) &- \frac{1}{k}\int_{b_{I-1}}^{r} dr' \left(f_i(kr)\,g_i(kr') - g_i(kr)\,f_i(kr')\right) \sum_{j=1}^{N} V_{ij}(r')\,\psi^I_{jn}(r') \\ &= f_i(kr)\,A^I_{in} - g_i(kr)\,B^I_{in} \end{aligned} \tag{10}$$

where the constants A^I_{in} and B^I_{in} are equal to

$$\begin{aligned} A^I_{in} &= \delta_{in} + \frac{1}{k}\int_0^{b_{I-1}} dr' g_i(kr') \sum_j V_{ij}(r')\,\psi_{jn}(r') \\ B^I_{in} &= \frac{1}{k}\int_0^{b_{I-1}} dr' f_i(kr') \sum_j V_{ij}(r')\,\psi_{jn}(r') \end{aligned} \tag{11}$$

The wave functions $\psi^I_{in}(r)$ in the interval I can be written as linear combinations of unknown functions $y^I_{ip}(r)$ and $z^I_{ip}(r)$ [13]

$$\psi^I_{in}(r) = \sum_{p=1}^{N} \left(y^I_{ip}(r)\,A^I_{pn} - z^I_{ip}(r)\,B^I_{pn}\right) \tag{12}$$

Substituting decomposition (12) into equations (10) we obtain the integral equations in the I-th interval for functions $y^I_{in}(r)$ and $z^I_{in}(r)$

$$y^I_{in}(r) - \frac{1}{k}\int_{b_{I-1}}^{r} dr' \left(f_i(kr)\,g_i(kr') - g_i(kr)\,f_i(kr')\right) \sum_{j=1}^{N} V_{ij}(r')\,y^I_{jn}(r') = \delta_{in}\,f_i(kr) \tag{13}$$

$$z^I_{in}(r) - \frac{1}{k}\int_{b_{I-1}}^{r} dr' \left(f_i(kr)\,g_i(kr') - g_i(kr)\,f_i(kr')\right) \sum_{j=1}^{N} V_{ij}(r')\,z^I_{jn}(r') = \delta_{in}\,g_i(kr) \tag{14}$$

According to the driving terms on the right hand side of equations (13) - (14) the functions $y^I_{in}(r)$ and $z^I_{in}(r)$ can be called the regular and irregular solutions in the interval I. They form a complete system of $2N$ linear independent solutions of the Schrödinger equations (1) within the radial interval I. Substituting the decomposition (12) in equations (11), simple recurrence relations for the coefficients A^I_{in} and B^I_{in} can be obtained

$$\begin{aligned} A^I_{in} &= A^{I-1}_{in} + \sum_{p=1}^{N} \left((gVy)^{I-1}_{ip}\,A^{I-1}_{pn} - (gVz)^{I-1}_{ip}\,B^{I-1}_{pn}\right) \\ B^I_{in} &= B^{I-1}_{in} + \sum_{p=1}^{N} \left((fVy)^{I-1}_{ip}\,A^{I-1}_{pn} - (fVz)^{I-1}_{ip}\,B^{I-1}_{pn}\right) \end{aligned} \tag{15}$$

with initial values $A^1_{in} = \delta_{in}$, $B^1_{in} = 0$ and $I \geq 2$. The coefficients of A^{I-1}_{pn} and B^{I-1}_{pn} in (15) are given by

$$\begin{aligned}
(gVy)^{I-1}_{ip} &= \frac{1}{k}\int_{b_{I-2}}^{b_{I-1}} dr' g_i(kr') \sum_{j=1}^{N} V_{ij}(r')\, y^{I-1}_{jp}(r') \\
(gVz)^{I-1}_{ip} &= \frac{1}{k}\int_{b_{I-2}}^{b_{I-1}} dr' g_i(kr') \sum_{j=1}^{N} V_{ij}(r')\, z^{I-1}_{jp}(r') \\
(fVy)^{I-1}_{ip} &= \frac{1}{k}\int_{b_{I-2}}^{b_{I-1}} dr' f_i(kr') \sum_{j=1}^{N} V_{ij}(r')\, y^{I-1}_{jp}(r') \\
(fVz)^{I-1}_{ip} &= \frac{1}{k}\int_{b_{I-2}}^{b_{I-1}} dr' f_i(kr') \sum_{j=1}^{N} V_{ij}(r')\, z^{I-1}_{jp}(r') \qquad (16)
\end{aligned}$$

Thus the original problem (1) is reduced to obtaining a complete set of regular $y^I_{in}(r)$ and irregular $z^I_{in}(r)$ solutions in the interval I. From these solutions, using decomposition (12), global solutions $\psi^I_{in}(r)$ can be obtained. Note that the $y^I_{in}(r)$ and $z^I_{in}(r)$ in the I-th interval are calculated independently of solutions on other intervals. Below we will present the detailed derivation only for regular solutions $y^I_{in}(r)$. For irregular solutions $z^I_{in}(r)$ similar relations can easily be obtained.

The Green's function constructed from the $f_i(kr)$ and $g_i(kr)$ solutions of the free Schrödinger equation (7) was used explicitly in (13) and (14). In reality, any potentials can be added into equation (7) to obtain potential-modified functions $f_i(kr)$ and $g_i(kr)$ in the I-th interval. These potentials must however be subtracted from the diagonal potentials $V_{ii}(r)$ in equations (13) and (14), respectively. For example, the diagonal potentials V_{ii} themselves may be used for $f_i(kr)$ and $g_i(kr)$ calculations. This allows to account for a sizeable part of the correlations induced by the interactions before an attempt is made to solve the system of coupled equations. But now we lose knowledge about analytical properties of $f_i(kr)$ and $g_i(kr)$ functions. As a reasonable compromise, the value of the diagonal potential at any fixed point within the I-th interval (for example, b_{I-1} - the beginning of interval I) can be used to represent the interval. Then functions $f_i(k_i r)$ and $g_i(k_i r)$ will still be solutions of the free Schrödinger equation (7) but with new (scaled) energies $E_i = E$ - $(\hbar^2/2m)\, V_{ii}(b_{I-1})$ and, correspondingly, with new linear momenta $k_i = \sqrt{2m|E_i|}/\hbar$. Then we get new integral equations for calculations of local regular solutions

$$\begin{aligned}
y^I_{in}(r) &- \frac{1}{k_i}\int_{b_{I-1}}^{r} dr' \left(f_i(k_i r)\, g_i(k_i r') - g_i(k_i r)\, f_i(k_i r')\right) \sum_{j=1}^{N} V^I_{ij}(r')\, y^I_{jn}(r') \\
&= \delta_{in}\left(f_i(k_i r)\, a_i - g_i(k_i r)\, c_i\right) \qquad (17)
\end{aligned}$$

where $V^I_{ij}(r) = V_{ij}(r)$ - $\delta_{ij} V_{ii}(b_{I-1})$ and where the constants a_i and c_i in the driving term are fixed by the requirement that $y^I_{in}(r)$ must satisfy the initial values built into equations

(13): $y^I_{in}(b_{I-1}) = \delta_{in}\, f_i(k\, b_{I-1})$ and $y^{I'}_{in}(b_{I-1}) = \delta_{in}\, k f'_i(k\, b_{I-1})$

$$\begin{aligned} a_i &= \frac{k}{k_i} f'_i(k\, b_{I-1})\, g_i(k_i\, b_{I-1}) - f_i(k\, b_{I-1})\, g'_i(k_i\, b_{I-1}) \\ c_i &= \frac{k}{k_i} f'_i(k\, b_{I-1})\, f_i(k_i\, b_{I-1}) - f_i(k\, b_{I-1})\, f'_i(k_i\, b_{I-1}) \end{aligned} \tag{18}$$

When all $k_i = k$, the equations (17) reduce to equations (13). In equations (17) the channel energies E_i depend on values of diagonal potentials $V_{ii}(b_{I-1})$ and thus may have different signs, therefore different channels may be locally open or closed.

The integral equations (17) define an explicit structure for regular solutions $y^I_{in}(r)$

$$y^I_{in}(r) = f_i(k_i\, r)\, \alpha^I_{in}(r) - g_i(k_i\, r)\, \beta^I_{in}(r) \tag{19}$$

where the unknown functions $\alpha^I_{in}(r)$ and $\beta^I_{in}(r)$ are solutions of the following system of coupled integral equations

$$\begin{aligned} \alpha^I_{in}(r) &= \delta_{in} a_i + \frac{1}{k_i} \int_{b_{I-1}}^{r} dr'\, g_i(k_i\, r') \sum_{j=1}^{N} V^I_{ij}(r') \left(f_j(k_j\, r')\, \alpha^I_{jn}(r') - g_j(k_j\, r')\, \beta^I_{jn}(r') \right) \\ \beta^I_{in}(r) &= \delta_{in} c_i + \frac{1}{k_i} \int_{b_{I-1}}^{r} dr'\, f_i(k_i\, r') \sum_{j=1}^{N} V^I_{ij}(r') \left(f_j(k_j\, r')\, \alpha^I_{jn}(r') - g_j(k_j\, r')\, \beta^I_{jn}(r') \right) \end{aligned} \tag{20}$$

Now we return to the differential formulation of the respective equations.

Differential formulation

The system of integral equations (20) for the functions $\alpha^I_{in}(r)$ and $\beta^I_{in}(r)$ is equivalent to a system of the $2N$ coupled ordinary differential equations of the first order

$$\begin{aligned} \frac{d\alpha^I_{in}(r)}{dr} &= \frac{1}{k_i} g_i(k_i\, r) \sum_{j=1}^{N} V^I_{ij}(r) \left(f_j(k_j\, r)\, \alpha^I_{jn}(r) - g_j(k_j\, r)\, \beta^I_{jn}(r) \right) \\ \frac{d\beta^I_{in}(r)}{dr} &= \frac{1}{k_i} f_i(k_i\, r) \sum_{j=1}^{N} V^I_{ij}(r) \left(f_j(k_j\, r)\, \alpha^I_{jn}(r) - g_j(k_j\, r)\, \beta^I_{jn}(r) \right) \end{aligned} \tag{21}$$

with initial values $\alpha^I_{in}(b_{I-1}) = \delta_{in} a_i$ and $\beta^I_{in}(b_{I-1}) = \delta_{in} c_i$. Multiplying the first equation by $f_i(k_i\, r)$ and the second by $g_i(k_i\, r)$, we see that these equations have the special properties, $f_i(k_i\, r)\, d\alpha^I_{in}(r)/dr = g_i(k_i\, r)\, d\beta^I_{in}(r)/dr$. Equations (21) also allow to investigate explicitly the reasons that catalyze loss of linear independence for different solution sets.

We have to estimate the qualitative behaviour of the regular $f_i(x)$ and irregular $g_i(x)$ functions. For closed channels, the regular (irregular) functions (9) are monotonously increasing (decreasing) with increasing arguments. Both functions never equal zero at finite arguments. For open channels there are two regions where functions $f_i(x)$ and $g_i(x)$ (8) have qualitatively different behaviour. At small arguments they have monotonic

behaviour similar to that for closed channels. At large arguments they oscillate like cosine or sine functions. Instead of $f_i(x)$ and $g_i(x)$ functions in the region of oscillations it is convenient to introduce the modulus $M_i(x)$ and phase $\theta_i(x)$ functions [12]

$$M_i(x) = \sqrt{f_i^2(x) + g_i^2(x)}\,; \quad f_i(x) = M_i(x)\cos\theta_i(x)\,; \quad g_i(x) = M_i(x)\sin\theta_i(x) \qquad (22)$$

Modulus $M_i(x)$ is never equal to zero. From the Wronskian relation it also follows that $\theta_i'(x) = -1/M_i^2(x)$.

The presence of centrifugal barriers is natural for dynamics described by Schrödinger equations. It is possible to account for them analytically by introducing regular $f_i(k_i r)$ and irregular $g_i(k_i r)$ solutions of the free Schrödinger equations (7). Explicit centrifugal barriers drop out and their influence on the full solution is described by the $f_i(k_i r)$ and $g_i(k_i r)$ functions in the equations (21). The regular and irregular functions of different orders are mixed in the equations. These functions have quantitatively different behaviour, some may be rather small while others are very large. The difference in absolute values can easily reach many orders of magnitude. Under such circumstances it is difficult to keep an acceptable level of the accuracy in numerical solution of coupled equations. The lack of accuracy leads to loss of the linear independence of different solutions. A possible way out is to make a rearrangement of coupled equations such that the different behaviour of free solutions will be minimized. There exist only three suitable combinations: the product of free functions $f_i(x)\,g_i(x)$ and their logarithmic derivatives $f_i'(x)/f_i(x)$ and $g_i'(x)/g_i(x)$. After rearrangement the necessary requirements to the numerical accuracy for solutions of the new system of coupled equations become significantly weaker. *Such rearrangement of equations is just the main idea of this article*.

To illustrate our point, Figure (1) shows the regular $f_i(x)$ and irregular $g_i(x)$ functions for closed (a) and open (b) channels with $\mathscr{L}_i$ = 3/2, 19/2 and 39/2 represented by the solid, dash and dash-dot lines, respectively. (In the hypersherical harmonics method these values of $\mathscr{L}_i$ correspond to calculations with hypermoment K = 0, 8 and 18, respectively.) We see that changes in scales for absolute values of free solutions can easily span twenty orders of magnitude. (Figure (1) shows variations from 10^{-10} to 10^{+10}). Variations of logarithmic derivatives for these functions, on the other hand, shown in Figure (2), span only a few (2 - 3) orders of magnitude.

Now we assume that in the I-th interval the first N_0 channels have free functions $f_i(x)$ and $g_i(x)$ with arguments x lying in the region of monotonic behaviour. All closed and a part of the open channels are included into this number. The rest, channels from N_0 + 1 to N are open, and arguments of free functions are in the region of oscillations. In the first N_0 channels the absolute values of free solutions may vary over a wide scale while they are restricted to about unity in the last (N - N_0) ones. We will transform the system of equations (21) in such a way that free solutions enter into the new system of equations as logarithmic derivatives with rather restricted variations in absolute scale. For functions with arguments in the region of oscillations the logarithmic derivatives become infinite at the points where the functions have zeros. This is a reason for special selection of such channels. Thus instead of the relation (19) for a regular solution $y_{in}^I(r)$

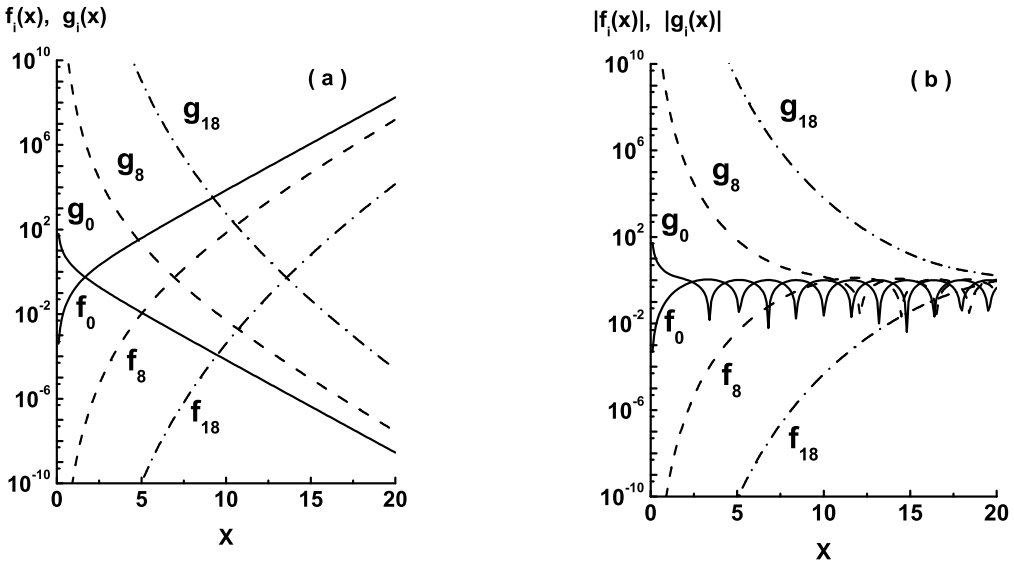

FIGURE 1. The regular $f_i(x)$ and irregular $g_i(x)$ solutions of the free Schrödinger equations for negative (a) and positive (b) energies. The solid, dash and dash-dot lines correspond to calculations with hypermoments $K = 0$, 8 and 18, respectively.

we use a more explicit decomposition for different components i

$$\begin{aligned} y^I_{in}(r) &= f_i(k_i r)\,\alpha^I_{in}(r) - g_i(k_i r)\,\beta^I_{in}(r), \qquad 1 \le i \le N_0 \\ &= M_i(k_i r)\left(\cos(\theta_i(k_i r))\,\alpha^I_{in}(r) - \sin(\theta_i(k_i r))\,\beta^I_{in}(r)\right), \; N_0+1 \le i \le N \end{aligned} \tag{23}$$

Let us first consider the equations for channels $i \le N_0$. Differentiating functions $y^I_{in}(r)$, using equations (21) and the Wronskian relation for free solutions we can get the following set of equations for $i \le N_0$

$$\begin{aligned} \frac{dy^I_{in}(r)}{dr} &= k_i \frac{f_i'(k_i r)}{f_i(k_i r)}\, y^I_{in}(r) + \gamma^I_{in}(r) \\ \frac{d\gamma^I_{in}(r)}{dr} &= -k_i \frac{f_i'(k_i r)}{f_i(k_i r)}\, \gamma^I_{in}(r) + \sum_{j=1}^{N} V^I_{ij}(r)\, y^I_{jn}(r) \end{aligned} \tag{24}$$

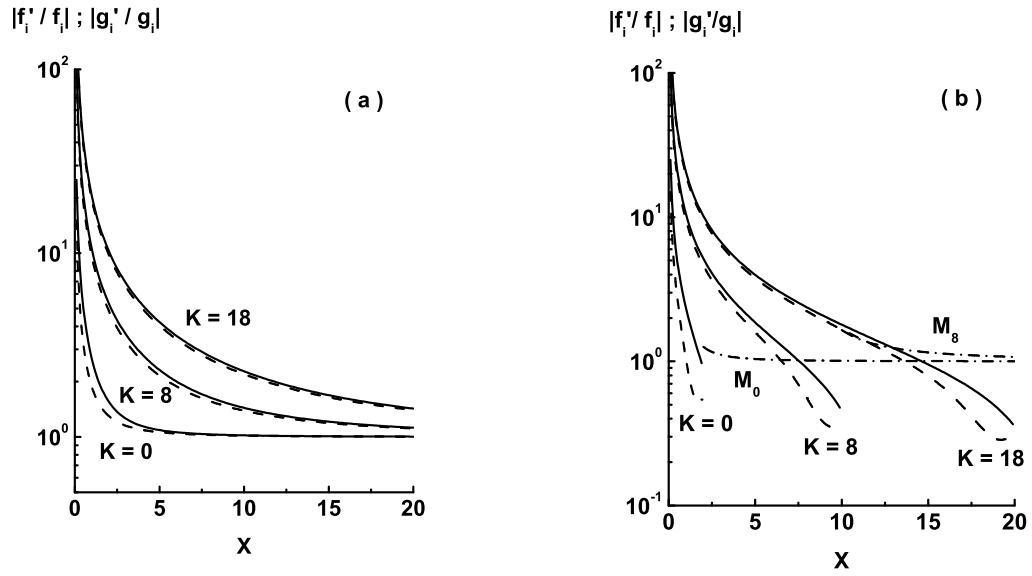

FIGURE 2. Absolute values of the logarithmic derivatives of regular $f_i(x)$ (solid line) and irregular $g_i(x)$ (dash line) solutions of the free Schrödinger equations for negative (a) and positive (b) energies for hypermoments $K = 0$, 8 and 18. The dash-dotted lines show moduli (22) $M_0(x)$ and $M_8(x)$ of free solutions in the region of oscillations.

where the function $\gamma^I_{in}(r) = k_i \beta^I_{in}(r)/f_i(k_i r)$. For $i > N_0$ the following set of equations can be obtained

$$\begin{aligned} \frac{dy^I_{in}(r)}{dr} &= k_i \frac{M_i'(k_i r)}{M_i(k_i r)} y^I_{in}(r) + \gamma^I_{in}(r) \\ \frac{d\gamma^I_{in}(r)}{dr} &= -k_i \frac{M_i'(k_i r)}{M_i(k_i r)} \gamma^I_{in}(r) + \sum_{j=1}^{N} V^I_{ij}(r)\, y^I_{jn}(r) - \frac{k_i^2}{M_i^4(k_i r)} y^I_{in}(r) \end{aligned} \tag{25}$$

where $\gamma^I_{in}(r) = k_i \left(\sin(\theta_i(k_i r))\, \alpha^I_{in}(r) + \cos(\theta_i(k_i r))\, \beta^I_{in}(r)\right)/M_i(k_i r)$. Initial values for functions $y^I_{in}(r)$ and $\gamma^I_{in}(r)$ are equal to

$$\begin{aligned} y^I_{in}(b_{i-1}) &= \delta_{in} f_i(k b_{I-1}) \qquad ; \quad 1 \le i \le N \\ \gamma^I_{in}(b_{i-1}) &= \delta_{in} f_i(k b_{I-1}) \left(k \frac{f_i'(k b_{I-1})}{f_i(k b_{I-1})} - k_i \frac{f_i'(k_i b_{I-1})}{f_i(k_i b_{I-1})} \right) \quad ; \quad 1 \le i \le N_0 \\ \gamma^I_{in}(b_{i-1}) &= \delta_{in} f_i(k b_{I-1}) \left(k \frac{f_i'(k b_{I-1})}{f_i(k b_{I-1})} - k_i \frac{M_i'(k_i b_{I-1})}{M_i(k_i b_{I-1})} \right) \quad ; \quad N_0 < i \le N \end{aligned} \tag{26}$$

For cases when $k_i = k$ and $i \leq N_0$ the initial values for functions $\gamma^I_{in}(b_{i-1})$ are equal to zero. Finding functions $y^I_{in}(r)$ and $\gamma^I_{in}(r)$ we obtain simultaneously the derivatives $y^{I'}_{in}(r)$ via equations (24) and (25).

The systems of equations (24) - (25) include the bare potentials $V^I_{ij}(r)$ without the multiplications on functions $f_i(k_i r)$ and $g_i(k_i r)$ occurring in equations (21). The free solutions appear in the new equations (24) - (25) only as logarithmic derivatives. Thus huge differences in scales of absolute values that may exist for functions $f_i(x)$ and $g_i(x)$ with different indices i are significantly reduced, to relatively mild variations of absolute values for logarithmic derivatives. Hence requirements on accuracy of numerical methods applied for solving the coupled radial Schrödinger equations become essentially weaker and the loss of linear independence for different solution sets due to insufficient numerical accuracy, is greatly reduced.

Expressions (24) - (25) correspond to calculations of regular solutions $y^I_{in}(r)$. For irregular solutions $z^I_{in}(r)$ we can proceed analogously and get for $i \leq N_0$ the following system of equations

$$\begin{aligned} \frac{dz^I_{in}(r)}{dr} &= k_i \frac{g_i'(k_i r)}{g_i(k_i r)} z^I_{in}(r) + \eta^I_{in}(r) \\ \frac{d\eta^I_{in}(r)}{dr} &= -k_i \frac{g_i'(k_i r)}{g_i(k_i r)} \eta^I_{in}(r) + \sum_{j=1}^{N} V^I_{ij}(r) z^I_{jn}(r) \end{aligned} \tag{27}$$

and for $i > N_0$ equations parallel to those of (25) (by just changing notations: $y^I_{in}(r) \rightarrow z^I_{in}(r)$ and $\gamma^I_{in}(r) \rightarrow \eta^I_{in}(r)$). Initial values for functions $z^I_{in}(r)$ and $\eta^I_{in}(r)$ are equal to

$$\begin{aligned} z^I_{in}(b_{i-1}) &= \delta_{in} g_i(k b_{I-1}) \quad ; \quad 1 \leq i \leq N \\ \eta^I_{in}(b_{i-1}) &= \delta_{in} g_i(k b_{I-1}) \left(k \frac{g_i'(k b_{I-1})}{g_i(k b_{I-1})} - k_i \frac{g_i'(k_i b_{I-1})}{g_i(k_i b_{I-1})} \right) \quad ; \quad 1 \leq i \leq N_0 \\ \eta^I_{in}(b_{i-1}) &= \delta_{in} g_i(k b_{I-1}) \left(k \frac{g_i'(k b_{I-1})}{g_i(k b_{I-1})} - k_i \frac{M_i'(k_i b_{I-1})}{M_i(k_i b_{I-1})} \right) \quad ; \quad N_0 < i \leq N \end{aligned} \tag{28}$$

We see that if in the formulas above for $y^I_{in}(r)$, the regular functions $f_i(x)$ are replaced by the irregular functions $g_i(x)$, we get expressions for calculations of irregular solutions $z^I_{in}(r)$. The new systems (24) and (27) show explicitly why regular and irregular solutions behave in qualitatively different way. The differences of respective equations for $i \leq N_0$ are in the terms that include the logarithmic derivatives of free solutions. Since $f_i'(x)/f_i(x)$ and $g_i'(x)/g_i(x)$ have comparable absolute values and different signs they force solutions to change in opposite directions. For components $i > N_0$ in the regions of oscillations both solutions $y^I_{in}(r)$ and $z^I_{in}(r)$ obey equations where only the modulus function $M_i(k_i r)$ of free solutions appears at the place of $f_i(k_i r)$ and $g_i(k_i r)$.

In practice, it is convenient to scale solutions $y^I_{ip}(r)$ and $z^I_{ip}(r)$ by factors $f_p(k b_{I-1})$ and $g_p(k b_{I-1})$, respectively, for channels p where the functions $f_p(k b_{I-1})$ and $g_p(k b_{I-1})$ have monotonic behaviour (while we do not scale solutions for channels p where their absolute values oscillate around unity)

$$y^I_{ip}(r) = \tilde{y}^I_{ip}(r) f_p(k b_{I-1}) \quad ; \quad \tilde{A}^I_{pn} = f_p(k b_{I-1}) A^I_{pn} \tag{29}$$

$$z^I_{ip}(r) \;=\; \tilde{z}^I_{ip}(r)\, g_p(k\, b_{I-1}) \quad ; \quad \tilde{B}^I_{pn} = g_p(k\, b_{I-1})\, B^I_{pn}$$

Then, wave functions $\psi^I_{in}(r)$ (see (12)) on interval I can be written as linear combinations of the $\tilde{y}^I_{ip}(r)$ and $\tilde{z}^I_{ip}(r)$ functions

$$\psi^I_{in}(r) = \sum_{p=1}^{N} (\tilde{y}^I_{ip}(r)\, \tilde{A}^I_{pn} - \tilde{z}^I_{ip}(r)\, \tilde{B}^I_{pn}) \tag{30}$$

where the initial values for functions $\tilde{y}^I_{ip}(r)$ and $\tilde{z}^I_{ip}(r)$ at the radius $r = b_{I-1}$ are reduced to the Kronecker symbol. The integrals in (16) can be scaled in similar ways, for example $(gVy)^I_{ip} = g_i(k\, b_{I-1})\, (\widetilde{gVy})^I_{ip}\, f_p(k\, b_{I-1})$ etc. Thus, the recurrence relations (15) for coefficients A^I_{in} and B^I_{in} are transformed, and read

$$\begin{aligned}
\tilde{A}^I_{in} &= \frac{f_i(k\, b_{I-1})}{f_i(k\, b_{I-2})} \left\{ \tilde{A}^{I-1}_{in} + f_i(k\, b_{I-2})\, g_i(k\, b_{I-2}) \sum_{p=1}^{N} \left((\widetilde{gVy})^{I-1}_{ip}\, \tilde{A}^{I-1}_{pn} - (\widetilde{gVz})^{I-1}_{ip}\, \tilde{B}^{I-1}_{pn} \right) \right\} \\
\tilde{B}^I_{in} &= \frac{g_i(k\, b_{I-1})}{g_i(k\, b_{I-2})} \left\{ \tilde{B}^{I-1}_{in} + f_i(k\, b_{I-2})\, g_i(k\, b_{I-2}) \sum_{p=1}^{N} \left((\widetilde{fVy})^{I-1}_{ip}\, \tilde{A}^{I-1}_{pn} - (\widetilde{fVz})^{I-1}_{ip}\, \tilde{B}^{I-1}_{pn} \right) \right\}
\end{aligned}$$

This scaling gives significant reduction of the absolute value variations within radial interval I for all functions and coefficients in the formulas above.

Matching and normalization

For bound state case ($E < 0$) we have two sets of the N linear independent solutions of systems (5) and (6), regular $\psi^{reg}_{in}(r)$ and irregular $\psi^{irr}_{in}(r)$, respectively. Wave functions $\psi^{reg}_{in}(r)$ are regular at the origin while $\psi^{irr}_{in}(r)$ vanish at infinity. We demand that at some (matching) point r_m a linear combinations of wave functions and derivatives for both sets become equal to a each other

$$\begin{aligned}
\sum_{n=1}^{N} \psi^{reg}_{in}(r_m)\, \lambda_n &= \sum_{n=1}^{N} \psi^{irr}_{in}(r_m)\, \mu_n \\
\sum_{n=1}^{N} \psi^{reg'}_{in}(r_m)\, \lambda_n &= \sum_{n=1}^{N} \psi^{irr'}_{in}(r_m)\, \mu_n
\end{aligned} \tag{31}$$

Here $\{\lambda_n\}$ and $\{\mu_n\}$ are unknown mixing coefficients that must be found from solving the homogeneous system of $2N$ linear equations (31). A solution exists only if the determinant of the system constructed from wave functions and derivatives equals to zero. This may only happen at a discrete value of the energy E, which is the energy of a bound state. Hence we have a procedure searching for the energy of bound states. First, the energy intervals, where the determinant changes sign, are defined. Then the search for zero of the determinant within the energy interval gives the bound state

energy. Knowing sets of solutions for this energy we can arbitrarily fix one of the mixing coefficients (say by putting it equal to unity) and the rest of them can be found by solving the inhomogeneous system of $(2N-1)$-equations obtained from (31). Finally a bound state wave function, obtained as linear combination of $\psi_{in}^{reg}(r)$ and $\psi_{in}^{irr}(r)$, is normalized to have unit norm.

For continuum states ($E > 0$) the asymptotic form ($r \to \infty$) for linear combinations of radial wave functions from system (5) may be written as

$$\begin{aligned} \sum_{p=1}^{N} \psi_{ip}(r)\,\lambda_{pn} &= F_i(k\,r)\,\delta_{in} + G_i(k\,r)\,K_{in} \\ \sum_{p=1}^{N} \psi'_{ip}(r)\,\lambda_{pn} &= k\left(F_i'(k\,r)\,\delta_{in} + G_i'(k\,r)\,K_{in}\right) \end{aligned} \tag{32}$$

Solutions of this system allow us to define the $\boldsymbol{K}$-matrix elements K_{in} and matrix of mixing coefficients $\{\lambda_{pn}\}$ for normalization of linear independent sets of radial functions $\psi_{ip}(r)$. The $\boldsymbol{K}$-matrix is related to the scattering $\boldsymbol{S}$-matrix appearing in formula (4) by the equation

$$\boldsymbol{S} = (1 + \imath\boldsymbol{K})(1 - \imath\boldsymbol{K})^{-1} \tag{33}$$

This procedure gives the $\boldsymbol{S}$ (or $\boldsymbol{K}$) matrix and N independent sets of radial wave functions with necessary asymptotic behaviour.

DISCUSSION

The centrifugal potentials are an important part of the dynamics described by the system of coupled radial Schrödinger equations and usually singled out explicitly. Numerical solutions of Schrödinger equations in regions where motions are under barriers lead to mixing of large and small components that coexist at these conditions. When accuracy of numerical integration is not enough for tracing of different solutions, such mixing may lead to loss of linear independence. This is one of the major problems in numerical solutions of coupled system of equations. The method suggested here, tries to remedy this, and consists of two steps. First, the radial domain is split into finite intervals. A complete set of fundamental solutions has to be obtained at every interval independently on solutions in other intervals. The second step consists in a rearrangement of equations to a set which is less prone to developing numerical instabilities. To this end, the second order equations are reduced to a system of the first order equations. In mathematical textbooks on ordinary differential equations, the general method to transform second order equations $y'' = F(x,y)$ into a double systems of first order equations is usually formulated via introduction of new variables $\gamma = y'$ for the first derivative of solutions y. In our scheme this general idea is developed further taking into account the specific structure of Schrödinger equations. If the function f is a solution of the free Schröedinger equation with centrifugal barrier then the special transformation $\gamma = y'$ - $k\,(f'/f)\,y$ accounts for the influence of centrifugal barriers explicitly and in a most effective way. As the result, centrifugal barriers drop out from the final system of first order differential equations,

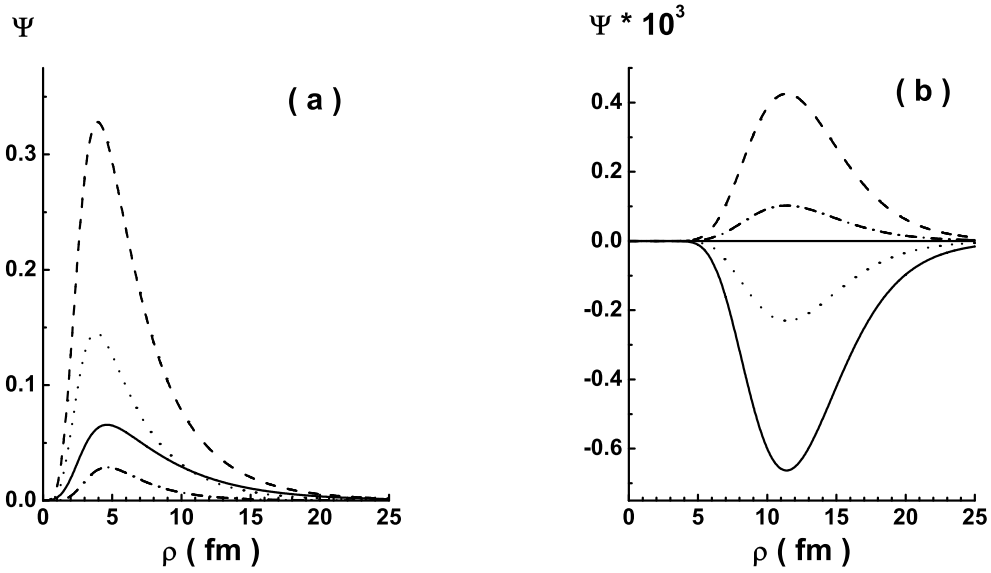

FIGURE 3. Different components of the ^{6}He ground state wave function $\psi^{J\pi}_{KLSl_xl_y}(\rho)$. The solid, dash, dot and dash-dot lines show components with quantum numbers $(K, L = S, l_x = l_y)$ equal to: a) (0, 0, 0), (2, 0, 0), (2, 1, 1) and (4, 0, 2), respectively; and b) (20, 1, 9), (20, 1, 7), (20, 1, 5) and (20, 1, 3), respectively.

and their influence on dynamics appears only via the free solutions appearing as logarithmic derivatives. Since variations of the magnitude of logarithmic derivatives for free solutions are essentially milder, compared to the variations of their absolute values, the conditions for developing numerical instabilities are strongly suppressed.

TABLE 1. Root mean square (r.m.s.) values of hyperradii ($\langle\psi^{J\pi}_{KLSl_xl_y}|\rho^2|\psi^{J\pi}_{KLSl_xl_y}\rangle^{1/2}$) and weights of different components of the ^{6}He ground state wave function. The r.m.s. hyperradius for the whole ground state wave function is equal to 5.55 fm.

K, L = S, $l_x = l_y$	0 0 0	2 0 0	2 1 1	4 0 2	20 1 9	20 1 7	20 1 5	20 1 3
r.m.s. (fm)	6.80	5.40	5.22	5.75	12.36	12.36	12.36	12.36
weight, %	4.1	77.0	14.5	0.6	5.10^{-4}	2.10^{-4}	6.10^{-5}	1.10^{-5}

Below we will demonstrate an application of the new method to solution of a concrete physical problem. A good example is the calculation of the ground state wave functions for light nuclei within cluster few-body models [14]. The method of hyperspherical harmonics is very convenient for description of three-body structure of two-neutron halos

that appears in some nuclei, like the Borromean nuclei ^{6}He, ^{11}Li, etc, at the very edge of nuclear stability (see recent works [15, 16] and references therein for more detailed discussion of successes and challenges of this approach). The relative motion of three clusters is described in the space of hyperspherical coordinates (ρ, Ω_5) and the nuclear wave function $\Psi^{J\pi}$ is decomposed on a basis of hyperspherical harmonics $\Upsilon_{K\nu}(\Omega_5)$ [14], $\Psi^{J\pi}$ = $\sum_{K\nu} \psi^{J\pi}_{K\nu}(\rho)\,\Upsilon_{K\nu}(\Omega_5)$. Here ρ, Ω_5 and K are the hyperradius, hyperangles and the hypermoment, respectively. The index ν denotes all quantum numbers which are necessary, in addition to K, for a complete identification of the basis. If the Schrödinger equation for wave function $\Psi^{J\pi}$ is multiplied by hyperspherical harmonics $\Upsilon_{K\nu}(\Omega_5)$ from the left and integrated over hyperangles Ω_5, a system of coupled hyperradial differential equations similar to (1) is obtained. In this system the effective orbital angular momenta $\mathscr{L}_i$ = K_i + 3/2, where K_i is hypermoment in the i-th channel, and matrix elements $V_{ij}(\rho)$ of the all intercluster interactions in the basis of hyperspherical harmonics, depend only on the hyperradius ρ. More details about development of the model and applied interactions can be found in [17]. As an example, we will consider the calculation of the 0^+ ground state wave function of the ^{6}He nucleus. All possible hyperharmonics up to a value of K = 20 are included in the wave function decomposition, giving a system of Schrödinger equations with $\sim$ 70 coupled channels. A few wave function components with lowest and highest values of hypermoment K are shown in Figures (3(a)) and (3(b)), respectively. Table (1) also gives weights of the respective components and also shows their r.m.s. values of the hyperradius ρ. It is interesting to note the different localization (in hyperradius ρ) of components with different values of the hypermoment K, hence of the generalized orbital angular momentum. Components with larger values of K are more strongly suppressed at small values of the hyperradius, while their maxima are shifted to larger ρ. The r.m.s. values of the hyperradius for each hyperharmonic component are for the largest K values more then two times the value for small K. Note that weights of components that peak far out in the exterior region are rather small. This behaviour is in accordance with intuitive expectations about the role that (centrifugally suppressed) components with high K values should play in the wave function decomposition.

Some questions, important for practical applications, are not discussed in this article. For example, what numerical methods are suited for solving the new system of equations, what partitions of whole radial domain into smaller parts are the most effective (the formulation above was for arbitrary radial intervals) and so on. It is clear that these questions can be answered in different ways and practical prescriptions should take into account the specific features of the problem and should be optimized for any concrete model. To cover these issues, the physical models must be explicitly formulated and thus the scope of this article would have to be essentially expanded. Since our main aim was to present the general idea of the method, these important practical questions will have to be illuminated elsewhere.

CONCLUSION

The dynamics of a system of coupled radial Schrödinger equations may be very versatile and complicated due to coupling potentials, but also carry general features due to universality of the kinetic energy operator. These universal properties are contained in

different centrifugal barriers and lead to appearance of difficulties in numerical solutions of coupled equations in regions where the motion for some channels is classically forbidden. Such classically forbidden regions exist even in cases when coupling potentials are absent, and solutions within such regions are described by Bessel functions with known analytical properties. The absolute scales for free solutions may be very different. Coupling potentials mix and modify free solutions with different absolute values when they are propagated via forbidden regions. If numerical accuracy is not high enough, the propagation leads to development of numerical instabilities in solution vectors. The novel method suggested in this paper rearranges the coupled equations such that free solutions only enter in combinations with minimal variations of absolute values. As a result, the new system is less prone to develop numerical instabilities.

ACKNOWLEDGMENTS

S.N.E. is thankful to the University of Bergen for hospitality. This work was supported by the Russian Foundation for Basic Research grants RFBR 08-02-00892, RFBR 08-02-00089-a.

REFERENCES

1. R. G. Gordon, *J. Chem. Phys.* **51**, 14 (1969).
2. R. A. White and E. F. Hayes, *J. Chem. Phys.* **57**, 2985 (1972).
3. L. Gr. Ixaru, *Comput. Phys. Commun.* **20**, 97 (1980).
4. T. N. Rescigno and A. E. Orel, *Phys. Rev. A* **25**, 2402 (1982).
5. L. D. Tolsma and G. W. Veltkamp, *Comput. Phys. Commun.* **40**, 233 (1986).
6. B. R. Johnson, *J. Chem. Phys.* **69**, 4678 (1978).
7. J. M. Hutson, *Comput. Phys. Commun.* **84**, 1 (1994).
8. P. G. Burke, A. Hibbert, and W. D. Robb, *J. Phys. B: Atom. Molec. Phys.* **4**, 153 (1971).
9. I. J. Thompson, F. M. Nunes, and B. V. Danilin, *Comput. Phys. Commun.* **161**, 87 (2004).
10. A. Deloff, *Ann. Phys.* **322**, 1373 (2007).
11. Z. A. Anastassi and T. E. Simos, *Phys. Rep.* **284**, 1 (2009).
12. M. Abramowitz and L. A. Stegun, *Handbook of Mathematical Functions*, Nat. Bur. Std., New York, 1964.
13. R. A. Gonzales, S.-Y. Kang, I. Koltracht, and G. Rawitscher, *J. Comp. Phys.* **153**, 160 (1999).
14. M. V. Zhukov, B. V. Danilin, D. V. Fedorov et al., *Phys. Rep.* **231**, 151 (1993).
15. B. V. Danilin, N. B. Shul'gina, S. N. Ershov, and J. S. Vaagen, *Phys. At. Nucl.* **72**, 1324 (2009).
16. S. N. Ershov, L. V. Grigorenko, J. S. Vaagen, and M. V. Zhukov, *J. Phys. G: Nucl. Part. Phys.* **37**, 064026 (2010).
17. B. V. Danilin, I. J. Thompson, M. V. Zhukov, and J. S. Vaagen, *Nucl. Phys. A* **632**, 383 (1998).

Properties of ^{26}Mg and ^{26}Si in the sd shell model and the determination of the ^{25}Al(p,γ)^{26}Si reaction rate[1]

W. A. Richter*, B. Alex Brown†, A. Signoracci† and M. Wiescher**

*Department of Physics, University of the Western Cape, Private Bag X17, Bellville 7535, South Africa
†Department of Physics and Astronomy, and National Superconducting Cyclotron Laboratory, Michigan State University, East Lansing, Michigan 48824-1321, USA
**Department of Physics and Joint Institute for Nuclear Astrophysics, University of Notre Dame, Notre Dame, IN 46556, USA

Abstract. We present results for levels in ^{26}Si (the mirror of nucleus ^{26}Mg). The calculated gamma-decay lifetimes and ^{25}Al to ^{26}Si spectroscopic factors together with experimental information on the levels of excited states are used to determined the ^{25}Al(p,γ)^{26}Si reaction rates together with a theoretical error on this rate based on the use of the USDA and USDB interactions.

Keywords: nuclear shell model, gamma-decay lifetime
PACS: 26.30.-k, 21.60.Cs, 21.10.Sf, 21.10.Tg

INTRODUCTION

The production mechanism and production site for the long-lived radioactive isotope ^{26}Al has been of interest since the first indications of ^{26}Al enrichment in meteoritic inclusions was observed [1]. Understanding its origin would serve as a unique signature for nucleosynthesis in novae and supernovae. The main reaction sequence leading to ^{26}Al is ^{24}Mg(p,γ)^{25}Al($\beta^+ + \nu$)^{25}Mg(p,γ)^{26}Al. At the high-temperature conditions expected for shell carbon burning and explosive neon burning the ^{25}Al(p,γ)^{26}Si reaction becomes faster than the ^{25}Al β decay. Since ^{26}Si β decays to the short-lived 0^+ state of ^{26}Al, the long-lived (5^+) state becomes depleted.

The properties of the states of ^{26}Si required for the calculation of the ^{25}Al(p,γ)^{26}Si reaction rate are the energies, J^π values, proton-decay widths and gamma-decay widths for levels above the proton decay threshold of 5.51 MeV. Experiments have established the energy of some levels [2]. But there is uncertainty in their J^π values and (based on the known levels of ^{26}Mg) many levels have not yet been observed. Theoretical input is needed for the unobserved levels as well as the gamma and proton decay widths for all of the levels.

Several advances are made in this paper. A new method is used to calculate the energies of levels in ^{26}Si based upon the observed energies of levels of the analogue states

[1] This work was supported by NSF grant PHY-0758099 and Joint Institute for Nuclear Astrophysics, NSF-PFC

in ^{26}Al and ^{26}Mg, together with a calculation of the c-coefficient of the isobaric-mass-multiplet equation (IMME). Also the gamma and proton decay widths are calculated with several Hamiltonians to find their values and to estimate their theoretical uncertainties.

This paper follows from recent work on the properties of $(0d_{5/2}, 0d_{3/2}, 1s_{1/2})$ sd-shell nuclei that include new Hamiltonians [3], a comprehensive study of electromagnetic and beta-decay observables [4] and a comprehensive study of the properties of states in ^{26}Mg [5]. For ^{26}Mg assignments between theory and experiment for about 50 levels in ^{26}Mg levels up to 10 MeV in excitation have been made, based on a comparison of the experimental and theoretical electron scattering data cross sections and electromagnetic transition strengths [5]. Because of the uncertainty in levels of ^{26}Si, conventionally levels are assigned on the basis of known levels in the mirror nucleus ^{26}Mg. In the next section we base these assignments on a new and improved method.

PROCEDURE FOR DETERMINING ^{26}SI ENERGY LEVELS.

In the present work we make use of a novel method of calculating energy levels in ^{26}Si by using the measured binding energies of the T=1 partners and a theoretical value of the c coefficient of the IMME [6]. Specifically

$$B_{th}(^{26}\mathrm{Si}) = 2B(^{26}\mathrm{Al}) - B(^{26}\mathrm{Mg}) + 2c_{th}. \quad (1)$$

In Fig. 1 values of c from experiment and theory are compared for states in ^{26}Si ordered according to increasing experimental energy. The calculated values of c are obtained from

$$c_{th} = [B_{th}(^{26}\mathrm{Si}) - 2B_{th}(^{26}\mathrm{Al}) + B_{th}(^{26}\mathrm{Mg})]/2. \quad (2)$$

The experimental values are obtained for states where all three members of the multiplet are known. In general a good correspondence can be seen, the largest deviations being less than 30 keV. There is considerable state dependence with c values ranging from 300 keV (for the 0^+ ground state) down to 180 keV. Thus where data is not available in ^{26}Si to determine the c coefficient from experiment, a fairly reliable value can be obtained from the theoretical calculation, and the binding energies for states in ^{26}Si can be then be obtained from Eq. 1, with experimental values of binding energy for corresponding states in ^{26}Al and ^{26}Mg (when they are known in both).

Testing calculated excitation energies against known values in ^{26}Si indicates that corresponding levels can be obtained very accurately. This is shown in Fig. 2. The calculated values can then be used as a guide to the correct spin/parity assignments for measured levels in ^{26}Si. Where no levels in ^{26}Si are known, levels can be predicted. Two such levels are indicated by crosses in Fig. 2.

The three levels that are just above the proton-decay separation energy of 5.51 MeV and of potential importance for the capture reaction at low temperatures are indicated by the arrows in Fig. 2. The J^π of levels 16 and 17 are from the recent analysis of Wrede [7] where arguments for the J^π are based on all available data for these states.

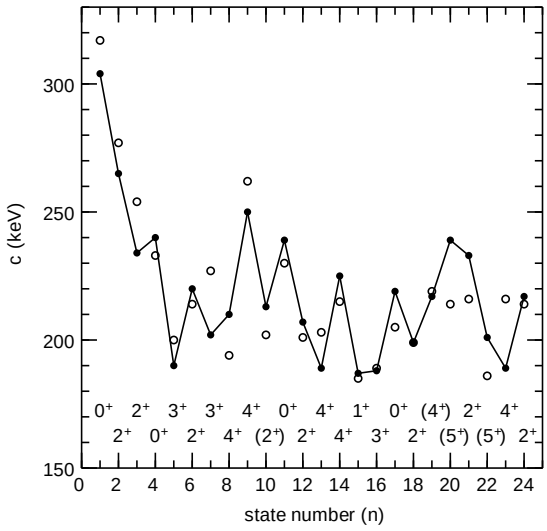

FIGURE 1. c coefficients from the isobaric mass multiplet equation (IMME: $E = a + bT_z + cT_z^2$) versus state number (in order of increasing energy) in ^{26}Si based on experimental energies (closed circles) and energies calculated from USDB (crosses).

RESULTS FOR THE REACTION RATE

The resonant reaction rate for capture on a nucleus in an initial state i, $N_A < \sigma v >_{\mathrm{res}\,i}$ for isolated narrow resonances is calculated as a sum over all relevant compound nucleus states f above the proton threshold [8]

$$N_A < \sigma v >_{\mathrm{res}\,i} = 1.540 \times 10^{11} (\mu T_9)^{-3/2} \times \sum_f \omega\gamma_{if}\ \mathrm{e}^{-\mathrm{E_{res}}/(kT)}\ \mathrm{cm^3\,s^{-1}mole^{-1}}. \quad (3)$$

Here T_9 is the temperature in GigaK, $\mathrm{E}_{res} = \mathrm{E}_f - \mathrm{E}_i$ is the resonance energy in the center of mass system, the resonance strengths in MeV for proton capture are

$$\omega\gamma_{if} = \frac{(2J_f+1)}{(2J_p+1)(2J_i+1)} \frac{\Gamma_{\mathrm{p}\,if}\Gamma_{\gamma f}}{\Gamma_{\mathrm{total}\,f}}. \quad (4)$$

$\Gamma_{\mathrm{total}\,f} = \Gamma_{\mathrm{p}\,if} + \Gamma_{\gamma f}$ is a total width of the resonance level and J_i, J_p and J_f are target (^{25}Al), the proton projectile ($J_p = 1/2$), and states in final nuclues (^{26}Si), respectively. The proton decay width depends exponentially on the resonance energy and can be calculated from the proton spectroscopic factor C^2S_{if} and the single-particle proton width $\Gamma_{\mathrm{sp}\,if}$ as $\Gamma_{\mathrm{p}\,if} = C^2S_{if}\Gamma_{\mathrm{sp}\,if}$. The single-particle proton widths were calculated from $\Gamma_{\mathrm{sp}} = 2\gamma^2 P(\ell, R_c)$ [9], with $\gamma^2 = \frac{\hbar^2 c^2}{2\mu R_c^2}$ and where the channel radius R_c was chosen to match the width obtained from an exact evaluation of the proton scattering cross section from a Woods-Saxon potential well and $Q = 0.1 - 0.5$ MeV. This simple model matches exact calculations in the sd-shell to within about 10%, and has the advantage that it

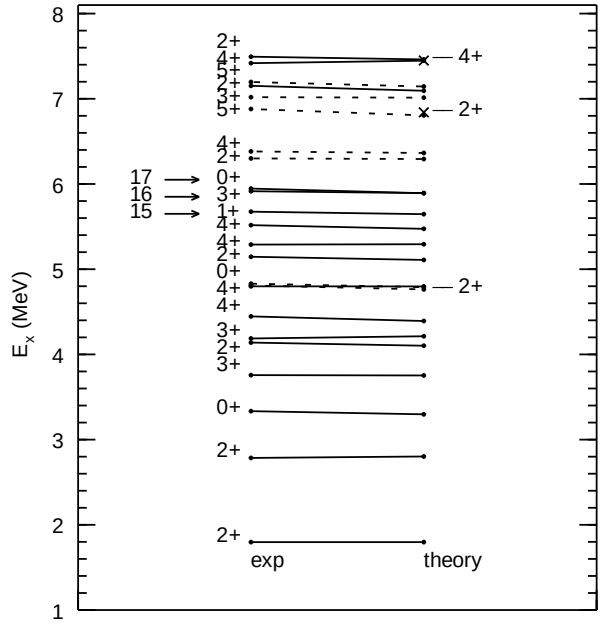

FIGURE 2. Adopted experimental excitation energies in ^{26}Si [2] versus predicted energies E_{th} based on experimental binding energies of ^{26}Mg and ^{26}Al and the theoretical c coefficient (USDB) (Eq. 1). The crosses correspond to predicted energies without experimental counterparts.

is fast and can be easily extrapolated to energies below 0.1 MeV where the scattering calculation becomes computationally difficult. We use a Coulomb penetration code from Barker [10].

The total rp reaction rates have been calculated for each of the interactions USD, USDA and USDB. The Q values required were based on measured energies in ^{26}Si, and where they were not known values calculated from Eq. 1 were used. In the cases with energies near 8 MeV and above where the energy of the T=1 state in ^{26}Al was not known, the energy of the state in ^{26}Si is based on the shift obtained from the average of five states in ^{26}Mg near 8 MeV. Above 8 MeV we use the energies obtained with USDB that includes the addition of about 170 states with $J^\pi \leq 5^+$ up to 14 MeV in excitation energy. The 0^+ state at 6.461 MeV [2] is much lower than the predicted energy of the fifth 0^+ state with USDB (at 8.040 MeV). Theory predicts a 1^+ state (at 6.620 MeV) which has no experimental counterpart. We have used the theoretical results of the 1^+ state for Γ_p and Γ_γ, instead of the 0^+ state.

Fig. 3 shows the results for the capture rate obtained using the properties of ^{26}Si. The Γ_p and Γ_γ in this case are all based on the USDB Hamiltonian. The contribution between log(T9)= -0.7 and 0.5 is dominated by the properties of the 3^+ state at 5.915 MeV (number 16). Since $\Gamma_\gamma < \Gamma_p$ the rate is determined by Γ_γ.

Above log(T9) of about 0.8 there will be contributions from negative parity states that should be taken from Hauser-Feshbach statistical model estimates for negative parity states [11].

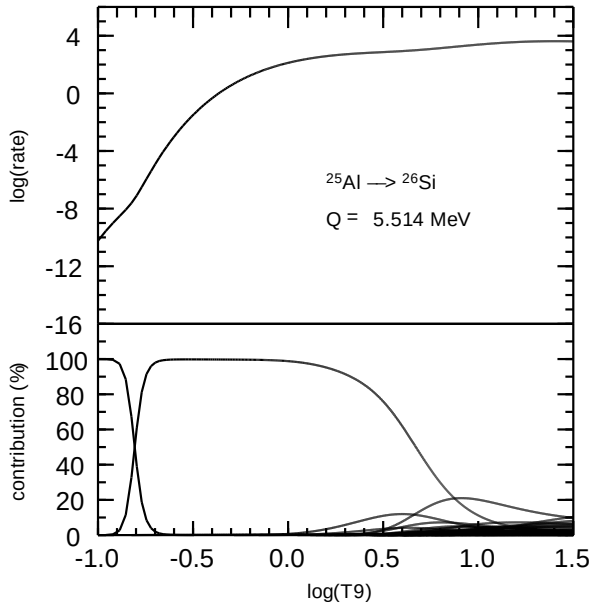

FIGURE 3. The total rp reaction rate versus temperature T9 (GigaK) (top panel) and the contribution of each of the final states (lower panel) with USDB. In the lower panel the dominant contribution below log(T9) = -0.8 is from state number 15, the 1^+ state at 5.675 MeV. Between log(T9) = -0.7 and 0.5 the dominant contribution is from state number 16, the 3^+ state at 5.915 MeV. Γ_γ calculated for ^{26}Si levels.

CONCLUSIONS

Because the calculation of the rp reaction rate for the ^{25}Al(p,γ)^{26}Si requires a knowledge of the energy levels in ^{26}Si, and many levels are uncertain, we have adopted a novel method of determining levels which is partly based on experiment and partly on theory. For the experimental part we used well-known binding energies of the T=1 analogue states of ^{26}Si. For the theoretical part we used calculated c coefficients of the isobaric mass multiplet equation. We have demonstrated that a good correspondence between theoretical and experimental values of the c coefficient for sd-shell nuclei exists. The method leads to a reliable prediction of energy levels in ^{26}Si. Using energy values in ^{26}Si constrained by our method for the Q values of the proton capture process on ^{25}Al, we obtained the required spectroscopic factors and gamma decay lifetimes for rate calculations from shell-model calculations using the new sd-shell interactions USDA and USDB. For comparison we also used the older USD interaction.

Reaction rates as well as contributions from individual states in ^{26}Si were then obtained for the different interactions. The variation in the rates give some indication of the theoretical error due to the use of different interactions and approximations for the gamma widths, and amounts to overall error band of $\pm$ 40%. It can also be concluded that using theoretical gamma widths from the mirror nucleus ^{26}Mg instead of ^{26}Si is an adequate approximation. The effect of negative parity states should also still be considered.

Acknowledgments This work is partly supported by NSF Grant PHY-0758099 and the National Research Foundation of South Africa.

REFERENCES

1. T. Lee, D. A. Papanantassiou and G. J. Wasserburg, Astrophys. J. Lett. **211**, L107 (1977); **220**, L21 (1978).
2. A. Matic et al., Phys. Rev. C **82**, 025807 (2010).
3. B. A. Brown and W. A. Richter, Phys. Rev. C **74**, 034315 (2006).
4. W. A. Richter, S. Mkhize and B. A. Brown, Phys. Rev. C **78**, 064302-1 (2008).
5. W. A. Richter and B. A. Brown, Phys. Rev. C **80**, 034301 (2009).
6. W. E. Ormand and B. A. Brown, Nucl. Phys. A **491**, 1 (1989).
7. C. Wrede, Phys. Rev. C **79**, 035803 (2009).
8. W. A. Fowler and F. Hoyle, Ap. J. Suppl. **9**, 201 (1964).
9. A. M. Lane and R. G. Thomas, Rev. Mod. Phys. **30**, 257 (1958).
10. F. C. Barker, Phys. Rev. C **63**, 047303 (2001); and private communication.
11. R. Crowter, **Masters Thesis** (University of Surrey, Guildford Surrey, United Kingdom, 2007), unpublished.

Self-consistent models of nuclear clustering

S. M. Wyngaardt*, T. T. Ibrahim*,**, J. Ndayishimye* and S. M. Perez‡,†

*Department of Physics, University of Stellenbosch, P.O. Box 1529, Stellenbosch 7599, South Africa
†iThemba LABS, P.O. Box 722, Somerset West 7129, South Africa
**Department of Physics, University of Ilorin, PMB 1515 Ilorin, Nigeria
‡Department of Physics, University of Cape Town, Private Bag, Rondebosch 7700, South Africa

Abstract. In recent years a phenomenological core-cluster has been constructed with a Saxon-Woods plus cubic Saxon-Woods term successfully predicts a reasonable number of observable phenomenon which is related to alpha clustering. This model, however successful, lacks a microscopic description of clustering phenomenon in nuclear systems. A fully microscopic formalism is presented, where the core and cluster baryon densities are derived from a relativistic mean field approach. The Lorentz covariant IA1 representation of the nucleon-nucleon interaction is folded with the derived core and cluster densities. Theoretical predictions of the ground-state decay half-life and positive parity energy band of ^{212}Po are obtained with the relativistic mean field formalism and compared to predictions made with the phenomenological Saxon-Woods plus cubic Saxon-Wood core-cluster potential.

Keywords: nucleon-nucleon interaction, nuclear clustering
PACS: 21.45.-v, 21.60.Gx, 24.10.Jv, 27.80.+w, 23.60.+e

INTRODUCTION

Clustering phenomenon is one of the essential features of nuclear matter which has been studied in great detail [1] in nuclear physics. In the physics of unstable nuclei, clustering is one of the central areas of study. The cluster-core interaction lies central to the identification of clustering in the nuclear matter and the description of clustering phenomenon in various nuclei. During the last decade the modified phenomenological Saxon-Woods plus Cubic Saxon-Woods cluster potential has successfully described various phenomenon related to alpha clustering in light as well as even-even heavy nuclei. In order to fully describe clustering in nuclear systems one would have to develop a microscopic model of the phenomenon at the nucleon-nucleon scale.

At a more microscopic level the core-cluster interaction may be constructed from a nucleon-nucleon interaction. Prior to the development of the Saxon-Wood plus Saxon-Wood cubed potential form, such a microscopic interaction had been employed in various forms to describe α cluster bound states in light nuclei [2] and the exotic decays in heavy nuclei [3]. In recent years the microscopic M3Y-type potential model has been extended to describe the alpha decay half-lives and the structure of heavy nuclei [4], [5], and [6]. An application of the interaction to ^{94}Mo and ^{212}Po in particular suggests a good amount of α clustering in these nuclei [7].

Relativistic mean field theory (RMFT) [8] has proven to be very successful in describing various properties of nuclear structure [9]. In this work a RMFT description of clustering is presented and a comparison is made between the experimental ground-state

decay half-lives and band energy spectral of ^{212}Po and cluster model predictions of these quantities which were obtained from the Saxon-Woods + cubic Saxon-Woods potential, double folded M3Y nucleon-nucleon interaction [10] and the microscopic RMFT based core-cluster interaction.

THE BINARY CLUSTER MODEL

This model is based on the preformed binary cluster model for which the decay half life is given by

$$T_{1/2} = \hbar \frac{\ln 2}{\Gamma}, \tag{1}$$

where Γ represents the cluster decay width. For the breakup of a nucleus into the core and cluster the decay width is defined by the relationship

$$\Gamma = P \frac{\hbar^2}{2\mu} \frac{exp(-2\int_{r_2}^{r_3} k(r)dr)}{\int_{r_1}^{r_2} [k^{-1}(r)]dr} \tag{2}$$

with P being the core-cluster preformation probability in the parent nucleus, μ is reduced mass of the core-cluster system and $k(r)$ is cluster wavenumber. The wavenumber depends on both the decay energy (E) and the core-cluster potential $V(r)$, and is given by

$$k(r) = \sqrt{\frac{2\mu}{\hbar^2}|E - V(r)|}. \tag{3}$$

The energy band structure of the quasi-boundstates can be obtained from a combination of the Bohr-Sommerfeld (BS) quantization integral

$$\int_{r_1}^{r2} \sqrt{\frac{2\mu}{\hbar^2}\left[E_l - V(r)\right] dr} = (2n+1)\frac{\pi}{2} \tag{4}$$

and the Wildermuth condition $G = 2n + l$, where n is the number of nodes of the radial wavefunction and l is the orbital angular momentum of the cluster state. G defines the global quantum number of the core-cluster relative motion. The interaction between the core and cluster, $V(r)$, is described by the sum of the attractive nuclear cluster-core potential $U(r)$, the Coulomb potential between the two charged centres, and the centrifugal potential.

CORE CLUSTER POTENTIALS

Phenomenological core-cluster interaction

The recently developed modified Saxon-Wood with an additional cubic Saxon-Woods core-cluster phenomenological potential

$$U(r) = U_0 \left[\frac{x}{1 + exp\left(\frac{r-R}{a}\right)} + \frac{1-x}{1 + exp\left(\frac{r-R}{3a}\right)^3} \right] \tag{5}$$

is found to consistently reproduce not only the alpha and exotic decay half-lives, but also correctly predict the level properties of nuclei in the rare earth and the actinide region. This potential is parameterized in terms of the potential depth (U_0), nuclear radius (R), diffuseness (a), and x is a mixing parameter. Despite its success this potential model tells us very little about the microscopic nature of clustering in closed shell nuclei.

Relativistic mean field construction of the cluster-core potential

In the IA1 representation of the nucleon-nucleon scattering amplitude [12]

$$F = F^S I^a I_b + F^V \gamma_a^\mu \gamma_{\mu b} + F^{PS} \gamma_a^5 \gamma_{5b} + F^T \sigma_a^{\mu\nu} \sigma_{\mu\nu b} + F^A \gamma_a^5 \gamma_a^\mu \gamma_b^5 \gamma_{\mu b}, \tag{6}$$

Lorentz covariance, parity conservation, isospin invariance, and the constraint that the free nucleons are on the mass shell imply that the invariant NN scattering operator F be written in terms of the five complex functions for pp and five for pn scattering. The quantities $\lambda_i^L = (I, \gamma^\mu, \gamma^5, \sigma^{\mu\nu}, \gamma^5\gamma^\mu)$ represent the five Dirac gamma matrices [13], and the index $(i = a, b)$ labels the two interacting nucleons. The index L labels the scalar, vector, pseudo-scalar, tensor and axial terms.

Out of the Lorentz covariant McNeil, Ray and Wallace (MRW) construction of the optical potential for nucleon-nucleus scattering [11], arises the double folded MRW form which describes the cluster-core potential

$$U^L(r, \varepsilon) = -\frac{4\pi i p}{Mc^2} \int \frac{d^3q}{(2\pi)^3} e^{i\mathbf{q}\cdot\mathbf{r}} F^L(q, \varepsilon) \int d^3r' e^{-i\mathbf{q}\cdot\,\mathbf{r}'} \rho_1^L(r') \int d^3r'' e^{-i\mathbf{q}\cdot\,\mathbf{r}''} \rho_2^L(r''), \tag{7}$$

where r represents the separation distance between the cluster (1)and core (2)center, and ε is the laboratory energy of the nucleons in the cluster. The momentum of the nucleons in the nucleon-nucleon (NN)center of mass system is given by p while M represents the nucleon mass. Equation (7) contains the Lorentz covariant nucleon-nucleon scattering amplitudes $F^L(q, \varepsilon)$, which are functions of the NN centre of mass momentum transfer $(\vec{q})$ and nucleon laboratory energy (ε), as well as the respective cluster and core densities ρ_1^L and ρ_2^L.

The Walecka model is based on a relativistic mean field theory with an effective Lagrangian which describes the NN interaction via the electromagnetic interaction and the effective meson fields [8]. The dynamical equation which results from the Lagrangian is given by

$$\hat{H}\psi(\mathbf{r}) = \left(i\alpha \cdot \nabla - g_v \gamma^0 V^0(r) + \beta[M - g_s \phi(r)]\right)\psi(\mathbf{r}) = E\psi(\mathbf{r}) \tag{8}$$

with the Dirac Hamiltonian operator ($\hat{H} = i\alpha \cdot \nabla - g_v \gamma^0 V^0(r) + \beta[M - g_s \phi(r)]$), vector and scalar fields g_v and g_s respectively, as well as the zeroth component vector field (V_0)

and scalar field (ϕ). Equation (8) has both positive and negative solutions $U(\mathbf{r})$ and $V(\mathbf{r})$, and thus the field operator can be expanded as

$$\hat{\psi}(\mathbf{r}) = \sum_{\Lambda} \left[A_{\Lambda} U_{\Lambda}(\mathbf{r}) + B^{\dagger}_{\Lambda} V_{\Lambda}(\mathbf{r}) \right]. \tag{9}$$

The baryon and antibaryon creation operators $A^{\dagger}_{\Lambda}$ and $B^{\dagger}_{\Lambda}$ satify the standard anti-commutator relationships and the index Λ specifies the full set of single-particle quantum numbers, which for a spherically symmetric and parity conserving system, are the usual angular momentum and parity quantum numbers, as given by reference [13]. The positive-energy spinor can be written as

$$U_{\Lambda} \equiv U_{njlmt}(\mathbf{r}) = \begin{pmatrix} i\left[G_{njlt}(r)/r\right]\Phi_{jlm} \\ \left[F_{njlt}(r)/r\right]\Phi_{jl+1m} \end{pmatrix} \varsigma_t, \tag{10}$$

where Φ_{jlm} is the angular momentum and spin dependent part of the solution and n and ς_t represents the principal quantum number and two component isospinor which is labeled by the isospin projection t. The functions $G(r)$ and $F(r)$ represent the radial wave functions for the upper and lower components of the positive energy spinor U_{Λ}
Neglecting the negative-energy spinors the local baryon (ρ_B) and scalar (ρ_s) densities can be derived from the positive-energy solutions

$$\left.\begin{matrix} \rho_B(\mathbf{r}) \\ \rho_s(\mathbf{r}) \end{matrix}\right\} = \sum_{\Lambda} \bar{U}_{\Lambda}(\mathbf{r}) \begin{pmatrix} \gamma^0 \\ I \end{pmatrix} U_{\Lambda}(\mathbf{r}). \tag{11}$$

MODEL PREDICTIONS AND CONCLUSIONS

For the BMP phenomenological form of the cluster-core potential prediction of the positive parity alpha band energy structure of ^{212}Po the parameters U_0 = 208 MeV, a = 0.66 fm, x = 0.30 and $R = 6.784$ were used with G = 18 [15].
The Walecka based RMFT prediction uses the experimental masses $M = 939$ MeV, $m_v = m_{\omega} = 738$ MeV, $m_{\rho} = 770$ MeV, $m_s = 520$ MeV, and $\alpha = e^2/4\pi = 1/137.36$ are used. The coupling constants for the scalar, vector, and ρ-meson are $g_s^2 = 109.6$, $g_v^2 = 190.4$, and $g_{\rho}^2 = 65.23$ respectively. We apply the Dirac-Hartree code Timora [14] to calulate the scalar and vector densities for both the protons and neutrons. The densities of the core and cluster systems are inturn used to calculate the core-cluster potential by means of the double folded MRW method.
The results of the calculated α-decay half-life of the ground-state as predicted by the phenomenological BMP, the microscopic M3Y with phenomenological core and cluster baryon densities [15], and MRW double folded relativistic mean field nucleon densities with Lorentz covariant NN scattering amplitudes are compared with experimental data [16] in Table I. Table II compares the predicted band energy structure from the BMP, M3Y and RMFT model calculations with available experimental data [16].
From the results in Table (1) and (2) one see that the Saxon-Woods plus cubic Saxon-Woods potential and the RMFT based model gives a reasonable prediction of the half-life of the 0^+, while the microscopic M3Y based model underpredict the ground-state

alpha decay half-life of ^{212}Po by a factor of approximately 2. Furturemore the energy spectra of the excited α states are predicted reasonably well both the Saxon-Woods plus cubic Saxon Woods core-cluster potential and the self-consistent RMFT core-cluster model where as the microscopic M3Y model potential results in a clear inversion of the energy spectra.

TABLE 1. The experimental ground state decay of ^{212}Po and the corresponding values obtained with the BMP (5), double folded M3Y, and the self-consistent RMFT potentials.

$T_{1/2}$(Exp) ns	$T_{1/2}$(BMP) (ns)	$T_{1/2}$(M3Y) (ns)	$T_{1/2}$(RMFT) (ns)
300	348.0	157.4	299.6

TABLE 2. The experimental energy level scheme of ^{212}Po and the calculated spectra obtained with the BMP (5), double folded M3Y and self-consistent RMFT potentials.

J^{π}	E_{exp} (MeV)	E_{BMP} MeV	E_{M3Y}	E_{RMFT} (MeV)
0^+	0.000	(0.495)	−0.004	0.203
2^+	0.727	0.659	−0.067	0.421
4^+	1.132	0.948	−0.229	0.699
6^+	1.355	1.318	−0.508	0.857
8^+	1.476	1.730	−0.930	1.085
10^+	1.834	2.145	−1.538	1.319
12^+	2.702	2.519	−2.358	1.553
14^+	2.885	2.805	−3.437	1.787
16^+	–	2.941	−4.800	2.021
18^+	2.921	2.841	−6.477	2.255

ACKNOWLEDGMENTS

The authors would like to acknowledge the National Research Foundation and the University of Stellenbosch for financially supporting this project.

REFERENCES

1. M.Freer and A.C.Merchant, J.Phys.G **23**, 261 (1997).
2. B. Buck, C. B. Dover and J. P. Vary, Phys. Rev. C **11**, 1803 (1975).
3. B. Buck, A. C. Merchant, Phys. Rev. C **39**, 2097 (1989).
4. F. Hoyler, P. Mohr and G. Staudt, Phys. Rev. C **50**, 2631 (1994).
5. C. Xu and Z. Ren, Nucl. Phys. A **753**, 174 (2005); Nucl. Phys. A **760**, 303 (2005).
6. D. N. Basu, J. Phys. G: Nucl. Part. Phys. **29**, 2079 (2003):Phys. Lett. B **566**, 90 (2003).
7. S. Ohkubo, Phys. Rev. Lett. **74**, 2176 (1995).
8. J. D. Walecka, Ann. Phys. (N.Y) **83**, 491 (1974).
9. P. Ring, A. V. Afanasjev and J. Meng, Lecture notes in Physic, vol. **482**, (Springer Berlin Heidelberg, 2007).
10. G. R. Satchler and W. G. Love, Phys. Rep **55**, 183 (1979).
11. J. A. McNeil, L. Ray and S. J. Wallace, Phys. Rev. C **27**, 2123 (1983).

12. J. A. McNeil, J. Shepard, and S. J. Wallace, Phys. Rev. Lett. **50**, 1439 (1983); J. Shepard, J. A. McNeil, and S. J. Wallace *ibid* **50**, 1443 (1983).
13. J. D. Bjorken and S. D. Drell, *Relativistic Quantum Mechanics*, 2nd edition (McGraw-Hill,New York, 1964).
14. K. Langanke, J. A. Maruhn, S. E. Koonin, *Computational Nuclear Physics*, vol. **1**, Springer Berlin Heidelberg)
15. T. T. Ibrahim, PhD Thesis, unpublished (2007).
16. A. B. Garnsworthy et al, J. Phys. G: Nucl. Part. Phys. **31**, 1851 (2005).

Nuclear structure and neutrinoless double beta decay

Fedor Šimkovic

Laboratory of Theoretical Physics, JINR Dubna, 141980 Dubna, Moscow region, Russia
Department of Nuclear Physics and Biophysics, Comenius University, Mlynska dolina, SK-84248 Bratislava, Slovakia

Abstract. The status of calculation of the neutrinoless double beta decay ($0\nu\beta\beta$-decay) nuclear matrix elements (NMEs) is reviewed. The spread of published values of NMEs is discussed. The main attention is paid to the recent progress achieved in the evaluation of the $0\nu\beta\beta$-decay NMEs in the framework of the quasiparticle random phase approximation (QRPA). The obtained results are compared with those of other nuclear structure approaches. The problem of reliable determination of the $0\nu\beta\beta$-decay NMEs is addressed. It is manifested that the uncertainty associated with the calculation of the $0\nu\beta\beta$-decay NMEs can be diminished by suitable chosen nuclear probes.

Keywords: double beta decay, nuclear matrix element, QRPA
PACS: 23.10.-s; 21.60.-n; 23.40.Bw; 23.40.Hc

INTRODUCTION

The fundamental importance of the search for $0\nu\beta\beta$-decay,

$$(A,Z) \rightarrow (A,Z+2)+2e^{-}, \tag{1}$$

is widely accepted. After 70 years the brilliant hypothesis of Ettore Majorana is still valid and is strongly supported by the discovery of neutrino oscillations and by the construction of the Grand Unified Theories. The $0\nu\beta\beta$-decay is currently the most powerful tool to clarify if the neutrino is a Dirac or a Majorana particle. This issue is intimately related with the origin of neutrino masses having a strong impact also on astrophysics and cosmology.

The main aim of the experiments on the search for $0\nu\beta\beta$-decay is the measurement of the effective Majorana neutrino mass $m_{\beta\beta}$. Under the assumption of the mixing of three massive Majorana neutrinos the effective Majorana neutrino mass $m_{\beta\beta}$ takes the form

$$m_{\beta\beta} = U_{e1}^2\, m_1 + U_{e2}^2\, m_2 + U_{e3}^2\, m_3. \tag{2}$$

Here, U_{ei} and m_i $(i = 1,2,3)$ are elements of Pontecorvo-Maki-Nakagawa-Sakata (PMNS) neutrino mixing matrix and masses of neutrinos, respectively.

Experimental searches for the $0\nu\beta\beta$-decay, of ever increasing sensitivity, are being pursued worldwide. However, interpreting existing results as a measurement of the Majorana neutrino effective mass and planning new experiments, depends crucially on the knowledge of the corresponding nuclear matrix elements that govern the decay rate. Accurate determination of the nuclear matrix elements, and a realistic estimate of their uncertainty, is of great importance.

CURRENT STATUS OF THE $0\nu\beta\beta$-DECAY NMES

The inverse value of the $0\nu\beta\beta$-decay half-life for a given isotope (A,Z) is a product of the effective mass of Majorana neutrinos $m_{\beta\beta}$, the known phase-space factor $G_{0\nu}(Q_{\beta\beta},Z)$ (depending on nuclear charge Z and the energy release $Q_{\beta\beta}$ of the reaction) and the nuclear matrix element $M^{0\nu}$, which depends on the nuclear structure of the particular isotope under study [1]:

$$(T^{0\nu}_{1/2})^{-1} \;=\; G_{0\nu}(Q_{\beta\beta},Z)\;|M^{0\nu}|^2\;|m_{\beta\beta}|^2. \tag{3}$$

From the measurement of half-life of the $0\nu\beta\beta$-decay only the product $|m_{\beta\beta}|\;\;|M^{0\nu}(A,Z)|$ of effective neutrino mass and nuclear matrix element can be determined. Clearly, the accuracy of the determination of $|m_{\beta\beta}|$ from the measured $0\nu\beta\beta$-decay half-life is mainly given by our knowledge of nuclear matrix elements. Without accurate calculation of the $0\nu\beta\beta$-decay NMEs, it is not possible to reach qualitative conclusions about neutrino masses, the type of neutrino mass spectrum and CP violation.

The nuclear matrix elements for $0\nu\beta\beta$-decay must be evaluated using tools of nuclear structure theory. Unfortunately, there are no observables that could be directly linked to the magnitude of $0\nu\beta\beta$-decay nuclear matrix elements and that could be used to determine them in an essentially model independent way. The calculation of the $0\nu\beta\beta$-decay matrix elements is a difficult problem because ground and many excited states of open-shell nuclei with complicated nuclear structure have to be considered.

The main two basic approaches used for evaluation of double beta decay NMEs are the Quasiparticle Random Phase Approximation (QRPA) [2, 3] and the Large Scale Shell Model (LSSM) [5]. Both methods have the same starting point, namely a Slater determinant of independent particles. However, there are substantial differences between both approaches, namely the kind of correlations they include are complementary. The QRPA treats a large single particle model space, but truncates heavily the included configurations [2]. The LSSM, by a contrast, treats a small fraction of this model space, but allows the nucleons to correlate in arbitrary ways [4].

Due to its simplicity the QRPA is a popular technique to calculate the $0\nu\beta\beta$-decay NMEss. One of the most important factors of the QRPA calculation of the $0\nu\beta\beta$-decay NMEs is the way how the particle-particle strength of the nuclear Hamiltonian g_{pp} is fixed. It has been shown that by adjusting g_{pp} to the $2\nu\beta\beta$-decay rates the uncertainty associated with variations in QRPA calculations of the $0\nu\beta\beta$-decay NMEs can be significantly eliminated [2]. In particular, the results obtained in this way are essentially independent of the size of the basis, the form of different realistic nucleon-nucleon potentials, or on whether QRPA or renormalized QRPA (take into account Pauli exclusion principle) is used.

Matrix elements for the double beta decay are calculated also by angular momentum projected (with real quasi-particle transformation) Hartree-Fock-Bogoliubov (P-HFB) wave functions [6] and by the Interacting Boson Model (IBM) [7]. The P-HFB allows only, that neutron pairs with angular momenta 0^+, 2^+, 4^+, $\cdots$ are transformed into two protons in the $0\nu\beta\beta$-decay. In addition the pairs different from 0^+ are strongly suppressed compared to the results of the LSSM and the QRPA. The approaches LSSM and

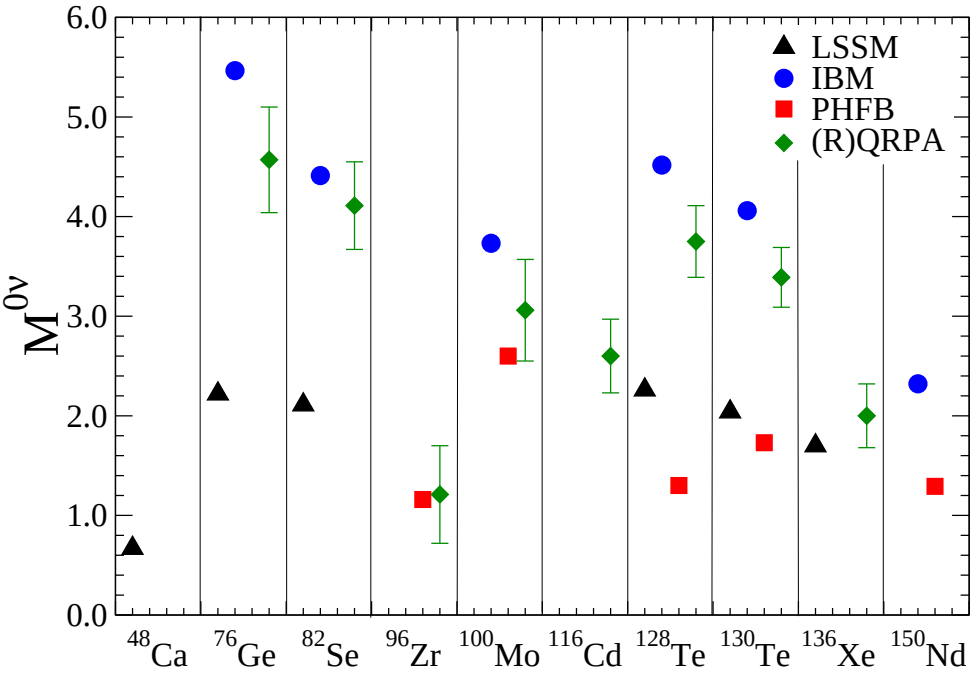

FIGURE 1. The $0\nu\beta\beta$-decay NMEs calculated within different nuclear structure approaches: Large Scale Shell Model (LSSM) [5], (Renormalized) Quasiparticle Random Phase Approximation (R)QRPA [3], Projected Hartree-Fock Bogoliubov approach (P-HFB) [6] and Interacting Boson Model (IBM) [7]. The Miller-Spencer Jastrow two-nucleon short-range correlations are taken into account.

QRPA show also, that other neutron pairs contribute strongly, which can not be included into real P-HFB. One would need to extend the P-HFB approach to complex quasiparticle transformations and probably also to several orthogonal P-HFB configurations. IBM is even more restrictive: It allows only that 0^+ and 2^+ neutron pairs are changed into proton pairs.

The calculated $0\nu\beta\beta$-decay NMEs within these approaches are presented in Fig. 1. It is surpricing that the IBM results agree well with the QRPA ones. Results of these aproaches exhibit some dependence on A unlike the LSSM values, which are practically the same except for ^{48}Ca. The value of the $0\nu\beta\beta$-decay NME for this isotope is suppressed as ^{48}Ca is a magic nucleus.

REDUCING THE UNCERTAINTY IN NMES

The improvement of the calculation of double beta decay nuclear matrix elements is a very important and challenging problem. The uncertainty associated with the calculation of the $0\nu\beta\beta$-decay NMEs can be diminished by suitable chosen nuclear probes. A complementary experimental information from related processes like charge-exchange reactions, muon capture and charged current (anti)neutrino-nucleus reactions is highly required. A direct confrontation of nuclear structure models with data from these processes might improve quality of nuclear structure models. The constrained parameter

space of nuclear models is a promising way to reduce uncertainty in the calculated $0\nu\beta\beta$-decay NMEs.

As a practice, knowledge of the $2\nu\beta\beta$-decay rate and of the ordinary decay ft values were used to constrain the nuclear model parameters, in particular when the quasiparticle random phase approximation (QRPA) was employed [3]. Clearly, when other relevant data become available, and the nuclear model is constrained to reproduce them, confidence in the deduced $0\nu\beta\beta$-decay NMEs is increased. Recently, a set of such data, the occupation numbers of neutron valence orbits in the initial ^{76}Ge and final ^{76}Se nuclei, were determined in a series of measurements of cross sections for neutron and proton adding and removing transfer reactions [8].

The occupancies of valence neutron and proton orbits determined experimentally in Refs. [8], represent important constraints for nuclear models used in the evaluation of the $0\nu\beta\beta$-decay NMEs. In Ref. [9] the input mean field has been modified in such a way that the valence orbits in the model obey these constraints. Within QRPA and its generalizations it was found that it is important to also choose the variant of the basic method that makes such comparison meaningful by conserving the average particle number in the correlated ground state. When following this procedure, but otherwise keeping the same steps as in evaluation of $M^{0\nu}$ within QRPA before, the conclusion was that for the $^{76}Ge \rightarrow ^{76} Se$ transition the matrix element is smaller by 25%, reducing the previously bothersome difference with the shell model prediction noticeably. Clearly, having the experimental orbit occupancies available and adjusting the input to fulfill the corresponding constraint makes a difference. It would be very useful to have similar constraints available also in other systems, in particular for ^{130}Te and/or ^{136}Xe.

Charge-exchange reactions of (p,n) and (n,p) type at intermediate energies and at forward angles, i.e., low momentum transfers ($q_{tr} \sim 0$ and $\Delta L = 0$), selectively excite Gamow-Teller (GT) transitions owing to the dominance of the $V_{\sigma\tau}$ component of the effective interaction. However, experiments which employ the elementary (p,n) and (n,p) reactions have rather limited resolution and alternatives to them have now successfully been established through the (n,p)-type $(d,^2He)$ or $(t,^3He)$ reactions and the (p,n)-type $(^3He,t)$ reaction. Resolutions on the order of 100 keV in the case of $(d,^2He)$, 190 keV for $(t,^3He)$ and 30 keV for $(^3He,t)$ have routinely been achieved [10].

The connection between the two-neutrino double beta decay ($2\nu\beta\beta$-decay) half-life and the GT transition strength B(GT) is as follows:

$$\left(T^{2\nu}_{1/2}\right)^{-1} = G^{2\nu}(Q,Z)\left|M^{2\nu}_{DGT}\right|^2, \tag{4}$$

where $G^{2\nu}(Q,Z)$ is a phase-space factor depending on the Q-value of the reaction and the Z-value of the decaying nucleus. It contains squared the weak interaction coupling constant g_A. The $2\nu\beta\beta$-decay matrix element can be deduced by combining GT^+ and GT^- distributions in the following way:

$$\begin{aligned} M^{2\nu}_{DGT} &= \sum_m \frac{M^{GT^+}_m \cdot M^{GT^-}_m}{Q_{\beta\beta}/2 + m_e + E_x(1^+_m) - E_0}, \\ B(GT^\pm) &= \frac{1}{2J_i+1}\left|M^{GT^\pm}\right|^2. \end{aligned} \tag{5}$$

Here, $(E_x(1^+_m) - E_0)$ is the energy difference between the m^{th} intermediate 1^+ state and the initial ground state. $Q_{\beta\beta}$ is the Q-value of the $\beta\beta$-decay, and the $\sum_m$ runs over all states of the intermediate nucleus. In this approach the effect of a destructive interference among contributions of different states of intermediate nucleus to $M^{2\nu}_{DGT}$ is neglected.

The results of the charge-exchange reaction experiments therefore furnish important information about the nuclear physics relevant for double β-decay [10]. This information directly feed into model calculations, which are aimed at describing reliably the nuclear physics around both decay variants, the $2\nu\beta\beta$-decay and the $0\nu\beta\beta$-decay. A high energy resolution of the order of 30 keV, which can presently only be obtained at the RCNP facility in Osaka, allows a precise determination of the GT strength distribution. The high resolution can give significant insight into the details of the nuclear structure. It may be important to understand if the concentration of the low-energy B(GT) strength within a single strong transition, as was observed in the case of ^{96}Zr and ^{100}Mo, is a somewhat general feature of nuclei with masses $A \sim 100$ or above [10]. An open question is the $2\nu\beta\beta$-decay half-life of ^{136}Xe, which has been not measured yet. The reason of suppression of this process is not known. Clearly, explanation of these effects has significant bearing on the double β-decay rate.

we note that a possibility to study charge-changing and particle transfer reactions at iThemba Labs in South Africa is under discussion.

CONCLUSION AND OUTLOOK

Many new projects for measurements of $0\nu\beta\beta$-decay have been proposed, which hope to probe effective neutrino mass $m_{\beta\beta}$ down to 10-50 meV. Nuclear matrix elements need to be evaluated with uncertainty of less than 30% to establish the neutrino mass spectrum and CP violating phases. The improvement of the calculation of the nuclear matrix elements is a very important and challenging problem.

Recently, there has been significant progress in understanding the source of the spread of calculated NMEs. Nevertheless, there is no consensus among nuclear theorists about their correct values, and corresponding uncertainty. However, a recent development in the field is encouraging. There is a reason to be hopeful that the uncertainty will be reduced.

An important cross-check for nuclear models would be to explore the structure of the intermediate odd-odd nuclei by the charge exchange reactions. There are possibilities for improving the QRPA calculation of NMEs, e.g., by taking into account the deformation of parent and daughter nuclei. Further progress in the NSM calculation will be possible due to increasing computer speed and memory. This will allow to extend the considered model spaces. The exactly solvable models can also help to find the ultimate solution of this important problem. It is also clear that in order to have confidence in calculated NMEs multiple $0\nu\beta\beta$-decay experimental results are required.

ACKNOWLEDGEMENT

I acknowledge the support of the VEGA Grant agency of the Slovak Republic under the contract No. 1/0639/09.

REFERENCES

1. F. T. Avignone, S. R. Elliott, and J. Engel, *Rev. Mod. Phys.* **80**, 481 (2008).
2. V.A. Rodin, A. Faessler, F. Šimkovic, and P. Vogel, Phys. Rev. C **68**, 044302 (2003); Nucl. Phys. A **766**, 107 (2006) and erratum Nucl. Phys. A **766** 107 (2006).
3. F. Šimkovic, A. Faessler, V. Rodin, P. Vogel and J. Engel, Phys. Rev. C **77**, 045503 (2008); F. Šimkovic, A. Faessler, H. M´uther, V. Rodin, M. Stauf, Phys. Rev. C **79**, 055501 (2009).
4. E. Caurier, G. Martinez-Pinedo, F. Nowacki, A. Poves, and A.P. Zuker, Rev. Mod. Phys. **77**, 427 (2005).
5. E. Caurier, J. Menendez, F. Nowacki, A. Poves, Phys. Rev. Lett. **100**, 052503 (2008).
6. K. Chaturvedi, R. Chandra, P. K. Rath, P. K. Raina and J. G. Hirsch, Phys. Rev. C **78**, 054302 (2008).
7. J. Barea, F. Iachello, Phys. Rev. C **79**, 044301 (2009).
8. J. P. Schiffer et al., Phys. Rev. Lett. **100**, 112501 (2008); B. P. Kay et al., Phys. Rev. C **79**, 021301 (2009).
9. F. Šimkovic, A. Faessler, and P. Vogel, Phys. Rev. C **79**, 015502 (2009).
10. E.-W. Grewe et al., Phys. Rev. C **76**, 054307 (2007); Phys. Rev. C **78**, 044301 (2008); S. Rakers et al.; Phys. Rev. C **71**, 054313 (2005); K. Yako et al., Phys. Rev. Lett. **103**, 012503 (2009).

Covariant relativistic separable kernel approach for the electrodisintegration of the deuteron at high momentum transfer

S.G. Bondarenko, V.V. Burov and E.P. Rogochaya

Joint Institute for Nuclear Research, Dubna, Russia

Abstract. The electrodisintegration of the deuteron for the kinematic conditions of the JLab experiment E-94-019 is considered. The calculations are performed within the covariant Bethe-Salpeter approach with the separable kernel of interaction. The results are obtained within the relativistic plane wave impulse approximation and compared with the experimental data and other models. The influence of nucleon electromagnetic form factors is investigated.

Keywords: Bethe-Salpeter equation; Separable ansatz; Deuteron electrodisintegration
PACS: 25.10.+s; 25.30.Fj; 11.10.St

FORMALISM

The deuteron electrodisintegraton is considered within the Bethe-Salpeter (BS) approach [1] with a separable kernel of NN interactions. It is based on the solution of the BS equation:

$$\Phi^{JM}(k;K) = \frac{i}{(2\pi)^4} S_2(k;K) \int d^4p V(p,k;K) \Phi^{JM}(p;K) \tag{1}$$

for the bound state of the neutron-proton (np) system with the total angular momentum J and its projection M which is described by the BS amplitude Φ^{JM}. Here the total $K = k_p + k_n$ and the relative $k = (k_p - k_n)/2$ momenta are used instead of the proton k_p and neutron k_n momenta. In general, the BS amplitude can be decomposed by the partial-wave states through the generalized spherical harmonic $\mathscr{Y}$ and the radial part ϕ [2] as:

$$\Phi^{JM}_{\alpha\beta}(k;K_{(0)}) = \sum_a (\mathscr{Y}_{aM}(\mathbf{k}) U_C)_{\alpha\beta} \; \phi_a(k_0, |\mathbf{k}|; K^2_{(0)}), \tag{2}$$

where $K_{(0)} = (M_d, 0)$ is the total momentum of the NN system in its rest frame (here it is the deuteron rest frame called the laboratory system, LS); M_d is a mass of the deuteron; U_C is the charge conjugation matrix; α, β denote matrix indices; a is a short notation of the partial-wave state $^{2S+1}L^{\rho}_J$ with spin S, orbital L and total J angular momenta, ρ means positive- or negative-energy partial-wave state. $S_2(k;K)$ is the free two-particle Green function:

$$S_2^{-1}(k;K) = \left(\tfrac{1}{2} K\cdot\gamma + k\cdot\gamma - m\right)^{(1)} \left(\tfrac{1}{2} K\cdot\gamma - k\cdot\gamma - m\right)^{(2)}.$$

In calculations, it is more convenient to use the BS vertex function Γ^{JM} which is connected with the BS amplitude by the following relation:

$$\Phi^{JM}(k;K) = S_2(k;K)\Gamma^{JM}(k;K). \tag{3}$$

After using the decomposition of type (2) for the vertex function the relation between Φ^{JM} and Γ^{JM} radial parts can be deduced:

$$\phi_a(k_0,|\mathbf{k}|) = \sum_b S_{ab}(k_0,|\mathbf{k}|;s)g_b(k_0,|\mathbf{k}|), \tag{4}$$

where S_{ab} is the one-nucleon propagator [2]. To solve the BS equation (1) we use the separable ansatz for the interaction kernel

$$V_{ab}(p_0,|\mathbf{p}|;k_0,|\mathbf{k}|;s) = \sum_{i,j=1}^{N} \lambda_{ij}(s)g_i^{[a]}(p_0,|\mathbf{p}|)g_j^{[b]}(k_0,|\mathbf{k}|), \tag{5}$$

where N is a rank of the kernel, g_i are model functions; λ is a parameter matrix satisfying the symmetry property $\lambda_{ij}(s) = \lambda_{ji}(s)$; k $[p]$ is the relative momentum of the initial [final] nucleons; $s = (p_p + p_n)^2$ where p_p is the outgoing proton and p_n is the neutron momentum, respectively. If the radial part of the vertex function Γ_{JM} is written in the following form:

$$g_a(p_0,|\mathbf{p}|) = \sum_{i,j=1}^{N} \lambda_{ij}(s)g_i^{[a]}(p_0,|\mathbf{p}|)c_j(s), \tag{6}$$

the initial integral BS equation (1) is transformed into a system of linear homogeneous equations for the coefficients $c_i(s)$:

$$c_i(s) - \sum_{k,j=1}^{N} h_{ik}(s)\lambda_{kj}(s)c_j(s) = 0, \tag{7}$$

where

$$h_{ij}(s) = -\frac{i}{4\pi^3}\sum_a \int dk_0 \int \mathbf{k}^2 d|\mathbf{k}| \frac{g_i^{[a]}(k_0,|\mathbf{k}|)g_j^{[a]}(k_0,|\mathbf{k}|)}{(\sqrt{s}/2 - E_{\mathbf{k}} + i\varepsilon)^2 - k_0^2} \tag{8}$$

and $E_{\mathbf{k}} = \sqrt{\mathbf{k}^2 + m^2}$. Using (4) and taking into account only positive-energy partial-wave states for the deuteron ${}^3S_1^+$, ${}^3D_1^+$ the radial part of the BS amplitude can be written as:

$$\phi_a(k_0,|\mathbf{k}|) = \frac{g_a(k_0,|\mathbf{k}|)}{(M_d/2 - E_{\mathbf{k}} + i\varepsilon)^2 - k_0^2}. \tag{9}$$

Thus, using the separable functions g we can calculate observables describing the np system.

CROSS SECTION

The exclusive $d(e,e'n)p$ process when all particles are unpolarized can be described by the cross section in LS:

$$\frac{d^3\sigma}{dQ^2 d|\mathbf{p}_n| d\Omega_n} = \frac{\sigma_{\rm Mott}\pi \mathbf{p}_n^2}{2(2\pi)^3 M_d E_e E'_e} \times$$
$$\times \left[l^0_{00} W_{00} + l^0_{++}(W_{++}+W_{--}) + l^0_{+-}\cos 2\phi \ 2{\rm Re}W_{+-} - l^0_{+-}\sin 2\phi \ 2{\rm Im}W_{+-} \right.$$
$$\left. - l^0_{0+}\cos\phi \ 2{\rm Re}(W_{0+}-W_{0-}) - l^0_{0+}\sin\phi \ 2{\rm Im}(W_{0+}+W_{0-}) \right], \quad (10)$$

where $\sigma_{\rm Mott} = (\alpha \cos\frac{\theta}{2}/2E_e \sin^2\frac{\theta}{2})^2$ is the Mott cross section, $\alpha = e^2/4\pi$ is the fine structure constant; E_e [E'_e] is the energy of the initial [final] electron; Ω'_e is the outgoing electron solid angle; θ is the electron scattering angle; $Q^2 = -q^2 = -\omega^2 + \mathbf{q}^2$, where $q = (\omega, \mathbf{q})$ is the momentum transfer. The outgoing neutron is described by the momentum $\mathbf{p}_n$ and the solid angle $\Omega_n = (\theta_n, \phi)$ with the zenithal angle θ_n between $\mathbf{q}$ and $\mathbf{p}_n$ momenta and azimuthal angle ϕ between $(\mathbf{ee}')$ and $(\mathbf{qp}_n)$ planes. The photon density matrix elements have the following form:

$$l^0_{00} = \frac{Q^2}{\mathbf{q}^2}, \quad l^0_{0+} = \frac{Q}{|\mathbf{q}|\sqrt{2}}\sqrt{\frac{Q^2}{\mathbf{q}^2} + \tan^2\frac{\theta}{2}},$$
$$l^0_{++} = \tan^2\frac{\theta}{2} + \frac{Q^2}{2\mathbf{q}^2}, \quad l^0_{+-} = -\frac{Q^2}{2\mathbf{q}^2}. \quad (11)$$

The hadron density matrix elements W can be calculated using Cartesian components of the hadron tensor

$$W_{\mu\nu} = \frac{1}{3}\sum_{s_d s_n s_p} \left| < np : SM_S | j_\mu | d : 1M > \right|^2, \quad (12)$$

where S is a spin of the np pair and M_S is its projection, and the photon polarization vectors ε according to the relation

$$W_{\lambda\lambda'} = W_{\mu\nu}\varepsilon^\mu_\lambda \varepsilon_{\lambda'}{}^\nu, \quad (13)$$

here λ, λ' are photon helicity components [3]. The hadron current j_μ in (12) can be written according to the Mandelstam technique [4] and, within the relativistic impulse approximation, has the following form:

$$< np : SM_S | j_\mu | d : 1M > =$$
$$i\sum_{r=1,2}\int \frac{d^4p}{(2\pi)^4} {\rm Sp}\left\{ \Lambda(\mathscr{L}^{-1}) \bar{\psi}_{SM_S}(P^{\rm CM}, p^{\rm CM}) \Lambda(\mathscr{L}) \times \right.$$
$$\left. \Gamma^{(r)}_\mu(q) S^{(r)}\left(\frac{K_{(0)}}{2} - (-1)^r p - \frac{q}{2}\right) \Gamma^M\left(K_{(0)}, p + (-1)^r\frac{q}{2}\right) \right\}, \quad (14)$$

the sum over $r = 1,2$ corresponds to the interaction of the virtual photon with the proton and with the neutron in the deuteron, respectively. The total $P^{\rm CM}$ and the relative $p^{\rm CM}$ momenta of the outgoing nucleons are considered in the final np pair rest frame (center-of-mass system, CM) and can be written in LS using the Lorenz-boost transformation along the $\mathbf{q}$ direction. The Lorenz transformation of the np pair wave function ψ_{SM_S} from CM to LS is:

$$\Lambda(\mathscr{L}) = \quad \left(\frac{1+\sqrt{1+\eta}}{2}\right)^{\frac{1}{2}} \left(1 + \frac{\sqrt{\eta}\gamma_0\gamma_3}{1+\sqrt{1+\eta}}\right). \tag{15}$$

where $\eta = \mathbf{q}^2/s$. The interaction vertex is chosen in the on-mass-shell form:

$$\Gamma_\mu(q) = \gamma_\mu F_1(q^2) - \frac{1}{4m}\left(\gamma_\mu \not{q} - \not{q}\gamma_\mu\right) F_2(q^2), \tag{16}$$

here $F_1(q^2)$ is the Dirac form factor, $F_2(q^2)$ - Pauli form factor. The form factors are described by the dipole fit model [5] or modified dipole fit [6, 7]. If the outgoing nucleons are supposed to be non-interacting it is the so-called plane-wave approximation. In this case the np pair wave function can be written in the following form:

$$\bar{\Psi}_{SM_S}(P,p;p^*) \;\rightarrow\; \bar{\Psi}^{(0)}_{SM_S}(P,p;p^*) = (2\pi)^4 \bar{\chi}_{SM_S}\delta(p-p^*), \tag{17}$$

where $p^* = (0,\mathbf{p}^*)$ is the relative momentum of on-mass-shell nucleons, χ_{SM_S} describes spinor states of the pair. Taking into account the representation (17), the hadron current (14) can be transformed into a sum:

$$< np : SM_S|j_\mu|d : 1M >= i \sum_{r=1,2} \left\{ \Lambda(\mathscr{L}^{-1})\bar{\chi}_{SM_S}\left(P^{\rm CM}, p^{\rm CM*}\right)\Lambda(\mathscr{L})\Gamma^{(r)}_\mu(q) \cdot \right.$$
$$\left. \cdot S^{(r)}\left(\frac{K_{(0)}}{2} - (-1)^r p^* - \frac{q}{2}\right)\Gamma^M\left(K_{(0)}, p^* + (-1)^r\frac{q}{2}\right)\right\}. \tag{18}$$

In the paper the cross section of the exclusive electrodisintegration of the deuteron $d^2\sigma/dQ^2 d|\mathbf{p}_n|$ [8] is calculated. It can be obtained from (10) after integration over the neutron solid angle:

$$\frac{d^2\sigma}{dQ^2 d|\mathbf{p}_n|} = \int\limits_{\Omega_n} \frac{d^3\sigma}{dQ^2 d|\mathbf{p}_n| d\Omega_n} d\Omega_n. \tag{19}$$

According to [8] the integration is performed over Ω_n: $20^\circ \leqslant \theta_n \leqslant 160^\circ$, $0^\circ \leqslant \phi \leqslant 360^\circ$. Four different Q^2 are considered. The obtained results are discussed in the next section.

DISCUSSION AND CONCLUSION

In this paper the exclusive cross section of the electrodisintegration (19) for the kinematic conditions of the JLab experiment [8] is calculated within the Bethe-Salpeter

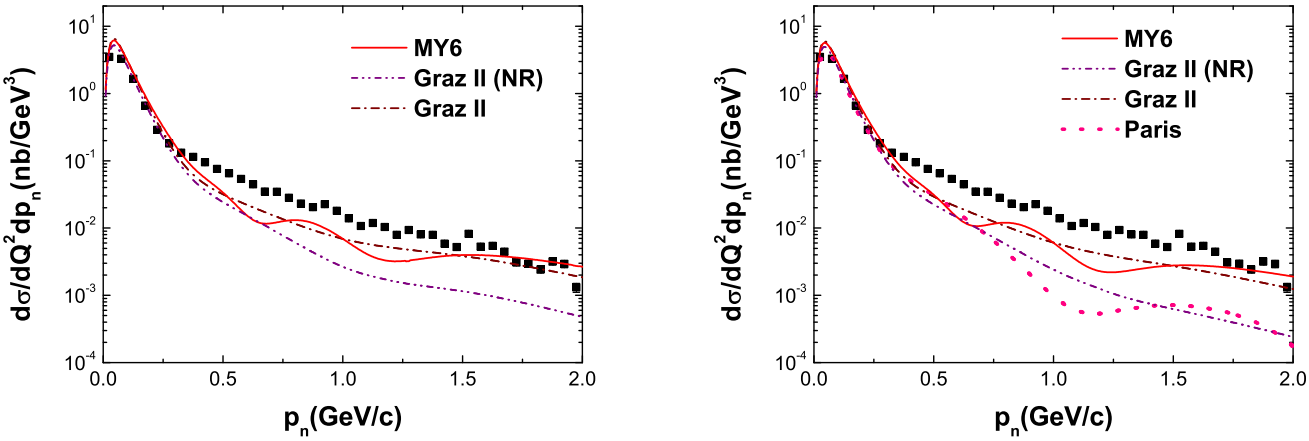

FIGURE 1. The cross section (19) for $Q^2 = 2 \pm 0.25\,\mathrm{GeV}^2$ depending on the neutron momentum $\mathbf{p}_n$ is considered. Calculations with Graz II (NR) [11] (purple dash-dot-dotted line), Graz II [12] (brown dash-dotted line), MY6 [9] (red solid line) and Paris [10] (pink dotted line) are present. The dipole fit [5] (on the left) and modified dipole fit [5, 6, 7] (on the right) models for nucleon electromagnetic form factors are considered.

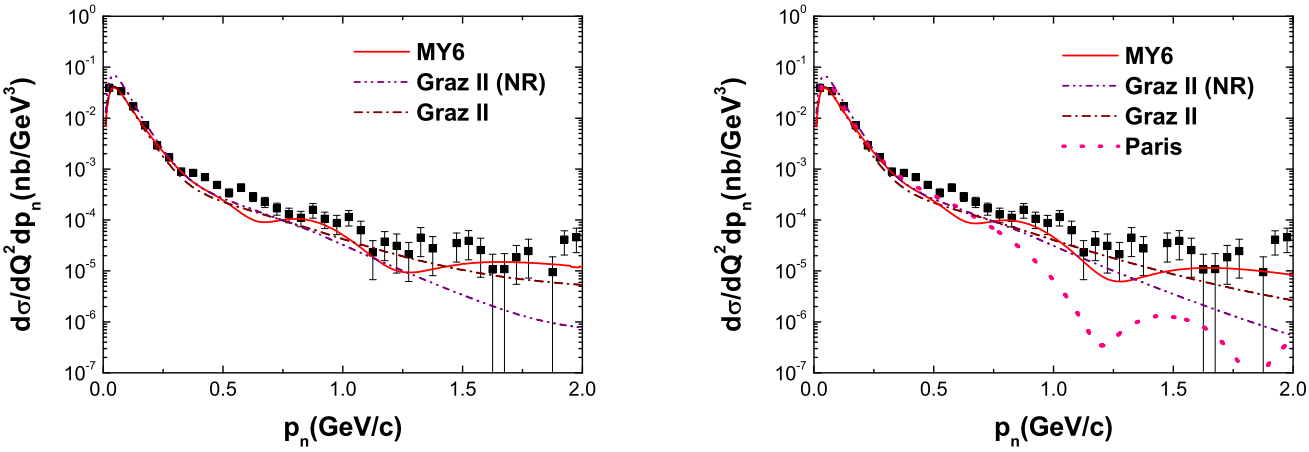

FIGURE 2. As in Fig.1, but for $Q^2 = 5 \pm 0.5\,\mathrm{GeV}^2$.

approach with the rank-six separable kernel MY6 [9]. The calculations are performed within the relativistic plane-wave impulse approximation. The obtained results are compared with the experimental data and other theoretical models, the Paris potential [10], the nonrelativistic Graz II (NR) [11] and relativistic Graz II [12] separable interaction kernels.

In Fig.1, the cross section depending on the outgoing neutron momentum $\mathbf{p}_n$ is present for Q^2=2 GeV^2. The dipole fit [5] (figure on the left) and modified dipole fit [6, 7] (figure on the right) models for the nucleon electromagnetic form factors are considered. From

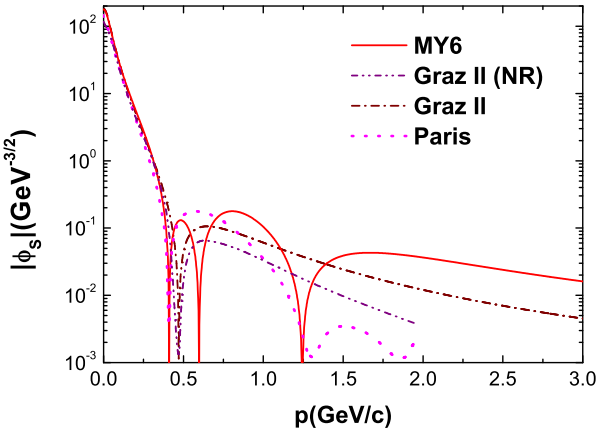

FIGURE 3. The wave function (9) at $k_0 = M_d/2 - E_{\mathbf{k}}$ for the $^3S_1^+$ partial-wave state in the deuteron rest frame for the MY6 model in comparison with those of Graz II (NR) [11], Graz II [12], and Paris [10].

the figure, a good agreement with the experimental data can be seen at low neutron momenta $|\mathbf{p}_n| \leqslant 0.25$ GeV/c. The discrepancy between the theoretical calculations and the experiment increases with the increase of $|\mathbf{p}_n|$ for the nonrelativistic separable Graz II (NR) [11] and Paris [10] potential models. For the relativistic MY6 [9] and Graz II [12] separable models, a good agreement with the experimental data can be seen not only at low $\mathbf{p}_n$ but also at high $|\mathbf{p}_n|$>1.5 GeV/c.

In Fig.2, the cross section for Q^2=5 GeV^2 is present. As in previous figure, two models of nucleon electromagnetic form factors are considered. The relativistic MY6 and Graz II models agree with the experimental data much better than for Q^2=2 GeV^2 whereas the nonrelativistic Graz II (NR) and Paris potentials deviate from the experimental points at $|\mathbf{p}_n|$>0.25 GeV/c increasingly more than in previous case (Fig.1). Therefore, it can be concluded that the influence of relativistic effects increases with the increase of the energy of the nucleons and the momentum transfer.

It should be noticed that the behavior of the calculated cross section is similar to the behavior of the corresponding wave function for the deuteron $^3S_1^+$ partial-wave state which is shown in Fig.3. From the comparison of Figs.1, 2 and Fig.3, it is seen that the cross section at high $|\mathbf{p}_n|$ is similar to the asymptotic form of the $^3S_1^+$ wave function.

From Figs.1,2, it is seen that results obtained within the dipole fit model [5] for nucleon electromagnetic form factors are similar to those obtained with modified form factors [6, 7]. Thus, we can summarize that the choice of nucleon electromagnetic form factors does not play an important role in the description of the cross section at high momentum transfer. It is interesting that the results calculated within the dipole fit model, which does not describe the behavior of the electric form factor of the proton at high Q^2, is virtually undistinguishable from those obtained with the modified proton electric form factor [6]. However, the final conclusion which model gives the best result can be made only when negative-energy partial-wave states (P waves) and final state interaction effects will be taken into account.

ACKNOWLEDGMENTS

Authors would like to thank the organizers of the 2nd South Africa - JINR Symposium for a possibility to present this work.

REFERENCES

1. E. E. Salpeter, and H. A. Bethe, *Phys. Rev.* **84**, 1232–1242 (1951).
2. S. G. Bondarenko, V. V. Burov, A. V. Molochkov, G. I. Smirnov, and H. Toki, *Prog. Part. Nucl. Phys.* **48**, 449–535 (2002) [nucl-th/0203069].
3. V. Dmitrasinovic, and F. Gross, *Phys. Rev.* **C 40**, 2479–2497 (1989).
4. S. Mandelstam, *Proc. Roy. Soc. Lond.* **A 233**, 248–266 (1955).
5. H. Pietschmann, and H. Stremnitzer, *Lett. Nuovo Cim.* **2**, 841–845 (1969).
6. O. Gayou et al. (Jefferson Lab Hall A), *Phys. Rev. Lett.* **88**, 092301 (2002) [nucl-ex/0111010].
7. S. Galster et al., *Nucl. Phys.* **B 32**, 221–237 (1971).
8. K. S. Egiyan et al. (CLAS), *Phys. Rev. Lett.* **98**, 262502 (2007) [nucl-ex/0701013].
9. S. G. Bondarenko, V. V. Burov, W.-Y. Pauchy Hwang, E.P. Rogochaya, *Nucl. Phys.* **A**, doi:10.1016/j.nuclphysa.2010.08.007, 17 pp. [1002.0487 [nucl-th]].
10. M. Lacombe et al., *Phys. Rev.* **C 21**, 861–873 (1980).
11. L. Mathelitsch, W. Plessas, and W. Schweiger, *Phys. Rev.* **C 26**, 65–76 (1982).
12. G. Rupp, and J. A. Tjon, *Phys. Rev.* **C 41**, 472–483 (1990).

Summary of search for tetrahedral deformations in the mass 160 region

M.A. Stankiewicz

Department of Physics, University of Cape Town, Rondebosch, 7700, South Africa
iThemba LABS, P.O. Box 722, Somerset West, 7129 South Africa

Abstract. Recent theoretical work has suggested that some nuclei in the rare earth region might exhibit tetrahderal deformations. Several nuclei have been studied at iThemba LABS, resulting in evidence against the possibility of low-lying tetrahedrally deformed bands. In this paper we present results suggesting that the next set of candidates is also not tetrahedrally deformed. This region of the nuclear landscape still contains several interesting features, particularly the discrepancies in B(E2)/B(E1) ratios within the octupole bands, and deserves further study.

INTRODUCTION

In recent years, there has been interest in various regions of the periodic table regarding nuclear deformations [1, 2, 3, 4]. Work by Dudek *et al.* [2], has suggested that the region around Gd and Yb and neutron number 90 might exhibit tetrahedral deformations at a fairly low excitation energy (within 1 MeV of the yrast band). Several experiments were performed at iThemba LABS to look for these candidate tetrahedral bands and see if they agree with the theoretical predictions. The results obtained for ^{154}Gd and ^{160}Yb have been published [5]. In this article, we will summarize the experimental results finished to date, together with the status of the further analysis of nuclei in the region of interest.

Theoretical motivation

The nuclear surface in in the instrinsic frame is often exapanded as [6]

$$R(\theta,\phi) = R_0 \left[1 + \sum_{\lambda=2}^{4} \sum_{\mu=0}^{\lambda} \alpha_{\lambda\mu} Y_{\lambda\mu}(\theta,\phi) \right]. \quad (1)$$

The $\lambda = 2$ terms correspond to quadrupole deformations, which are well established, while $\lambda = 3$ terms correspond to octupole deformations. The low-lying negative parity bands are generally intepreted as octupole vibrations with pronounced α_{30}.

Calculations that included α_{32} deformations have been performed [3] that suggest that potential energy minima occur at specific regions akin to shell-gaps. Specifically, if $\alpha_{20} = 0$, an α_{32} deformation corresponds to a tetrahedral shape. Tetrahedral shell gaps have been calculated to occur at 64, 70, 90 and 94, which correspond to the nuclei

from ^{154}Gd to ^{164}Yb. In addition, Dudek *et al.* [2] have shown that if a nucleus has a sizable tetrahedral deformation, it will behave almost as a tetrahedral rotor and exhibit the T_d symmetry. The nucleus must then have a zero quadrupole moment, implying a lack of E2 transitions in the tetrahedral band. The negative parity bands in the nuclei in the region of interest were usually interpreted as vibrational Y_{30} octupoles [7], but the vanishing in-band transitions at lower spin offers an alternative interpretation as 'tetrahedral candidates'.

EXPERIMENTAL RESULTS

To try and verify the predictions, several experiments have been run at iThemba LABS using the AFRODITE gamma ray detector array, which consists of eight HPGe segmented clover detectors. The reactions included ^{152}Sm(α,2n)^{154}Gd at 25 MeV, and ^{147}Sm(^{16}O,3n)^{160}Yb at 73 MeV. Approximately 0.5×10^9 $\gamma\gamma$ conincidence events were collected for the former reaction, and 2×10^9 in the latter. The complete analysis and results have already been published [8, 9, 5].

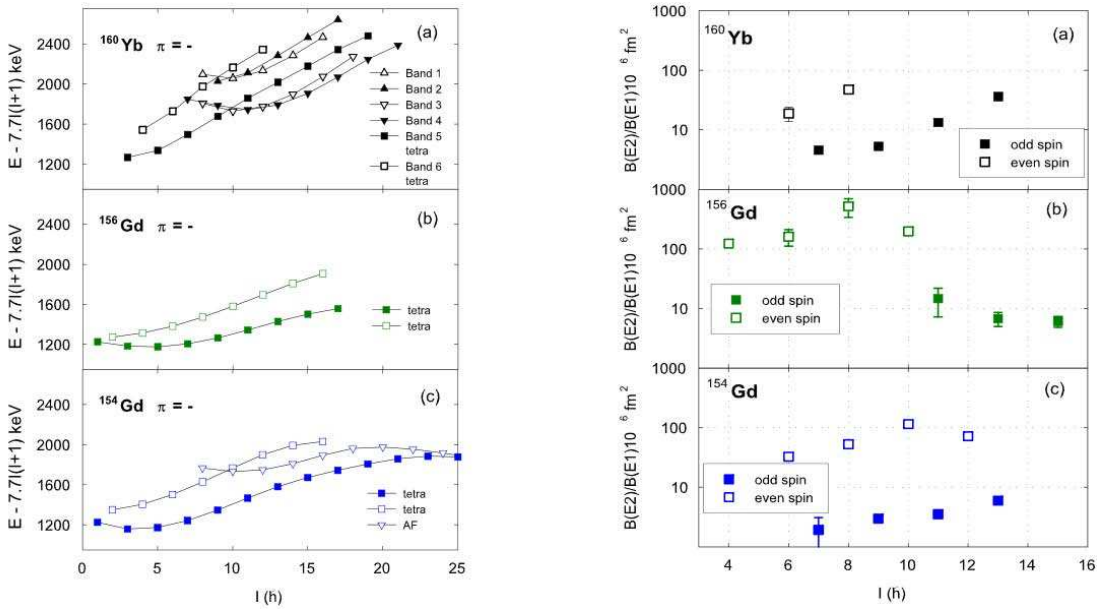

FIGURE 1. Left, energies of negative parity band levels in ^{160}Yb, ^{166}Gd and ^{164}Gd, less a rigid rotor reference against spin. Right shows the branching ratios for in-band (E2) vs out-of-band (E1) transitions in the candidate tetrahedral bands [5].

The results are shown above. The data from ^{156}Gd [10] is shown for comparison, as that was considered one of the best candidates for a tetrahedral nucleus [3]. For low spin states (below $10\hbar$), the octupole bands (labelled 'tetra' in the figure) show a fairly similar structure, both in the sign of the signature splitting between the two spin partners, and the magnitude of splitting. At higher spin, there are interactions with the negative parity two quasiparticle bands, which distort the picture.

Additionally, if one considers the branching ratio of the in-band transitions $B(E2, I \rightarrow I-2)$, against out-of-band transitions to the ground state band $B(E1, I \rightarrow I-1)$ for odd

and $B(E1, I \rightarrow I)$, for even spins, one finds a staggering of the data. The observed ratios indicate that the in odd spin bands, the E2 transitions are very unfavoured, making their study difficult. The ratio could be due to the a natural suppression of the E2 transitions due to a low quadruple moment, which is the expected signature of the tetrahedral deformation, but alternately the ratio could be low simply due to very high E1 strengths.

Bark *et al.* [5] performed a careful analysis of the energies and branching ratios of the negative parity bands, and resolved the interactions and quadrupole moments with band-mixing calculations. The calculations found $Q_{t_T} \sim 4$ eb, which corresponds to a significant quadrupole deformation. This is against the expectation of the zero quadrupole moment required for the tetrahedral rotor, indicating that the low-lying negative parity bands are most likely normal octupole vibrations. The calculated quadrupole moments also disallow an explanation of the staggered B(E2)/B(E1) ratios based on the suppression of in-band transitions in the odd octupole bands. At this time there is no complete explanation of the discrepancy between odd and even spin branching ratios.

The result of the non-tetrahedral nature of ^{160}Yb does not preclude nearby nuclei from containing structures that are interesting. By performing a systematic study of the negative parity bands in the nuclei Gd, Dy, Er and Yb, with neutron numbers 88, 90 and 92 (figure 2), one can observe that the behaviour of the bands depends strongly on N, yet individual features remain to be understood. Unfortunately, a lot of the experimental data on the negative parity bands remains unknown, especially down to the very low spins. This is partly due to the low strength of the in band E2 transitions, making the transitions near the low end of the octupole bands difficult to populate and observe. The data on the B(E2)/B(E1) branching ratios are even less known.

In an attempt to learn more about this region, two more nuclei in this region were recently studied at iThemba. The reactions were ^{147}Sm(^{12}C,3n)^{156}Er and ^{152}Sm(^{12}C,4n)^{160}Er, as a slightly different neutron number has a direct effect on the nuclear shape. Approximately 1.8×10^9 $\gamma\gamma$ conincidence events were collected for each reaction.

The preliminary results are included above. The low-lying negative parity bands have been extended in both nuclei, but the branching ratios of in-band and out of band transitions are not yet available.

It is apparent that in ^{156}Er the candidate tetrahedral bands behave similarly to the other $N = 88$ nuclei at low spin (below $10\hbar$). The odd band partner is lower in excitation energy and the two band partners proceed in an almost parallel manner. Around spin 10 however, the two bands experience deviations from the expected behaviour, most likely due to the interaction of the bands with the two quasi-particle band. The expectation is that a careful band-mixing calculation can clear up these uncertainties. The negative parity bands in ^{160}Er appear to contain a similar structure to the other well-studied nuclei in the region, but there is no complete information for the other $N = 92$ nuclei, making the careful comparisons difficult.

CONCLUSION

The rare earth region of $64 \leq Z \leq 70$ and $88 \leq N \leq 92$ remains a very interesting one indeed. To date there seems to be no evince supporting the existence of tetrahedrally

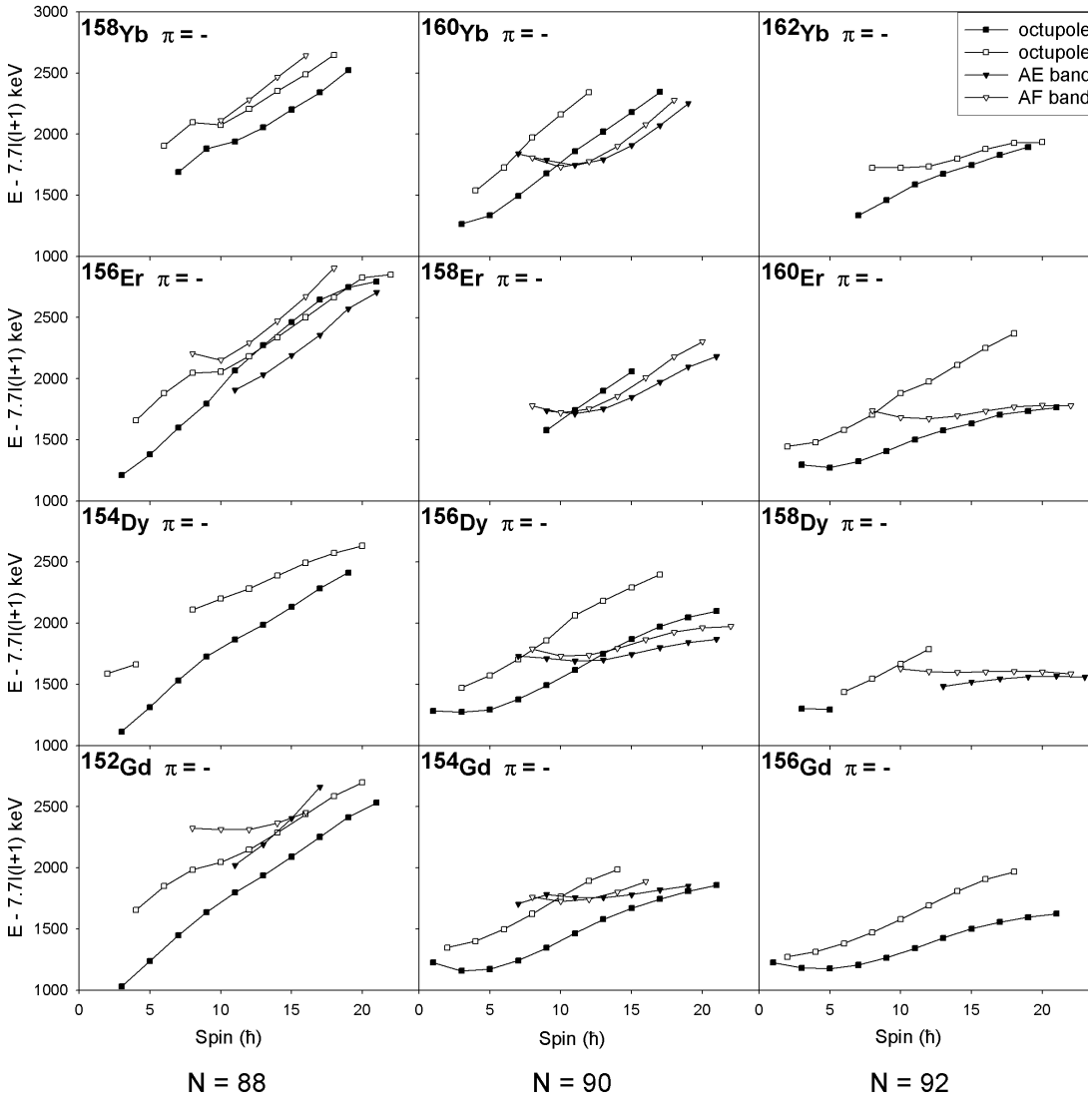

FIGURE 2. Systematics of the negative parity bands in the Gd-Yb region, for $N = 88, 90, 92$. The octupole (candidate tetrahedral) bands are marked with squares, and the two quasi-particle bands are marked with triangles. Data collected from nndc. The bands for ^{158}Dy are tentative spin and parity assignments

deformed nuclei in the region, although the search for evidence has not been exhaustive. There are several results that remain unexplained, including he nature of the variation in the branching ratios in the negative parity bands. It is hoped that the RPA calculations can shed some light on the systematic behaviour of the observed bands.

ACKNOWLEDGMENTS

I would like to thank Dr. Rob Bark for his assistance in the writing of this paper, and the accelerator group at iThemba LABS for the technical support. This work has been supported by the National Research Foundation of South Africa.

REFERENCES

1. S. Takami *et al.*, Phys. Lett. **B 431**, 242 (1998)
2. J. Dudek *et al.*, Phys. Rev. Lett. **88**, 252502 (2002)
3. J. Dudek *et al.*, Phys. Rev. Lett. **97**, 072501(2006)
4. N. Schunck *et al.*, Phys. Rev. **C69**, 061305 (2004)
5. R.A. Bark *et al.*, Phys. Rev. Lett. **104**, 022501 (2010)
6. J.M. Eisenberg and W. Greiner, Nuclear Models (1975)
7. P.E. Garret *et al.*, J.Phys. G **31**, S1855 (2005)
8. R.A. Bark *et al.*, J.Phys G **31**, S1747 (2005)
9. J.F. Sharpey-Shafer *et al.*, Proc. XIIV Intern. Winter Meeting on Nucl. Phys., Bormio, Itali, p.295 (2006)
10. C.W. Reich, Nucl. Data Sheets **99**, 753 (2003)

Reflection asymmetry in ^{220}Th and dinuclear model

T.M. Shneidman*, G.G. Adamian*, N.V. Antonenko*, R.V. Jolos* and W. Scheid†

*Joint Institute for Nuclear Research, 141980 Dubna, Russia
†Institut für Theoretische Physik der Justus-Liebig-Universität, D–35392 Giessen, Germany

Abstract. The negative parity bands with different values of K in ^{220}Th are analyzed within the dinuclear system model which was previously used for description of the ground state alternating-parity bands with $K = 0$ in deformed actinides. The model is based on the assumption that the cluster type shapes are produced by the collective motion in the mass-asymmetry coordinate. To describe the reflection-asymmetric collective modes characterized by the nonzero values of K, the intrinsic excitations of clusters are taken into account. The observed excitation spectrum, angular momentum dependence of the parity splitting and of the staggering behavior of the $B(E1)/B(E2)$ ratios are explained.

Keywords: dinuclear system
PACS: 21.60.Ev,21.60.Gx

INTRODUCTION

In the even-even isotopes of actinides and also in the heavy Ba and Ce isotopes the low-lying negative parity states are observed together with the usually presented collective positive-parity states combined into rotational or quasirotational ground-state bands. Formation of the positive-parity rotational or quasirotational bands is connected in general to the quadrupole collective motion, while the lowering of the negative-parity states is a signature of the presence of the reflection asymmetric collective mode. There are several approaches to treat the collective motion related to the reflection asymmetric degrees of freedom. One of them is based on the concept of the nuclear mean field [1] which has a static mirror asymmetric deformation or is characterized by a large amplitude of reflection asymmetric vibrations around the equilibrium shape. Another approach is based on the assumption that the reflection asymmetric shape is a consequence of the α-clustering in nuclei [2]. It is also known from the Nilsson-Strutinsky type calculations for light nuclei that nuclear configurations corresponding to the minima of the potential energy contain particular symmetries which are related to certain cluster structures [3, 4]. Several calculations performed for heavy nuclei [5, 6, 7] have shown that configurations with large equilibrium quadrupole deformations and low-lying collective negative parity states are strongly related to clustering. We mention also a different approach to description of the properties of the alternating parity bands which is based on the idea of the aligned octupole phonons [8, 9].

The main idea of the cluster model developed in [7, 10, 11] is that a dynamics of a reflection asymmetric collective motion can be treated as a collective motion of nucleons

between two clusters or as a motion in a mass-asymmetry coordinate. Such collective motion simultaneously creates deformations with even and odd-multipolarities. The choice of the collective coordinates and the procedure of the calculation of the potential energy and of the inertia coefficients for the Hamiltonian of the model are based on the concept of the dinuclear system (DNS). This concept was first introduced to explain the experimental data on deep inelastic and fusion reactions. Later on it was applied to the description of the nuclear structure phenomena, like alternating parity bands, mentioned above, and superdeformed states [12, 13]. The dinuclear system (A,Z) consists of two fragments (A_1,Z_1) and (A_2,Z_2) with $A = A_1 + A_2$ and $Z = Z_1 + Z_2$ kept in touching configuration by a a molecular-type nucleus-nucleus potential. As it was shown by our calculations, the α-cluster DNS ${}^{A}Z \rightarrow^{(A-4)} (Z-2)+{}^{4}$He gives a significant contribution to the formation of the low-lying nuclear states. This is also in agreement with the fact that these nuclei are good alpha-emitters.

Within this approach the existing experimental data on the angular momentum dependence of the parity splitting in the excitation spectra and the multipole transition moments (E1,E2,E3) of the low-lying alternating parity states in odd and even actinides ${}^{220-228}$Ra, ^{223,225,227}Ac, ${}^{222-224,226,228-232}$Th, ^{231}Pa, ${}^{232-234,236,238}$U and ^{240,242}Po and the medium mass nuclei ^{144,146,148}Ba, ^{151,153}Pm, ^{146,148}Ce ^{153,155}Eu and ^{146,148}Nd are well described. The good agreement between the results of calculations and the experimental data support a cluster interpretation of the reflection-asymmetric states.

However, previously we have considered in the even-even nuclei only the low-lying collective negative parity states with K=0. At the same time, there are experimental data which indicate on a presence of the low-lying collective states related to the reflection-asymmetric modes which are characterized by nonzero values of K. It can happens also that K is not a good quantum number if nuclei are located in a transitional region between deformed and spherical ones. A good example is ^{220}Th [14] whose energy spectra is a challenge for the theoretical approaches. To describe in the framework of the cluster approach the properties of the low-lying collective states related to the reflection-asymmetric collective mode and characterized by nonzero values of K we should take into account intrinsic excitations of the clusters forming a nucleus under consideration. It is the aim of the present investigation to extend the dinuclear system model to take into account such excitations.

MODEL

Hamiltonian

As illustrated in Fig. 1, the degrees of freedom chosen to characterize a dinuclear system with nearly spherical heavy cluster are related to description of the rotation of the DNS as a whole, the quadrupole oscillations of the heavy fragment, and the transfer of nucleons between the fragments. The Hamiltonian of the model can be presented in the form

$$\hat{H} = \hat{H}_0 + \hat{V}_{int}, \tag{1}$$

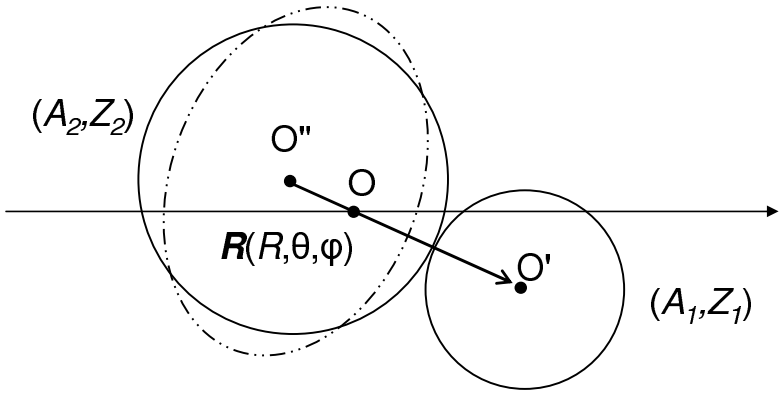

FIGURE 1. Schematic picture illustrates degrees of freedom used in the model to describe dinuclear system. Orientation of the vector of the relative distance R is defined by the angles $\Omega(\theta,\phi)$ with respect to the laboratory frame system.

where $\hat{H}_0$ describes independent fragments of the system and $\hat{V}_{int}$ describes the interaction between the fragments.

We assume that the heavy cluster is spherical and perform harmonic quadrupole oscillations around the spherically symmetric shape with frequency $\hbar\omega_0$, while the light cluster stays in its ground state. This assumption is in agreement with the suggestion made in [19] that some nuclei in the region of N=130 may have a shape with a significant octupole deformation but a negligible quadrupole deformation.

Then for $\hat{H}$ we have the following expression

$$\hat{H} = \hbar\omega_0\hat{n} + \frac{\hbar^2}{2\mu(\xi)R^2}\hat{L}^2 - \frac{\hbar^2}{2B_\xi}\frac{1}{\xi}\frac{\partial}{\partial\xi}\xi\frac{\partial}{\partial\xi} + U(R,\xi,\alpha_{2\mu}), \tag{2}$$

where, for convenience, we use positively-defined variable ξ instead of a usual definition of the mass-asymmetry coordinate $\eta = (A_1 - A_2)/(A_1 + A_2)$

$$\xi = 2A_2/A = 1 - \eta. \tag{3}$$

In equation (2), $\mu(\xi)$ is the reduced mass of the DNS, $R(\xi)$ is the distance between the centers of mass of the fragments, $\hat{n}$ is the operator of the number of the quadrupole phonons of heavy cluster, $\alpha_{2\mu}$ describes quadrupole oscillations of the surface of the heavy fragment and $\hat{L}^2$ is the operator of the square of angular momentum of the relative rotations of the two fragments

$$L^2 = -\left[\frac{1}{\sin\theta}\frac{\partial}{\partial\theta}\sin\theta\frac{\partial}{\partial\theta} + \frac{1}{\sin^2\theta}\frac{\partial^2}{\partial\phi^2}\right]. \tag{4}$$

Angles $\Omega = (\theta,\phi)$ (see Fig.1) describes the orientation of the relative distance vector $\mathbf{R}$ with respect to the laboratory coordinate system.

Above, B_ξ is a mass tensor and $U(R,\xi,\alpha_{2\mu})$ is a potential energy. The potential energy of the dinuclear system is determined as

$$U(R,\xi,\alpha_{2\mu}) = B_1 + B_2 - B_{12} + V(R,\xi,\alpha_{2\mu}). \tag{5}$$

Here, B_1, B_2 and B_{12} are the binding energies of the fragments and the compound nucleus, respectively. The nucleus-nucleus potential in (5)

$$V(R,\xi,\alpha_{2\mu}) = V_{Coul}(R,\xi,\alpha_{2\mu}) + V_{nucl}(R,\xi,\alpha_{2\mu}) \tag{6}$$

is the sum of the Coulomb potential

$$V_{Coul}(R,\xi,\alpha_{2\mu}) = \frac{e^2 Z_1 Z2}{R} + \frac{3}{5}\frac{e^2 Z_1 Z2}{R^3} R_{01}^2 \sum_{\mu} \alpha_{2\mu}^* Y_{2\mu}(\theta,\phi) + ... \tag{7}$$

and the nuclear interaction potential

$$V_{nucl}(R,\xi,\alpha_{2\mu}) = \int \rho_1(\mathbf{r_1})\rho_1(\mathbf{R}-\mathbf{r_2})F(\mathbf{r_1}-\mathbf{r_2})d^3\mathbf{r_1}d^3\mathbf{r_2}, \tag{8}$$

where $F(\mathbf{r_1}-\mathbf{r_2})$ is a Skyrme-type density dependent effective nucleon-nucleon interaction. V_{nucl} can be expanded in degrees of $\alpha_{2\mu}$. The procedure of calculation used in this paper is described in [17]. Since in our case the amplitude of the quadrupole oscillations is small only the terms linear in $\alpha_{2\mu}$ in the expansion of $V(R,\xi,\alpha_{2\mu})$ are considered. Thus, $V(R,\xi,\alpha_{2\mu})$ can be presented as

$$V(R,\xi,\alpha_{2\mu}) = V(R,\xi) + V_0(\xi)\sum_{\mu} \alpha_{2\mu}^* Y_{2\mu}(\theta,\phi), \tag{9}$$

where V_0 is determined by the nuclear and Coulomb parts of the nucleus-nucleus interaction potential. For the H_0 and V_{int} we obtain

$$\hat{H}_0 = \hbar\omega_0\hat{n} + \frac{\hbar^2}{2\mu(\xi)R^2}\hat{L}^2 - \frac{\hbar^2}{2B_\xi}\frac{1}{\xi}\frac{\partial}{\partial\xi}\xi\frac{\partial}{\partial\xi} + V(R,\xi), \tag{10}$$

and

$$V_{int} = V_0(\xi)\sum_{\mu} \alpha_{2\mu}^* Y_{2\mu}(\theta,\phi). \tag{11}$$

In this paper $\hbar\omega_0$ is considered as a free parameter which is fixed by the description of the energy of 2_1^+ state. The numerical calculation have shown that E(2_1^+) is described if we take $\hbar\omega_0$=0.47 MeV. Below we assume that the value of R is fixed and corresponds to the touching configuration of two clusters forming a dinuclear system with mass asymmetry ξ. Thus, $R = R(\xi)$.

Our analysis of the mass-asymmetry motion in ^{220}Th have shown that the motion in coordinate ξ can be separated from the other degrees of freedom and the system is in its lowest state with respect to the mass-asymmetry. The reason for this is that the energy of the first exited state related to the mass-asymmetry degree of freedom is high enough to neglect its influence on the low-energy part of the spectra. Neglecting the excitations in the variable ξ we average Hamiltonian $\hat{H}$ over $\Psi_0(\xi)$ which describes motion in ξ in the ground-state. As a result we obtain

$$\hat{H}_0 = \hbar\omega_0\hat{n} + \frac{\hbar^2}{2\mu(\xi_0)R(\xi_0)^2}\hat{L}^2 + E_0(\xi_0). \tag{12}$$

Averaging over $\Psi_0(\xi)$, yield the effective value of ξ, namely, ξ_0 located between ξ=0, which corresponds to the mononucleus configuration and $\xi = \xi_\alpha = 8/A$. In equation (12) $E_0(\xi_0)$ is the zero-point energy of the motion in ξ, which is unimportant for further consideration. The calculation have been performed with ξ_0=0.2ξ_α. Using this value of ξ_0 we can calculate the interaction energy of the dinuclear system as described in [17]. This gives $V_0(\xi_0)$=11 MeV for the interaction between vibrational and rotational degrees of freedom (see Eq.(11)).

The collective quadrupole coordinate $\alpha_{2\mu}$ can be expressed in terms of the creation and annihilation operators of the quadrupole bosons

$$\hat{\alpha}_{2\mu} = \beta_0(d^+_{2\mu} + \tilde{d}_{2\mu}), \tag{13}$$

with $\beta_0 = \sqrt{\hbar/2B\omega_0}$. Again, as in the case of $\hbar\omega_0$, the mass parameter of the quadrupole motion B is not fixed in the model. The value of B and, respectively, β_0 can be retrieved by fitting the experimental value $B(E2, 2^+ \to 0^+)$. According, to [18], the reduced transition probabilities for the lowest levels of ^{220}Th satisfy the rotor model expression with quadrupole model Q_0=540 e fm^2. This yields β_0=0.12.

If we neglect the interaction term $\hat{V}_{int}$ in (1) the eigenfunctions of the Hamiltonian can be constructed as

$$\Psi^{IM}_{(n\tau n_\Delta I_1)I_2} = [|n\tau n_\Delta I_1) \times Y_{I_2}]_{(IM)}\,, \tag{14}$$

where $|n\tau n_\Delta I_1)$ represents the n-boson wave function of the heavy nucleus, with the seniority τ and angular momentum I_1. Since the quadrupole oscillations have positive parity, the parity of the states (14) is determined by the angular momentum of the relative rotation of the fragments $p = (-1)^{I_2}$. The energies of the states (14) are given in this approximation by the expresssion

$$E_{nI_1I_2I} = \left[\hbar\omega_0 n + \frac{\hbar^2}{2\mu R^2} I_2(I_2+1)\right]. \tag{15}$$

The set of the wave functions (14) can be used as a basis to construct the eigenfunction of the Hamiltonian $\hat{H}$ in the form

$$\Psi_{IM,p} = \sum_{I_1 I_2} \sum_{n_{I_1}\tau_{I_1}} a^{(I,p)}_{n_{I_1}\tau_{I_1}I_1I_2} [|n_{I_1}\tau_{I_1}I_1) \times Y_{I_2}]_{(IM)}\,, \tag{16}$$

where coefficients $a^{(I,p)}_{n_{I_1}\tau_{I_1}I_1I_2}$ should be obtained by a diagonalization of $\hat{H}$. The matrix elements of $\hat{V}_{int}$ between the states (14) have the following form

$$\begin{aligned}\langle \Psi^{IM}_{(n'\tau'I'_1)I'_2} | \hat{V}_{int} | \Psi^{IM}_{(n\tau I_1)I_2} \rangle \quad &= (-1)^{I_1+I'_2+I} V_0\beta_0 \sqrt{\frac{5}{4\pi}(2I_2+1)}(I_2020|I'_20) \\ &\times \begin{pmatrix} I'_2 & I'_1 & I \\ I_1 & I_2 & 2 \end{pmatrix} (n'\tau'I'_1||(d^+ + \tilde{d})||n\tau I_1),\end{aligned} \tag{17}$$

where the reduced matrix elements of the boson operators can be calculated using the boson fractional parentage coefficients

$$\left[d^{n-1}(\alpha_1 I_1)dI|\}d^n\alpha I\right] = \frac{1}{\sqrt{n}}\frac{1}{\sqrt{2I+1}}(d^n\alpha I||d^+||d^{n-1}\alpha_1 I_1)$$
$$\left[d^{n-1}(\alpha_1 I_1)dI|\}d^n\alpha I\right] = (-1)^{I-I_1}\frac{1}{\sqrt{n}}\frac{1}{\sqrt{2I+1}}(d^{n-1}\alpha_1 I_1||\tilde{d}||d^n\alpha I). \quad (18)$$

Two-level solution

Although our calculations have been performed using a sufficiently large basis providing convergence the calculations have shown that the ground-state band and the first excited negative parity band can be presented with a good accuracy as a superposition of two basis states of the form (14). For the ground state band the two level approximation yields the wave function of the form (I can have only even values)

$$\Psi_I^{g.s.} = \sin[\gamma_0(I)]\left[|\frac{I}{2}\frac{I}{2}I)\times Y_0\right]_{(IM)} - \cos[\gamma_0(I)]\left[|\frac{I-2}{2}\frac{I-2}{2}(I-2))\times Y_2\right]_{(IM)} \quad (19)$$

where

$$\sin[\gamma_0(I)] = \frac{1}{\sqrt{2}}\left(1+\frac{1}{\sqrt{1+\left(\frac{V_0\beta_0}{\sqrt{2\pi}\Delta}\right)^2 I}}\right)^{1/2} \quad (20)$$

and for the energy we obtain

$$\varepsilon_I^{g.s.} = \hbar\omega\frac{I}{2} + \frac{\Delta}{2}\left[1-\sqrt{1+\left(\frac{V_0\beta_0}{\sqrt{2\pi}\Delta}\right)^2 I}\right]. \quad (21)$$

In the last expressions $\Delta = \frac{3\hbar^2}{\mu R^2} - \hbar\omega$.

For the first excited negative parity band we have

$$\Psi_I^{n.p.} = \sin[\gamma_1(I)]\left[|\frac{I-1}{2}\frac{I-1}{2}(I-1))\times Y_1\right]_{(IM)} + \cos[\gamma_1(I)]\left[|\frac{I+1}{2}\frac{I+1}{2}(I+1))\times Y_1\right]_{(IM)}, \quad (22)$$

where

$$\sin[\gamma_1(I)] = \frac{1}{\sqrt{2}} \left(1 + \frac{1}{\sqrt{1 + \left(\sqrt{\frac{12}{5\pi}} \frac{V_0 \beta_0}{\hbar\omega} \right)^2 \frac{(I+1)(2I+3)}{(2I+1)}}} \right)^{1/2} \tag{23}$$

and the energy is given as

$$\varepsilon_I^{n.p.} = \hbar\omega \frac{(I-1)}{2} + \frac{\hbar^2}{\Im} + \hbar\omega \left[1 - \sqrt{1 + \left(\sqrt{\frac{12}{5\pi}} \frac{V_0 \beta_0}{\hbar\omega} \right)^2 \frac{(I+1)(2I+3)}{(2I+1)}} \right]. \tag{24}$$

Angular momentum I can take only odd values.

Multipole Moments

Electric multipole operators are given by the expression

$$\hat{Q}_{\lambda\mu} = \int \rho(\mathbf{r}) r^\lambda Y^*_{\lambda\mu} d\tau. \tag{25}$$

For the dinuclear system we assume that

$$\rho(\mathbf{r}) = \rho_1(\mathbf{r}) + \rho_2(\mathbf{r}), \tag{26}$$

where ρ_i $(i = 1,2)$ are the densities of the DNS fragments. Using (26) we can rewrite the expression of the electric multipole moments for the DNS in the following form

$$\hat{Q}_{\lambda\mu} = \sum_{\lambda_1, \lambda_1+\lambda_2=\lambda} \sqrt{\frac{4\pi(2\lambda+1)!}{(2\lambda_1+1)!(2\lambda_2+1)!}} \left[\hat{q}_{\lambda_1}^{(\lambda_1\lambda_2)} \times Y_{\lambda_2}(\Omega) \right]_{\lambda\mu}, \tag{27}$$

where

$$\hat{q}_{\lambda_1}^{(\lambda_1\lambda_2)} = \left[\left(\frac{A_1}{A} \right)^{\lambda_2} Q_{\lambda_1}^{(2)} + (-1)^{\lambda_2} \left(\frac{A_2}{A} \right)^{\lambda_2} Q_{\lambda_1}^{(1)} \right] R^{\lambda_2}. \tag{28}$$

In the last expression $Q^{(i)}$ $(i = 1,2)$ are the intrinsic multipole moments of the DNS fragments.

Since we assume that the light fragment is spherical and can not be excited in the considered energy range the only nonzero moment for the first fragment is $Q_0^{(1)} = Z_1/\sqrt{4\pi}$. The second fragment is assumed to perform the quadrupole oscillations around

the spherical shape. Thus, in the linear approximation with respect to the deformation, we have two nonzero moments for the second fragment: $Q_0^{(2)} = Z_2/\sqrt{4\pi}$ and $Q_2^{(2)} = \frac{3Z_2R_2^2}{4\pi}\alpha_{2\mu}^*$. Therefore, we can write the explicit expressions for the dipole and quadrupole moment of the DNS in the form

$$Q_{1\mu} = e\frac{A_1Z_2 - A_2Z_1}{A}R \cdot Y_{1\mu}(\Omega) \tag{29}$$

for the dipole moment and

$$Q_{2\mu} = e\frac{A_1^2Z_2 + A_2^2Z_1}{A^2}R^2 \cdot Y_{2\mu}(\Omega) + Q_{(2)}^{2\mu} \tag{30}$$

for the quadrupole moment.

Reduced transition probabilities

Using expression (16) for the wave function and (27) for the multipole operators we can calculate the reduced transition probabilities as the

$$B(E\lambda, I_i \to I_f) = \frac{|<I_f||Q_\lambda||I_i>|^2}{2I_i+1} \tag{31}$$

The reduced matrix elements for the multipole operator Q_λ between the initial state i and the final state j has the following form

$$\begin{aligned}
&<I_jp_j||Q_\lambda||I_ip_i>= \\
&\sum_{\lambda_1\lambda_2}\sum_{\{i\}\{j\}} a_{n_{I_1}\tau_{I_1}I_1I_2}^{(I_jp_j)*} a_{n_{I_1'}\tau_{I_1'}I_1'I_2'}^{(I_ip_i)} (n_{I_1}\tau_{I_1}I_1||q_{\lambda_1}^{(\lambda_1\lambda_2)}||n_{I_1'}\tau_{I_1'}I_1')C_{I_2'0\lambda_20}^{I_20}\sqrt{\frac{(2\lambda+1)!}{(2\lambda_1+1)!(2\lambda_2+1)!}} \\
&\times\sqrt{(2i+1)(2j+1)(2\lambda+1)(2i_2+1)(2\lambda_2+1)}\begin{Bmatrix} I_1 & I_2 & I_j \\ I_1' & I_2' & I_i \\ \lambda_1 & \lambda_2 & \lambda \end{Bmatrix},
\end{aligned} \tag{32}$$

where $\lambda_1 = \lambda - \lambda_2$, and $\{i\}(\{j\})$ stands for the set of quantum numbers of the initial (final) states.

Using the two-level solutions for the ground-state and the first excited negative parity bands we can easily calculate the $B(E2)$-values for the intraband transitions and the values of $B(E1)$ for the transitions between these bands.

In the case of the quadrupole transitions we have for the transitions between the states of the ground state band

$$\begin{aligned}
&B(E2, I^{g.s.} \to (I-2)^{g.s.}) = \\
&(-q_0^{(2,0)}\sin[\gamma_0(I)]\cos[\gamma_0(I-2)] + q_2^{(0,2)}\sqrt{\frac{I}{2}}\sin[\gamma_0(I)]\sin[\gamma_0(I-2)] \\
&+q_2^{(0,2)}\sqrt{\frac{(I-2)}{2}}\cos[\gamma_0(I)]\cos[\gamma_0(I-2)])^2
\end{aligned} \tag{33}$$

and for the transition between the negative parity states

$$B(E2, I^{n.p.} \to (I-2)^{n.p.}) =$$
$$(-q_0^{(2,0)} \sqrt{\frac{6(2I-3)}{5(2I-1)}} \sin[\gamma_0(I)] \cos[\gamma_0(I-2)] + q_2^{(0,2)} \sqrt{\frac{I-1}{2}} \sin[\gamma_0(I)] \sin[\gamma_0(I-2)]$$
$$+ q_2^{(0,2)} \sqrt{\frac{(2I-3)(2I+3)(I+1)}{2(2I-1)(2I+1)}} \cos[\gamma_0(I)] \cos[\gamma_0(I-2)])^2. \quad (34)$$

In the last two expressions we have

$$q_0^{(2,0)} = e_{eff} \frac{A_1^2 Z_2 + A_2^2 Z_1}{A^2} R^2,$$
$$q_2^{(0,2)} = e_{eff} \frac{3}{4\pi} Z_1 R_1^2 \beta_0. \quad (35)$$

For the dipole transitions between the two bands our calculations yields

$$B(E1, I^{g.s.} \to (I-1)^{n.p.}) =$$
$$\frac{q_0^2}{2I+1} \left\{ \sqrt{2I-1} \sin[\gamma_0(I)] \cos[\gamma_1(I-1)] + \sqrt{\frac{6(2I+1)}{5}} \cos[\gamma_0(L)] \sin[\gamma_1(I-1)] \right\}^2,$$
$$B(E1, I^{n.p.} \to (I-1)^{g.s.}) = q_0^2 \sin^2[\gamma_1(I)] \sin^2[\gamma_0(I-1)], \quad (36)$$

where

$$q_0 = e_{eff} \frac{A_1 Z_2 - A_2 Z_1}{A} R.$$

RESULTS OF CALCULATIONS

The results of calculations of the energy spectra of the ground state band and the two lowest negative parity bands for the ^{220}Th are presented in Fig.2 together with the available experimental data. the The Hamiltonian (1) has been diagonalized numerically. One can see the overall good agreement between the calculated and experimental spectra.As a consequence of the harmonic quadrupole oscillations of the heavy fragment, the ground-state band and the first negative parity bands exhibit approximately an equidistant spectra.

The calculation shows that mainly two eigenvectors of $\hat{H}_0$ are present in the wave function of the states of the ground state band. Namely, $\left[|\frac{I}{2}\frac{I}{2}(I)) \times Y_0\right]_{(IM)}$ and $\left[|\frac{I-2}{2}\frac{I-2}{2}(I-2)) \times Y_2\right]_{(IM)}$. The contribution of the first of them is predominant at low angular momenta. As a consequence at low angular momenta the ground state band has an equidistant spectrum with the energy differences determined mainly by the frequency of the harmonic quadrupole oscillations of the heavy fragment. With increase of the angular momentum, the distance between the levels is slightly increased, due to the growing admixture of the component $\left[|\frac{I-2}{2}\frac{I-2}{2}(I-2)) \times Y_2\right]_{(IM)}$ to the wave function.

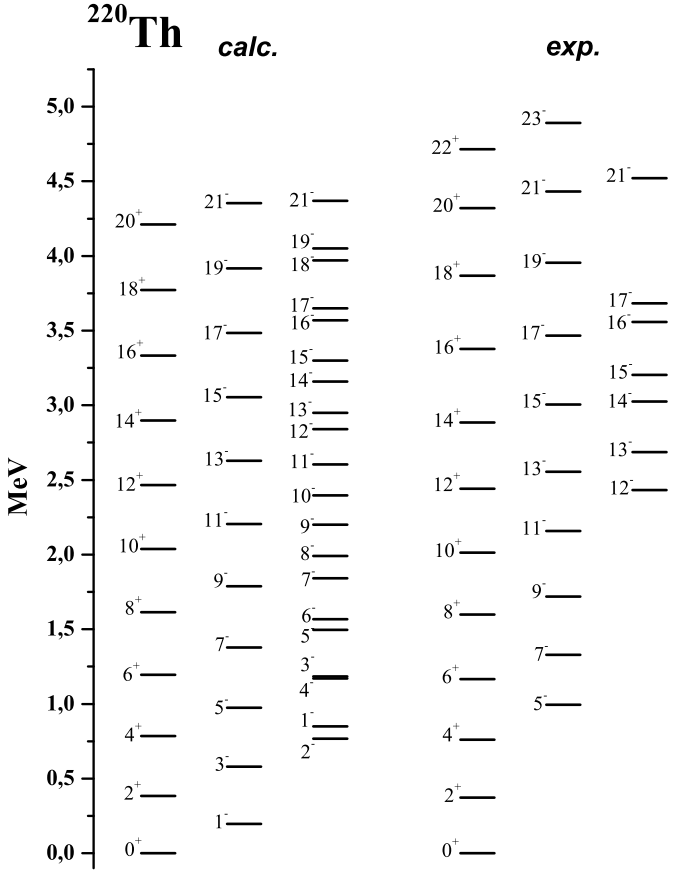

FIGURE 2. Calculated and experimental level scheme of ^{220}Th. Experimental energies, spin and parity assignments are taken from [14].

This introduces a small nonlinear dependence of the γ-transition energies on the angular momentum.

The same equidistant structure with the frequency slightly growing with angular momentum holds for the first negative parity band. Again, the calculation shows that mainly two eigenstates of $\hat{H}_0$ are present in the wave function. Namely, $\left[|\frac{I-1}{2}\frac{I-1}{2}(I-1))\times Y_1\right]_{(IM)}$ and $\left[|\frac{I+1}{2}\frac{I+1}{2}(I+1))\times Y_1\right]_{(IM)}$. The contribution of the later component while being small at I=0 is growing with angular momentum. The energy differences between the states in the negative parity band at low angular momentum are again determined mainly by the frequency of the quadrupole oscillations of the heavy fragment.

The angular momentum dependence of the frequency $\omega_{vib} = E_\gamma/2$, defined as a half of the energy difference between the energies of two neighborhood levels of the ground state band and of the first excited negative parity band is illustrated in Fig.3. One can see the sharp decrease of the experimental values of E_γ for the transition $10^+ \to 8^+$ in the ground state band and for the transition $13^- \to 11^-$ in the negative parity band which can be a consequence of the backbending phenomena. The backbending in these bands can be related to a rotational alignment of the nucleonic orbitals as it is mentioned in [14].

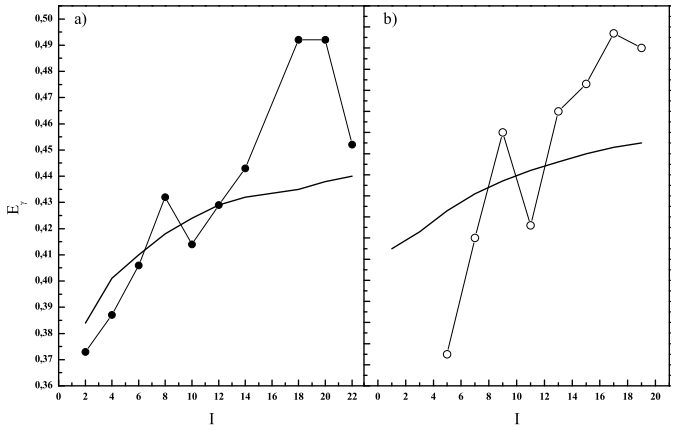

FIGURE 3. Calculated (line) and experimental (solid circles connected by lines) energies of γ transitions between subsequent levels of the ground state band (a) and the first negative parity band (b). Experimental values are taken from [14].

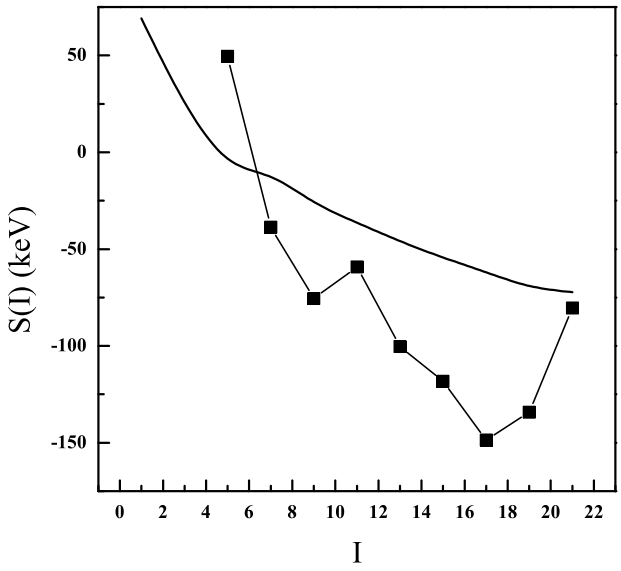

FIGURE 4. Calculated (lines) and experimental (solid squares connected by lines) values of parity splitting (see Eq.(37)). Experimental values are taken from [14].

The model considered above does not provide a mechanism which could be responsible for the experimentally observed behavior of the γ-transition energies. However, it is seen from Fig. 3 that the interval of variation of ω_{vib} with angular momentum observed experimentally and obtained in calculations is not large. The frequencies vary from 185 keV to 240 keV. By taking into account the length of the spectra in both energy and angular momentum, we see that the frequency can be treated with a good accuracy as a constant.

Dependence of the experimental and calculated values of a parity splitting in the ground state and the first negative parity bands, treated as a unified alternating parity

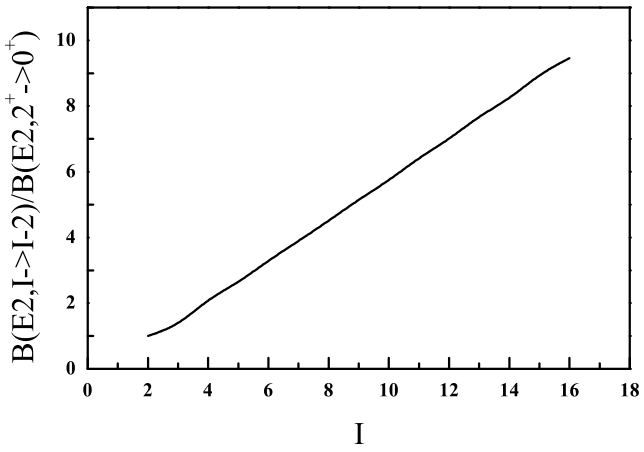

FIGURE 5. Angular momentum dependence of the ration of the reduced transition probabilities $B(E2, I \to (I-2))/B(E2, 2^+ \to 0^+)$ for the quadrupole transitions between the subsequent levels in the ground state band and the first negative parity band.

band, on angular momentum is illustrated in Fig.4. The parity splitting is defined by the expression [14]

$$S(I^-) = E(I^-) - \frac{(I+1)E^+_{(I-1)} + IE^+_{(I+1)}}{2I+1}. \tag{37}$$

It is seen from the figure that for the low angular momenta the parity splitting is positive and becomes negative with angular momentum increase. The possibility for the negative values of the parity splitting is related to the fact that the ground-state band and the first negative parity band are of the vibrational type. In this case the sign of the parity splitting is determined by the difference in the energies characterizing the quadrupole vibrations of the heavy fragment and the rotation of the light fragment around the heavy one. Indeed, in the zero approximation $E(I^-) = \frac{1}{2}\omega(I-1) + \frac{\hbar^2}{2\mu R^2}$, $E(I^+) = \frac{1}{2}\omega I$ and therefore $S(I^-) = \frac{\hbar^2}{2\mu R^2} - \frac{1}{2}\omega\frac{2I}{(2I+1)}$. Thus, for $\frac{\hbar^2}{2\mu R^2} < \frac{1}{2}\omega$, $S(I^-)$ can take negative values. In the case of the rotational bands, the value $S(I)$ must stay positive, achieving a zero value for the ideal unperturbed rotational bands of a nucleus with a stable octupole deformation.

The important feature of the spectra is an appearance at low energy of the second excited negative parity band which contains the states of the even and odd angular momenta. This band has an interesting features. The state with angular momentum I=2 is lower than the state with I=1. With increase of angular momentum the normal level sequence is restored. The reason for such a behavior is related to a significant contribution of the states $\left[|\frac{I+1}{2}\frac{I+1}{2}(I+1))\times Y_1\right]_{(I+1,M)}$ and $\left[|\frac{I+1}{2}\frac{I+1}{2}(I+1))\times Y_1\right]_{(I+2,M)}$ into the wave functions for even and odd angular momenta, respectively. In the limit of $\hat{V}_{int}$ is going to zero these two states become degenerate.

It is assumed above that the intrinsic excitations of the heavy cluster are described by the quadrupole harmonic oscillator model. We know that an excitation spectrum generated by this model is characterized by a high degree of a degeneracy. So, it is

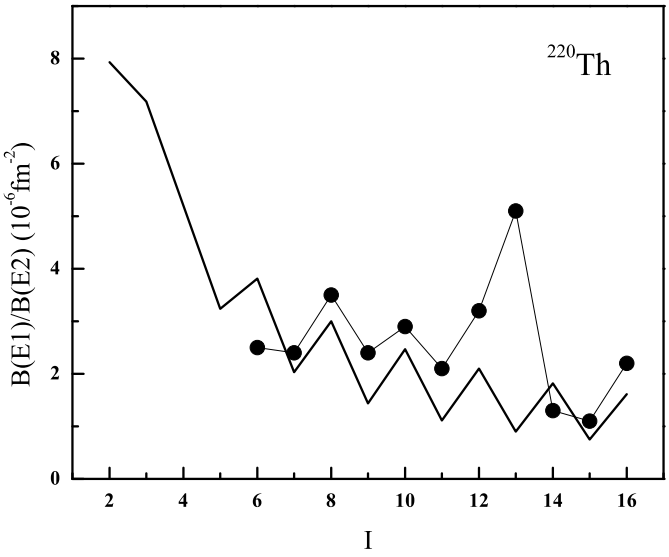

FIGURE 6. $B(E1)/B(E2)$ ratio as a function of the initial angular momentum for transitions in the ground and the first negative parity bands. Experimental values (filled circles) are taken from [14].

interesting to know to what extent the traces of these degeneracies are seen in the spectrum generated by the full Hamiltonian which contains also the interaction term.

First of all, it is interesting at what excitation energies appears the second excited 2^+ state and the first excited 0^+ state which has the same excitation energy as the 4_1^+ state in the case of the quadrupole harmonic oscillator. For ^{220}Th we obtain $\mathrm{E}^*(2_2^+)$=1161 keV and $\mathrm{E}^*(0_2^+)$=896 keV. For the $\mathrm{E}^*(4_1^+)$ we have 717 keV.

Experimentally the excited bands of the positive parity have not been observed in ^{220}Th. There are known 10^+ and 8^+ states with the excitation energies around 2 MeV. However, it is not clear either these states are two-quasiparticle or they belong to the excited rotational bands. Thus, the experimental information on the excitation energies of the 2_2^+ and 0_2^+ states and on their characteristics is very important for the check of the suggested model.

In Fig.5, the values of the ratio $B(E2, I \to I-2)/B(E2, 2^+ \to 0^+)$ are presented as a function of the initial angular momentum. As it should be in the case of harmonic quadrupole oscillations of the heavy fragment the values of $B(E2)$ increase linearly with I. They does not show any changes in the behavior for transitions between the members of the ground-state band and the first negative parity band since the underlying quadrupole constituents in both bands are the same. Thus, the experimentally observed staggering of the $BE1/BE2$ ratios can be attributed to the staggering of the $B(E1)$ values (see Fig. 6).

Such a staggering behavior of $B(E1)$ can be qualitatively explained analyzing the equation (36). We can see that the reduced transition probability B(E1) for the transition from the state I of the ground state band to the state (I-1) of the first excited negative parity band consist of two contributions, since both dipole transitions are allowed (see Eqs.(19,22)): from the component $\left[|\frac{I}{2}\frac{I}{2}(I)) \times Y_0\right]_{(IM)}$ to $\left[|\frac{I}{2}\frac{I}{2}(I)) \times Y_1\right]_{(I-1,M)}$ and from

the component $\left[|\frac{I-2}{2}\frac{I-2}{2}(I-2))\times Y_2\right]_{(IM)}$ to $\left[|\frac{I-2}{2}\frac{I-2}{2}(I-2))\times Y_1\right]_{(I-1,M)}$. In the opposite case of transition from the states of the negative parity band to the states of the positive parity belonging to the ground state band, we have only one allowed transition, namely, from the component $\left[|\frac{I}{2}\frac{I}{2}(I))\times Y_1\right]_{(I+1,M)}$ to the component $\left[|\frac{I}{2}\frac{I}{2}(I))\times Y_0\right]_{(I,M)}$. The transition from $\left[|\frac{I+2}{2}\frac{I+2}{2}(I+2))\times Y_1\right]_{(I+1,M)}$ to $\left[|\frac{I-2}{2}\frac{I-2}{2}(I-2))\times Y_2\right]_{(I,M)}$ is forbidden because the dipole operator does not change a number of the quadrupole phonons.

The $B(E1)/B(E2)$ ratio as a function of an initial angular momentum is presented in Fig.6. Calculated ratios for the odd initial angular momentum (i.e. for transitions from the states of the negative parity) lie systematically lower than the ratios for the even initial angular momentum (transitions from the state of the ground state band). This is in agreement with the experimental data with the exception of two data points at 13^- and 14^+ . As it is mentioned in [14] the large value of $B(E1)/B(E2)$ ratio at 13^- can be attributed to the loss of $E2$ strength in the backbending. The rather small $B(E1)/B(E2)$ value for the 14^+ attributed to the spread of $E1$ strength due to the presence of two 13^- final states.

CONCLUSION

We have suggested a cluster interpretation of the properties of the multiple negative parity bands in ^{220}Th. The collective motion related to the cluster degree of freedom leads to the admixture of the very asymmetric cluster configurations to the intrinsic nucleus wave function. To take into account the reflection asymmetric modes with nonzero values of K, the harmonic quadrupole oscillations of the heavy cluster is considered. The resulting energy spectrum consists of the ground state band and several negative parity bands which exhibit nearly equidistant behavior. The angular momentum dependence of the parity splitting is described. The possibility for the negative values of the parity splitting is related in the model to the interplay between the quadrupole vibrations of the heavy fragment and the rotational motion of the light fragment. We describe the observed staggering behavior of the $B(E1)/B(E2)$-rations as a function of the angular momentum. The $BE(1)$ transitions from the state of the negative parity to the state of the positive parity is hindered, in this case in a contrast to the transitions from the positive to the negative parity state the $E1$ transition operator relates only a part of the components of the wave functions of the bands. The results of calculations are in overall agreement with the experimental data. This work is a further development of the previously developed approaches [7, 10, 11].

REFERENCES

1. P. Butler and W. Nazarewicz, *Rev. Mod. Phys.* **68**, 349 (1996).
2. F. Iachello and A.D. Jackson, *Phys. Lett.* **B108**, 151 (1982).
3. W.D.M. Rae, *Int. J.Mod. Phys.* **A3**, 1343 (1988).
4. M.Freer, A.C. Merchant, *J.Phys.* **G23**, 261 (1997).
5. W. Nazarewicz, J.X. Saladin et al., *Phys. Lett.* **B322**, 304 (1994).
6. S. Aberg, L.-O. Jonsson, *Z. Phys.* **A349**, 205 (1994).

7. T.M. Shneidman et al. *Nucl. Phys.* **A671**, 119 (2000).
8. Ch. Briancon, and I.N. Mikhailov, in *Proc. Int. Conf. on Nucl. Structure, Reactions and Symmetries*, edited by R. A. Meyer and V. Paar, World Scientific, Singapore, 1986, v.1, p.131.
9. S. Frauendorf, *Phys. Rev.* **C77**, 021304(R) (2008).
10. T.M.Shneidman, G.G.Adamian, N.V.Antonenko, R.V.Jolos, *Phys.Rev.* **C74**, 034316 (2006).
11. T.M.Shneidman, G.G.Adamian, N.V.Antonenko, R.V.Jolos, W.Scheid, *Phys.Rev.* **C67**, 014313 (2003).
12. G.G.Adamian, N.V.Antonenko, R.V.Jolos, Yu.V.Palchikov, W.Scheid, T.M.Shneidman, *Phys.Rev.* **C69**, 054310 (2004).
13. G.G.Adamian, N.V.Antonenko, R.V.Jolos, Yu.V.Palchikov, W.Scheid,*Phys.Rev.* **C67**, 054303 (2003).
14. W. Reviol et al., *Phys. Rev.* **C74**, 044305 (2006).
15. W. Nazarewicz, G.A. Leander, and J. Dudek, *Nucl. Phys.* **A467**, 437 (1987).
16. T. Otsuka, and M. Sugita, *Phys. Lett.* **B209**, 140 (1988).
17. G.G. Adamian, N.V. Antonenko, R.V. Jolos, S.P. Ivanova and O.I. Melnikova, *Int. J. Mod. Phys.* **E5**, 191 (1996).
18. W.Bonin et al., *Z. Phys.* **A322**, 59 (1985).
19. N. Schulz et al., *Phys. Rev. Lett.* **63**, 2645 (1989).

SESSION: NUCLEAR REACTIONS

Chairpersons: R.V. Jolos and F. Šimkovic

Web knowledge base on low-energy nuclear physics

A. S. Denikin[*,†], V. I. Zagrebaev[†], A. V. Karpov[†], A. P. Alekseev[**], N. M. Jacobs[‡] and T. S. Maluleke[‡]

[*]*Dubna International University, Dubna, 141980, Moscow region, Russia*
[†]*Flerov Laboratory of Nuclear Reactions, JINR, Dubna, 141980, Moscow region, Russia*
[**]*Chuvash State University, Tcheboksary, 428015, Chuvash Republic, Russia*
[‡]*University of Stellenbosch, Private Bag X1, Matieland 7602, South Africa*

Abstract. The Web knowledge base on low-energy nuclear physics is described. The project is aimed at developing models and corresponding computing codes for comprehensive theoretical analysis of experimental data on low and intermediate energy nuclear reactions. Accumulated knowledge base experimental data and computational codes are available on web-servers http://nrv.jinr.ru/nrv/ and http://nrv.sun.ac.za/ with free accessibility to any remote user through any web-browser of choice.

Keywords: Nuclear models, simulation of nuclear reaction, nuclear experimental data, data analysis, web-software.
PACS: 29.85.-c, 29.50.+v, 29.87.+g, 07.05.Rm, 07.05.Tp

INTRODUCTION

Over the past hundred years progress in nuclear physics has generated a vast amount of the experimental data both on nuclear properties and on reactions induced by nuclear particles. This data currently resides in literature or in special databases. Advances in internet technology has however led to the development of Web based nuclear databases in recent years. These nuclear databases, as a rule, supply users with ordinary text files of tabular information are limited to specific information of a specific type. An example of this is the web-server http://depni.sinp.msu.ru/cdfe supported by the Center for photonuclear experiments data (INP MSU, Moscow) that provides an access to a number of databases on properties of atomic nuclei and their interaction with elementary particles, on giant dipole resonance parameters, on nuclear scientific reference data and others. Part of these databases were adopted from the data-servers in Lawrence Berkeley National Laboratory (http://ie.lbl.gov/) and Brookhaven National Laboratory (http://www.nndc.bnl.gov/), which also provide access through the Internet. Similar data archives were organized on the site of the Nuclear Energy Agency (http://www.nea.fr/dbdata/). V.G.Khlopin Radium Institute in collaboration with the U.S. Department of Energy, where a gamma ray spectra catalog (http://www.atom.nw.ru/ skv/) has been developed. The Nuclear Data group at the Triangle Universities Nuclear Laboratory (http://www.tunl.duke.edu/nucldata/index.shtml) is responsible for the evaluation of light nuclei within the United States Nuclear Data Network and the international Nuclear Structure and Decay Data Evaluators Network.

The databases cited above form part of a long list web based databases currently available.

Certainly cumulative data and its free accessibility assist in the day-to-day work of a modern nuclear physicist. However, variety of data requirements, for example, in the case of planning new experiments results in the work consisting of the following steps. Firstly, a search for available experimental data in the databases. Secondly processing the collected data, in some cases this includes the analysis of the data within appropriate theoretical model. Thirdly, simulation of experiment and choice of effective parameters of the experimental set-ups. Fourthly, when the experiment is completed, the measured data have to be processed and analyzed with the help of the modern physical approaches. All these steps require considerable amount of time, resources and experience.

In order to simplify this work our Web based database system combines databases on nuclear properties and experimental cross sections of nuclear reactions along with computer codes of theoretical models in a unique system which we name the Knowledge Base on Low Energy Nuclear Physics. The system can be accessed on the web-servers http://nrv.jinr.ru/nrv/ (FLNR JINR, Russia) and http://nrv.sun.ac.za/ (Stellenbosch University, South Africa). The nuclear physics Knowledge base adresses the following two problems . (i) Fast and visual access of experimental data on nuclear structure and cross sections of nuclear reactions, a possibility for processing and systematization of these data, their comparison and plotting of the studied regularities. (ii) Analysis of experimental data and modeling of the processes of nuclear dynamics within the modern foolproof codes based on the well-established physical approaches all in a window of a Web-browser. A set of coupled algorithms of nuclear dynamics, experimental data bases on nuclear structure and nuclear reactions, and a system of special net codes for analysis, management, representation and handling of user's queries and obtained results of calculations form altogether what is usually called "knowledge base".

KNOWLEDGE BASE ON LOW ENERGY NUCLEAR PHYSICS

Our Knowledge base differes from the current existing nuclear databases in three distinct ways. (i) In addition to the text information, the Knowledge base contains special programs for graphic representation of data, performs comparative analysis of the data and provides systematics of all kinds over a group of nuclei or the whole nuclear map. (ii) Our databases on the experimental cross sections of nuclear reactions contain the digitized data. Besides significant simplification of their control, this allows one to perform overall processing these data, make graphical comparison of the cross sections with each other and, finally, analyze these data within theoretical models. All these actions are made in the window of any Web-browser without installing any additional computational codes and graphical packages. (iii) The complicated computational programs of modeling the low-energy nuclear dynamics form the main part of the developed system. Taken together with the experimental data on nuclear properties they form the "nuclear knowledge base". As far as we know, for the first time, the complicated computational codes of modeling nuclear dynamics featuring a graphical interface for visual display of data input and graphical representation and also handling of the obtained results in the window of Web-browser, are available in the Internet without a necessity on the part

TABLE 1. Components of the Knowledge base on low energy nuclear physics

Nuclear Map: nucleus property data*	**Nuclear reaction data**	**Nuclear models, Nuclear decay**	**Nuclear reaction models**
Spin, parity, abundance	HI elastic scattering	Shell model	Elastic scattering (Optical mode,
Half-life, decay modes	HI complete fusion	Nuclear fission	Classical model)
Nuclear masses	Evaporation residues	Decay of excited nuclei	Inelastic scattering (DWBA)
Excited states			Heavy-ion fusion (Coupled channel
Metastable states			model, Empirical model)
Nuclear radii			Evaporation residues formation
Nuclear radii			(Monte-Carlo)
G.s. deformations			Driving potential
Electro-magnetic properties			Nuclear reaction kinematics (2-body,
			3-body, Q-calculator)

* Most of experimental data are taken from National Nucleur Data Center, http://www.nndc.bnl.gov

of the user to download any of the programs. Beside easiness and convenience of use, this method allows unifying,analysis and processing of the experimental data within the well-established standard models.

The functioning components of the knowledge base are listed in Table 1. Below we give a short description of its main parts.

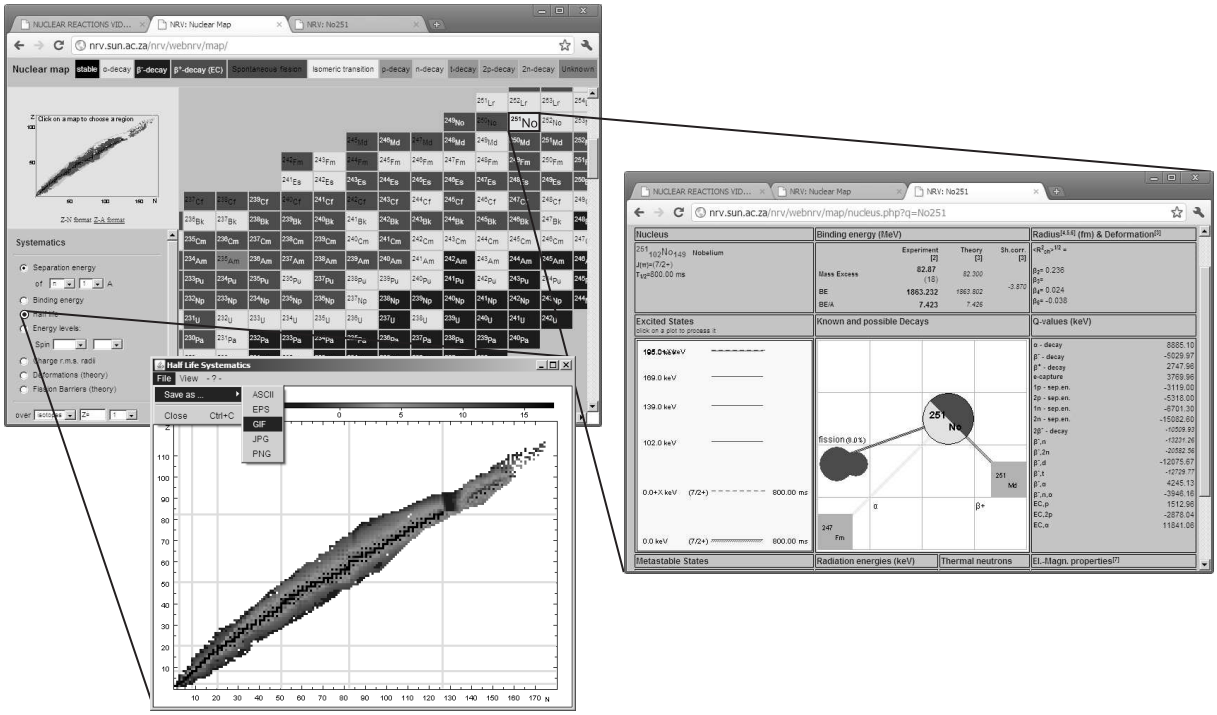

FIGURE 1. Nuclear Map – the databases on properties of an individual atomic nucleus in combination with special software for graphic representation of the data, performing their comparative analysis and obtaining systematizations of all kinds over a group of nuclei or the whole nuclear map.

Nuclear Map and Nuclear Reaction Data

Nuclear Map is a part of the knowledge base combining few databases on all kinds of nucleus properties (see Table 1) adopted from different sources [1, 2, 3, 4, 5, 6, 7]. The Nuclear Map is organized in form of the hypertext table where each cell (colored in correspondence with the main decay branch) represents the web-link to the page with detailed information on the properties of corresponding atomic nucleus. It is demonstrated in Fig. 1 (right side). In particular, on this page user may find the data on spin and parity of the ground state of the nucleus, its binding energy and mass, charge radius and ground state deformations, Q-values of possible decays. Information on observed decay branches (with their probabilities) and structure of excited states are shown also in graphical form (see Fig. 1). Finally, user obtains the data on metastable states, known γ-radiation energies, the capture cross section of thermal neutron, and additional electromagnetic properties (magnetic momentum, transition probabilities and others).

In a number of cases it is necessary to compare certain characteristic over a group of nuclei. This possibility is also realized in the Nuclear Map. With the help of a friendly interface user may send a corresponding query to the Knowledge base. It results in a web-page with the required data in graphical form. In Fig. 1 (at the bottom), in particular, the nuclear half-life systematics is shown over all nuclear map. It is important to mention that data are shown in separate Java window which has its own menu (see Fig. 2) and provides the user with the possibility to process obtained data and, in particular, to save

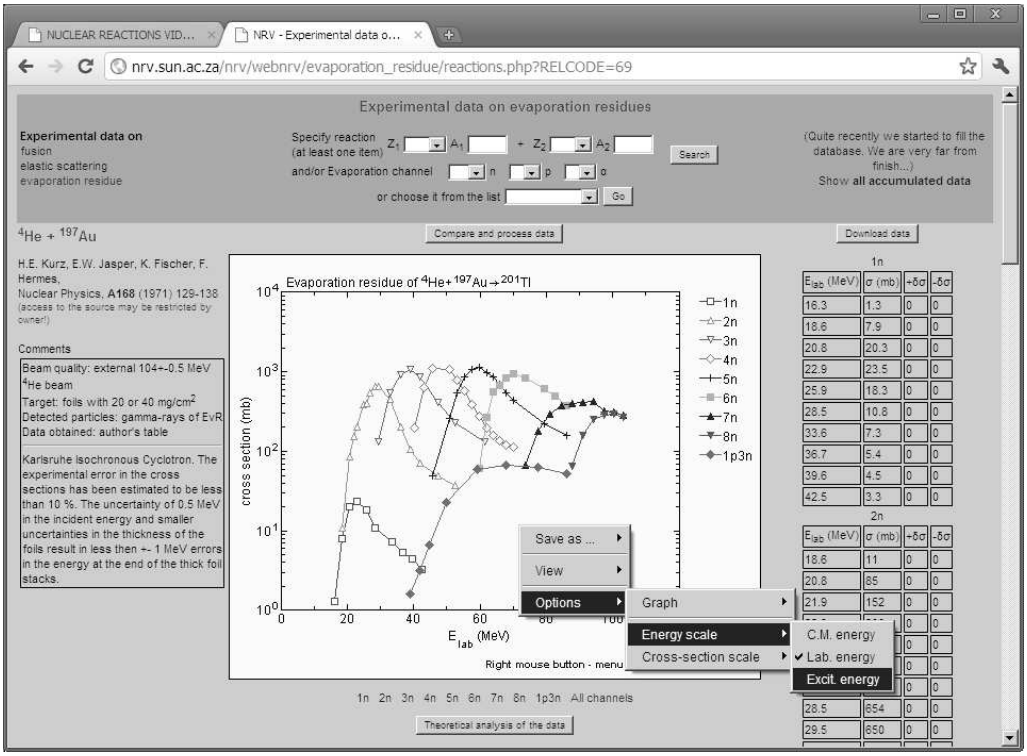

FIGURE 2. Experimental data on cross section of evaporation residue formation in reaction ^{4}He + ^{197}Au → ^{201}Tl. Besides the cross section values the database contains information on authors, original source of the data and details of experimental procedure. All information is downloadable in text or graphical format.

it in textual (ASCII), bitmap (GIF, JPG, PNG) or post-script (EPS) format. The wide use of Java applets makes the Knowledge base handy for the subsequent data processing. The applets allow one to realize just within Web-browser window all the possibilities like an application installed in a user computer.

The Knowledge base also includes databases on the cross sections of nuclear reactions. Among them are (i) the elastic scattering cross sections for the reactions induced by light nuclei (with mass A<20), (ii) the heavy-ion complete fusion cross section and (iii) the evaporation residues cross sections. Last two databases are unique ones. They contain experimental points, reference data and detailed information of the measurement procedure (beam characteristics, target conditions, experimental set-up, measured products and others). The information for these databases were obtained either by digitizing corresponding tables and plots published in main nuclear physical journals or directly from authors. We covered a period of time from 1970 up to present days and keep the databases in up-to-date state. At the moment the databases consist data on more then 1600 reactions, i.e. about 15 000 experimental points. As an example the data on the evaporation residue cross section for the reaction ^{4}He + ^{197}Ag for various channels are shown in Fig. 2.

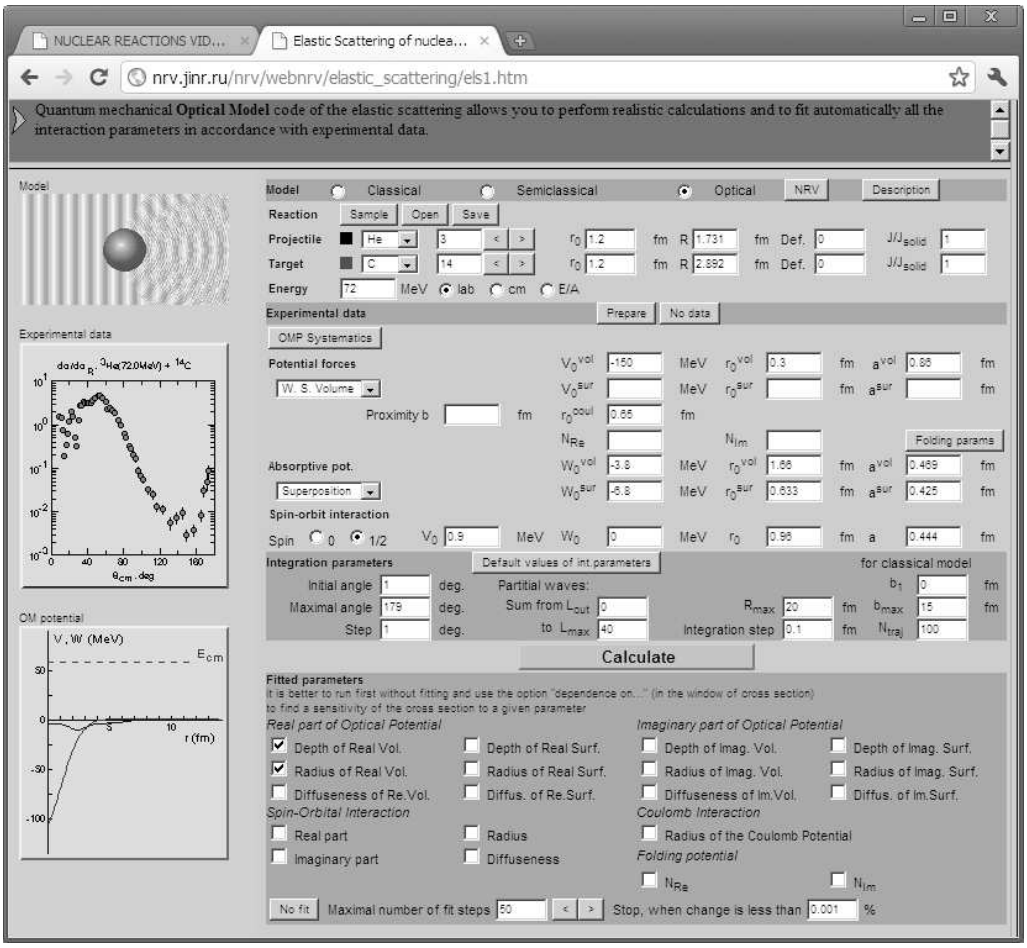

FIGURE 3. Web-form for preparation of the optical model parameters – reaction partners, collision energy, experimental data, optical model potential, integration and fitting parameters.

Nuclear Models and Nuclear Reaction Models

It was mentioned above that one of the main features of the Knowledge base is the possibility to run the computer codes modeling nuclear reaction dynamics. The theoretical models available at the moment in the Web Knowledge base are listed in Table 1. We include on the Knowledge base only the well-established models either coded by us or adopted from the open sources (distributed by author, published or stored in approved code-banks). Originally these codes are the Fortran text supplied with complicated manuals describing the structure of input file. Often the preparation of the input turns out to be difficult even for an experienced user with good knowledge the theoretical approach in detail.

In order to avoid these difficulties we have developed a comprehensible web-form which allows the user to define all input parameters for each theoretical model included to the Knowledge base. As an example such a web-form is shown in Fig. 3. Using this form user may prepare parameters and run the calculation of the differential cross

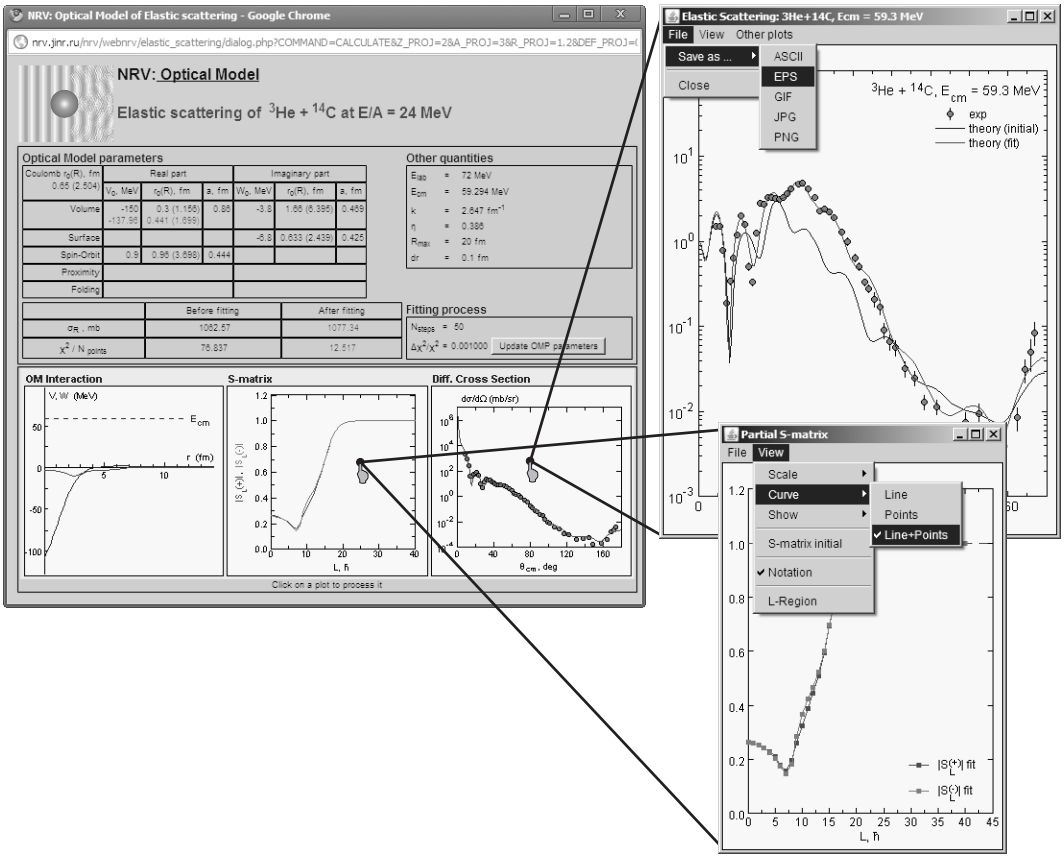

FIGURE 4. Web page with the results of the optical model calculation performed within the Knowledge base for ^{3}He + ^{14}C elastic scattering at the laboratory energy $E = 72$ MeV. Java applets represent data in graphical form and provide additional possibilities to process the obtained results.

section of nuclear elastic scattering. Working with the model user may obtain advices on the optical model parameters based on published systematics or may perform automatic fit in order to find the optimal choice of the parameters. Optionally user may choose different types of the optical potential, such as Woods-Saxon volume or surface potential and their superposition, proximity potential and DDM3Y folding potential. It is possible to request the experimental data on elastic scattering available in the corresponding database of the Knowledge base or to input user's own data. The short theoretical description and main references are also given. The input information is visualized with the help of Java applet incorporated into the web-form (see Fig. 3). Altogether the web-form elements provide friendly interface for parameter preparation and subsequent running the optical model code. Work within all the models of the Knowledge base are organized in the same way.

Basing on the model parameters defined by user the system creates input file and runs the calculation code. All codes of the Knowledge base are run on the sever side only. User does not need to download and to install any executable files on his/her computer. Special services (combination of Java applet and server-side service program) inform user on the calculation progress and show intermediate results. This scheme allows us

to run a long-time calculation such as a couple-channel model of heavy-ion fusion, for example, and to be sure in getting the results even after many-hours of computation. Note also that all user's data (input parameters, experimental data and others) are stored on the Knowledge base server in unique directory which is not accessible for other users.

When calculations are completed, the user obtains a final web-page which contains the results in text and graphical representation. In particular, Fig. 4 demonstrates the result of the optical model calculation of elastic scattering for ^{14}C(^{3}He,^{3}He) reaction at E_{lab} = 72 MeV. One may see the initial parameters and the fitted ones, the total reaction cross section and some reaction characteristics. Java applets in this web-page give a visual representation of the optical model interaction, elastic S-matrix elements and elastic scattering differential cross section. These Java applets are not static elements. By clicking on the Java applet the user activates a separate Java window with menu including many additional options for processing the obtained results. Particularly, in the Java window showing the elastic scattering cross section the user is able to change the scale of the graph, transform cross section to the laboratory or center of mass system, plot cross section as a ratio to the Rutherford cross section and so on. The S-matrix also can be replotted in different forms and different scales. One of the most important options available in all the Java windows of the Knowledge base is a possibility to save the obtained results to user's hard-disk for further use. As it can be seen in Fig. 4 we realize a possibility to save data both in text and graphical form.

The Knowledge base includes also Java classes for representation of 3-dimensional objects. They are very useful in the case of plotting the multi-dimensional functions like a nucleus-nucleus driving potential, shell-model nucleon wave functions, 3-D total scattering wave function and others. In Fig. 4 (at the left), for instance, the 3-D scattering wave function is shown for ^{3}He + ^{14}C elastic scattering at $E_{\rm lab}$ = 72 MeV.

In addition to the obvious scientific application, the Knowledge base has an educational aspect as well. For instance, within the optical model we realize a tool that allows a study of the dependance of the elastic scattering cross section on different parameters of optical potential. By varying the optical model parameters and observing the corresponding changes on the structure of the angular distribution, the student gets a feel of the sensitivity of differerent parametes of the optical potential. In Fig. 5 (at the right) the curves demonstrate the cross section calculated with the optical potentials different by the value of radius of its real part. One can see the shift and stretch of the interference structure of the angular distribution which can be easily related with the change of the size of the scattering field. Thus, basing on the descriptions of theoretical models and on the tools realized in different components of the Knowledge base one may develop a series of practical exercises for students studying nuclear physics.

PERSPECTIVES

Recently a mirror server of the Knowledge base was placed in operation at Stellenbosch University (South Africa). Within this collaboration we are going to develop the Knowledge base in order to give theoretical support to the experimental studies which are planned or already performed in the laboratories of South African institutes, particularly, in the iThemba LABS. Among new components of the Knowledge base it is worth

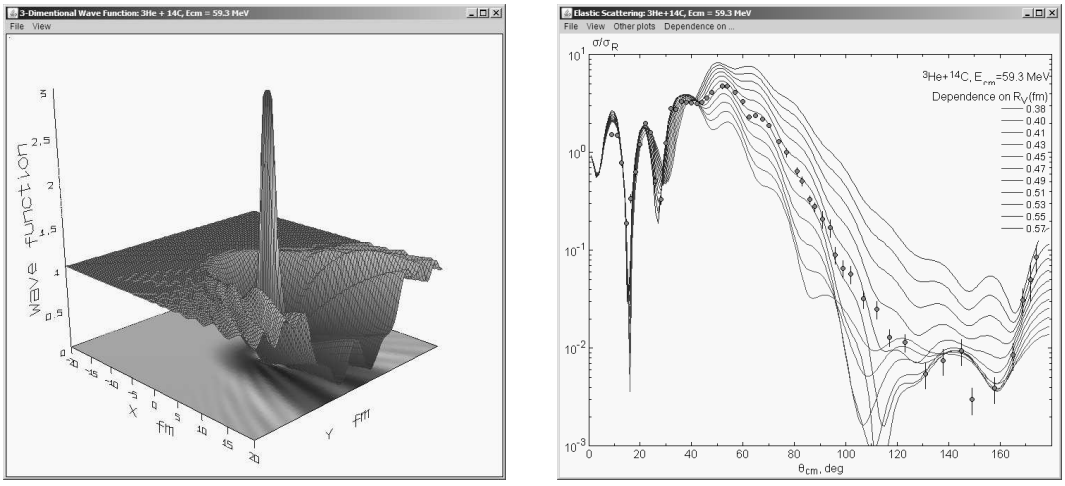

FIGURE 5. (Left) With the help of the optical model code user can calculate, plot and save a 3-D total scattering wave function. The wave function is calculated for ^{3}He + ^{14}C elastic scattering at $E_{\rm lab}$ = 72 MeV. (Right) The optical model code provides the possibility to investigate the influence of the optical model parameters on the elastic scattering angular distribution. In figure the dependence on the radius R_V of the real part of the optical potential is shown for ^{14}C(^{3}He,^{3}He) reaction at $E_{\rm lab}$ = 72 MeV.

mentioning the computer codes for the simulation of nuclear reaction experiments taking into account the detectors loading by the elastic scattering and inelastic events, effects of multiple scattering in a target sample, and providing the information on kinematical properties of future experiments.

We also plan to extend the Knowledge base with the following elements: (i) computer codes for the calculation of energy dependence of reaction cross section, (ii) codes for calculation of the inelastic scattering and transfer reactions in heavy-ion collisions within semiclassical approximation, (iii) codes for the phase shift analysis of resonant scattering of light nuclei, (iv) calculation of radioactive capture cross section at low astrophysical energies, (v) description of properties of different nuclear decay modes, (vi) creation and filling of new databases on nuclear properties, in particularly, databases on reduced transition probabilities $B(E\lambda)$ for heavy ions, and others.

ACKNOWLEDGMENTS

The project was supported by Russian Foundation for Basic Research within grant 09-07-00281-a and by grant of Department of Science and Technology of South African Republic.

REFERENCES

1. National nuclear data center, Brookheven National Laboratory (2010), http://www.nndc.bnl.gov.
2. G. Audi, and A. H. Wapstra, *Nucl. Phys. A* **595**, 409 (1995).
3. P. Moller, J. R. Nix, W. D. Myers, and W. J. Swiatecki, *At. Dat. Nucl. Dat. Tab.* **59**, 185 (1995).
4. E. G. Nadjakov, K. P. Marinova, and Y. P. Gangrsky, *At. Dat. Nucl. Dat. Tab.* **56**, 133 (1994).

5. I. Angeli, *Heavy Ion Physics* **8**, 23 (1998).
6. N. J. Stone, Table of nuclear magnetic dipole and electric quadrupole moments, Brookheven National Laboratory (2001), http://www.nndc.bnl.gov/nndc/stone_moments/.
7. G. Fricke, and K. Heilig, *Nuclear Charge Radii, Group I: Elementary Particles, Nuclei and Atoms*, vol. 20, Landolt and Bornstein, 2004.

On the analysis of two-dimensional distributions of experimental variables in heavy ion physics

D.V. Kamanin[*], Yu.V. Pyatkov[*,†], O.V. Falomkina[*,**], Yu.P. Pytyev[**], B.M. Herbst[‡] and W.H. Trzaska[§]

[*]*Joint Institute for Nuclear Research, 141980 Dubna, Moscow Region, Russia*
[†]*National Nuclear Research University MEPHI, 115409 Moscow, Russia*
[**]*Lomonosov Moscow State University, Physics Faculty, Computer Methods in Physics Division, 119899, Russia*
[‡]*University of Stellenbosch, Applied Mathematics, South Africa*
[§]*Department of Physics of University of Jyväskylä, Finland*

Abstract. We study the theoretical description of many nuclear reactions where the evolution of the nuclear system is described as a trajectory in multidimensional deformation space. We propose a strategy for revealing the trajectories in the space of experimental observables, at prescribed confidence levels.

Keywords: potential energy surface in the space of nuclear deformations, nuclear fission modes, morphological methods of image analysis
PACS: 25.70.Jj; 25.85.-w

In an earlier study we proposed a novel approach for extracting information from known mass-energy distributions of the nuclear reaction products by processing the $2D$ data directly [2]. A typical $M-E$ fragment distribution, for instance in the $^{233}U(n_{th},f)$ reaction, looks like at first sight like a smooth hill. Closer inspection shows that each $E = const$ slice of this distribution (see Fig. 1) is not absolutely smooth but rather display local irregularities (peaks), as indicated by the arrows.

The origin of the peaks becomes clear from the following considerations. The yield $Y(M|E)$ of the fission fragment (FF) with mass M at a fixed value of E is equal to,

$$Y(M|E) = \sum_{Z} Y(M,Z|E) \tag{1}$$

The marginalization in expression (1) is done over all possible values of the FF nuclear charge Z. Thus, the spectrum shown in Fig. 1 is a superposition of the partial mass spectra at fixed charges (so called isotope distributions) known from experiments [3]. Let us define the term: "fine structure" (FS). By definition, it is the local areas (peaks) of the $2D$ distribution indicating increased yields of FFs above a smooth background. As can be inferred from Fig. 1 the FS in this case is due to larger yields of the even-charged FFs. It is the well-known "odd-even staggering", based on proton pairing [1]. The peaks in the adjacent sections $E = \text{const}$ are correlated, forming regular structures on the $E-M$ plane in the form of ridges parallel to the E-axis [3]. Henceforth this structure will be referred to as "vertical ridges".

We pose the question, is there any fine structure in the FF mass-energy distribution, different from the vertical ridges produced by odd-even staggering and caused, conse-

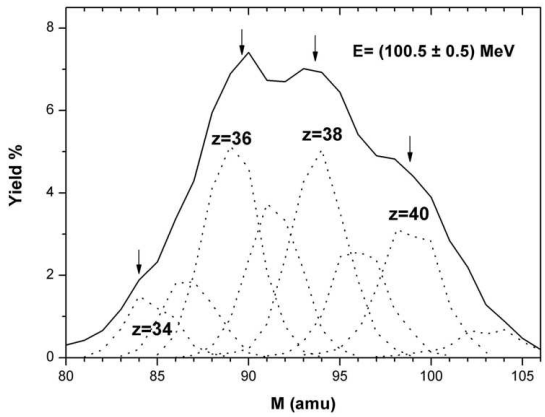

FIGURE 1. Section of the $E-M$ distribution for the energy of the fragment $E=(100.5\pm0.5)$ MeV [3]. The partial yields for the fixed nuclear charges are shown by dot lines.

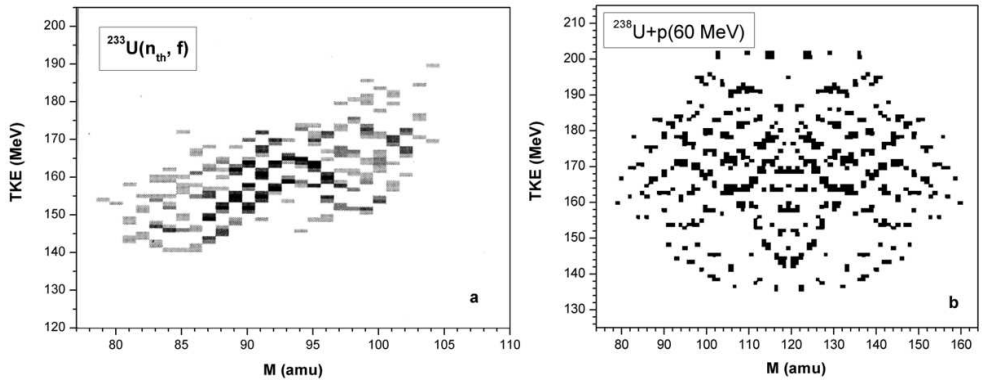

FIGURE 2. Snake-like FS exhibited by the TKE-M distributions of fragments from the reactions $^{233}U(n_{th},f)$ (a) and $^{238}U+p$ (60 MeV) (b). See text for details.

quently, by different physical processes? In order to automatically suppress the vertical ridges while searching for the fine structure, the sections $M=$ const are investigated, known to display local peaks [4, 5]. Methods based both on peak identification algorithms in gamma-ray spectroscopy and stochastic image processing are used in our investigations [2]. Fig. 2 shows examples of the FSs revealed in the total kinetic energy-mass (TKE-M) distributions of the fragments. Initial data were obtained using time-of-flights spectrometers described in [6, 7]. Darker points in the gray scale map (see Fig. 2a) correspond to higher intensities of the effect. Only the lighter mass peaks of the fission fragments are shown.

The symmetry shown in Fig. 2b is due to both the method of measurement of the fragment mass ("two velocities" method [1]), and the filter used [8].

Basically the FS represents a series of snake-like curves sometimes exhibiting bifurcation points [2, 8].

What are the reasons for investigating the specific FS observations? In the modern view, the evolution of the decaying nuclear system, for instance in fission, is mainly

determined by the potential energy of the system as a function of the parameters of its deformation or, in a $3D$ presentation by a potential energy surface (PES). Distinct potential valleys of the PES [11, 12] give rise to the preferable trajectories (realizations) of the system in the deformation space. As is shown by [13], at any point of the system's descent down the fission valley a scission can appear to occur, indicating a fission event in the space of experimental observables. In other words, the trajectories in the deformation space as a continuous sequence of nuclear states in the fission valley is mapped to continuous trajectories (smooth curves) in the plane of experimental observables [14], choosing the FF total kinetic energy and mass chosen variables in Fig. 2, for example. Thus we believe [15] the FS under discussion to be an image of the distinct fission process.

So far the weak point of the proposed data processing procedure is an absence of a quantitative confidence in the persistence of the extracted FS. Here the problem is exacerbated by the fact that we are looking for a new phenomenon, i.e. no prior knowledge about the shape of the structures is available.

In order to address this difficulty the following approach, based on the morphological methods of image analysis proposed in [9], is developed.

Let $\tilde{f}$ be an experimentally measured signal (i.e., the mass-energy distribution) that can be represented as follows

$$\tilde{f} = S + h + \nu, \tag{2}$$

where S is the image of a smooth "substrate", h a signal that might contain several instances of FSs, and ν additive noise (i.e. generated by some probability density function). At the first stage, the smooth underlying substrate S is extracted from the signal $\tilde{f}$, yielding $f = h + \nu$. Different methods can be used to extract S, using spline interpolation for example [2, 16]. During the second stage, the FS is extracted from the signal f, using methods based on morphological image analysis.

Let us briefly recall some of the definitions of morphological image analysis. An *image* $f(\cdot)$ is a square-integrable, integer valued function on a subset X of the Euclidean plane $\mathscr{R}^2$. X is called the *field of vision*, with $f(x)$ the brightness of the point $x \in X$. In the case under consideration $X = \{x_1, \ldots, x_n\}$, and the images $\tilde{f}(\cdot)$ $f(\cdot)$, $S(\cdot)$, $h(\cdot)$, and $\nu(\cdot)$ of (2) are defined at exactly the same points and are considered to be the elements of the Euclidean plane $\mathscr{R}^n$. The measurement error $\nu \in \mathscr{R}^n$ is considered to be a random image having zero mean, $\mathbf{E}\nu = 0$, and covariance matrix $\sigma^2 I$, where $I \in (\mathscr{R}^n \to \mathscr{R}^n)$ is the identity matrix, with σ^2 unknown.

The image of the FS is written as $\omega(\cdot)$ and is defined on a variable shape, variable size subset Ω of the field of vision X. Let us define the *shape* of the image $\omega(\cdot)$, as the set of images

$$V_\omega = \{\omega(\cdot), \omega(x) = c_1 \chi_{A_1}(x) + c_2 \chi_{A_2}(x),\ \ c_1 \geq c_2,\ \ c_1, c_2 \in \mathscr{R}_1,\ \ x \in \Omega\}, \tag{3}$$

with

$$\chi_{A_i}(x) = 1,\ \ x \in A_i;\ \ \textit{and}\ \ \chi_{A_i}(x) = 0,\ \ x \notin A_i;\ \ (i = 1, 2)$$

V_ω is a convex closed cone in $\mathscr{R}^2$ and in $\mathscr{R}^n$. In this definition A_1 and A_2 are different regions of Ω of constant brightness. According to this definition, the *shape* of the image of an object therefore consists of all images of the object that differ in brightness in regions of Ω of constant brightness.

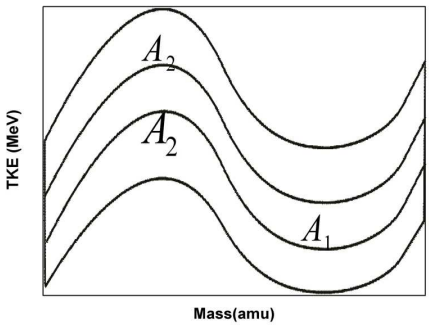

FIGURE 3. Example of regions $A_1, A_2 \subset \Omega$ of constant brightness of an image of the FS

In Fig. 3 regions $A_1, A_2 \subset \Omega$ of constant brightness of a FS image are shown. In this figure, the field of vision is split into regions A_1, A_2, with A_1 the "fine structure" itself, and A_2 the surrounding region. The shape (in the usual sense) and the size of the regions A_1 and A_2 are defined by the researcher. Note that the expected shape is postulated by the user, this procedure returns the confidence in the actual presence of the shape in the image. In our case the the postulated shape is derived from Fig. 2. The brightness of regions A_1 and A_2 are supposed to remain constant. The fact that the brightness at points that belong to the "fine structure" is greater than at surrounding points is reflected by the condition $c_1 \geq c_2$ in (3).

The projection P, defined below, of some image $g(\cdot)$ defined on Ω, onto the shape V_ω is the image $(P_{V_\omega} g)(\cdot)$. It exists and is unique, because V_ω is convex closed cone (see [9]),

$$(P_{V_w} g)(x) = \hat{c}_1 \chi_{A_1}(x) + \hat{c}_2 \chi_{A_2}(x),\ x \in \Omega, \tag{4}$$

where $\hat{c}_1, \hat{c}_2$ are the solutions of the following minimization problem,

$$\int_\Omega (g(x) - \hat{c}_1 \chi_{A_1}(x) - \hat{c}_2 \chi_{A_2}(x))^2 dx = \min_{c_1, c_2 \in \mathscr{R}_1 c_1 \geq c_2} \int_\Omega (g(x) - c_1 \chi_{A_1}(x) - c_2 \chi_{A_2}(x))^2 dx \tag{5}$$

We now consider the problem of FS extraction within the framework of the above formulated signal registration model as a statistical hypothesis testing problem, H – for image f there exists a fragment f_ω, represented as

$$H : \exists f_\omega = g + \nu,\ \exists t \in T,\ g \in t(V_\omega),\ \nu \in (0, \sigma^2 I),\ \sigma^2 > 0,\ \|\nu\|^2 << \|g\|^2, \tag{6}$$

where the shape of g, up to translation and scaling coincide with (3), and $t \in T$ is a translation and scaling transformation with T the set of all such transformations. The alternative hypothesis K simply states: such a fragment does not exist.

To solve this hypothesis testing problem the following functional is used [9],

$$j(z) = \frac{||(I - P_{V_\omega}) z||^2}{||(P_{V_\omega} - P_{V_U}) z||^2}. \tag{7}$$

where z is the image under consideration, $P_{V_U} z$ is a projection of the image $z(\cdot)$ onto the shape U of the uniform field of vision,

$$U = \{u(\cdot), u(x) = \text{ const} \cdot \chi_\Omega(x),\ x \in \Omega\}. \tag{8}$$

The functional (7) has following properties:

1. Assume that the fragment f_ω exists and satisfies the condition (6), but cannot be represented as

$$f_\omega = g + \nu, \exists t \in T,\ g \in t(U), \nu \in (0, \sigma^2 I),\ \sigma^2 > 0. \tag{9}$$

   The numerator in (7) equals $||(I - P_{V_\omega})\nu||^2$, the denominator equals $||(P_{V_\omega} - P_{V_U})\nu + (P_{V_\omega} - P_{V_U})g||^2$ and has values of $O(\|g\|^2)$. Thus the value of the functional (7) is small, because $\|\nu\|^2 << \|g\|^2$.
2. Assume that the fragment f_ω exists and satisfies the condition (9). In this case the numerator in (7) equals $||(I - P_{V_\omega})\nu||^2$ and has values of $O(\|\nu\|^2)$. The denominator equals $||(P_{V_\omega} - P_{V_U})\nu||^2$ and also has values of $O(\|\nu\|^2)$. The functional $j(z)$ is therefore $O(1)$.
3. Assume that the fragment f_ω satisfying the condition (6) or (9) does not exist. The numerator in (7) equals $||(I - P_{V_\omega})\nu + (I - P_{V_\omega})g||^2$ and is of $O(\|g\|^2)$. The denominator, which equals $||(P_{V_\omega} - P_{V_U})\nu + (P_{V_\omega} - P_{V_U})g||^2$, is also of $O(\|g\|^2)$, and again the functional $j(z)$ is $O(1)$.

Hence, only in the first case is the value of the functional (7) small, because $\|\nu\|^2 << \|g\|^2$.

The decision rule is as follows: hypothesis H is accepted if by means of translation and scaling, a fragment f_ω, such that $j(f_\omega) \leq A$ can be found, where A is a constant empirically determined, as explained below. Otherwise H is declined.

The value of the functional (7) is considered as a measure of the closeness between image z and the image with shape (3). Note that the functional (7) is invariant with respect to variations of the image's brightness and contrast values, i.e. to transformations $z \to \alpha z + \beta$, where α is a number, and β is an image defined on Ω.

The value of the constant A is defined as follows. First of all using experimental data the value of A determined that appears acceptable for an image of the proposed FS. A value of $A = 40$ appears to be appropriate. The reliability of this value is verified by means of experiments on synthetic data. We use 10000 synthetic images of smooth substrates S with additive Poisson-distributed noise. The noise parameters were the same as in real experiment. The methods that have been proposed in [2, 16] are used to remove the noise from the smooth substrate. Subsequently an empirical distribution of the values of the functional (7) at the specified noise levels is determined. Based on this distribution the probability is estimated as $P(j \leq A) = 0.001$, see Fig. 4. This is the probability of erroneously accepting the hypothesis against the closest alternative, "uniform field of vision". According to the properties of the functional (7), this probability estimates an upper bound for the probability of erroneously accepting the hypothesis against the alternative, "fragment does not exist". This criterion is analogous to the principle of the locally uniformly of the most powerful criterion [17].

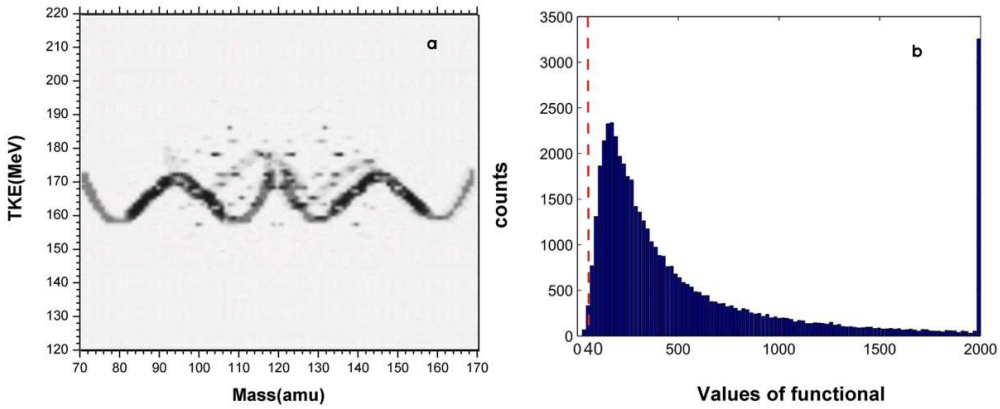

FIGURE 4. (a) The fine structure revealed at the same TKE-M distribution, as is shown at Fig. 2 (b). (b) The spectrum of functional (7) values, obtained based on model data. The dotted line shows the threshold value A, for which $P(j \leq A) = 0.001$.

According to this statistical analysis, the probability that the "fine structure" obtained from real experimental data is due to noise, is small. Fig. 4a) shows the result of the "fine structure" extracted from real experimental data using the method described above, as compared with the result obtained earlier in Fig. 2b).

The proposed method enables one to search for structures that have different shapes, and should also be useful in other contexts.

In summary, we emphasize the two main aspects of this approach to the analysis of two-dimensional distributions of experimental observables originated from nuclear reactions.

1. Multi-valley structures of the potential energy surface of nuclear system, at least in fusion, fission and quasifission reactions, describe different discrete reactions along these valleys. Each reaction manifests itself as a trajectory in the space of experimental observables such as mass-asymmetry and total kinetic energy, coupled with prescession elongation of the system. Visualization of these trajectories (revealing the fine structure) can give access to unique physical information, unknown in the past.
2. In order to obtain quantitative estimates of our confidence in the extracted structures, we developed a mathematical approach based on morphological methods of image analysis. Within its framework, one estimates the probability of random (due to the noise) realizations of the structure (or its scaled versions). This provides necessary confidence in the observations for subsequent physical analysis.

REFERENCES

1. The Nuclear Fission Process, edited by Cyriel Wagemans, CRC Press, 1991.
2. Yu. V. Pyatkov et al., *Nucl. Instr. and Methods A* **488**, 381–399 (2002).
3. U. Quade et al., *Nucl. Phys. A* **487**, 1–36 (1988).
4. M. N. Rao et al., *Nucl. Instr. and Methods A* **313**, 227–232 (1992).

5. T. Ohtsuki et al., *Phys. Rev. Lett.* **66**, 17–20 (1991).
6. A. A. Alexandrov et al., *Nucl. Instr. and Methods A* **303**, 323–331 (1991).
7. W. H. Trzaska et al., cP 392, AIP Press, p.1059, (1997).
8. W. H. Trzaska et al., *Proc. Symposium on Nuclear Clusters, Rauischholzhausen, Germany* 2002, pp. 237-242.
9. Yu. P. Pytyev, Morphological Image Analysis in *Pattern Recognition and Image Analysis*. Vol. 3, No. 1, 1993, pp. 19–28.
10. O. V. Falomkina et al., Heavy Ion Physics, FLNR JINR Scientific Report 2001-2002, Dubna 2003, pp. 149–150.
11. V. V. Pashkevich, *Nucl. Phys. A* **169**, 275–293 (1971).
12. U. Brosa et al., *Phys. Rep.* **197**, 167–262 (1990).
13. J. F. Berger et al., *Nucl. Phys. A* **428**, 23–36 (1984).
14. Yu. V. Pyatkov et. al., *Nucl. Phys. A* **624**, 140-156 (1997).
15. Yu. V. Pyatkov et al., *Phys. of Atomic Nuclei* **67**, 1726-1730 (2004).
16. O. V. Falomkina et al., Heavy Ion Physics, FLNR JINR Scientific Report 2003 - 2004, Dubna, Russia, 2006, pp. 158–159.
17. C. R. Rao (chief ed.). Handbook of Statistics, Vols 1-18. New York and Amsterdam: North Holland/Elsevier Science Publishers.

The spectrum of ^{6}Be populated in the charge-exchange ^{1}H(^{6}Li,^{6}Be)n reaction

V. Chudoba[*,†], I.A. Egorova[**], M.S. Golovkov[*], L.V. Grigorenko[*,**], R.A. Bark[‡], A.S. Fomichev[*], A.V. Gorshkov[*], V.A. Gorshkov[*], G. Kaminski[*,§], S.A. Krupko[*], Yu.L. Parfenova[*], S.I. Sidorchuk[*], R.S. Slepnev[*], L. Standyło[*,¶], S.V. Stepantsov[*], G.M. Ter-Akopian[*], R. Wolski[*,§] and M.V. Zhukov[‖]

[*]*Flerov Laboratory of Nuclear Reactions, JINR, Dubna, RU-141980 Russia*
[†]*Institute of Physics, Silesian University in Opava, Bezručovo nám. 13, 74601 Czech Republic*
[**]*Bogoliubov Laboratory of Theoretical Physics, JINR, Dubna, RU-141980 Russia*
[‡]*iThemba LABS, Post Office Box 722, Somerset West 7129, South Africa*
[§]*Institute of Nuclear Physics PAN, Radzikowskiego 152, PL-31342 Kraków, Poland*
[¶]*The Andrzej Soltan Institute for Nuclear Studies, Hoża 69, 00-681 Warszawa, Poland*
[‖]*Fundamental Physics, Chalmers University of Technology, S-41296 Göteborg, Sweden*

Abstract.
^{6}Be spectrum populated in the charge-exchange ^{1}H(^{6}Li,^{6}Be)n reaction was studied experimentally. The known 0^{+} ground state (g.s.) and excited 2^{+} state were observed. Above the 2^{+} state a broad energy hump extending up to 15 MeV is present in the spectrum. This hump is apparently composed of negative parity states and its interpretation as the isovector soft dipole mode connected to the ^{6}Li g.s. is suggested.

Keywords: Charge-Exchange Reaction, Correlation Measurements, Few-Body and Many-Body Systems
PACS: 23.20.En, 25.10.+s, 25.40.Kv, 27.20.+n

INTRODUCTION

The ^{6}Be isotope has been for a long time the subject of experimental study. Out of the first series of experimental works the last one [1] was published far ago and only very recently two new experimental works [2], [3] were carried out. One should emphasize the two aspects of interest of this nucleus.
(i) The g.s. of ^{6}Be is particle unstable and this nucleus is the lightest ground state true two-proton ($2p$) emitter. $2p$ radioactivity is an exclusive quantum-mechanical phenomenon when a sequential decay is not possible and the three final-state fragments are emitted simultaneously [4].
(ii) The ^{6}Be nucleus is an isobaric partner of ^{6}He which is a classical halo nucleus. Enormous efforts has been invested in the recent two decades in the studies of the halo aspect of the ^{6}He structure. To examine the correlation in the neutron halo one has to excite or destroy the ^{6}He nucleus. This embarrasses the interpretation of experimental data because one has to take into account the reaction mechanism. Recently it has been demonstrated in Ref. [2] that a valuable alternative to study of ^{6}He itself could be a

precision study of correlations in the decay of ^{6}Be states.

This work is aimed at the study of the properties of the ^{6}Be continuum above the first excited state (2^+ state at $E_T = 3.03$ MeV; E_T is energy above the two-proton breakup threshold [6]). This part of ^{6}Be spectrum will be explained by the population of negative parity states. We will interpret such an exclusive population as a novel effect: the isovector soft dipole excitation mode. Having in mind the interest attracted by soft dipole mode studies in exotic dripline halo nuclei as a tool for nuclear structure and nuclear astrophysics we dedicate this work to prove the existence of such a new phenomenon.

EXPERIMENTAL SETUP

The experiment was carried out at the U400M cyclotron in the Flerov Laboratory of Nuclear Reactions, JINR (Dubna, Russia). The ^{6}Be spectrum was populated in the charge-exchange ^{1}H(^{6}Li,^{6}Be)n reaction. On one hand, this reaction was chosen because of its presumably simple mechanism. On the other hand, in this inverse kinematic case, the ^{6}Be decay products (α + p + p) fly out in relatively narrow cone in the forward direction in laboratory frame. The latter makes possible to detect all decay products with reasonable efficiency in a wide range of ^{6}Be excitation energy. Such condition allowed us to study the reaction in the whole angular range.

The 32 MeV/A ^{6}Li beam was delivered by the cyclotron and transported by the ACCULINNA fragment separator [5] into an experimental chamber. The beam with typical intensity of 3×10^7 s^{-1} was focused in an area of diameter 5 mm in the center of the cryogenic hydrogen target. 4 mm thick gas cell was filled with hydrogen at pressure of 3 bar and cooled down to a temperature of 35 K.

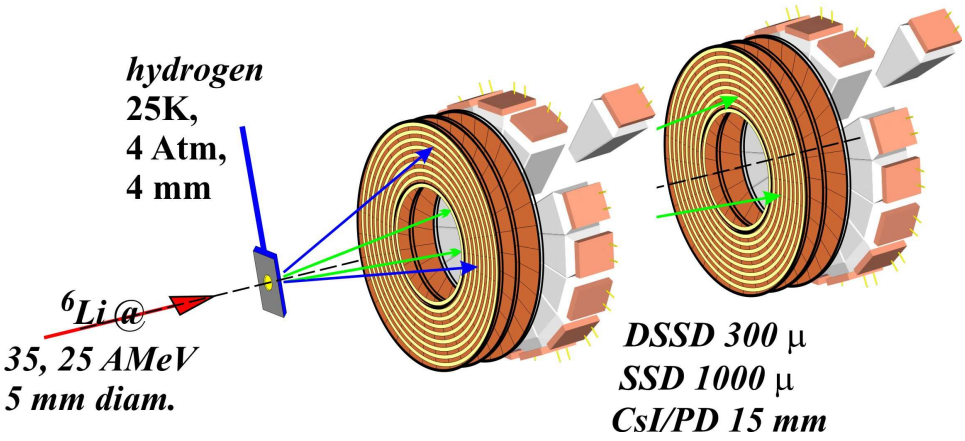

FIGURE 1. (color online) Detector system setup.

Reaction products were detected using two identical telescopes positioned 91 and 300 mm downstream of the target (see Fig. 1). Each telescope consisted of a 300 μm thick annular double side silicone strip detector (DSSD) and of a 1000 μm thick annular single side silicone strip detector (SSSD), both of them had an active area with the outer and inner diameters of 82 and 32 mm, respectively, and a 28 mm central hole. The silicon detectors were backed by 19 mm thick CsI(Tl) detectors forming an array with outer

and inner diameters of 97 and 37 mm, respectively. The DSSD were segmented into 32 sectors on front side and 32 rings on back side providing position information of the measured particles. The SSSD and CsI(Tl) array were segmented into 16 sectors. Particle identification was performed by standard ΔE-E method. The angular ranges of the far and the near telescope were $3.2^\circ - 7.5^\circ$ and $10.9^\circ - 24.2^\circ$, respectively, in the laboratory system.

DATA ANALYSIS

In this work only the triple α + p + p coincidences, originating from the ^{6}Be decay, were analysed. Registration of the triple coincidences corresponded to the complete kinematical measurement for the ^{1}H(^{6}Li,^{6}Be)n reaction and allowed us to reconstruct all possible spectra and correlations.

Invariant mass spectrum

Invariant mass spectrum of ^{6}Be measured in the whole angular range is presented in Fig. 2. Two peaks in the spectrum at the energies E_T = 1.3 MeV and E_T = 3.0 MeV show the population of the known ground 0^+ and excited 2^+ states ([6] and Refs. therein). The width of the g.s. is 0.092 MeV [6]. Measured width of the ^{6}Be g.s. peak ($\sim$0.5 MeV) is determined by our experimental resolution.

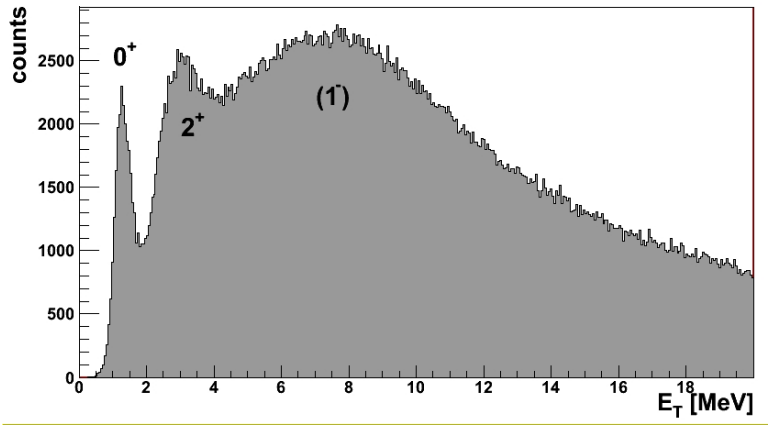

FIGURE 2. ^{6}Be invariant mass spectrum.

The main part of the counts in the spectrum comes from a broad hump centred at about 8 MeV. It should be noted that the shape of the spectrum shown in Fig. 2 is affected by the detection efficiency. In the case of triple coincidences the efficiency depends on many parameters. Generally, this function depends on the energy and angular correlations of the decay products. The calculations of efficiency were carried out on the basis of Monte Carlo simulations which take into account all details of the experimental setup.

Angular distribution

Fig. 3 shows a two-dimensional plot of the invariant mass energy versus the CM angle of ^{6}Be from the ^{1}H(^{6}Li,^{6}Be)n reaction. The left panel presents the measured data, the right panel shows the same data after correction for efficiency. In the presented spectra there are well pronounced three regions saving the positions of its maxima at different angles θ_{Be}. This fact allowed us to assume that this peaks correspond to the population of separate states and allowed us proceed to the analysis of this phenomena. As the first step of analysis we made effort to clarify the angular behaviour of the measured spectra (see Fig. 3). The whole angular range of the invariant mass spectrum was divided into 18 equal bins and each bin was corrected for efficiency. The whole spectrum could be represented as a sum of three terms corresponding to the known 0+, 2+ states and the broad structure above 4 MeV:

$$\frac{d\sigma}{dE_T d\theta_{Be}} = \sum_{i=1}^{3} f_i(\theta_{Be}) F_i(E_T) \tag{1}$$

Peaks at energies about 1.3 and 3.0 MeV were fitted using the Breit-Wigner profiles. For the broad hump between E_T = 4 MeV and E_T = 14 MeV the function suited to approximate the experimental data was chosen as.

$$\begin{aligned}
&\sigma_{J\pi} \sim \frac{\Gamma_{J\pi}(E)}{(E-E_r)^2 + \left(\frac{\Gamma_{J\pi}(E)}{2}\right)^2}, \\
&\Gamma_{J\pi}(E) \sim \alpha \left(\frac{E}{{}^{(J\pi)}E_r}\right)^2 + (1-\alpha)\left(\frac{E}{{}^{(J\pi)}E_r}\right)^4, \\
&\alpha \sim 0.65\,,\ J\pi = \ 0+, 2+; \quad \Gamma_{1-} \sim E_r^{3/2}
\end{aligned} \tag{2}$$

An example of such a decomposition for an angular range of $30^\circ - 40^\circ$ is given in Fig. 4. The integral of (2) gives the population cross section for each state in the invariant mass spectrum (see Fig. 4).

The most forward focused state is 0^+, the first excited state 2^+ cross section is shifted to backward angles. The broad hump has a maximum in between of the g.s. 0+ and first e.s. 2^+ maxima. Based on this feature of the observed angular distributions we assume it reasonable to attribute a ΔL = 1 angular momentum transfer to the origin of this hump. Such a momentum transfer corresponds to the population of states in ^{6}Be with the most probable spin-parity J^π = 1^-. It should be emphasised that the cross section for the population of these negative parity states highly exceeds the population of the known 0^+ and 2^+ states. So we are dealing here with the strong effect in the population of the ^{6}Be continuum.

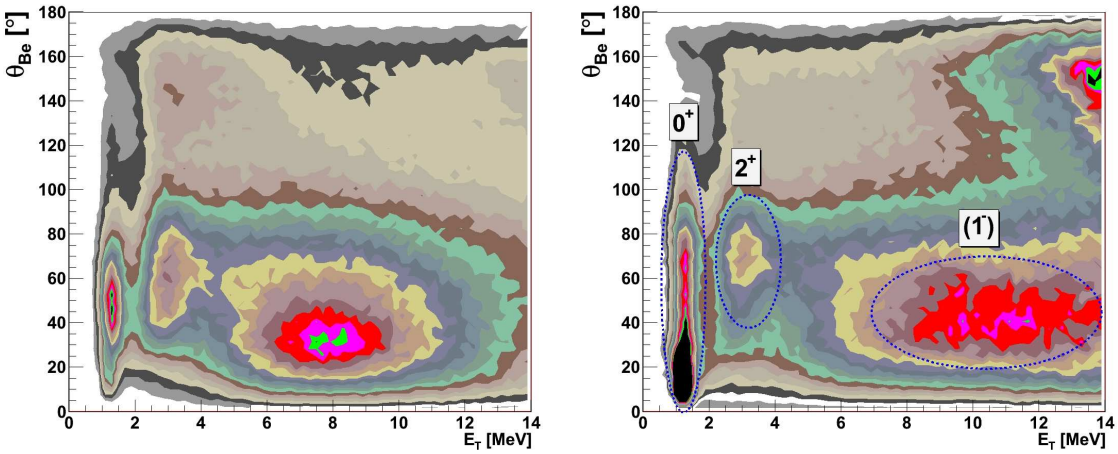

FIGURE 3. (color online) Invariant mass ^{6}Be energy versus θ_{Be}. The measured spectrum is shown in the left panel, the same data after correction for efficiency are shown in the right panel. In both spectra there are well visible three peaks depicted by dashed elipses. Position of these peaks does not depend on the angle θ_{Be}.

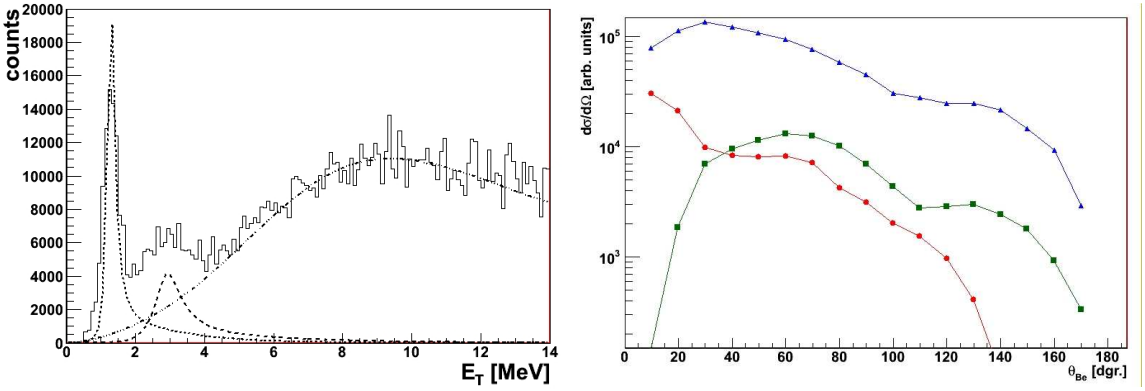

FIGURE 4. (color online) Left: Example of the decomposition of experimental spectrum measured in angular range $\theta_{Be} \in (30^\circ, 40^\circ)$ and corrected for efficiency (see explanation in the text). Right: Angular distribution for the ^{1}H(^{6}Li,^{6}Be)n reaction. Cross section is presented in arbitrary units. Circles and squares correspond to population of g.s. 0^+ and first e.s. 2^+. Triangles depict the population of the broad bump centered at energy of about 10 MeV.

CONCLUSION

The spectrum of ^{6}Be was studied experimentally in the charge-exchange ^{1}H(^{6}Li,^{6}Be)n reaction. The spectrum up to 15 MeV of excitation is completely described by population of three states 0^+ at 1.37 MeV, 2^+ at 3.05 and 1^- at $\sim 4-12$ MeV. The 1^- continuum is interpreted as a novel phenomenon – the isovector soft dipole excitation mode – opening qualitatively new opportunities of the nuclear structure studies. We expect that the further analysis will confirm our supposition and will give some additional information about the ^{6}Be structure.

REFERENCES

1. O. V. Bochkarev *et al.*, *Sov. J. Nucl. Phys.* **55**, 955 (1992).
2. L. V. Grigorenko *et al.*, *Phys. Rev. C* **80**, 034602 (2009).
3. P. Papka *et al.*, *Phys. Rev. C* **81**, 054308 (2010)
4. V. I. Goldansky *Nucl. Phys.* **19**, 482 (1960).
5. A. M. Rodin *et al.*, *Nucl. Instr. Meth.* **A391**, 228 (1997).
6. D. R. Tilley *et al.*, *Nucl. Phys.* **A708**, 3 (2002).

Evaporation residues formation channels in heavy ion collisions

Sh. A. Kalandarov, G.G. Adamian and N.V. Antonenko

Bogoliubov Laboratory of Theoretical Physics, Joint Institute for Nuclear Research, Dubna, RU-141980, Russia

Abstract. Evaporation residues(ER's) formation channels in low energy heavy ion collisions is investigated within di-nuclear system model(DNS) [1] for the reactions $^{20}Ne+^{208}Pb$, $^{25}Mg+^{206}Pb$ and $^{36}S+^{nat}Pt$. The channels which involve cluster emission from excited intermediate system are investigated. The experimental data on velocity distributions of ER's can give a hint about the formation channels and it is in agreement with calculated average velocities for a certain ER's. For the reaction $^{64}Ni+^{164}Dy$, dependence of such cluster emission channels from bombarding energy is predicted.

Keywords: nuclear reactions,evaporation residues,cluster emission
PACS: PACS number(s): 25.70.Gh, 24.10.Pa, 24.60.Dr

INTRODUCTION

Study of nuclear reactions induced by heavy ions (HIs) is a topic of interest for last many years. At relatively low bombarding energies and values of impact parameters, HI reaction mechanism can be classified into complete fusion(CF), incomplete fusion(ICF) processes. In case of CF, the projectile is completely absorbed by the target nucleus, forming an excited composite system from which nuclear particles and/or gamma rays may be emitted subsequently. However, in case of ICF, the incident ion is assumed to break up into the fragments in the vicinity of nuclear field of the target nucleus, followed by fusion of one of the fragments with the target nucleus, while the remaining part of projectile goes on moving almost along the beam direction with approximately beam velocity. Theoretical and experimental studies of decay products in heavy ion collisions is very important to establish the role of different reaction mechanisms in producing the final reaction products, also it gives us a very important knowledge about the nuclear processes and structure of the nuclei. The reaction products can be divided into light evaporation particles, complex fragments, fission products and evaporation residues. In low energy nuclear reactions, for the relatively light systems, the evaporation particles and evaporation residues are the main reaction products, while for the heavy systems, fission process is responsible for the main reaction products. For both light and heavy systems, complex fragment emission channel is also always present, with relatively small cross sections comparing to the cross sections for the main reaction products. For the relatively light systems, the detailed investigations of complex fragment emission in complete fusion reactions was carried out both theoretically [2] and experimentally [3]. For the heavy systems, a good example of cluster emission is an observed cluster radioactivity of some heavy nuclei [4]. If the cluster decay is possible from ground state

of heavy nuclei, then with increasing excitation energy, it must become more easier. For experimental observation of cluster emission in heavy systems, these clusters should be measured in coincidence with a heavy partners. Also, velocity distributions of heavy partners(or ER's) can give a hint about such processes.

Here we investigate the mechanism of ER's formation in complete fusion reactions induced by HIs and we analyze all possible reaction channels which lead to the final ER's in the reactions $^{20}Ne + ^{208}Pb$, $^{25}Mg + ^{206}Pb$ and $^{36}S + ^{nat}Pt$. Cluster emission is treated under the assumption that light clusters are produced by collective motion of the nuclear system in the charge asymmetry coordinate, with further thermal escape over the Coulomb barrier. Emission barriers for complex fragments are calculated within the DNS model by using the double-folding procedure (with the Skyrme-type density-dependent effective nucleon-nucleon interaction) for the nuclear part of the nucleus-nucleus interaction potential. Both evaporation and binary decay are treated in the same way.

FORMATION AND DECAY OF THE COMPOUND NUCLEUS (CN) AND DINUCLEAR SYSTEM (DNS)

The emission process of complex fragments from the excited intermediate system, formed in heavy ion collisions, involves the motions in charge and mass asymmetry coordinates, which are defined here by the charge and mass (neutron) numbers $Z = Z_1$ and $A = A_1$ ($N = N_1 = A - Z$) of light nucleus of the DNS [1] formed by two touching nuclei, and the motion in the relative distance R between the centers of mass of nuclei. In the decoupled approximation the binary decay consists of two steps: (i) clustering or the formation of asymmetric DNS in the excited state with some probability and (ii) the decay of this DNS by the thermal overcoming the barrier in the nucleus-nucleus potential. The probability of cluster formation is calculated statistically by using the stationary solution of the master equation with respect to the charge and mass asymmetries and depends on the potential energy of the DNS configurations at touching distance and thermodynamical temperature of the system. The probability of the DNS decay in R coordinate is calculated by using the transition state method. This decay process depends on the termodynamical temperature of the DNS and the difference between the potential energies of the DNS configurations at the touching distance and at the barrier position.

The cross section of the charge particle emission from the excited intermediate system is calculated as follows

$$\sigma_{Z,A}(E_{\text{c.m.}}) = \sum_{J=0}^{J_{max}} \sigma_{Z,A}(E_{\text{c.m.}}, J) = \sum_{J=0}^{J_{max}} \sigma_{cap}(E_{\text{c.m.}}, J) P_{CN}(J) W_{Z,A}(E^*_{CN}, J), \qquad (1)$$

where $\sigma_{cap}(E_{c.m.}, J)$ is the partial capture cross section and $W_{Z,A}(E^*_{CN}, J)$ is the emission probability of a given particle from the excited nuclear system. Here, we consider the decay of excited intermediate system as a sequential light particle evaporation, which includes neutrons, protons, deuterons and tritones, and a cluster ($Z \geq 2$) emission.

CN formation and its consequent decay are not necessarily the ultimate results of the evolution of the initial DNS. In addition to contributions from a CN decay, the binary decay component is related to the quasifission (or multinucleon transfer) mechanism. In our model the fragments are produced as binary decay products of the DNS formed during the diffusion process along the mass (charge) asymmetry coordinate with and without stages of CN formation. The dominant reaction mechanism (complete fusion or quasifission) depends on the entrance channel and on the value of the angular momentum deposited into the system. In our model both components are taken into consideration.

Dinuclear system formation

The partial cross section for the formation of a dinuclear system is given as

$$\sigma_c(E_{\text{c.m.}}, J) = \pi \lambda\!\!\!^{-2}(2J+1)P_{\text{cap}}(E_{\text{c.m.}}, J), \tag{2}$$

where $\lambda\!\!\!^{-2} = \hbar^2/(2\mu E_{\text{c.m.}})$ is the reduced de Broglie wavelength and μ the reduced mass. The value of $\sigma_c(E_{\text{c.m.}}, J)$ defines the transition of the colliding nuclei over the Coulomb barrier with the probability $P_{\text{cap}}(E_{c.m.}, J)$ and the formation of initial DNS when the kinetic energy $E_{\text{c.m.}}$ and angular momentum J of the relative motion are transformed into the excitation energy and angular momentum of the DNS. The transition probability is calculated with the Hill-Wheeler formula $P_{\text{cap}}(E_{\text{c.m.}}, J) = (1 + \exp[2\pi(V(R_b, J) - E_{\text{c.m.}})/\hbar\omega(J)])^{-1}$, where the effective nucleus-nucleus potential V is approximated near the Coulomb barrier at $R = R_b$ by the inverted harmonic-oscillator potential with the barrier height $V(R_b, J)$ and the frequency $\omega(J)$.

The total capture section is

$$\sigma_c(E_{\text{c.m.}}) = \sum_{J=0}^{J_{max}} \sigma_{\text{c}}(E_{\text{c.m.}}, J) = \pi \lambda\!\!\!^{-2} \sum_{J=0}^{J_{max}} (2J+1)P_{\text{cap}}(E_{\text{c.m.}}, J), \tag{3}$$

where the maximum value of angular momentum J_{max} in general case is limited by the critical angular momentum J_{cr}, for which potential pocket for the entrance channel disappears. But here, since we are interested on evaporation residues formation channels, we set the maximal angular momentum as $J_{max} = 20\hbar$. For larger angular momentums, the initial DNS formed at the beginning of the reaction, mainly goes towards symmetric configuration and quasifission occur. So, higher angular momentums gives small contribution to ER's cross sections.

The excitation energy of the formed CN is determined as

$$E^*_{CN}(J) = E_{c.m.} + Q - E^{rot}_{12}(J), \tag{4}$$

where Q-value is determined as $Q = B_1 + B_2 - B_{12}$ and the rotational energy E^{rot}_{12} is not available for the internal excitation. Then the temperature of the CN is $T_{CN}(J) = \sqrt{E^*_{CN}(J)/a}$ within the Fermi-gas model. The level density parameter a is taken as $a = 0.114A + 0.162A^{2/3}$ from Ref. [5].

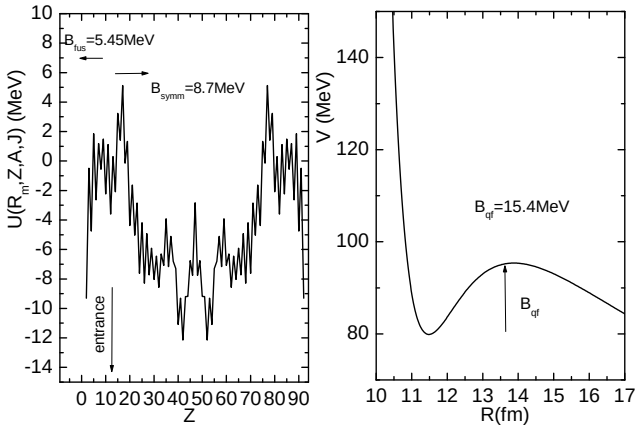

FIGURE 1. Driving potential(left side) and nucleus-nucleus potential(right side) for initial DNS for the $^{25}Mg + ^{206}Pb$ reaction. Fusion barrier B_{fus}, barrier for going to symmetric configuration B_{symm} and quasifission barrier B_{qf} are given.

Evolution of dinuclear system and decay

The time evolution of nuclear system in the charge and mass asymmetry coordinates is usually described in the framework of the transport model. In this approach the time dependence of the probability $P_{Z,A}(t)$ to find a system at the moment t in the state with charge Z and mass A asymmetries is calculated by the master equation [6]

$$\begin{aligned}\frac{d}{dt}P_{Z,A}(t) &= \Delta^{(-,0)}_{Z+1,A+1}P_{Z+1,A+1}(t) + \Delta^{(+,0)}_{Z-1,A-1}P_{Z-1,A-1}(t) \\ &+ \Delta^{(0,-)}_{Z,A+1}P_{Z,A+1}(t) + \Delta^{(0,+)}_{Z,A-1}P_{Z,A-1}(t) \\ &- (\Delta^{(-,0)}_{Z,A} + \Delta^{(+,0)}_{Z,A} + \Delta^{(0,-)}_{Z,A} + \Delta^{(0,+)}_{Z,A})P_{Z,A}(t), \end{aligned} \quad (5)$$

with initial condition $P_{Z,A}(0) = \delta_{Z,Z_i=0}\delta_{A,A_i=0}$, i.e. the CN ($Z_i$=0 or 1 and A_i=0 or 1 or 2 or 3) is treated as one of the available asymmetries. The transport coefficients ($\Delta^{(+,0)}_{Z,A}$, $\Delta^{(0,+)}_{Z,A}$) characterize the proton and neutron transfer rates from a heavy to a light nucleus or in opposite direction ($\Delta^{(-,0)}_{Z,A}$, $\Delta^{(0,-)}_{Z,A}$). In Eqs. (5) we take only the transitions $Z \rightleftharpoons Z \pm 1$ and $N \rightleftharpoons N \pm 1$ into account in the spirit of the independent-particle model.

For more clear understanding of DNS evolution, we present the most probable path in the potential energy surface to the complete fusion and symmetric DNS configurations. This path corresponds to the minimum of potential energy with respect to mass number A and relative distance coordinate R between DNS nuclei and called as driving potential. In Fig. 1, we present the driving potential for the $^{25}Mg + ^{206}Pb$ system and the nucleus-nucleus potential for initial DNS, where the corresponding barriers are pointed. The details of the calculation of potential energy surface(PES) and driving potential can be found in [7, 8].

Thus, the initial DNS evolves by nucleon transfer in three direction: to the complete fusion, to the quasifission from entrance channel and to the symmetric DNS configu-

rations. In the statistical approach, the probability of complete fusion(or overcoming fusion barrier) can be calculated as

$$P_{CN} = \frac{\rho_{fus}}{\rho_{fus} + \rho_{qf} + \rho_{symm}}, \tag{6}$$

where $\rho_{fus}, \rho_{qf}, \rho_{symm}$ are the level densities at the fusion barrier, quasifission barrier for the entrance channel and at the barrier in the way to symmetric DNS. The part of the system, which moves towards symmetric DNS configuration, goes to the quasifission channel. The quasifission barrier for the symmetric DNS is relatively small for heavy systems and the motion in relative distance R coordinate causes quasifission to occur. For the asymmetric DNS configurations, quasifission barrier is relatively high, and the lifetime of such a system is predestined by the time of neutron emission or fission, which can be sufficiently long to reach the mass and charge equilibrium limit in Eq. (5) for the asymmetric DNS and CN configurations behind the fusion barrier. So, the part of the system, which moves towards CN configuration will be localized mainly in that asymmetric DNS(or CN) configuration, for which potential energy surface has deepest minimum and will be statistically distributed among all possible asymmetric DNS and CN configurations. Thus, in the treatment of the formation of asymmetric DNS configurations, the equilibrium limit of the master equation can be imposed so that the probability $P_{Z,A}(E^*_{CN}, J)$ is proportional to the relevant level density ρ. At fixed total energy of the system the level density is proportional to $\exp[-U(R_m, Z, A, J)/T_{CN}]$ [6] and, thus, the DNS formation probability is written in the following way:

$$P_{Z,A}(E^*_{CN}, J) = \frac{\exp[-U(R_m, Z, A, J)/T_{CN}(J)]}{1 + \sum_{Z'=2,A'} \exp[-U(R_m, Z', A', J)/T_{CN}(J)]}, \tag{7}$$

where Z' and A' goes over all charges and masses of DNS configurations, which is behind the fusion barrier.

Since the potential energy of the DNS is determined relatively to the CN potential energy, the local excitation energy of each DNS is

$$E^*_{Z,A}(J) = E^*_{CN}(J) - U(R_m, Z, A, J). \tag{8}$$

If $E^*_{CN}(J) < U(R_m, Z, A, J)$, then the system can not reach the DNS configuration with charge Z and mass A asymmetries and its binary decay is energetically forbidden. To determine the temperature of the DNS, we use the Fermi-gas model expression $T_{Z,A}(J) = \sqrt{E^*_{Z,A}(J)/a}$.

The probability of the thermal penetration of the Coulomb barrier (the decay of the DNS in R into two fragments or the binary decay with $Z \geq 2$) can be written in complete analogy with the fission probability in the transition state formalism (we use here high temperature limit) as

$$P^R_{Z,A} \sim \exp[-B^{qf}_R(Z, A, J)/T_{Z,A}(J)]. \tag{9}$$

The theoretical description of the binary decay and the light particle evaporation processes should be on the same basis and we use the same expression (9) for calculating the probabilities of the neutron, proton, deuteron and tritone emissions. In

the calculations the temperature and emission barriers for these particle are the following: $T_{Z=0,A=0}(J) = T_{Z=0,A=1}(J) = T_{Z=1,A=0}(J) = T_{Z=1,A=1}(J) = T_{Z=1,A=1}(J) = T_{CN}(J)$ and $B_R^{qf}(Z=0,A=1,J) = B_n$ for the neutron with binding energy B_n, $B_R^{qf}(Z=1,A=0,J) = B_p + V_C^{(p)}$ for the proton with binding energy B_p and the Coulomb barrier $V_C^{(p)}$, $B_R^{qf}(Z=1,A=1,J) = B_d + V_C^{(d)}$ for the deuteron with binding energy B_d and the Coulomb barrier $V_C^{(d)}$, and $B_R^{qf}(Z=1,A=2,J) = B_t + V_C^{(t)}$ for the tritone with binding energy B_t and the Coulomb barrier $V_C^{(t)}$. The Coulomb barriers for outgoing proton, deuteron and tritone are taken as in Ref. [9]

$$V_C^{(i)} = \frac{e^2(Z'-1)}{1.7[(A'-m_i)^{1/3} + m_i^{1/3}]}, \tag{10}$$

where Z' and A' is a charge and mass numbers of nucleus which emits the light charge particle $''i''$ (i=p, d, t) and m_i is the mass number of the light charge particle.

The binary cluster emission process is imagined as a two step process. The system evolves in charge and mass asymmetry coordinates to reach a statistical equilibrium in mass asymmetry coordinate so that the probability of finding the system in each asymmetric DNS configuration and CN configuration depends on the potential energy $U(R_m,Z,A,J)$. After the formation, the excited DNS can decay in R coordinate into the two fragments if the local excitation energy of DNS is enough to overcome the barrier in R. If the system reaches B.G. point, then it goes to the fission channel, since the potential energy decreases towards symmetric DNS configurations. So the fission probability is equal to the probability of reaching B.G. point in driving potential. We note, that such a treatment is only valid if the particle emission barrier and B.G. point height is sufficiently high relatively to local barriers in charge(mass) asymmetry coordinate, otherwise it is a rough approximation.

So, the emission probability $W_{Z,A}(E^*_{CN},J)$ of a certain cluster from the excited CN is the product of the DNS formation probability and the DNS decay probability:

$$\begin{aligned} W_{Z,A}(E^*_{CN},J) &= \frac{P_{Z,A}P^R_{Z,A}}{\sum_{Z',A'} P_{Z',A'}P^R_{Z',A'}} \\ &= \frac{\exp[-U(R_m,Z,A,J)/T_{CN}(J)]\exp[-B_R^{qf}(Z,A,J)/T_{Z,A}(J)]}{\sum_{Z',A'}\exp[-U(R_m,Z',A',J)/T_{CN}(J)]\exp[-B_R^{qf}(Z',A',J)/T_{Z',A'}(J)]}. \end{aligned} \tag{11}$$

Here, $U(R_m,Z,A,J)$=0 for the n, p, d and t-evaporation channels and $\exp[-B_R^{qf}(Z',A',J)/T_{Z',A'}(J)] = 1$ for the B.G. point DNS configuration, since it describes the fission channel. In this sense, the height of B.G. point relatively to CN energy is equal to the fission barrier. Thus, the competition between the evaporation channel, the cluster emission channel and the fission channel is taken into consideration in the very natural way.

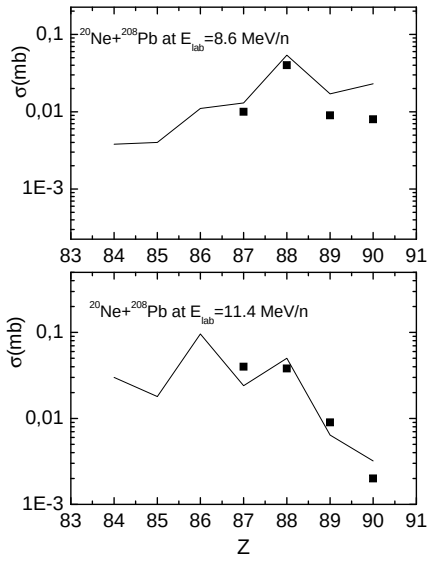

FIGURE 2. Evaporation residues charge distributions in the reaction $^{20}Ne +^{208} Pb$ at bombarding energies $E_{lab} = 8.6MeV/nucleon$ and $E_{lab} = 11.4MeV/nucleon$

For the binary decay channel, the excitation energies of the emitted complex fragment and residue nucleus are, respectively,

$$E^*_L(Z,A,J) = [E^*_{Z,A}(J) - B^{qf}_R(Z,A,J)]\frac{A}{A_t},$$
$$E^*_H(Z,A,J) = [E^*_{Z,A}(J) - B^{qf}_R(Z,A,J)]\frac{A_2}{A_t}, \quad (12)$$

where $A_t = A + A_2$ is the total mass number of the DNS and $E^*_{Z,A}(J) - B^{qf}_R(Z,A,J)$ the excitation energy of the DNS at the Coulomb barrier. We assume that the excitation energy and the angular momentum of the DNS is shared between the DNS nuclei proportionally to their mass numbers and moment of inertia, respectively.

CALCULATED RESULTS

In the calculations, we use the formulas (1), (6) and (11) to treat the sequential statistical decay (the evaporation of light particles and/or the binary decay) of the excited intermediate system. The generation of whole cascade of decay channels is performed by the Monte Carlo method. We continue to trace the decay processes until all fragments become cold (the excitation energy of fragments is smaller than its neutron emission threshold). The number n of generation of the events in the Monte Carlo technique was chosen according to the smallest decay probability which is $\sim 1/n$. The generated events were written in output files and then the all decay channels which leads to ER's

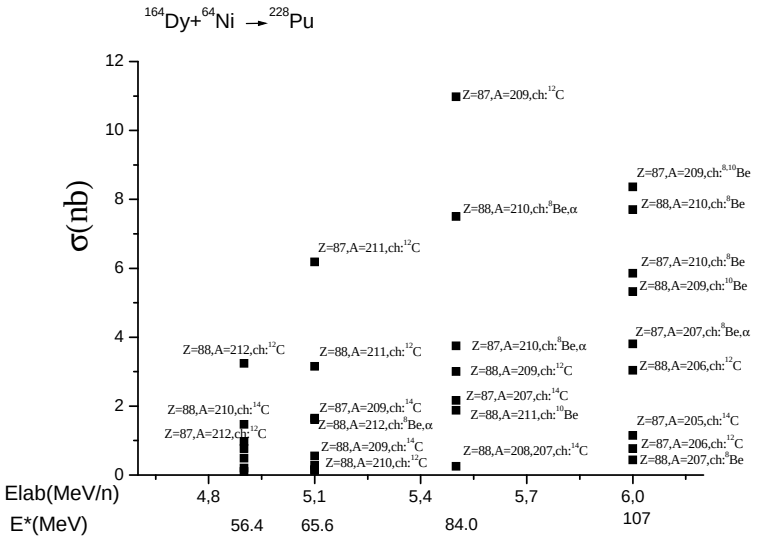

FIGURE 3. Dependence of cluster emission in the $^{64}Ni + ^{164}Dy$ reaction from bombarding(excitation) energy

were analyzed. The average values of ER's velocities is calculated from kinematics, namely from the energy conservation and momentum conservation laws, with taking into account possible particle evaporation along with binary decay.

To check the validity of our model for heavy systems, we compare the calculated charge distributions for evaporation residue products for the reaction $^{20}Ne + ^{208}Pb$ at bombarding energies $E_{lab} = 8.6MeV/nucleon$ and $E_{lab} = 11.4MeV/nucleon$. The excitation energy of CN is $E_{ex} = 98.8MeV$ and $E_{ex} = 150MeV$, respectively. In Fig. 2 the calculated ER's cross sections

$$\sigma_Z(E_{\text{c.m.}}) = \sum_A \sigma_{Z,A}(E_{\text{c.m.}}) \tag{13}$$

are in good agreement with the experimental data [10]. The experimental behavior of the charge distributions are reproduced for both bombarding energies. The odd-even effects are visible in the charge distributions for ER's. This fact indicates the influence of shell structure of the DNS nuclei on the evolution and decay of the system. Thus, the presented model is able to reproduce experimental ER's cross section both in shape and quantity.

The evaporation residues formation channels for the reaction $^{20}Ne + ^{208}Pb$ at bombarding energies $E_{lab} = 8.6MeV/nucleon$ and $E_{lab} = 11.4MeV/nucleon$ are tabulated in Table 1. The contribution for total cross section from each channel is given as in percentage. From the table, one can say which residual nuclei are formed with a cluster emission. The same analysis was performed for the reaction $^{25}Mg + ^{206}Pb$ at $E_{lab} = 5.9MeV/nucleon$ and $E_{lab} = 8.7MeV/nucleon$, for which the experimental study was done recently in GSI with velocity filter SHIP [11]. The cross sections and velocity distributions of residual nuclei have been measured.Only reaction residues leaving

TABLE 1. The competition between ER-channels in $^{20}Ne+^{208}Pb$ at E = 8.6MeV/A(first two column) and E = 11.4MeV/A(last two column).

	COMPETITION CHANNELS	Rate (percent)	COMPETITION CHANNELS	Rate (percent)
	6n,2p,^{14}C	37	12n,4α	10
Po	8n,α,^{12}C	18	(12-11)n,α,$^{12,14}C$	15
	8n,^{18}O	18	10n,2p,α,^{8}Be	10
	6n,2p,3α	18	11n,2p,3α	50
	6n,2p,α,^{8}Be	9	10n,4p,2α	15
	8n,1p,$^{12,14}C$	42	(13-12)n,1p,$^{12,14}C$	10
At	7n,1p,3α	50	12n,1p,3α	20
	7n,1p,α,^{8}Be	8	12n,1p,α,^{8}Be	6
			11n,3p,2α	55
			11n,2p,$^{3,2}H$,2α	5
			11n,5p,α	4
	(10-9)n, $^{12,14}C$	12	14n, ^{12}C	1
Rn	8n, 3α	40	13n, 3α	4
	8n,^{8}Be,α	10	13n,2p,^{8}Be	5
	8n,^{8}Be,2p	4	12n,2p,2α	45
	8n,2p,2α	32	12n,1p,$^{3,2}H$, 2α	5
	6n,2p,2 $^{3,2}H$,α	2	12n,4p,α	35
			11n,3p,$^{3,2}H$,α	5
	7n,2p,$^{3,2}H$,α	10	(14-13)n,3p,α	57
Fr	8n,1p,2α	90	13n,1p,2α	16
			14n,5p	20
			11n,4p,$^{3,2}H$	7
	10n,2α	37	14n,2α	5
Ra	9n,2p,α	63	(15-14)n,2p,α	52
			14n,4p	40
			13n,3p,$^{3,2}H$	3

the target at angles of up to 2° with respect to the beam direction are accepted by the entrance aperture of SHIP. It corresponds to the fact, that the measured velocity distributions correspond to the light particle emission channels and/or the cluster emission channel in which cluster were emitted in opposite or along the direction to the beam direction. When cluster is emitted in opposite(along) direction, from kinematics we get the velocity of residue nucleus which is larger(smaller) than compound nucleus velocity. We note here, that in our calculations, the contributions from compound nucleus, quasifission process and multinucleon transfer are not separated, since our model treat these processes in the same basis, so the results here represent contributions from all of these processes. Velocity distributions which is presented in [11] are in a very good agreement with our estimations from the kinematics of cluster decay. It is very important

TABLE 2. The competition between ER-channels in $^{25}Mg+^{206}Pb$ at E = 8.7MeV/n(E^* = 118MeV).

	COMPETITION CHANNELS	Rate (percent)	ER	COMPETITION CHANNELS	Rate (percent)
	n,$Ne^{20,22}$	30		n,3α	40
Po	n,1p,F^{19}	10		n,2p,2α	40
	n,2α,$^{12,14}C$	30	Ra	n,4p,α	10
	n,α,$O^{16,18}$	15		n,α,$^{8,10}Be$	5
	n,5α	10		n,$^{12,14}C$	5
	n,3α,$^{8,10}Be$	5			
	n,1p,α,$^{12,14}C$	34		n,3p,α	90
At	n,1p,4α,	34	Ac	n,1p,2α	5
	n,1p,2α,$^{8,10}Be$	10		n,2p,Li^7	5
	n,1p,$O^{16,18}$	17			
	n,2p,N^{15}	5			
	n,$O^{16,18}$	5		n,2α	5
Rn	n,4α	15	Th	n,2p,α	85
	n,α,$^{12,14}C$	15		n,4p	5
	n,2α,$^{8,10}Be$	5			
	n,2p,3α	60			
	n,1p,$^{12,14}C$	5			
Fr	n,1p,α,$^{8,10}Be$	10			
	n,3p,2α	15			
	n,1p,3α	70			

support for our suggested mechanism of evaporation residue formation, since with other mechanisms than cluster decay, the residual nuclei will have very similar velocity to the compound nucleus velocity. One more possibility is incomplete fusion(ICF), where it takes place not full momentum transfer, thus the residual nuclei will have smaller velocities. But at this bombarding energies, the contribution from ICF process expected to be very small. The competition channels for the case of $E_{lab} = 8.7 MeV/nucleon$ is presented in Table 2. In Fig. 3 we presented the dependence of cluster emission channels in the reaction $^{64}Ni+^{164}Dy$, which leads to the evaporation residues Fr, Ra, from bombarding energy. The residual nuclei and the emitted clusters are written for each bombarding energy. The cross sections are rather small comparing with the reaction $^{20}Ne+^{208}Pb$ at bombarding energy $E_{lab} = 8.6 MeV/nucleon$. It is so, because complete fusion probability(or probability of overcoming fusion barrier) P_CN in equation (1), is smaller for the reaction $^{64}Ni+^{164}Dy$ then for more asymmetric reaction $^{20}Ne+^{208}Pb$. The optimal bombarding energy to observe the cluster emission from heavy nuclei depends on the excitation energy of intermediate system formed during the collision. For the $^{64}Ni+^{164}Dy$ reaction, the optimal excitation energy is around 90 MeV, and it corresponds to the bombarding energy 5.5 – 5.6MeV/nucleon.

SUMMARY

Cluster decay of the excited intermediate system formed in heavy ion collisions is described in the framework of dinuclear system concept. The mechanism of cluster emission is treated under the assumption that the light clusters are produced by a collective motion of the nuclear system in the charge asymmetry coordinate with further thermal penetration through the Coulomb barrier. The emission barriers for complex fragments are calculated by using the double-folding formalism for the nuclear part of the nucleus-nucleus interaction potential. The competition between the evaporation channel and binary decay channel is taken into consideration in a unique way. Our approach describes well the experimental production cross sections for evaporation residues. Performed analysis of all possible channels leading to evaporation residues are very helpful for the interpretation of experimental observations. The measured velocity distributions are in good agreement with the suggested mechanism of cluster decay.

ACKNOWLEDGMENTS

This work was supported by DFG and RFBR. The IN2P3-JINR, MTA-JINR, and Polish-JINR Cooperation programs are gratefully acknowledged.

REFERENCES

1. V.V. Volkov,Izv. AN SSSR ser. fiz. **50**, 1879 (1986); G.G. Adamian, N.V. Antonenko, and W. Scheid, Nucl. Phys. A **618**, 176 (1997); G.G. Adamian, N.V. Antonenko, W. Scheid, and V.V. Volkov, Nucl. Phys. A **627**, 361 (1997); G.G. Adamian, N.V. Antonenko, W. Scheid, and V.V. Volkov , Nucl. Phys. A **633**, 409 (1998).
2. L.G. Moretto and G.J. Wozniak, Progress in Particle and Nuclear Physics, **21**, pp. 401–457; Sh.A. Kalandarov *et al.*, Phys. ReV. C **82**, 044603 (2010).
3. L.G. Moretto, Nucl. Phys. A **247**, 211 (1975); K.X. Jing *et al.*,Nucl. Phys. A **645**, 203 (1999); J. Boger and J.M. Alexander, Phys. Rev. C **50**, 1006 (1994).
4. D. Hasegan and S.P. Tretyakova, in Particle Emission from Nuclei, vol. II, ed. D.N. Poenaru and S.M. Ivascu, CRC, Boca Raton, FL, USA, (1989); Nuclear Decay Modes, ed. D.N. Poenaru, Institute of Physics, Bristol, UK, (1996).
5. A.V. Ignatyuk, *Statistical properties of excited atomic nuclei* (Energoizdat, Moscow, 1983).
6. G.G. Adamian, A.K. Nasirov, N.V. Antonenko, and R.V. Jolos, Phys. Part. Nucl. **25**, 583 (1994); G.G. Adamian, N.V. Antonenko, R.V. Jolos, and A.K. Nasirov, Nucl. Phys. A **551**, 321 (1993).
7. G.G. Adamian, N.V. Antonenko, R.V. Jolos, S.P. Ivanova, and O.I. Melnikova, Int. J. Mod. Phys. E **5**, 191 (1996).
8. G.G. Adamian, N.V. Antonenko, and W. Scheid, Nucl. Phys. A **678**, 24 (2000).
9. A.S. Zubov, G.G. Adamian, N.V. Antonenko, S.P. Ivanova, and W. Scheid, Phys. Rev. C **68**, 014616 (2003).
10. M.Veselsky, S. Saro, F.P.Hessberger, V.Ninov, S.Hofmann, D.Ackermann, Z. Phys. A **356**, 403-410 (1997).
11. Sophie Heinz, Int. J. Mod. Phys. E **17**, 2231-2234 (2008).

Multi-cluster decays of heavy nuclei – studies in progress

D.V. Kamanin*, Yu.V. Pyatkov*,†, W. von Oertzen**, A.A. Alexandrov*, I.A. Alexandrova*, O.V. Falomkina*,‡, N. Jacobs§, N.A. Kondratjev*, Yu.N. Kopatch*, E.A. Kuznetsova*, Yu.E. Lavrova†, V. Malaza§, S. Mullins¶, A.N. Tyukavkin†, W. Trzaska‖ and V.E. Zhuchko*

*Joint Institute for Nuclear Research, 141980 Dubna, Moscow Region, Russia
†National Nuclear Research University MEPHI, 115409 Moscow, Russia
**Helmholtz-Zentrum Berlin, Glienickerstr. 100, 14109 Berlin, also Fachbereich Physik, Freie Universität
‡Lomonosov Moscow State University, Physics Faculty, Computer Methods in Physics Division, 119899, Russia
§Faculty of Military Science, Military Academy, Saldanha 7395, South Africa
¶iThemba Laboratory for Accelerator Based Sciences, Somerset West 7129, South Africa
‖Department of Physics of University of Jyväskylä, Finland

Abstract. Experimental results in favour of the existence of a new type of cluster decay called "collinear cluster tri-partition", CCT, are presented. They are based on two different experiments with binary coincidences and measurements of the masses and energies of the two fragments, as well as using in one of the experiments observables sensitive to the nuclear charge of the fission fragments. A relatively high yield of the CCT-effect (more than 10^{-3} per binary fission) is likely due to the favourable Q-values (more positive than binary) and is expected due to a collective motion through very elongated (hyper-deformed) pre-scission shapes of the mother system. The process is considered to result from a sequential process, where a heavy cluster (lead as in the case of known cluster radioactivity) is replaced by pairs of two lighter clusters such as the magic isotopes of Sn/Ni or Sn/Ge.

Keywords: ternary fission, cluster decay
PACS: 23.70.+j; 25.85.Ca; 25.85.Ec

INTRODUCTION

Nuclear fission, a process where a heavy nucleus decays into two fragments of intermediate mass (e.g. Ba + Kr) has been identified by Hahn and Strassmann in 1938. It was discovered by chemical analysis while iradiating natural Uranium with thermal neutrons [1]. Shortly afterwards Petrzhak and Flerov [2] observed spontaneous fission of the ^{238}U isotope. The energy release in the fission process was immediately calculated by all leading physicists at that time to be very large, typically 200–205 MeV (e.g. Meitner and Frisch [3]). The large value is due to the larger binding energy per nucleon (E_B/N) in the mass range around mass $A = 54$ (iron, $E_B/N = 8.2$ MeV), as compared to the value at the end of the periodic table, $E_B/N = 7.2$ MeV. This fact could have been noticed four years before these discoveries, because of the existence of the liquid drop model and the nuclear mass formula of Bethe and Weizsäcker [4]. However, the large collective motion through a large deformation (today called super-deformation) was considered to

be unlikely.

Fission of heavy low-excited nuclei into three fragments of comparable masses, so called "true ternary fission", has been intensively investigated soon after the discovery of fission. Swiatecki [5] has shown within the framework of the liquid drop model that fission into three heavy fragments is energetically more favourable than binary fission for all nuclei with fission parameters $30.5 < Z^2 / A < 43.3$. In 1963 Strutinsky [6] has calculated the equilibrium shapes of the fissioning nucleus and has shown, that along with the ordinary configuration with one neck, there is the possibility of more complicated elongated configurations with two and even three necks, at the same time it was stressed, that such configurations are much less probable. Later Diehl and Greiner [7, 8] have shown a preference for prolate over oblate saddle-point shapes for the fission of a nucleus into three fragments of similar size. Such pre-scission configurations could lead to almost collinear separation of the decay partners, at least in a sequential fission process. Actually the Coulomb interaction in the total potential energy is the smallest for linear arrangements of the three fragments. Furthermore results demonstrating a decisive role of shell effects in the formation of the multi-body chain-like nuclear molecules were obtained also by Poenaru et al. [9].

On the experimental side there have been multiple attempts to find the true ternary fission in low energy fission by means of counting techniques and in radiochemical studies. The schemes of the spectrometric experiments were based on the assumption of comparable angles between all three fragments emitted [10, 11]. Masses of the fragments were calculated in this case based on experimental values of the energies and angles. Contradictory results have been obtained; these were treated as showing the absence of fission fragments in the vicinity of mass fifty both in binary and ternary fission [12]. At the same time almost collinear ternary decays of excited heavy nuclear systems were known from the experiments in Ref. [13, 14] at the early stage of our work.

Bearing in mind the results mentioned above, we came to the conclusion, that collinear tri-partition of low-excited heavy nuclear systems would be a promising field of research. In our first experiments dedicated to this problem [15, 16] some indications of such processes were already observed. At least one of the decay products detected was a magic nucleus. By analogy with known cluster decay (or lead radioactivity), the process has been called "collinear cluster tri-partition" (CCT).

EXPERIMENTS

In the present work we describe the results of two different experiments devoted to the search for collinear tri-partition of heavy nuclei. In these experiments binary coincidences with two detector systems placed at relative angles of 180^0 are measured, see Figs. 1 and 2. Among all known detection methods to measure the masses of nuclear reaction products, the TOF-E (time-of-flight *vs* energy) method is the only one which uniquely allows the study of multi-body decays. In this method both, the fragment velocities V, obtained by means of TOF and the energy E, are measured for each detected fragment individually. The fragment mass M_{TE} is calculated simply using the equation $M_{TE} = 2E/V^2$. For a three-body decay six variables determine the kinematics (e.g. 3 masses and 3 velocities). Adding momentum and energy conservation reduces the num-

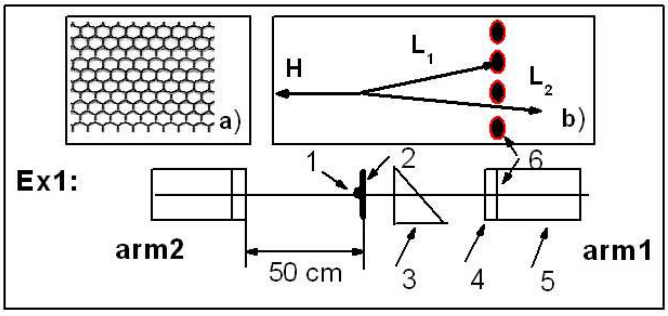

FIGURE 1. Scheme of (Ex1) for coincidence measurements of two fragments of the fission decay of ^{252}Cf. This experiment has been performed at the FOBOS setup [17]. Here: 1 – Cf source, 2 – source backing, 3 – micro-channel plate (MCP) based timing "start" detector, 4 – position sensitive avalanche counter (PSAC) as "stop" detector, 5 – ionization chamber (BIC) with the supporting mesh, 6 – the mesh of the entrance window. The front view of the mesh is shown in the insert a), an enlarged mesh section is presented in the insert b). After passage of the two fragments through the source backing, two light fragments L_1 and L_2, are obtained with a small angle divergence due to multiple scattering. In (b) we show that one of the fragments (L_1) can be lost hitting the metal structure of the mesh, while the fragment L_2 reaches the detectors of the arm 1. The source backing (2) exists only on one side and causes the mentioned angular dispersion in the direction towards the right arm1.

ber of independent variables to four. In our experiments two masses and two velocities are determined for two fragments observed at a relative angle of 180^0. All the results presented below are obtained within the framework of the "missing–mass" approach. With the two-arm spectrometers binary coincidences have been measured, with a special mechanism, which blocks the registration of a third fragment, as explained below and in Fig.1. This means that only two fragments were actually detected in each fission event and their total mass, the sum M_s will serve as a sign of a multi-body decay if it is significantly smaller than the mass of the initial system.

Experiment Ex1

In the first experiment (Ex1, Fig. 1), performed at the FOBOS [17] setup in the Flerov Laboratory of Nuclear Reactions (FLNR) of the Joint Institute for Nuclear Research (JINR) in Dubna [17], about 13×10^6 coincident binary fission events of ^{252}Cf were collected. The TOF of the fragment was measured over a flight path of 50 cm between the "start" detector, label (3) in Fig. 1, which is based on micro-channel plates (MCP) placed next to the ^{252}Cf-source and "stop" obtained by position sensitive avalanche counters (PSAC, 4). The source activity was 370 fissions/sec, it was deposited on a Al_2O_3 backing of 50 $\mu g/cm^2$ thickness and 18 mm in diameter – (1). Through the measurements of the position of the fragments in the PSAC's, this information provided also the fragment's emission angle with a prescission of 1^0. The energies of those coincident fragments which passed through the PSACs were measured in the Bragg ionization chambers (BIC, label 5 in Fig. 1). The entrance windows of the large BIC are made of 1 μm thick aluminized Mylar, with a diameter of 385 mm. To withstand the pressure of the counting gas, the delicate window foil has to be supported by a two-

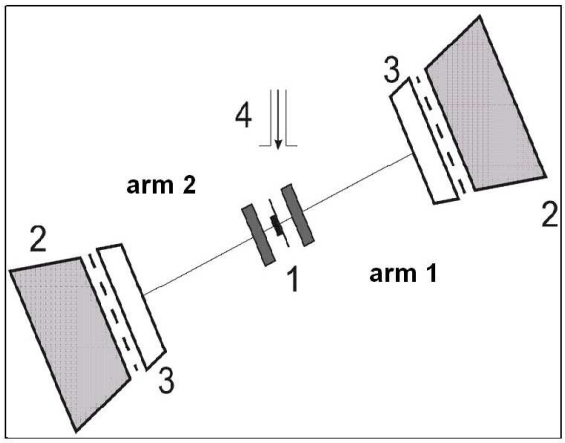

FIGURE 2. The scheme (Ex2) of the mini-FOBOS spectrometer which includes a "start" avalanche counter with an internal target (1), Bragg ionization chambers (BIC) (2) and "stop" position-sensitive avalanche counters (PSAC) (3). The target is irradiated by a collimated beam of thermal neutrons (4).

fold structure – a concentric heavy carrier of a transparency of 94% and an adjacent etched Ni-mesh having a cell dimension of 2.7 mm in diameter and 0.9 mm bulkhead in between the open pores. The thickness of the mesh is about 1 mm. The geometrical structure of the mesh is hexagonal, its front view is shown in the insert, a), of Fig. 1, a mesh section is presented in the insert b). The mesh reduces the total transparency to 75%. This mesh is a very important peculiarity of the present experiments as explained below (see Fig. 1).

Experiment Ex2

For a better understanding of the unusual decay channel in ^{252}Cf (sf) we planned to investigate different fissile systems at different excitation energies up to the threshold of the survival of nuclear shells. One of the reactions we had chosen in an additional experiment was fission induced by thermal neutrons in ^{235}U(n_{th}, f).

The experiment (Ex2) was performed with a beam of thermal neutrons of the IBR-2 reactor in the Frank Laboratory of Neutron Physics of the JINR with the help of the double-armed TOF-*E setup* in the mini-FOBOS [18] spectrometer. The overall statistics processed in this experiment *was* about 2×10^6 fission events. The scheme of the setup is shown in Fig. 2. The spectrometer is also based on FOBOS detector modules. The start detector is a symmetrical avalanche counter with an internal target. An active layer of the target material was prepared by evaporation of 100 μg/cm^2 of ^{235}U on an Al_2O_3 backing of 50 μg/cm^2 thickness. In this case along with measuring the fission fragment (FF) time-of-flight (TOF) and their energies (E), two more parameters being sensitive to the nuclear charge are added. The drift time of a track formed after stopping of a fragment in the gas volume of the BIC is known to be linked with the fragment nuclear charge [19]. The corresponding parameter was measured as the time difference between the PSAC signal and the signal from the Frisch grid of the BIC. Special calibration procedures

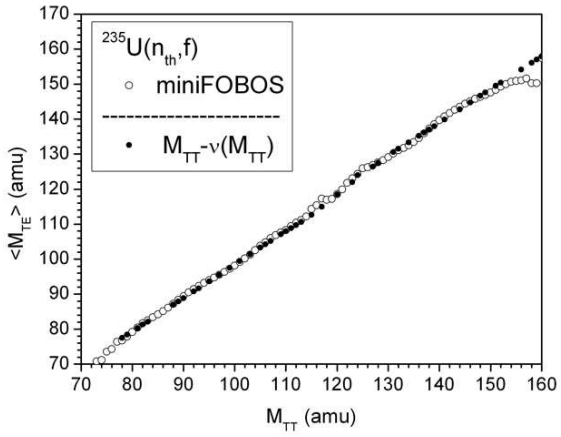

FIGURE 3. Correlation of the mean values of the experimental mass $<M_{TE}>$ (post-neutron emission) *vs* mass ,M_{TT}, obtained in the present TOF-TOF analysis. The shift due to neutron emission $\nu(M_{TT})$ [22] has been taken into account.

have been worked out for the FF nuclear charge determination [20]. According to the tests carried out before, the charge resolution does not exceed 3.8 units (FWHM) for the FF from the light mass peak, while the mean values for each fixed charge are correctly determined.

The second independent variable, which is also sensitive to the nuclear charge, is the specific energy loss of the FF in the gas volume of the PSAC [17]. This parameter proved to be very useful also for the selection of the CCT events.

In both experiments similar procedures for the TOF-E calibration and the calculation of the M_{TE} masses were used. In brief, the mass spectrum of binary decays, which depends on the measured variables and parameters to be determined, was forced to fit the known mass spectrum of ^{252}Cf fission [21]. The data presented in Fig. 3 were obtained in the following way. For each fixed experimental M_{TT}(TOF, TOF) mass a corresponding mean value of M_{TE} was obtained. $M_{TT}{}^{(1)}$ (primary i.e. before neutron emission fragment mass) was calculated as $M^{(1)}{}_{TT} = M_c/\ (1 + V_1/V_2)$, where M_c – the mass of the fissioning system, $V_{1,2}$ – velocities of the coincident fragments (indexes correspond to the numbers of the spectrometer arms). The values $<M_{TE}>$ are compared with the value expected for i.e. M_{TT} - $\nu(M_{TT})$, where $\nu(M_{TT})$ – mean number of neutrons emitted from the fragment with mass M_{TT}, taken from Ref. [22]. Thus, Fig. 3 demonstrates an absence of shifts (essential nonlinearity) in the calibration of the M_{TE} masses. This point is very important for the correct treatment of the data, especially for the mass characteristics and the peculiarities discussed below such as peaks and ridges in the spectra and distributions, respectively.

RESULTS AND ANALYSIS

The analysis is based on the presentation and discussion of two-dimensional diagrams of the registered masses (M_1 and M_2), in which the sum M_s of the two masses can be discussed. The events with total masses $M_s = M_1 + M_2$ will appear as diagonal lines in

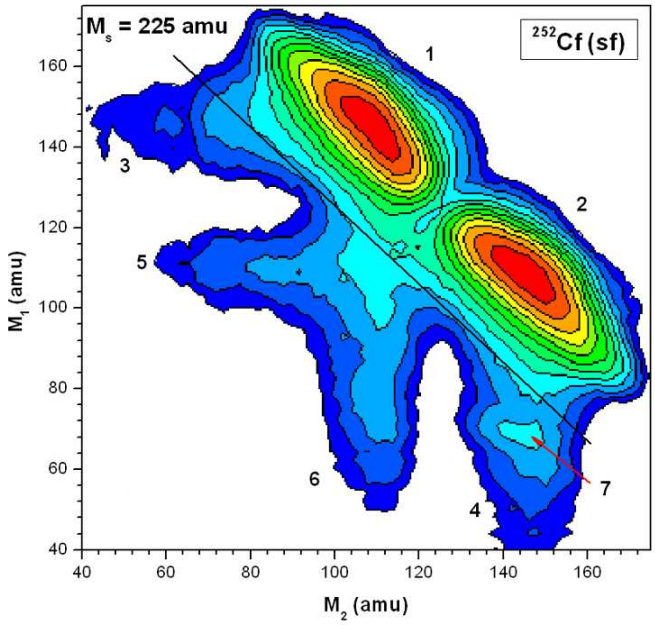

FIGURE 4. (Color online) Contour maps (in logarithmic scale, the steps between colors are approximately a factor 2.5) of the mass-mass distribution of the collinear fragments, detected in coincidence in the two opposite arms of the FOBOS spectrometer in (Ex1). The additional bump (7) in arm1 is inducated by an arrow. See text for more details.

the mass correlation plot. From these two-dimensional presentations further projections onto the individual axes M_1 or M_2 are made.

Results of experiment Ex1, ^{252}Cf (sf)

Fig. 4 shows in a logarithmic scale the two-dimensional distribution ($M_2 - M_1$) of the two registered masses of the coincident fragments in the experiment (Ex1). In this FOBOS setup M_1 is defined as the fragment mass derived from the arm pointing to wards the detector arm with the additional dispersive (scattering) materials. Only collinear fission events with a relative angle of 180 ± 2^0 were selected, which corresponds to the typical angular spread for conventional binary fission fragments.

The "tails" in the mass distributions marked 3–6 in Fig. 4 extending from the regions (1) and (2) which are used to mark the conventional binary fission, are mainly due to the scattering of fragments on both the foils and on the grid edges of the "stop" avalanche counters and the ionization chambers. Once again we emphasize the small but important asymmetry in the experimental arrangement for the two arms, which consists in the thin source backing (50 μg/cm^2 of Al_2O_3) for the "rear side" of the target and the "start" detector foil located only in arm 1 (Fig. 4). An astonishing difference in the counting rate and in the shapes of the "tails" (3) and (4) attracts attention. In the case shown in Fig. 4 there is a distinct bump, marked (7), on top of the latter "tails" (4). The bump is located in a region corresponding to a large "missing" mass. In Fig. 4 the line for the measured

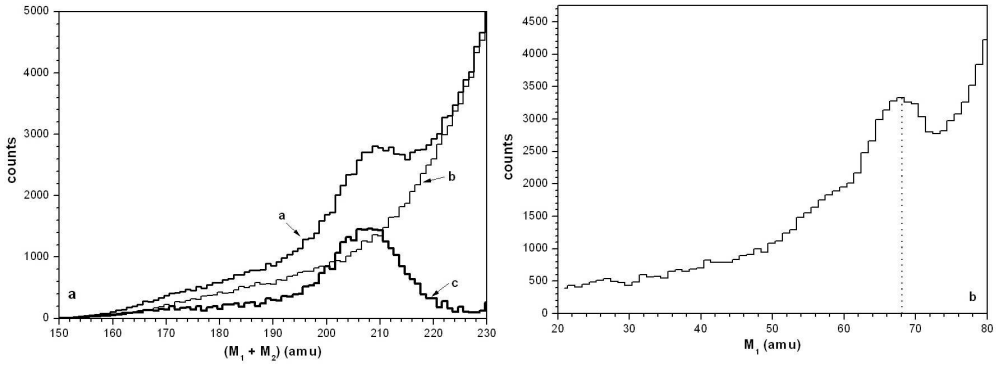

FIGURE 5. The bump "7" from (Ex1) in Fig. 4 is analyzed. In Fig. 5a) the spectra of the summed masses M_s for the "tails" (4 and 3) shown as spectrum *a* and *b*, respectively, are compared. The result of the subtraction of spectrum, b, from spectrum, a, (difference spectrum) is marked as c. On the rigth side, part b), the projection of the bump onto the M_1 axis is shown.

total mass $M_s = M_1 + M_2 = 225$ amu is shown as a border line separating these interesting events from normal binary fission. The statistical significance of the events in the structure (7) can be deduced from Fig. 5, where the spectra of total (summed) masses M_s for the "tails" (4) and (3) are compared. The yield of the events in the difference spectrum *c*, is $(4.7\pm0.2)\times10^{-3}$ relative to the total number of events in the distribution shown in Fig. 4. It is only a lower limit of the yield due to the reasons discussed below. In order to explain the differences in the "tails" (4) and (3) mentioned above (see also Fig. 7), the following scenario is proposed, the corresponding geometry has been shown in Fig. 1 (insert b). We assume that in ternary fission the three fragments are emitted collinearly due to two sequential binary decays. Two of the fragments are emitted in one direction but become separated in their velocity vectors with a small angle difference of $\sim1^0$ after passing the scattering media, due to multiple scattering [23]. These media are the backing of the source and the foil of the start detector both located only on the side of tail (4). For instance, for a ^{70}Ni fragment with the energy 70 MeV the mean angle of multiple scattering in the backing is equal to 0.64^0 while the tail of the angular distribution extends up to 2^0. As a result two fragments continue to fly in the same direction with a small angle divergence. It should be stressed that the influence of the backing onto the yield of ternary events was mentioned already in Ref. [11].

Thus, if both fragments pass on and enter into the (BIC), we register a signal corresponding to the sum of the energies of the two fragments. In this case the event will be treated as binary fission with the usual parameters. In the other cases only the proper energy (mass) of one of the light fragments is measured, because the second one is stopped (lost) in the supporting grid of the ionization chamber. Just the absence of a similar grid is likely the reason why the authors of the work in Ref. [24] have failed to observe collinear ternary decays of ^{252}Cf (sf) using the time-of-flight method.

For a more detailed analysis of the bump we have constructed the contour map of the two-dimensional mass-mass distribution obtained by subtraction of the "tail" (3) from the "tail" (4) (Fig. 6a). No additional normalization was used.

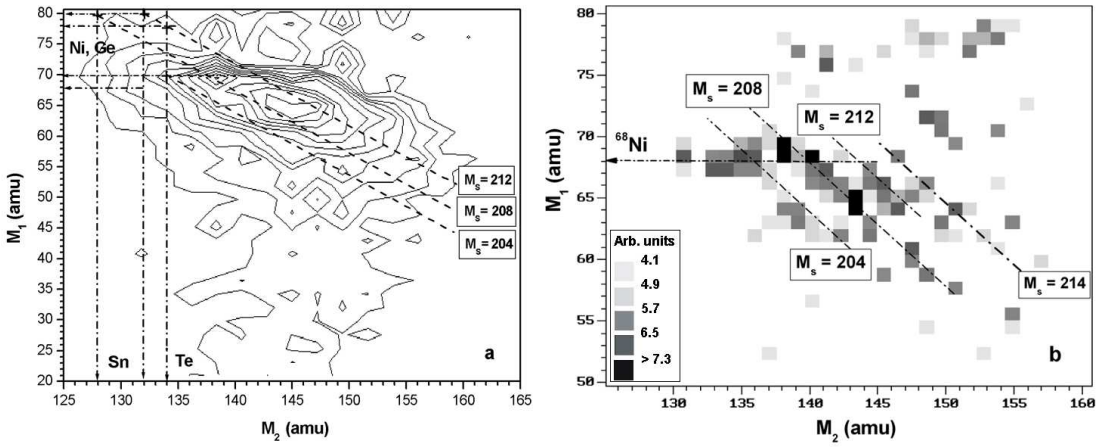

FIGURE 6. Left side, a).: The figure depicts as a $2D$-contour map (M_1 *vs* M_2) the difference between the "tails" (4) and (3), for the events measured in Ex1, with the system shown in Fig. 1; note the expanded scale for the lighter mass fragments (M_1). Dashed lines tilted by 45^0 with respect to the M_2 axis correspond to a fixed total mass of the two detected fragments $M_s = M_1 + M_2 =$ const. Part b): the same as in a), however, passed through a second derivative filter which emphasizes local peaks in each section of M_s = const. The ridges correspond to different values of M_s (204, 208, 212 and possibly 214 amu). The arrows in the figures mark positions of magic isotopes on the mass axis. Their role in the CCT process is discussed in the text.

This distribution is almost free from experimental background originating from scattered fragments of normal binary fission. Some features of this $2D$ plot can be further emphasized by a process, where a second derivative filter is applied (Fig. 6b), a method which is typically used in the search for peaks in gamma spectra and which is explained in more detail in Refs. [25, 26]. The vertical scale for the squares is defined in the insert to this figure. The maxima of the peaks extend over certain linear regions of M_2 = const, which are found predominantly as discrete diagonal lines, marked in Fig. 6b). Note that they correspond to the total masses $M_s =$ const with values of 204, 208, 212 and perhaps 214 amu, respectively. To show the positions of the tilted ridges on the map of the bump they are marked by the dashed lines in Fig. 6a). As can be deduced from the figure, the ridges go through crossing points corresponding to different combinations of two fragments with magic nucleon numbers (marked by the dot-dashed arrows). These marked points could be related to mass values with magic subsystems, well-known from binary fission [27, 28] as follows (corresponding Q values for ternary decays expressed in rounded numbers are marked in braces): $204 \rightarrow {}^{70}$Ni ($Z = 28$) + ^{134}Te {241 MeV} or ^{72}Ni + ^{132}Sn ($Z = 50$) {251 MeV}, $208 \rightarrow {}^{80}$Ge + ^{128}Sn {261 MeV} and for $212 \rightarrow {}^{80}$Ge + ^{132}Sn {257 MeV}, ^{78}Ni + ^{134}Te {228 MeV} or ^{68}Ni + ^{144}Ba {217 MeV} and for $M_s = 214 \rightarrow {}^{82}$Ge + ^{132}Sn {226 MeV}. It should be reminded that the Q value that corresponds to the most probable binary partition of ^{252}Cf is about 216 MeV.

Of course, at the moment this interpretation of the tilted ridges is only a hypothesis to be confirmed by other results shown below.

The ridges discussed are crossed as well by the horizontal ridge (seen via a bunching of contour lines in Fig. 6a). The projection of the bump onto the M_1 axis (Fig. 5b) confirms this conclusion. The effect can be linked with the isotopes of ^{68,70}Ni, which

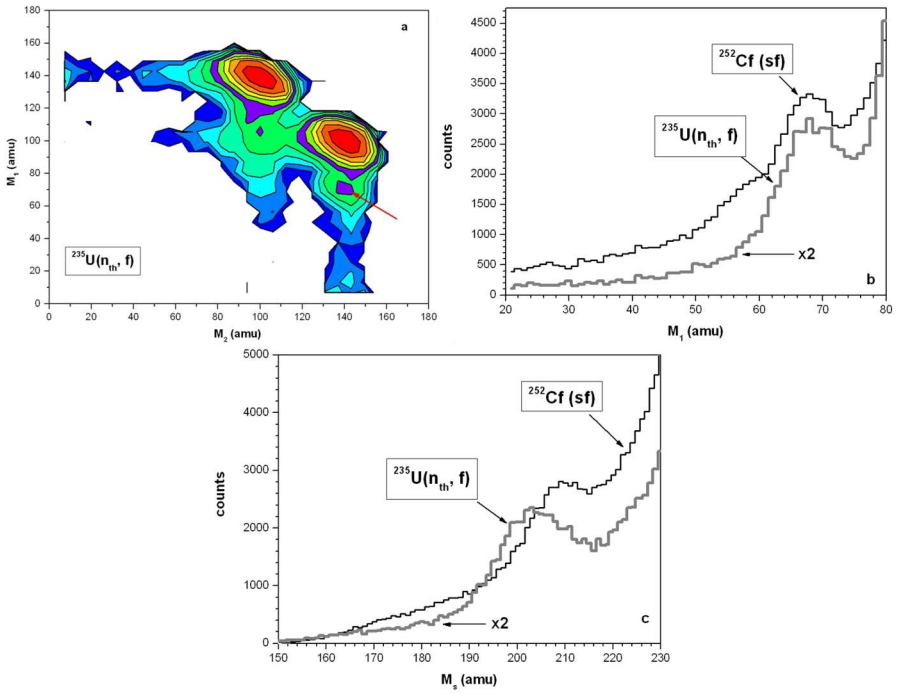

FIGURE 7. (Color online)a) The FF mass-mass distribution (logarithmic scale) obtained for the ^{235}U(n_{th},f) reaction. b) Projections of the bump onto the M_1 axis for comparison of the reactions discussed here. c) Projections of the bump onto the direction $M_s = M_2 + M_1 = \text{const}$.

are also magic [28].

Results of experiment Ex2, ^{235}U(n_{th},f)

The mere fact of the existence of the bump in the total mass on one side as discussed above, as well as the presence of its internal structure was confirmed in an experiment (Ex2) devoted to the ^{235}U(n_{th}, f) [29], in which nuclear charges were measured in addition.

A bump similar to that marked by an arrow in Fig. 4 is again well pronounced as shown in Fig. 7a). The yield of the events in the bump is $(5.1\pm0.4)\times10^{-3}$ relative to the total number of fission events detected. As in the previous case the bump is observed only in one spectrometer arm (marked by number 1) facing to the target backing. The projections of the bump onto the M_1 axis for both reactions are compared in Fig. 7b). The pronounced peaks in both cases are centered at the masses (68 ÷ 70) amu, associated with the magic isotopes of Ni. Projections onto the M_s = const direction are shown in Fig. 7c). Although the total masses of the corresponding two fissioning systems differ by 16 amu the projections of the bump onto this direction are shifted no greater than 6 amu. Such shift of the top yield in the frame of the wide peak could be assigned to the different population of the fission modes based on magic pairs of Sn/Ge or Sn/Ni isotopes in Cf and U* nuclei.

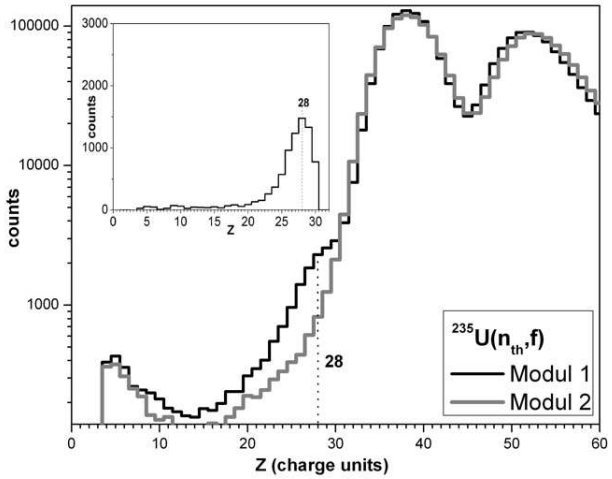

FIGURE 8. Nuclear charge spectra from the FF from the reaction ^{235}U(n_{th}, f), the FF are detected in the two opposite spectrometer arms. A difference in the yields (bump) presented in the upper panel in a linear scale is visible for the charges around Z = 28 (isotopes of Ni).

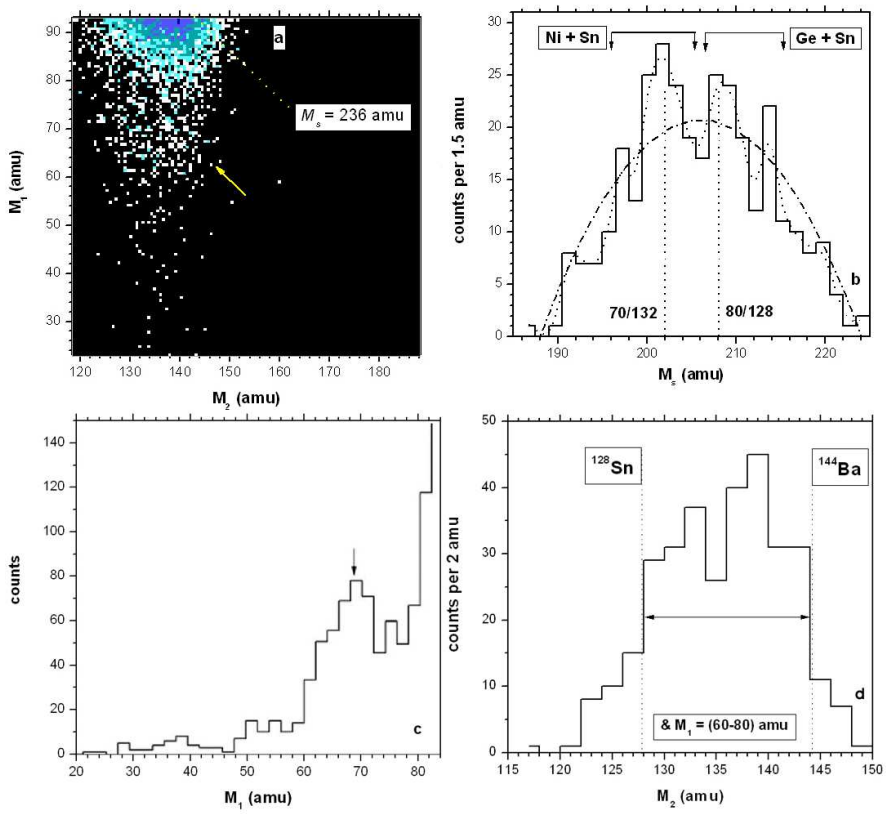

FIGURE 9. Upper row, a), mass-mass distribution of the fission events from the reaction ^{235}U(n_{th}, f) selected by the additional gate on the velocity-energy-loss, the V–dE matrix; b) Projection onto $M_1 + M_2$ = const direction. Parabolic and spline least squares fits are shown by dash-dot and dot lines respectively. c), Projection of the distribution onto M_1 axis; and d) Projection onto the M_2 axis for the events from the range M_1 = (60÷80) amu . See text for details.

We show the comparison of the spectra of nuclear charges of the measured FF in the two opposite spectrometer arms in Fig. 8. The result for the measured charges confirms the previous finding with the mass distributions, namely the existence of an additional bump in the arm with the scattering media. It confirms the hypothesis that the upper boundary of the additional bump (Fig. 7a), and b) is actually connected with Ni isotopes.

As was mentioned above, the presence of the tilted ridges M_s = const for the ^{252}Cf nucleus was revealed using a special mathematical process for the FF mass-mass distribution. This fact has been confirmed independently for the ^{236}U* system by using a selection with an additional parameter, the specific energy losses *dE* of the FF in the "stop" avalanche counter.

In Fig. 9 we show the mass-mass distribution of those FF, selected by the additional parameter of an increased energy loss in comparison to FF from the light mass peak of normal binary fission. In this way we can select the events when a "fork" of two fragments of a ternary decay fly into the same first spectrometer arm namely where the bump is observed. Total energy losses of these two fragments in the same counter have values, which are higher compared with the *dE* values for ordinary light fragments. It should be stressed that in this case the experimental variables used for gating (specific energy losses *vs* velocity) are not distorted due to scattering on the entrance grid of the BIC, being the main source of the background events.

In the bump region a tilted valley structure with reduced event density is clearly seen indicating the presence of ridges with specific total masses, M_s = const (Fig. 9a). It is marked by the tilted arrow. A projection of the bump onto this direction is shown in Fig. 9b), the left bracket in the spectrum shows the mass region of potential location of pairs of magic isotopes ^{128,132}Sn / ^{68,70,72}Ni. Similarly the right bracket corresponds to pairs ^{128,132}Sn / ^{80,82}Ge. At least two peaks centered at the partitions marked in the figure (70/132 and 80/128 amu) are statistically significant. Actually, a parabolic (structureless) fit shown by the dot-dash line gives χ^2/f = 2.1 (chi-square per degree of freedom), while a least squares approximation by the cubic spline (dot line) shows χ^2/f = 1.04.

A peak centered at 68 amu comes out in the projection of the bump onto the M_1 axis in Fig. 9c). Further as can be inferred from Fig. 9a) the heavy fragments involved in the bump are bounded by the mass numbers in the region 128–144 associated with magic nuclei of ^{128}Sn and ^{144}Ba. This conclusion is confirmed by the projection of the bump onto the corresponding axis (Fig. 9d), where the boundaries for Sn and Ba are shown. It should be noted that the internal structure of the bump seen in Fig. 9a) is reproduced as well if the selection is made using a gate based on the drift time [30].

SUMMARY

The present work has been devoted to the observation of a new multi-body decay channel called by us "collinear cluster tri-partition" (CCT). We observe in the mass-mass distributions (2*D*) a bump linked with large missing masses in the FF mass-mass distribution for cases, where one of the fragments passes through a scattering medium providing an angular divergence between the two CCT partners flying towards the same spectrometer arm. The second principal feature of the spectrometer to be stressed is the presence of the blocking structure (grid or mesh) at the entrance to the BIC. Only due

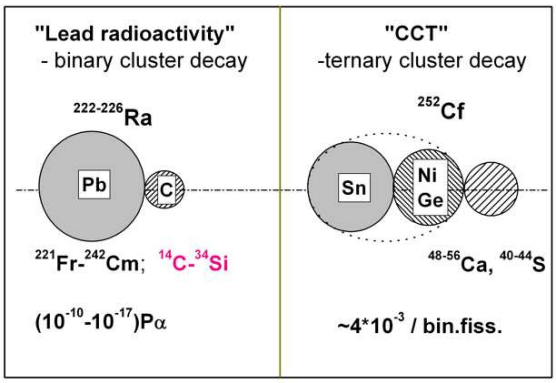

FIGURE 10. Cluster scheme for the comparison of the lead radioactivity with collinear cluster tri-partition.

to the sequential action of these two technical details, namely scattering and blocking allows the detection of a CCT event, in the frame of the missing mass method. Earlier studies of spontaneous fission of ^{252}Cf in the series of our experiments performed at different time-of-flight spectrometers [31] gave the same observation when both masses of the coincident fragments were identified in the frame of the velocity-energy (V–E) method. Bearing in mind, that potentially the scattering of fragments at the entrance to the E-detector could imitate these effects, we have used another approach with different experimental observables, being methodically independent from FF masses were needed. Such approach was realized in the other experiment Ex2 discussed in the present paper.

We have shown in Ex2 (Fig. 9), that the selection of the fission events using V–dE velocity-specific energy losses, confirmed not only the presence of the bump in the FF mass-mass distributions from the ^{235}U(n_{th}, f) reaction, but also confirmed its internal structure. In particular an effective cleaning of the bump region from the background in this case, allowed us to observe directly the tilted ridges (and, respectively, the valleys in between). These again were found to correspond to total masses of pairs of magic clusters namely (Ni/Sn) or (Ge/Sn). The ridges under discussion are actually linked with pairs of magic clusters, they are the same for the two fissioning systems, namely in ^{252}Cf and in ^{236}U*. These systems differ by 16 mass units, the position of the ridges stayed unchanged. It is believed that the ternary decay modes stand behind the tilted ridges and make clear physical sense formulated below in the "conclusions". In addition to the dE variable being absolutely independent from experimental mass values an estimation of the nuclear charge (Z) via the drift time in the ionization chambers is linked as well with the experimental fragment mass [20]. Thus the correct position of the bump in the nuclear charge of the fragments (projection on the Z axis in Fig. 8), gives clear arguments for the correctness of the origin of the bump.

CONCLUSIONS

Experimental results suggesting the existence of a new decay mode, the collinear cluster tri-partition (CCT) decay channel, have been presented. This decay mode manifests itself due to a particular bump corresponding to a specific missing mass in the FF mass-mass distributions. One of the decay modes which contribute to the bump can be treated as a new type of cluster decay as compared to the well known heavy ion or lead radioactivity. Key features of both are summed up in Fig. 10. The relatively high CCT yield can be understood if one assumes collective motion through hyper-deformed pre-scission shapes of the mother systems, which is supported by the fact that the linear arrangement realizes the lowest Coulomb potential energies of three clusters. We also emphasize, that the Q values for ternary fission are by 25–30 MeV more positive, again due to the formation of magic fragments, as in binary fission. The ternary fission process must be considered to proceed sequentially, with two neck ruptures in a short time sequence characteristic for binary fissions.

POSTSCRIPTUM

Discovering of the new type of multi-body decays of nuclei called CCT discussed here has rather long term history. First observation of the "strange" correlated events below the loci of conventional binary fission at the FOBOS setup was only first indication of the effect. Series of experiments at different time-of-flight spectrometers was needed to receive evidence that the effect is statistically reliable and well reproduced [31]. Strong arguments in favor of its physical nature presented above were obtained by attracting new experimental variables sensitive to the nuclear charge. Another experimental variable methodically independent from the fragments masses is a multiplicity of neutrons emitted in fission event. Most recent results in analysis of the neutron gated data are presented briefly below.

The experiment was performed at the FLNR of the JINR using COMETA (Correlation Mosaic E–T Array) setup [32, 33] (Fig. 11). It is double arm time-of-flight spectrometer which includes micro-channel plate (MCP) based "start" detector with the ^{252}Cf source inside, two mosaics of eight PIN diodes each and a "neutron belt" comprises 30 ^{3}He filled neutron counters. The geometry of the belt provides preferential detection of the neutrons emitted isotropically.

Fission fragments mass-mass distribution drown for the events where three neutrons (n = 3) were detected is shown in Fig. 12. The rectangle bounded by the magic nuclei attracts attention in the upper part of the figure. The tilted line corresponding to the fixed total mass of two detected fragments $M_s = M_1 + M_2 = 208$ amu (marked by the dash line) was also observed earlier.

Rectangular structure similar to this shown in Fig. 12b) was already discussed above (Fig. 9a). The evident difference between Figs. 9a) and 12b) consists in the masses of the light magic clusters namely ^{98}Sr and ^{108}Mo forming two opposite sides of the rectangle. Thus, we obtain independent confirmation of existence of the bump-like structure discussed earlier. We conclude as well that different pairs of magic clusters can be decisive for formation of the bump-like structures in the FF mass-mass distributions.

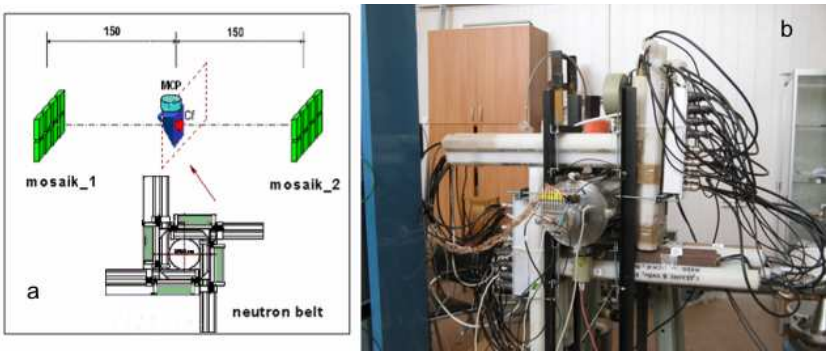

FIGURE 11. Scheme of the COMETA setup a), overall view of the spectrometer b).

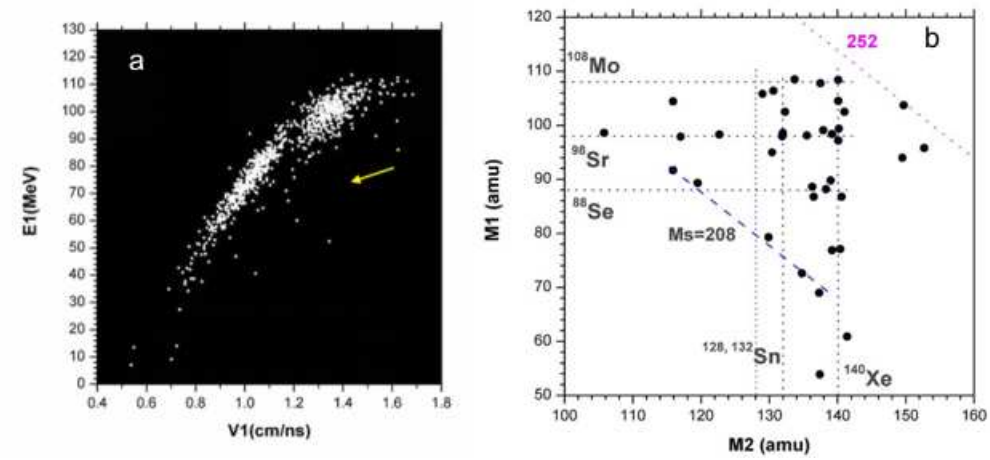

FIGURE 12. Velocity-energy distribution of the FF from ^{252}Cf (sf) under condition that three neutrons were detected in coincidence a). Mass-mass plot for the events beyond the loci of conventional binary fission in previous distribution b). Results were obtained at the COMETA setup.

It should be stressed that the COMETA setup was designed as an instrument for direct detection of all the partners of multi-body decays. Corresponding results obtained are the gratifying stuff for forthcoming presentations.

ACKNOWLEDGMENTS

This work is supported in part by the grant of the Department of Science and Technology of South Africa and by the grant of the Federal Ministry of Education and Research (BMBF) of Germany.

REFERENCES

1. O. Hahn and F. Strassmann, *Naturwissenschaften* **27**, 89–95 (1939).
2. K. A. Petrzhak and G. N. Flerov, *J. Phys.*, USSR **3**, 275–280 (1940).

3. L. Meitner and O. Frisch, *Nature* **143**, 239–240 (1939).
4. C. F. von Weizsäcker, *Z. Physik* **96**, 431–458 (1935).
5. W. J. Swiatecki, *Proceedings of the Second UN Conference on the Peaceful Uses of Atomic Energy, Geneva, 1958* United Nations, Geneva, 1958, Vol. **15**, pp. 651–659.
6. V. M. Strutinsky et al., *Nucl. Phys.* **46**, 639–659 (1963).
7. H. Diehl, W. Greiner, *Phys. Lett. B* **45**, 35–37 (1973).
8. H. Diehl, W. Greiner, *Nucl. Phys. A* **229**, 29–46 (1974).
9. D. N. Poenaru et al., *Phys. Rev. C* **59**, 3457–3460 (1999).
10. M. L. Muga, *Phys. Rev. Lett.* **11**, 129–131 (1963).
11. P. Schall et al., *Phys. Lett. B* **191**, 339–342 (1987).
12. F. Gönnenwein, *Nucl. Phys. A* **734**, 213–216 (2004).
13. S. A. Karamian et al., *Jadernaya Fizika* **5**, 959–965 (1963).
14. P. Glässel et al., *Z. Phys. A* **310**, 189–216 (1983).
15. Yu. V. Pyatkov et al., *Proceedings of the International Conference of Nuclear Physics "Nuclear Shells – 50 Years", Dubna, 1999*, edited by Yu.Ts. Oganessian et al., World Scientific, 2000, pp. 301–307.
16. Yu. V. Pyatkov et al., *Proceeding of the International Symposium on Exotic Nuclei EXON-2001, Baikal Lake, 2001*, edited by Yu. E. Penionzhkevich et al., World Scientific, 2002, pp. 181–185.
17. H.-G. Ortlepp et al., *Nucl. Instrum. Methods A* **403**, 65–97 (1998).
18. D. V. Kamanin et al., JINR Preprint Ð15-2007-182, Dubna, 2007.
19. A. Oed et al., *Nucl. Instrum. Methods* **205**, 451–453 (1983).
20. A. N. Tyukavkin et al., *Instrum. and Exp. Tech.* **52**, 508–518 (2009).
21. Yu. V. Pyatkov et al., JINR Preprint E15-2004-65, Dubna, 2004.
22. V. F. Apalin et al., *Nucl. Phys.* **71**, 553–560 (1965).
23. L. Meyer, *Physica Status Solidi (b)* **44**, 253–268 (1971).
24. A. V. Kravtsov and G. E. Solyakin, *Phys. Rev. C* **60**, 017601 (1999).
25. M. A. Mariscotti, *Nucl. Instr. and Methods* **50**, 309–320 (1967).
26. Yu. V. Pyatkov et al., *Nucl. Instr. and Methods A* **488**, 381–399 (2002).
27. B. D. Wilkins et al., *Phys. Rev. C* **14**, 1832–1863 (1976).
28. D. Rochman et al., *Nucl. Phys. A* **735**, 3–20 (2004).
29. Yu. V. Pyatkov et al., *Physics of Atomic Nuclei* **14**, 1309–1316 (2010).
30. D. V. Kamanin et al., *Int. Journal of Modern Physics E* **17**, 2250–2254 (2008).
31. Yu. V. Pyatkov et al., *Romanian Reports in Physics* **59**, 569–581 (2007).
32. Yu. V. Pyatkov et al., *Eur. Phys. J. A* **45**, 29–37 (2010).
33. D. V. Kamanin et al., *Proc. 18th International Seminar on Interaction of Neutrons with Nuclei (ISINN-18)*, 2010 in press.

SESSION: HADRON SPECTROSCOPY

Chairperson: S.B. Gerasimov

Transition form factors of pseudoscalar mesons: theory vs experiment

A.E. Dorokhov

JINR, Bogoliubov Laboratory of Theoretical Physics, Dubna, Russia

Abstract. Recently, the BABAR collaboration reported the measurments of the photon-pion transition form factor $F_{\pi\gamma\gamma^*}\left(Q^2\right)$, which are in strong contradiction to the predictions of the standard factorization approach to perturbative QCD. In the present talk, based on a nonperturbative approach to the QCD vacuum and on rather universal assumptions, we show that there exists two asymptotic regimes for the pion transition form factor. One regime with asymptotics $F_{\pi\gamma^*\gamma}\left(Q^2\right) \sim 1/Q^2$ corresponds to the result of the standard QCD factorization approach, while other violates the standard factorization and leads to asymptotic behavior as $F_{\pi\gamma^*\gamma}\left(Q^2\right) \sim \ln\left(Q^2\right)/Q^2$. Furthermore, considering specific nonlocal chiral quark models, we find the region of parameters, where the existing CELLO, CLEO and BABAR data for the pion transition form factor are successfully described.

Keywords: Pseudoscalar mesons, transition form factor, QCD
PACS: 14.40.Be,12.39.Ki

INTRODUCTION

The theory of hard exclusive processes, formulated within the factorization approach to perturbative quantum chromodynamics (pQCD), is based on the operator product expansion (OPE), the factorization theorems, and the pQCD evolution equations. In this context, the form factor for the photon-pion transition $\gamma^*\gamma^* \to \pi^0$, with both photons being spacelike (with photon virtualities $Q_1^2, Q_2^2 > 0$), was considered in [1, 2]. Since only one hadron is involved, the corresponding form factor $F_{\pi\gamma^*\gamma^*}(Q_1^2, Q_2^2)$ has the simplest structure for the pQCD analysis among the hard exclusive processes. The nonperturbative information about the pion is accumulated in the pion distribution amplitude (DA) $\varphi_\pi(x)$ for the fraction x of the longitudinal pion momenta p, carried by a quark. Another simplification is, that the short-distance amplitude for the $\gamma^*\gamma^* \to \pi^0$ transition is, to leading order, just given by a single quark propagator. Finally, the photon-pion form factor is related to the axial anomaly, when both photons are real.

Experimentally, the easiest situation is, when one photon virtuality is small and the other large. Under these conditions, the form factor $F_{\pi\gamma^*\gamma}(Q^2, 0)$ was measured at e^+e^- colliders by CELLO [3], CLEO [4] Collaborations (Fig. 1). In the region of large virtualities $Q^2 >> 1$ GeV^2, the pQCD factorization approach for exclusive processes predicts to leading order in the strong coupling constant [1, 2]

$$F_{\pi\gamma^*\gamma}^{\rm pQCD}(Q^2, 0) = \frac{2 f_\pi}{3Q^2} J, \tag{1}$$

where $J = \int_0^1 dx x^{-1} \varphi_\pi(x)$ is the inverse moment of the pion DA, and $f_\pi = 92.4$ MeV. The factor $1/Q^2$ reflects the asymptotic property of the quark propagator connecting

two quark-photon vertices (Fig. 2). The formula (1) is derived under the assumption, that the QCD dynamics at large distances (the factor Jf_π) and the QCD dynamics at small distances (the factor $1/Q^2$) is factorized. Moreover, under this assumption, the asymptotics is reached already at the typical hadronic scale of a few GeV^2. The pion DA $\varphi_\pi(x)$, in addition, evolves in shape with the change of the renormalization scale and asymptotically equals $\varphi_\pi^{\rm As}(x) = 6x(1-x)$. From this follows the famous asymptotic prediction (the straight dotted line in Fig. 1)

$$F_{\pi\gamma^*\gamma}^{\rm pQCD,As}(Q^2,0) = \frac{2f_\pi}{Q^2}. \tag{2}$$

Recently, the BABAR collaboration published new data (Fig. 1) for the $\gamma\gamma^* \to \pi^0$ transition form factor in the momentum transfer range from 4 to 40 GeV^2 [5]. They found the following puzzling result: At $Q^2 > 10$ GeV^2 the measured form factor multiplied by the photon virtuality $Q^2 F_{\pi\gamma^*\gamma}(Q^2,0)$ exceeds the predicted asymptotic limit (2) and, moreover, continues to grow with increasing Q^2. This result is in strong contradiction to the predictions of the standard QCD factorization approach mentioned above. The BABAR data very well match the older data obtained by the CLEO collaboration in the smaller Q^2 region, but extend to a much lager Q^2 values.

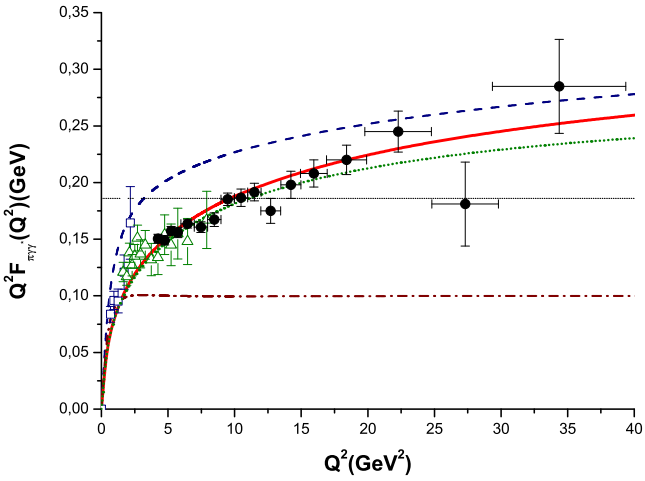

FIGURE 1. Photon-pion transition form factor in asymmetric kinematics for the instanton model with parameters $M_q = 125$ MeV, $\Lambda = 0.016$ GeV^{-2} (short pointed line), $M_q = 300$ MeV, $\Lambda = 1.3$ GeV^{-2}(dash-dotted line); and chiral model with parameters $M_q = 125$ MeV, $\Lambda = 0.0098$ GeV^{-2} (solid line) and $M_q = 300$ MeV, $\Lambda = 0.639$ GeV^{-2} (dashed line). The straight dotted line is asymptotic limit $2f_\pi$. The data points are from the CELLO [3] (empty squares), CLEO [4] (empty triangles) and BABAR (filled circles) [5] Collaborations.

NONLOCAL CHIRAL QUARK MODEL

We will analyze the photon-pion transition form factor in the gauged nonlocal chiral quark model based on the picture of nontrivial QCD vacuum. The attractive feature

of this model is, that it interpolates the physics at large and small distances. At low energy, it enjoys the spontaneous breaking of chiral symmetry, the generation of the dynamical quark mass, and it satisfies the basic low energy theorems. In particular, the correct normalization of the form factor by the axial anomaly $F_{\pi\gamma\gamma}(0,0) = 1/\left(4\pi^2 f_\pi\right)$, and the Goldberger-Treiman relation, connecting the quark-pion coupling $g_{q\pi}$ and the dynamical quark mass M_q with the physical pion decay constant f_π: $f_\pi = M_q/g_{q\pi}$. At energies much higher than the characteristic hadronic scale, it becomes the theory of free massless quarks (in chiral limit).

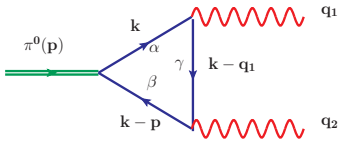

FIGURE 2. The triangle diagram in momentum and α-representation notation.

Let us discuss the properties of the triangle diagram (Fig. 2) at large photon virtualities. To this end, we do not need to completely specify the elements of the diagram technique, which are, in general, model dependent, but shall restrict ourselves to rather general requirements. All expressions will be treated in Euclidean space appropriate for the process under consideration and for the treatment of nonperturbative physics. The nonperturbative quark propagator, dressed by the interaction with the QCD vacuum, is

$$S(k) = \frac{\widehat{k} + m\left(k^2\right)}{D\left(k^2\right)}. \tag{3}$$

The main requirement to the quark propagator is, that at large quark virtualities $k^2 \to \infty$ one has

$$S(k) \to \frac{\widehat{k}}{k^2}. \tag{4}$$

We assume also, that the dynamical quark mass is a function of the quark virtuality k^2 and normalized at zero as $m(0) = M_q$. At large virtualities, it drops to the current quark mass m_{curr} faster than any power of k^{-2} (see the discussion in [6])

$$m\left(k^2\right) \sim M_q \exp\left(-\left(k^2\right)^a\right) + m_{curr}, \quad a > 0. \tag{5}$$

The denominator in (3) at large virtualities $k^2 \to \infty$ is $D\left(k^2\right) \to k^2$.

It is well known (see, e.g., [7, 8]), that the change of the quark propagator leads to a modification of the quark-photon vertex in order to preserve the Ward-Takahashi identity

$$\Gamma_\mu\left(k, q, k' = k + q\right) = -ie_q\left[\gamma^\mu - \Delta\Gamma_\mu\left(k, q, k' = k + q\right)\right]. \tag{6}$$

The term $\Delta\Gamma_\mu(q)$ is not uniquely defined, even within a particular model, especially its transverse part. The importance of the full vertex Γ_μ is, that the axial anomaly is reproduced [9], and thus the photon-transition form factor correctly normalized. Fortunately, due to the fact, that $\Delta\Gamma_\mu$ is not proportional to γ_μ matrix, the corresponding amplitude has no projection onto the leading twist operator. Thus, this term is suppressed, if a large

photon virtuality passes through the vertex, and hence does not participate in the leading asymptotics of the form factor. Its leading asymptotics results exclusively from the local part of the photon vertex

$$\Gamma_{\mu}^{\mathrm{As}}\left(k,q,k'=k+q\right)=-ie_{q}\gamma^{\mu}. \tag{7}$$

Furthermore, we need the quark-pion vertex,

$$\Gamma_{\pi}^{a}\left(p\right)=\frac{i}{f_{\pi}}\gamma_{5}\tau^{a}F\left(k_{+}^{2},k_{-}^{2}\right), \tag{8}$$

where k_{+} and k_{-} are the quark and antiquark momenta. In the following, the important feature of the vertex function $F\left(k_{+}^{2},k_{-}^{2}\right)$ will be its behavior in the limit, when one quark virtuality is asymptotically large (e.g., $k_{-}^{2}\rightarrow\infty$) and the other ($k_{+}^{2}$) remains finite. There are two possibilities,

$$F^{f}\left(k_{+}^{2},k_{-}^{2}\right)\rightarrow 0, \tag{9}$$

and

$$F^{uf}\left(k_{+}^{2},k_{-}^{2}\right)\rightarrow g\left(k_{+}^{2}\right). \tag{10}$$

Finally, one needs the projection of the pion state onto the leading twist operator

$$\Gamma_{\mu}^{5,\mathrm{As}}\left(k,q,k'=k+q\right)=\gamma^{\mu}\gamma^{5}. \tag{11}$$

This projection is determined by the matrix element $\left\langle 0\left|\overline{q}\gamma^{\mu}\gamma^{5}\tau^{a}q\right|\pi^{a}\left(p\right)\right\rangle=-i2f_{\pi,\mathrm{PS}}$, where the constant $f_{\pi,\mathrm{PS}}$ is (here $m'\left(u\right)=dm\left(u\right)/du$)

$$f_{\pi,\mathrm{PS}}^{2}=\frac{N_{c}}{4\pi^{2}}\int_{0}^{\infty}du\quad u\frac{F\left(u,u\right)}{D^{2}\left(u\right)}\left(m\left(u\right)-\frac{1}{2}um'\left(u\right)\right), \tag{12}$$

which coincides with the pion decay constant $f_{\pi,\mathrm{PS}}$ in the Pagels-Stokar form [11].

ASYMPTOTICS OF PION-PHOTON TRANSITION FORM FACTOR

The invariant amplitude for the process $\gamma^{*}\gamma^{*}\rightarrow\pi^{0}$ is given by

$$A\left(\gamma^{*}\left(q_{1},\varepsilon_{1}\right)\gamma^{*}\left(q_{2},\varepsilon_{2}\right)\rightarrow\pi^{0}\left(p\right)\right)=-ie^{2}\varepsilon_{\mu\nu\rho\sigma}\varepsilon_{1}^{\mu}\varepsilon_{2}^{\nu}q_{1}^{\rho}q_{2}^{\sigma}F_{\pi\gamma^{*}\gamma^{*}}\left(-q_{1}^{2},-q_{2}^{2}\right), \tag{13}$$

where ε_{i}^{μ} are the photon polarization vectors, $p^{2}=m_{\pi}^{2},q_{1}^{2}=-Q_{1}^{2},q_{2}^{2}=-Q_{2}^{2}$. In the effective nonlocal quark-model considered above, one finds the contribution of the triangle diagram to the invariant amplitude [10],

$$A\left(p^{2};q_{1}^{2},q_{2}^{2}\right)=A^{\mathrm{loc}}\left(p^{2};q_{1}^{2},q_{2}^{2}\right)+A^{\mathrm{nonloc}}\left(p^{2};q_{1}^{2},q_{2}^{2}\right),$$

where the first term contains only local part of the photon vertices and the second term comprises the rest.

As we discussed above, the leading asymptotics results from the local part of the amplitude, $A^{\rm loc}$. After taking the Dirac trace one obtains

$$A^{\rm loc}\left(p^2;q_1^2,q_2^2\right) = \frac{e^2N_c}{6\pi^2 f_\pi}\int\frac{d^4k}{\pi^2}F(k_+^2,k_-^2) \cdot\frac{m\left(k_+^2\right)\left(\varepsilon_{12kq_2}-\varepsilon_{12q_1q_2}\right)-m\left(k_-^2\right)\varepsilon_{12q_1k}+m\left(k_3^2\right)\varepsilon_{12pk}}{D\left(k_+^2\right)D\left(k_-^2\right)D\left(k_3^2\right)}, \quad (14)$$

where $p=q_1+q_2$, $q=q_1-q_2$, $k_\pm=k\pm p/2$, $k_3=(k_+-q_1)$, and $\varepsilon_{12kq_2}=\varepsilon_{\mu\nu\lambda\rho}\varepsilon_1^\mu\varepsilon_2^\nu k^\lambda q_2^\rho$, etc.

In order to analyze the asymptotic properties of the form factor, let us transform the integral in (14) formally into the α representation. Let us define for any function F of virtuality k^2, decaying at large virtuality as $1/k^2$ or faster, its α representation (Laplace transform)

$$F\left(k^2\right)=\int_0^\infty d\alpha e^{-\alpha k^2}f(\alpha), \qquad F\left(k^2\right)\sim f(\alpha), \quad (15)$$

where $F\left(k^2\right)$ is the image of the original $f(\alpha)$. Then, the momentum integral in (14) is transformed into the following expression for the form factor (in the chiral limit)

$$F^{\rm loc}_{\pi\gamma^*\gamma^*}\left(p^2=0;Q_1^2,Q_2^2\right) = \frac{N_c}{6\pi^2 f_\pi}\int\frac{d(\alpha\beta\gamma)}{\Delta^3}e^{-\frac{1}{\Delta}\gamma\left(\alpha Q_1^2+\beta Q_2^2\right)} \cdot\left[d(\gamma)\left(\alpha G_{m,0}(\alpha,\beta)+\beta G_{0,m}(\alpha,\beta)\right)+\gamma d_m(\gamma)G(\alpha,\beta)\right], \quad (16)$$

where $\Delta=\alpha+\beta+\gamma$ and $\int d(\alpha\beta\gamma)...=\int_0^\infty d\alpha\int_0^\infty d\beta\int_0^\infty d\gamma...$ In (16) we introduce the following notations

$$\frac{1}{D\left(k^2\right)}\sim d(\alpha), \qquad \frac{m\left(k^2\right)}{D\left(k^2\right)}\sim d_m(\alpha), \quad (17)$$

$$\frac{F(k_+^2,k_-^2)}{D\left(k_+^2\right)D\left(k_-^2\right)}\sim G(\alpha,\beta), \quad \frac{m\left(k_+^2\right)F(k_+^2,k_-^2)}{D\left(k_+^2\right)D\left(k_-^2\right)}\sim G_{m,0}(\alpha,\beta). \quad (18)$$

Asymmetric kinematics I

Let us now consider the asymmetric kinematics $Q_1^2=Q^2, Q_2^2=0$. Then one has

$$F^{\rm loc}_{\pi\gamma^*\gamma}\left(0;Q^2,0\right) = \frac{N_c}{6\pi^2 f_\pi}\int\frac{d(\alpha\beta\gamma)}{\Delta^3}e^{-\frac{\gamma\alpha}{\Delta}Q^2} \cdot\left[d(\gamma)\left(\alpha G_{m,0}(\alpha,\beta)+\beta G_{0,m}(\alpha,\beta)\right)+\gamma d_m(\gamma)G(\alpha,\beta)\right]. \quad (19)$$

Let us first consider the model with the quark-pion vertex possessing the property (9). The leading large Q^2 behavior corresponds to the integral over small γ and we get for $Q^2\to\infty$

$$F^{\rm loc,I}_{\pi\gamma^*\gamma}\left(0;Q^2,0\right)=\frac{N_c}{6\pi^2 f_\pi}\int\frac{d(\alpha\beta)}{(\alpha+\beta)^3}\frac{\alpha G_{m,0}(\alpha,\beta)+\beta G_{0,m}(\alpha,\beta)}{D\left(\frac{\alpha Q^2}{\alpha+\beta}\right)}.$$

After change of variables $\alpha \to xL, \beta \to (1-x)L$, we arrive at the representation

$$F^{\mathrm{loc,I}}_{\pi\gamma^*\gamma}\left(0;Q^2,0\right) = \frac{2}{3}\frac{f^2_{\mathrm{PS},\pi}}{f_\pi}\int_0^1 dx \frac{1}{D\left(xQ^2\right)}\varphi^f_\pi(x), \tag{20}$$

where the pion distribution amplitude is

$$\varphi_\pi(x) = \frac{N_c}{4\pi^2 f^2_{\mathrm{PS},\pi}}\int_0^\infty \frac{dL}{L} e^{x\bar{x}Lp^2}\left(xG_{m,0}(xL,\bar{x}L) + \bar{x}G_{0,m}(xL,\bar{x}L)\right), \tag{21}$$

Because in the considered case $\varphi_\pi(x)$ vanishes at the endpoints the actual asymptotics is in agreement with (1).

As we have already noted in Introduction the asymptotic behavior (1) is not seen in the BABAR data. Nevertheless, even for the case considered, in principle, it is possible to simulate in some wide preasymptotic kinematical region a logarithmically enhanced behavior of the form factor. This happens if one assumes that the pion DA entering (20) is almost flat $\varphi_\pi(x) \approx 1$, i.e. it is close to a constant everywhere except small vicinity near endpoints. Then, nonfactorizable asymptotic coefficient J^f appears [12]

$$J^L = Q^2\int_0^1 dx \frac{1}{D\left(xQ^2\right)}. \tag{22}$$

Let us consider some popular models of the nonperturbative quark propagator

$$\frac{1}{D\left(k^2\right)} = \frac{1-\exp\left(-k^2/\Lambda^2\right)}{k^2} \tag{23}$$

$$D\left(k^2\right) = k^2 + m^2(k). \tag{24}$$

The first expression has the property of analytical confinement [13, 14]and the second one is typical for chiral models. In quark models, where the first propagator is used, the parameter Λ has the meaning of a dynamical quark mass [15], $\Lambda \equiv M_q$, with typical values of $M_q = 200 - 300$ MeV. Inserting (23) into (22) it is possible to show that the leading asymptotic behavior as $Q^2 \to \infty$

$$J^L_{AC} = \ln\left(Q^2/M_q^2\right) + \mathrm{const}, \tag{25}$$

This result (25) is very close to the result obtained in [16] (Gaussian and logarithmic models), where the idea of flat pion distribution amplitude for explanation of the BABAR data was suggested (see also [17, 18]).

Asymmetric kinematics II

Now, let us consider the model with the quark-pion vertex possessing the property (10). It is convenient to rearrange the terms in the pion form factor in the following way

$$F^{\mathrm{loc,II}}_{\pi\gamma^*\gamma}\left(0;Q^2,0\right) = \frac{N_c}{6\pi^2 f_\pi}\int \frac{d(\alpha\beta\gamma)}{\Delta^3} e^{-\frac{\gamma\alpha}{\Delta}Q^2}\left\{\beta r_m(\beta)\right. \tag{26}$$

$$+\alpha G_{m,0}(\alpha,\beta)\,d(\gamma)+\beta\left[G_{0,m}(\alpha,\beta)-r_m(\beta)\right]$$
$$+\gamma G(\alpha,\beta)\,d_m(\gamma)+\beta r_m(\beta)\left[d(\gamma)-1\right]$$
$$+\beta\left[d(\gamma)-1\right]\left[\beta G_{0,m}(\alpha,\beta)-r_m(\beta)\right]\Big\},$$

where we introduce notations for the originals

$$\frac{g\left(k^2\right)}{D\left(k^2\right)}\sim r(\alpha),\qquad \frac{m\left(k^2\right)g\left(k^2\right)}{D\left(k^2\right)}\sim r_m(\alpha).$$

After standard manipulations with the integrals one obtains the following large-Q^2 asymptotic behavior as $Q^2\to\infty$ transformed to the momentum representation [12]

$$F^{As,\mathrm{II}}_{\pi\gamma^*\gamma}\left(0;Q^2,0\right)=\frac{1}{Q^2}\frac{N_c}{6\pi^2 f_\pi}\left[\int_0^\infty du\frac{m(u)\,g(u)}{D(u)}\ln\left(\frac{Q^2}{u}\right)+A\right], \tag{27}$$

$$A=\int_0^\infty du\frac{1}{D(u)}\int_0^1 dy\frac{m(yu)}{D(yu)}\left\{uF^{uf}(u,yu)-\left[u+2m^2(u)\right]g(yu)\right\}. \tag{28}$$

The asymptotic expression (27) generalizes the asymptotic formula (1) for the case when the standard factorization is violated.

THE INSTANTON AND CHIRAL MODELS

In the previous section we considered the asymptotic behavior of the pion transition form factor. In order to calculate this form factor in the whole kinematic region and compare with available experimental data, we should further specify our model assumptions. Let us introduce the momentum-dependent dynamical quark mass entering the propagator (3) as

$$m\left(k^2\right)=M_q f^2\left(k^2\right) \tag{29}$$

and take the profile function $f\left(k^2\right)$ in a Gaussian form $f\left(k^2\right)=\exp\left(-\Lambda k^2\right)$. Thus, the model contains two parameters, the dynamical quark mass M_q and the non-locality parameter Λ.

Next, we need to specify the nonlocal part of the vector vertex that does not participate in the leading asymptotics, but is very important in implementing the low energy theorems. The nonlocal part of the vector vertex in (6) is taken of the form [7]

$$\Delta\Gamma_\mu\left(k,q,k'=k+q\right)=\left(k+k'\right)_\mu\frac{m\left(k'^2\right)-m\left(k^2\right)}{k'^2-k^2}. \tag{30}$$

Further, we will consider two kinds of quark-pion vertex (8), the first given by

$$F_I\left(k_+^2,k_-^2\right)=M_q f\left(k_+^2\right)f\left(k_-^2\right), \tag{31}$$

and the second by

$$F_\chi\left(k_+^2,k_-^2\right)=\frac{1}{2}M_q\left[f^2\left(k_+^2\right)+f^2\left(k_-^2\right)\right]. \tag{32}$$

The first one is motivated by the instanton picture of QCD vacuum [19] and the second by the nonlocal chiral quark model advertised in [20]. We shall in the further discussion refer to vertex function (31), which has the $k^2 \to \infty$ behavior (9), as the instanton model, and to the other choice (32), corresponding to $k^2 \to \infty$ behavior(10), as the chiral model.

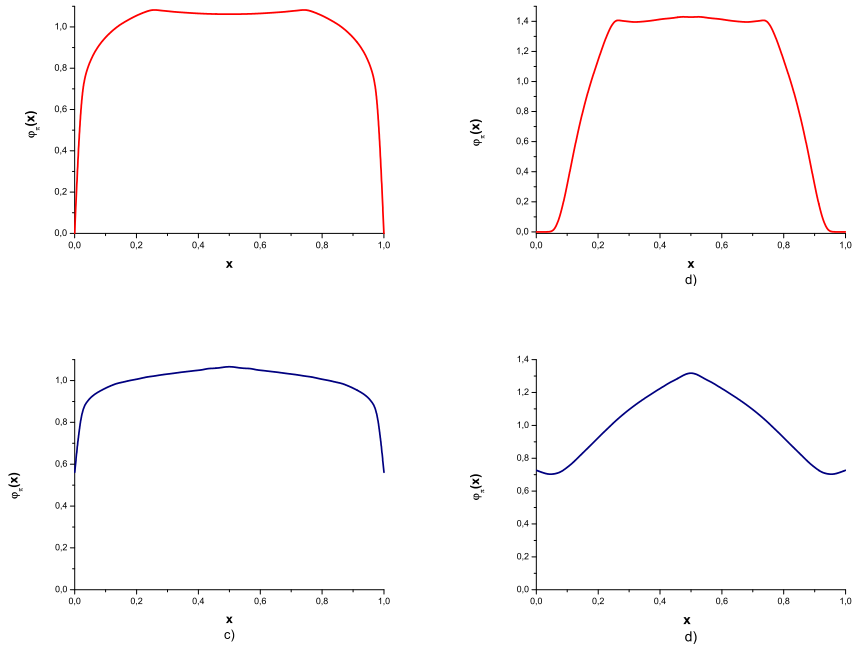

FIGURE 3. Pion distribution amplitude for the instanton model with parameters a) $M_q = 125$ MeV, $\Lambda = 0.016$ GeV^{-2} and b) $M_q = 300$ MeV, $\Lambda = 1.3$ GeV^{-2}; and chiral model with parameters c) $M_q = 125$ MeV, $\Lambda = 0.0098$ GeV^{-2} and d) $M_q = 300$ MeV, $\Lambda = 0.639$ GeV^{-2}.

In Fig. 3 the different shapes of the pion DA are shown as they are calculated within the instanton and chiral models for the values of the dynamical quark mass $M_q = 300$ MeV and $M_q = 125$ MeV. The parameter Λ is defined to fit the pion decay constant in chiral limit $f_\pi = 85$ MeV. For smaller M_q the pion DA is close to a flat shape. For larger M_q it is more sensitive to the nonlocal part of the photon vertex and, in case of the instanton model, it is strongly suppressed in the vicinity of endpoints.

THE BABAR DATA WITHIN THE INSTANTON AND CHIRAL MODELS

Let us consider the model predictions for the pion transition form factor in the asymmetric kinematics ($q_1^2 = Q^2, q_2^2 = 0$) in the region, where experimental data exist. In Fig. 1, we show the predictions for different values of M_q. For a quark mass $M_q = 300$ MeV the model dependence is very strong and the theoretical curves are very far from the experimental points. The chiral model overshoots the data, while the instanton model, in correspondence with the standard factorization scenario, shows the asymptotic $1/Q^2$ behavior very early, already at $Q^2 \sim 1$ GeV^2. It is clearly seen, that in order to describe

the BABAR data, one has to take the dynamical quark mass $M_q \approx 125$ MeV. Then both models have an qualitatively good description, with some preference to the chiral model.

The parameter space that describes the data up to 40 GeV^2 is rather narrow. For the chiral model it is $M_q \approx 125 \pm 10$ MeV, and for the instanton model it is $M_q \approx 130 \pm 5$ MeV. Thus in this region the instanton model simulate the logarithmically enhanced behavior due to rather flat pion DA. However, the further behavior of the form factor is rather different for different models. The instanton model finally reach its actual asymptotic $1/Q^2$ with the asymptotic coefficient given by

$$J^I = \frac{N_c}{4\pi^2 f_{\mathrm{PS},\pi}^2} M_q \int_0^\infty du \frac{u f(u)}{D(u)} \int_0^1 dy \frac{f(yu)\, m(yu)}{D(yu)}. \tag{33}$$

For the chiral model the logarithmic growth continues for all Q^2 with the asymptotics as $Q^2 \to \infty$ following from (27)

$$F_{\pi\gamma^*\gamma}^{As,\chi}\left(0;Q^2,0\right) = \frac{1}{Q^2}\frac{N_c}{12\pi^2 f_\pi}\left[\int_0^\infty du \frac{m^2(u)}{D(u)} \ln\left(\frac{Q^2}{u}\right) + A^\chi\right], \tag{34}$$

$$A^\chi = \int_0^\infty du \frac{m(u)}{D(u)} \int_0^1 dy \frac{m(yu)}{D(yu)} \left[u - 2m(u)\, m(yu)\right].$$

CONCLUSIONS

As it was stressed in Introduction the main problem to explain the BABAR data is the unstopped growth of the data points for $Q^2 F_{\pi\gamma\gamma^*}\left(Q^2\right)$ that is inconsistent with the predicted $Q^2 F_{\pi\gamma\gamma^*}\left(Q^2\right) \to$ constant, following from simple asymptotic properties of the massless quark propagator. The key point, to solve this problem, is to consider the properties of the pion vertex function $F(k_1^2, k_2^2)$ which is the analog of the light-cone pion wave function. There are two possibilities for the momentum dependence of the pion vertex function. In the limit, when one quark virtuality, k_1^2, goes to infinity, and the other, k_2^2, remains finite, the vertex function may not necessarily tend to zero. When it goes to zero, the pion DA $\varphi_\pi(x)$, which is a functional of the pion vertex function, is zero at the endpoints, $\varphi_\pi(0) = \varphi_\pi(1) = 0$, with either strong or weak suppression in the neighborhood of the endpoints $x = 0$ and $x = 1$. For the situation of strong suppression, the asymptotic $1/Q^2$ behavior of the pion form factor in asymmetric kinematics ($Q_1^2 = Q^2, Q_2^2 = 0$) is developed very early, in contradiction with the BABAR data. For weak suppression (resembling a flat distribution amplitude of the pion), the asymptotic $1/Q^2$ behavior is developed quite late, and can give a reasonable description of the data in the BABAR region with a $\ln Q^2/Q^2$ behavior in this region. For the other case of non-vanishing pion vertex function in the above limit, the pion DA $\varphi_\pi(x)$ is not zero at the endpoints, and therefore the asymptotic $\ln Q^2/Q^2$ behavior persists over the whole range, in particular in the BABAR region.

Concluding we may say, that the BABAR data being unique in their accuracy and covering a very wide kinematical range, are consistent with considerations based on nonperturbative QCD dynamics and may indicate specific properties of the pion wave function.

ACKNOWLEDGMENTS

The author acknowledges partial support from the Russian Foundation for Basic Research projects no. 10-02-00368.

REFERENCES

1. G. P. Lepage and S. J. Brodsky, Phys. Rev. **D22**, 2157 (1980).
2. S. J. Brodsky and G. P. Lepage, Phys. Rev. **D24**, 1808 (1981).
3. CELLO, H. J. Behrend *et al.*, Z. Phys. **C49**, 401 (1991).
4. CLEO, J. Gronberg *et al.*, Phys. Rev. **D57**, 33 (1998), hep-ex/9707031.
5. The BABAR, B. Aubert *et al.*, Phys. Rev. **D80**, 052002 (2009), 0905.4778.
6. A. E. Dorokhov, Eur. Phys. J. **C42**, 309 (2005), hep-ph/0505007.
7. J. Terning, Phys. Rev. **D44**, 887 (1991).
8. R. D. Bowler and M. C. Birse, Nucl. Phys. **A582**, 655 (1995), hep-ph/9407336.
9. R. S. Plant and M. C. Birse, Nucl. Phys. **A703**, 717 (2002), hep-ph/0007340.
10. A. E. Dorokhov, JETP Lett. **77**, 63 (2003), hep-ph/0212156.
11. H. Pagels and S. Stokar, Phys. Rev. **D20**, 2947 (1979).
12. A. E. Dorokhov, arXiv:1003.4693 [hep-ph].
13. G. V. Efimov and M. A. Ivanov, Int. J. Mod. Phys. **A4**, 2031 (1989).
14. G. V. Efimov and M. A. Ivanov, *The Quark Confinement Model of Hadrons* (, 1993), Bristol, UK: IOP, 177 p.
15. A. E. Radzhabov and M. K. Volkov, Eur. Phys. J. **A19**, 139 (2004), hep-ph/0305272.
16. A. V. Radyushkin, Phys. Rev. **D80**, 094009 (2009), 0906.0323.
17. A. E. Dorokhov, Phys. Part. Nucl. Lett. **7**, 229 (2010), 0905.4577.
18. A. E. Dorokhov, Nucl. Phys. Proc. Suppl. **198**, 190 (2010), 0909.5111.
19. D. Diakonov and V. Y. Petrov, Nucl. Phys. **B272**, 457 (1986).
20. B. Holdom, J. Terning, and K. Verbeek, Phys. Lett. **B245**, 612 (1990).

Exotic hadrons

N.I.Kochelev

JINR, Bogoliubov Laboratory of Theoretical Physics, Dubna, Russia

Abstract. We review the modern status of exotic hadrons. It is point out that complex structure of nonperturbative QCD vacuum gives a strong influence to the properties of exotic hadrons. The importance of the investigations of exotic hadron properties in quark-gluon plasma is emphasized.

Keywords: Exotic hadrons, instantons, QCD
PACS: 12.38.Lg,12.39.Mk

The constituent quark models are widely used for the description of hadron properties. In the framework of such approach the most observed meson states are quark-antiquark bound states and baryons are three-quark system. However, there are no an evident reasons to forbid the existence of so-called exotic states. For example, in various versions of the constituent quark model the multiquark states with number of quark and antiquark more then three should exist as well. Moreover, the quark-gluon hybrid states and glueballs which include valence gluons are under discussion now. There are two types of exotic states. Hidden exotic states can have the same quantum numbers as the ordinary hadrons. Open exotic states have quantum numbers which impossible to obtain within quark-antiquark and three-quark model for hadrons. Some of them may be with open and hidden exotics. The history of the hadron exotics was started many years ago in a famous Jaffe's papers [1]. Unfortunately, due to large masses of exotic states one might expect that they should decay very fast to usual hadrons. However, some possible exceptions from that rule was found. One of them is famous H-dihyperon with quark content $udsuds$. Indeed, it was shown within imporved bag model, that strong flavor- and spin-dependent instanton induced interaction between quarks might lead to deeply bound H-dibaryon state [2]. We should stress that instanton induced interaction is related to the complex topological structure of QCD vacuum [3, 4]. The importance of such interaction in spectroscopy of usual and exotic hadrons was shown in many papers (see, for example, reviews [5, 6]).

Recently, the development of the exotic spectroscopy was related mainly to attempts to discribe properties of θ^+ pentaquark which was expected to have small width (about 15 MeV) and small mass (about 1540 MeV) which has been predicted within soliton model for the baryons [7]. Within the constituent quark model such state is the bound state of two ud diquarks and one strange antiquark [8] or the bound state of ud diquark and $ud\bar{s}$ in the instanton-antiinstanton field [9, 10]. Unfortunately, experimental situation around this state is highly controversial. Some of the experimental groups, e.g. [11, 12], report on the observation of this state, but other high statistics experiments (see, for example [13]) do not see such resonance. Furthermore, it was shown recently, that more pronounced LEPs data [14] might be explained by final particle rescattering effect [15].

We should also emphasize that within the quark model it is rather difficult to explain

the modern experimental restrictions for the width of such resonance, $\Gamma < 1MeV$ [11]. Furthermore, the precise calculations of the θ^+ mass within the QCD sum rules [16] give larger value of its mass comparing to the soliton model prediction and show a very weak signal for the bound state. Within the soliton model θ^+ is the member of flavor antidecuplet. Therefore, if such model is correct, the other members of antidecuplet should exist as well. At the present time the candidate for nonstrange pentaquark $N^*(1685)$ is under discussion [17] and first experimental indication for the existence of such resonance was published very recently [18].

At present, increasing attention is coming to the problem of four-quark states, called tetraquarks. The interest to these states is related to the necessity to explain the scalar meson spectrum, which does not follow the predictions of naive quark-antiquark model. Central problem here is the sigma($f_0(600)$)- meson which probably has very complicated internal structure. For the long time even existence of such state was in doubts because the pion-pion scattering phase does not change on 90° at resonance. The problem has been solved in recent papers by Achasov with collaborators [19]. They show that within the sigma model the sigma-pole contribution is hidden in the large background amplitude of the pion-pion scattering. At the present time the sigma-meson is considered as a well established resonance with the mass around 440 MeV and the width about 540 MeV [20]. From the theoretical point of view the sigma-meson may include large admixture of four-quark state [21] or/and glueball [22], [23]. Furthermore, the properties of the sigma-meson in quark-gluon plasma (QGP) and in vacuum might be different. This observation open a new way to investigate the properties of QGP through changing of properties of the sigma-meson produced in heavy ion collisions [24], [25].

Very interesting bound states predicted within different QCD based approaches are hybrids, quark-gluon bound states. The famous candidate for such hybrid is $\pi(1600)$ state with exotic quantum numbers, $J^{PC} = 1^{-+}$. The evidence for $\pi(1600)$ was obtained for the first time by VES Collaboration at Protvino [26] and recently the search of this state was continued by E852 Collaboration at Brookhaven, by CLAS at CEBAF and by COMPASS at CERN. The result of the analysis of data coming from these experiments is rather controversial [27], [28], [29]. Therefore, the intensive search of hybrids is continued at several current experiments.

Glueball states are one of the firm predictions of QCD and their properties are studied in different approaches based on QCD, for example, within the lattice QCD and QCD sum rules (see review [30]). The main activity in this field is related to the investigation of low mass glueball states with zero spin and quantum numbers $J^{PC} = 0^{\pm+}$ and to tensor glueball, $J^{PC} = 2^{++}$. Recent calculations show significant mixing of zero spin glueballs with ordinary quarkonium states and therefore the ambiguity problem of theoretical interpretation of the experimental data for such states growths. From our point of view, cleaner glueball channel is the tensor channel, where the mixing with quark-antiquark states is expected to be very small.

It has been suggested that the glueballs can exist above deconfinement temperature and may play an important role in the dynamic of strongly interacting Quark-Gluon Plasma (QGP) [33, 31]. In particular, in [31] it is suggested that a very light pseudoscalar glueball can exist in QGP and might be responsible for the residual strong interaction between gluons. The lattice results showing a change of sign of the gluon condensate [32] and a small value of the topological susceptibility [35] above T_c can be explained

in the glueball picture as well. Furthermore, one expects that the suppression of the mixing between glueballs and quarkonium states in the QGP leads to a smaller width for former as compared to the vacuum [33]. This property opens the possibility for clear separation of the glueball and the quark states in heavy ion collisions. Such separation is rather difficult in other hadron reactions due to existence of strong glueball-quarkonium mixing in the vacuum.

In the conclusion we would like to mention the large numbers of exotic candidates, so-called XYZ mesons, with charm quark content, which were found recently in BES-II, BELLE and BaBar experiments. Most of such states have unexpected values of the masses and widths [36]. Investigation of the hadron exotics is included also in the future experiments: PANDA (FAIR), GlueX (CEBAF) and BES-III.

ACKNOWLEDGMENTS

The author is very grateful to A.E. Dorokhov, S.B. Gerasimov, Dong-Pil Min, Hee-Jung Lee and V. Vento for useful discussions. This work was supported in part by RFBR grant 10-02-00368-a and by Belarus-JINR grant.

REFERENCES

1. R. L. Jaffe, Phys. Rev. D **15**, 267 (1977); Phys. Rev. D **15**, 281 (1977).
2. A. E. Dorokhov and N. I. Kochelev, Preprint JINR-E2-86-847, (1986), arXiv:hep-ph/0411362.
3. T. Schäfer and E.V. Shuryak, Rev. Mod. Phys. **70**, 1323 (1998).
4. D. Diakonov, Prog. Par. Nucl. Phys. **51**, 173 (2003).
5. A. E. Dorokhov, Yu. A. Zubov and N. I. Kochelev, Sov. J. Part. Nucl. **23**, 522 (1992).
6. N. I. Kochelev, Phys. Part. Nucl. **36**, 608 (2005) [Fiz. Elem. Chast. Atom. Yadra **36**, 1157 (2005)].
7. D. Diakonov, V. Petrov and M. V. Polyakov, Prediction from chiral solitons," Z. Phys. A **359**, 305 (1997).
8. R. L. Jaffe, Phys. Rept. **409**, 1 (2005).
9. M. Karliner and H. J. Lipkin, Phys. Lett. B **575**, 249 (2003).
10. N. I. Kochelev, H. J. Lee and V. Vento, Phys. Lett. B **594**, 87 (2004).
11. T. Nakano *et al.* [LEPS Collaboration and LEPS collaboration and LEPS collaboration and], arXiv:0812.1035 [nucl-ex].
12. P. Z. Aslanyan, V. N. Emelyanenko and G. G. Rikhkvitzkaya, Nucl. Phys. A **755**, 375 (2005); Yu. A. Troyan, A. V. Beljaev, A. Y. Troyan, E. B. Plekhanov, A. P. Jerusalimov, G. B. Piskaleva and S. G. Arakelian, arXiv:hep-ex/0404003.
13. R. De Vita *et al.* [CLAS Collaboration], Phys. Rev. D **74**, 032001 (2006); B. McKinnon *et al.* [CLAS Collaboration], Phys. Rev. Lett. **96**, 212001 (2006).
14. T. Nakano [LEPS Collaboration], Nucl. Phys. A **835**, 254 (2010).
15. A. Martinez Torres and E. Oset, Phys. Rev. Lett. **105**, 092001 (2010).
16. H. J. Lee, N. I. Kochelev and V. Vento, Phys. Rev. D **73**, 014010 (2006).
17. V. Kuznetsov *et al.*, Acta Phys. Polon. B **39**, 1949 (2008).
18. V. Kuznetsov *et al.*, arXiv:1003.4585 [hep-ex].
19. N. N. Achasov, arXiv:0810.2601 [hep-ph].
20. H. Leutwyler, Nucl. Phys. Proc. Suppl. **186**, 338 (2009).
21. H. J. Lee and N. I. Kochelev, Phys. Rev. D **78**, 076005 (2008).
22. S. Narison, Nucl. Phys. Proc. Suppl. **186**, 306 (2009).
23. V. Vento, Phys. Rev. D **75**, 055012 (2007).
24. E. A. Kuraev and M. K. Volkov, Phys. Atom. Nucl. **62**, 128 (1999) [Yad. Fiz. **62**, 133 (1999)].
25. S. V. Molodtsov, A. N. Sissakian, A. S. Sorin and G. M. Zinovjev, Phys. Part. Nucl. Lett. **5**, 7 (2008).

26. G. M. Beladidze *et al.* [VES Collaboration], Phys. Lett. B **313**, 276 (1993).
27. G. S. Adams *et al.* [E852 Collaboration], Phys. Lett. B **657**, 27 (2007); A. R. Dzierba *et al.*, Phys. Rev. D **73**, 072001 (2006).
28. M. Nozar *et al.* [CLAS Collaboration], Phys. Rev. Lett. **102**, 102002 (2009).
29. M. Alekseev *et al.* [COMPASS Collaboration], "Observation of a $J^{PC} = 1^{-+}$ exotic resonance in diffractive dissociation of 190 GeV/c pi- into pi- pi- pi+," Phys. Rev. Lett. **104**, 241803 (2010).
30. V. Mathieu, N. Kochelev and V. Vento, Int. J. Mod. Phys. E **18**, 1 (2009).
31. N. Kochelev and D. P. Min, Phys. Lett. B **650**, 239 (2007).
32. D. E. Miller, Phys. Rept. **443**, 55 (2007).
33. V. Vento, Phys. Rev. D **75**, 055012 (2007).
34. B. Muller and J. L. Nagle, Ann. Rev. Nucl. Part. Sci. **56**, 93 (2006) [arXiv:nucl-th/0602029].
35. B. Alles, M. D'Elia and A. Di Giacomo, Nucl. Phys. B **494**, 281 (1997) [Erratum-ibid. B **679**, 397 (2004)] [arXiv:hep-lat/9605013].
36. S. Godfrey and S. L. Olsen, Ann. Rev. Nucl. Part. Sci. **58**, 51 (2008).

List of participants

Alexander Andreev	BLTP, JINR Dubna	andreev@theor.jinr.ru
Vladimir Belyaev	BLTP, JINR Dubna	belyaev@theor.jinr.ru
Vratislav Chudoba	FLNR, JINR Dubna	chudoba@jinr.ru
Andrej Denikin	FLNR, JINR Dubna	denikin@jinr.ru
Alexander Dorokhov	BLTP, JINR Dubna	dorokhov@theor.jinr.ru
Sergey Ershov	BLTP, JINR Dubna	ershov@theor.jinr.ru
Sergo Gerasimov	BLTP, JINR Dubna	gerasb@theor.jinr.ru
Walter D. Heiss	Stellenbosch Univ.	dieter@physics.sun.ac.za
Taofiq Ibrahim	Stellenbosch Univ.	ibrahim@sun.ac.za
Noel M. Jacobs	Stellenbosch Univ.	mkhujac@hotmail.com
Rostislav Jolos	BLTP, JINR Dubna	jolos@theor.jinr.ru
Nikolai Korchagin	UNC, Dubna	korchagin_s@list.ru
Nikolai Kochelev	BLTP, JINR Dubna	kochelev@theor.jinr.ru
Elena Kolganova	BLTP, JINR Dubna	kea@theor.jinr.ru
Dmitry Kamanin	FLNR, JINR Dubna	kamanin@jinr.ru
Shuhrat Kalandarov	BLTP, JINR Dubna	shuhrat@theor.jinr.ru
Mantile L. Lekala	UNISA	lekalml@unisa.ac.za
Anastasiya Malykh	BLTP, JINR Dubna	maw@theor.jinr.ru
Siyabonga N.Th. Majola	iTHEMBA labs	majola@tlabs.ac.za
Azwinndini Muronga	Univ. of Cape Town	azwinndini.muronga@uct.ac.za
Alexander Motovilov	BLTP, JINR Dubna	motovilv@jinr.ru
Rashid Nazmitdinov	BLTP, JINR Dubna	rashid@theor.jinr.ru
Andrej Naumkin	BLTP, JINR Dubna	naumkin@theor.jinr.ru
Sergey Nedelko	BLTP, JINR Dubna	nedelko@theor.jinr.ru
Prince O.G. Ogunbade	Univ. of Pretoria	pogos77@hotmail.com
Sergei Rakitianski	Univ. of Pretoria	Sergei.Rakitianski@up.ac.za
Werner A. Richter	Univ. of West. Cape	richter@sun.ac.za
Elena Rogochaya	BLTP, JINR Dubna	rogoch@theor.jinr.ru
Maciej A. Stankiewicz	iTHEMBA labs	mstankiewicz@gmail.com
Timur Shneidman	BLTP, JINR Dubna	shneyd@theor.jinr.ru
Sofianos A. Sofianos	UNISA	sasofianos@gmail.com
Sergey Sidorchuk	FLNR, JINR Dubna	sid@nrmail.jinr.ru
Victor Voronov	BLTP, JINR Dubna	voronov@theor.jinr.ru
Andrey Vdovin	BLTP, JINR Dubna	vdovin@theor.jinr.ru
Shaun M. Wyngaardt	Stellenbosch Univ.	shaunmw@sun.ac.za